AN ABSTRACT OF THE DISSERTATION OF

Jacqueline Katherine Garcia for the degree of Doctor of Philosophy in Radiation Health Physics presented on August 23, 2022

Title: Exploring Novel Contrast Agents with Anthropomorphic Mesh Models in MCNP

Abstract approved: _____

Steven Reese

Abstract: Breast cancer is the leading cancer in women with an estimated 13% of women in the United States developing a form of invasive breast cancer in her lifetime. The survival rate is estimated to be 85%, but the American Cancer Society estimates that early detection of breast cancer in the localized stage increases the breast cancer survival rate to 99%. However, early detection is dependent on the sensitivity of breast imaging techniques and currently, the sensitivity is suboptimal for women with dense breasts and obscure cancers. Recently, studies have indicated that exploring new contrast agents can provide access to improved sensitivity because of their potential to increase the effective Z of the target tissue. Furthermore, contrast-enhanced tomosynthesis is a viable imaging method that can provide a 3D view of the breast while providing tumor enhancement for improved visibility. This project aims to facilitate the search for practical contrast agents that can improve sensitivity during breast imaging. More specifically, the objective of this project is to find novel ways to improve the differentiation between tumor and glandular tissue by creating a realistic anthropomorphic model that not only considers the geometry of the breast but its physiological components as well. This project aims to combine

tomosynthesis breast imaging methods with novel contrast agents to explore their efficacy and limitations. To achieve the goals of this project, several techniques are employed. A realistic tomosynthesis environment is created by constructing a detailed Hologic tomosynthesis breast imaging machine, including the source, flat-panel detector, and support equipment, using MCNP. Realistic breast phantoms that consider geometric and biophysical accuracy are created by incorporating a time dependency into the model. Once the contrast agents are incorporated, their efficacy is calculated by quantifying tumor visibility as a function of breast size, density, tumor location, tumor stage, and tumor type. After running simulations, this project will generate clear and accurate radiographs demonstrating the structural components of the breast and the effects of contrast enhancement on any embedded tumors. The results will provide an indication of the contrast agents that provide promise. The data acquired in this project will provide insight on the process of creating an anthropomorphic breast phantom for tomosynthesis studies, as well as insight on setbacks that are identified with the methods used. Contrast-enhanced tomosynthesis is clinically possible and is a promising technique for improving sensitivity. This project explores this technique and provides insight on possible ways to improve breast imaging sensitivity.

Exploring Novel Contrast Agents with Anthropomorphic

Mesh Models in MCNP

by

Jacqueline Katherine Garcia

A DISSERTATION

submitted to

Oregon State University

in partial fulfillment of

the requirements for the

degree of

Doctor of Philosophy

Presented August 23, 2022

Commencement June 2023

Doctor of Philosophy dissertation of <u>Jacqueline Katherine Garcia</u> presented on <u>August 23, 2022</u>

APPROVED:

_____

Major Professor, representing Radiation Health Physics

_____

Head of the School of Nuclear Science and Engineering

_____

Dean of the Graduate School

I understand that my dissertation will become part of the permanent collection of Oregon State University libraries. My signature below authorizes release of my dissertation to any reader upon request.

_____

Jacqueline Katherine, Garcia, Author

ACKNOWLEDGEMENTS

I would like to thank the department of Nuclear Science and Engineering at Oregon State University for providing me with the opportunity to study, preform research, and grow.

I would like to thank my advisor, Dr. Steven Reese, for providing me with the opportunity to work on this project and for providing ideas. Thank you for being patient, understanding, and believing in me. I would also like to thank the professors at the department of Nuclear Science and Engineering for providing engaging lectures and for inspiring me so that I may one day contribute to the field.

I'd like to thank my committee, Camille Palmer, Lily Ranjbar, Salam Alhawsawsi, Russ Turner, and again, my advisor Steven Reese, for setting aside time for me and this project. This is a shared effort.

A special thank you to all the friends I met at Oregon State; you motivated me to do my best and vastly improved the quality of my time at Oregon State. A very special thank you to Aaron Bode for always believing in me and for teaching me to always look at the bright side of things, even in the most difficult times. I could not have done this without you.

A very special thank you to the Gates Millennium Foundation for funding my education, and that of several other scholars, as a 10-year commitment. You have impacted the lives of thousands of students.

Finally, I am grateful to have finished my education in the midst of a global pandemic; I would like to commemorate those you lost their lives before they were able to achieve their dreams and those who lost their lives working at the frontline of the COVID pandemic. There are many changes occurring as I complete my PhD and I am privileged to have made it this far because there are many POC and women who are not able to receive an education. Education is not universal, so let's work towards a world where it is.

TABLE OF CONTENTS

TABLE OF CONTENTS (Continued)

TABLE OF CONTENTS (Continued)

LIST OF FIGURES

LIST OF FIGURES (Continued)

LIST OF FIGURES (Continued)

LIST OF TABLES

DEDICATION

I dedicate this text to Aaron Bode, my family, and my friends.

Part I: Background

1 Introduction

1.1 Historical Context

1.1.1 The First Radiograph

In 1895, a radical discovery was made that would revolutionize medicine. Although previously explored by Morgan, Davy, and Faraday[1], the potential of x-rays wasn't uncovered until Wilheim Röntgen came across them while experimenting with a Crooke's tube emanating cathode rays.[2] Curious by the fact that these newly uncovered rays could pass through matter, Röntgen experimented with their ability to pass through human tissue. When his wife lent him a hand,[3] the first ever x-ray was produced and in that moment, he unknowingly discovered a branch of science that would lead to medical imaging, nonproliferation detection equipment, and much more. Shortly thereafter, numerous publications reported the potential of X-rays and several studies emerged eager to discover the potential behind them.[4,5] It had only been months after Röntgen's discovery that this novel x-ray technology was used in a surgical operation.[6] This was quickly followed by 'live' medical devices that led to the development of the fluoroscope in the following months.[7] It wasn't long before x-ray equipment further evolved into sophisticated devices that would be widespread in hospitals worldwide.

Shortly after the discovery of x-rays and x-ray-based equipment, the consequences of radioactive technology became apparent; scientists began reporting hair loss, burns, and other symptoms of radiation sickness due to the prolonged exposure of ionizing radiation.[8] Nonetheless, despite numerous reports associated with early x-ray imaging and experimentation, scientists failed to establish the connection between the two claiming the effects were due to UV rays; some went as far as to report that x-ray exposure

had no consequences at all.[9,10] Over the next few years, x-ray imaging equipment improved and imaging scanning times declined, reducing the number of reported injuries. Unfortunately, pioneers of x-ray equipment became ill with metastatic carcinoma and died at young ages.[11] Despite the obvious correlation between x-ray usage and adverse effects, doctors were lax with the administration of x-rays and increased the number of patients receiving a form of imaging from 1.31% in 1900 to 25.25% 1925.[12]

Due to the rising popularity of x-ray equipment, physicians became experts in x-ray tubes as they became dedicated in understanding and improving the technology in its early formative years; this led to the creation of radiologists.[13] These physicians were experts in both the science behind the tubes as well as the administration of them in a clinical setting. During these formative years, x-ray imaging became more accurate and more applicable (especially to large body parts) with the employment of more energetic rays.[14] During this time, early forms of films used for screening were replaced with a calcium tungsten screen that was developed by Thomas Edison who reported that exposure time vastly decreased from an hour to only a few minutes.[15] Soon after, glass tubes that were used as a means to generate x-rays for almost two decades were replaced by Coolidge tubes invented by William Coolidge. These tubes eliminated the need for gas and instead utilized a tungsten filament that supplied electrons to the anode. Due to the lack of gas, images became much clearer, and the amount of dose given to a patient could be clearly approximated.[16] This improvement paved the way for the modern radiology.

The concept of a rotating anode was suggested by Robert Wood and Coolidge.[17] They believed that a rotating anode could help distribute the heat formed by the electrons which would allow for a larger focal spot. This idea was not commercialized until ten years later when newly found Philips labs created the first marketable rotating anode.[18] This rotating anode allowed for reduced exposure times of up to 2 orders of magnitude. Ways to improve x-ray tubes quickly emerged as Philips, Varex, Siemens, and General Electric competed with one another to hold commercial advantage; copper was introduced in the design, new anode shapes were tested, shielding was improved, and x-ray beams became more reliable. In the midst of experimentation, new x-ray-based technologies arose, such as CT scanners, dental x-rays, angiography, and mammography.

1.1.2 The Development of Breast Imaging: From X-ray Film to Tomosynthesis.

      With the creation of x-ray technology, several physicists sought ways to use this technology to solve an assortment of medical problems. In 1913, Albert Salomon experimented with a primal form of mammography – he performed over 3,000 x-rays of mastectomies where he compared the differences between removed breasts and non-removed breasts.[19] He discovered the ubiquitous presence of calcifications in the removed breasts and more importantly, established distinguishable features found in breast cancer, therefore establishing the differences between cancerous and non-cancerous breasts seen in x-ray images. His work provided invaluable information on tumor growth and metastasis. Seventeen years later, Stafford Warren produced stereoscopic x-ray images to investigate mutations in the breasts caused by lactation and mastitis.[20] During his research, he correctly predicted 54 out of 58 breast cancer cases out of 119 women who underwent surgery. Despite research demonstrating a commercial potential for breast imaging, it wasn't until 20 years later when radiological parameters were created to accommodate breast imaging.

      Raul Leborgne was one of the first radiologists to establish modern radiology by expressing the need for radiological parameters and patient positioning during breast imaging. He focused on not only improving image quality, but also finding the differences between benign and cancerous calcifications.[21] A year later, in 1950, Leborgne developed the breast compression technique to improve image quality by reducing motion; this technique is still used today. These advances paved the road for what would be known as mammography, coined by Robert Egan.[22] Egan created the technique that combines low kVp with high mA in conjunction with single emulsion films to create the "Egan technique" which he later renamed. This technique focused on differentiating calcifications in breast tissue and with this technique, Egan and his team were able to identify 238 breast cancer cases out of 245. Although mammography's potential was evident with Egan's work, it took a study conducted by Philip Strax proving that mammograms reduce mortality to establish mammography as a widespread screening technique in a clinical setting.[23]

Egan's work created the fundamental technique behind mammography and in the following decades, the equipment used in his technique evolved to produce the technology available today. At the time of Egan's research, direct-exposure films were the standard 'detectors' used which required an exposure time of approximately six seconds.[24] The first major improvement following Egan's work was the introduction of xeromammography. Xeromammographic is a photoelectric technique that records x-rays images (breast images) onto a coated metal plate and it was created by John Wolfe with the collaboration of Xerox ©.[25] Xeroradiography was a preexisting imaging technique that had been adapted from xerographic photocopying; the technique was simply adapted to accommodate breast screening. Xeromammography was only around for a few years because it was still impractical despite it being an improvement from direct-exposure film. The technique was limited in its innovation potential and the exposure dose was still relatively high. A year later, DuPont introduced the first screen-film technology for mammography.[26] This new technique reduced the dose by about 10-20 times compared to direct-exposure and it also enhanced the contrast albeit by only a small margin.[27] This technique was an improvement from direct-exposure mammography because it used a single-screen, single-emulsion combination and it included a vacuum bag system that provided adequate screen-film contact. 3 years later, Kodak introduced screen-film combinations that paired with rare earth phosphor screens which cut the exposure dose by half and created sharper images. To this day, the majority of screen-film mammography is executed with a single intensifying screen paired with single emulsion film. Modern mammographic screens can include phosphors that contain metals from the lanthanide series, and the phosphors can also contain light absorbers to increase image sharpness.[28] Over the last few decades, much attention was placed into screen-film combinations and film processing to reduce the exposure dose to patients and improve image quality. Today, the dose received from a single screen-film mammography is about 50 times less than that received from direct-exposure filmed mammography.

While screen-film mammography improvements were made, the concept behind digital mammography was underway with the development of digital image receptors.[29] The electrical signals collected from these receptors could be read and manipulated on computer screens which provided

advantages over film-screen mammography. In 1996, the FDA released guidelines that companies needed to follow to develop digital mammography.[30] Four years later, General Electric's Senographe 2000D was approved by the FDA for clinical use thus introducing the world to digitalized mammography. The transition from film-screen to digital mammography was not a quick one; the new technology posed challenges that were not easily overlooked. The cost of the new equipment far exceeded that of the traditional media, equipment was far less intuitive and technicians struggled with troubleshooting, the spatial resolution was lower, and radiologist required retraining to understand the new equipment.[31] However, a major advantage that digital mammography provided over screen-film mammography was the improved accuracy among women with dense breasts.[32] As digital mammography gained popularity and funding, focus was placed onto improving the equipment to improve image quality. The sensitivity improved, dose decreased, and the resolution improved. This improvement was a long and ongoing process that slowly motivated hospitals to switch to digital techniques. The transition to digital provided advantages over film-screen technology and one of the most important advantages was, and still is, cross correlation with other imaging modalities.

Early applications of cross-correlating imaging modalities for breast imaging date back to the 1950s when Wild and Reid used ultrasound to detect breast malignancies.[33] Their goal wasn't to establish ultrasound imaging as screening tool but instead as a supplement to mammography. The purpose of using ultrasound in conjunction with mammography was to better differentiate benign from malignant tumors. Their early experimentation proved that supplementing mammography with ultrasound increased detection accuracy by a large margin. Following these positive results, sonographic equipment improved to better accommodate breast imaging.[34] In the late sixties and seventies, several studies took place that investigated the efficacy of ultrasound in breast imaging. The goal of these studies was to find the limitations in ultrasound imaging therefore multiple breast cancer types were included. The studies proved that although ultrasound was very successful in identifying ductal carcinoma, it could not identify medullary carcinoma due to its highly cellular and homogenous nature.[35] Nevertheless, the use and study of ultrasound breast imaging techniques continued until present day. In some cases, ultrasound has been used as a whole-breast

imaging technique. Although ultrasound imaging produces low-quality, low-resolution images, it is capable of locating small tumors in women with dense breasts at a higher rate than mammography.[36] In addition, the use of ultrasound as a supplementary tool to mammography wasn't abandoned; in 2003, the American College of Radiology Imaging Network found that supplementing mammography with ultrasound increased the detection of malignancies by 4.2 per 1000 cases.[37] Unfortunately, a mammography-ultrasound protocol is time consuming and the resources available to impellent this technique are not widely available. Given its potential, solutions for these limitations are still under investigation.[38]

Clinical use of magnetic resonance imaging, or MRI, for breast imaging was introduced in the mid 1980s.[39] Initial results were underwhelming; no significant improvements were achieved with MRI over mammography. However, the introduction of gadolinium contrast agents tremendously improved differentiation between tumors and normal breast tissue.[40] MRI has multiple advantages over mammography; MRI sequence can be selected to show structural and or metabolic functions, it has the highest sensitivity out of any breast imaging technique (over 90%), and it doesn't use ionizing radiation therefore there is minimal risk associated with this technique. However, MRI is very costly and time consuming making it impractical for screening purposes. In addition, the specificity is very low because of MRI's high false-positive rate, which leads to unnecessary biopsies.[41] Because of these downsides, MRI is typically reserved for high-risk patients, such as patients with genetic risk factors, or patients who have a history of cancer.[42] MRI isn't commonly used as a supplementary tool in screening mammography outside of high-risk patient screening, but it is often used as a diagnostic tool when mammography screening results demonstrate a potential malignancy.

Another breast imaging technique is breast computed tomography, or BCT. BCT uses very similar technology as mammography and it has no purpose as a supplementary mammography tool. Instead, BCT is used as its own diagnostic tool similar to MRI. The creation of BCT followed the advancement of mammography. As x-ray equipment improved, physicist pondered the idea of 3D imaging techniques. This led to the formulation of computed tomography which could produce 3D images by taking axial images around the whole patient. General Electric produced the first experimental breast CT scanner in the late

1970s and subsequent human trials ensued from 1976 to 1981.[43] The experimental BCT scanner used a single-slice fan bean that scanned patients in the pone position. The reconstructed images were coarse with a 1cm slice width and a voxel size of 1.56mm. In a study with 78 confirmed cancer cases, BCT paired with contrast media was able to detect 94% of cancer cases thus outperforming mammography by roughly 17%.[44] Despite the positive results, BCT was not supported because of the poor spatial resolution and excessive dose. Until the 21st century, BCT was ignored as a viable breast imaging technique. Recent modifications to CT equipment and techniques resparked interest in using CT for breast imaging; this new technique is known as digital breast tomosynthesis, or DBT.

Tomosynthesis is very similar to CT with the primary difference being the screening angle; while CT scans around the entire target, tomosynthesis uses a limited angle, typically between 30 and 60 degrees. The theoretical framework behind a limited angle imaging device was created in the 1930s by Ziedses des Plantes.[45] However, it wasn't until the development of digital detectors when tomosynthesis technology came to fruition. Until then, theories and methods surrounding tomosynthesis and tomosynthesis reconstruction were underway. In 1972, the term "tomosynthesis" was coined by Grant when he described a method for tomosynthesis reconstruction.[46] In the years that followed, variants of tomosynthesis imaging were developed but because they didn't use digital detectors, images produced by these methods experienced blurring from objects located outside the field of view.[47] The lack of digital detectors posed several challenges in acquiring projection images. A few years later, algorithms were developed to aid in image reconstruction, such as the matrix inversion tomosynthesis algorithm. Images were acquired with screen-film technology in a series of projections then digitized. The images were then reconstructed with the algorithm. The downside to this approach is the excessive amount of time needed to reconstruct the images. Despite the numerous improvements made in mammography technology and CT, the barriers surrounding tomosynthesis technology could not be overcome and so the technology was ignored for the rest of the 20th century. The 3D potential of tomosynthesis was achieved with the newly invented spiral CT, therefore there was little motivation to progress tomosynthesis.

With the invention of the flat-panel detector in the late 1990s, the obstacles preventing the use of tomosynthesis were overcome. The flat-panel detector allowed self-scanning without geometric distortion and high levels of noise. This detector permitted scanning and processing speeds fast enough to make tomosynthesis a feasible piece of equipment for a clinical setting. Research quickly ensued with the development of the flat-panel detector and scientists became highly interested in using tomosynthesis for breast imaging because it had the potential to offer the benefits of both mammography and CT.[48] The data acquired with tomosynthesis had very high resolution comparable with mammography (85-160 microns) and although it didn't provide a "full-view" of the breast like in CT, it still demonstrated comparable detection rates comparable to CT.[49] Dose studies conducted on tomosynthesis methods for breast imaging found that the dose increase administered by tomosynthesis compared to mammography was modest. Given the clinical benefits of tomosynthesis, the higher dose given by tomosynthesis over mammography didn't dissuade further research into the technology.[50] Continuous research led to dedicated use of tomosynthesis for breast imaging thus establishing digital breast tomosynthesis (DBT) as an official breast imaging technique. With these results, the FDA approved the use of DBT in a clinical setting in 2011, marking the beginning DBT as a screening method.[51]

1.1.3 The Evolution of Contrast Agents and their Revolutionary Impact

During the development of x-ray technology, scientists discovered ways to improve contrast in organs of interest with contrast media. Although it would take decades for the commercial use of iodinated contrast agents, the idea of using contrast agents in imaging came to light in 1904 when Hermann Rieder took radiographs of a patient who had ingested large amounts of bismuth subnitrate.[52] The radiographs revealed strong contrast of the stomach lining compared to the surrounding organs thus implicating bismuth as a 'contrast aid.' A couple decades later in 1929, Thorotrast was introduced into radiographic imaging as a contrast aid.[53] This contrast agent used thorium dioxide as the main attenuating molecule and although it provided adequate image enhancement, it was also radioactive. Its carcinogenic properties were discovered

in the 1950s when its correlation with stomach, liver, bile ducts, and bone cancers was discovered. It was eventually discontinued but not after it had been administered to millions of patients.

Around the same time that Thorotrast was discontinued, iodinated contrast agents were clinically introduced.[54] Soon after, Torsten Almen introduced non-ionic iodine contrast agents in the 1970s after learning of the discomfort that patients experienced with ionic iodine contrast agents due to their high osmolarity.[55] The first non-ionic iodine contrast agent that emerged was Amipaque, followed by Omnipaque about a decade later, which was then followed by Visipaque about another decade after. To this day, iodine-based contrast agents remain the most widely used contrast agents for x-ray-based imaging techniques with an estimate of 75 million annual doses.[56] Iodinated contrast agents were quickly and widely adopted due to their relatively low cost and multifunctionality aiding in several imaging techniques including computed tomography, venography, angiocardiography, myelography, conventional fluoroscopy and several others. Because iodinated contrast agents function through the circulatory system, they can be used anywhere the circulatory system is found making them highly versatile.

Since contrast agents are often paired with CT, most of the application of contrast agents in breast imaging are in BCT. However, as mentioned earlier, because of the high dose rates associated with BCT, contrast enhanced BCT isn't used as a breast cancer screening technique. The use of gadolinium for MRI imaging became commonplace in the 1980s. Shortly after, gadolinium enhanced breast MRI was shown to improve tumor visibility. The high cost of MRI disincentivizes this practice in addition to the fact that MRI can already achieve high sensitivity without the extra cost of contrast agents.[57] On the other hand, early studies of contrast enhanced mammography proved the technique increased tumor visibility without the high costs implicated with MRI and without the high dose implicated with BCT.[58] The discovery of digital mammography introduced a method in breast imaging known as dual-energy contrast-enhanced mammography. This technique slightly increased the exposure dose associated with conventional digital mammography, but it allowed radiologists to subtract two images, such as non-enhanced and enhanced images of the same region, to find regions with high contrast. This allowed radiologist to better differentiate tumors.

Contrast agents have only been around for a few decades, and they have not evolved much since the 1980s. The main reason for this is because it is difficult to find contrast agents that satisfy all of the requirements needed for clinical applications, including: improving the contrast between the target and the background by at least a factor of two, a high mole percent of the primary attenuating agent (such as iodine), a reasonable retention time, and favorable biodistribution, among other qualities.[59] In x-ray based imaging technologies, contrast agents are valuable if they improve sensitivity, provide biochemical information about a tissue or region, and if they provide information on the status of an organ or tissue. A current interest in contrast agent evolution is exploring new materials or methods that can increase contrast further than current standards. New materials are currently being explored that can improve current contrast provided by iodine-based contrast agents. More specifically speaking, physicists are looking for ways to increase the Hounsfield Unit (HU) gap between the target and the surrounding tissue in CT imaging.[60] Since the same standards apply to other forms of x-ray-based imaging, these new contrast agents would also improve target differentiation in mammography and tomosynthesis. Exploring novel pharmacokinetic methods that can improve contrast, such as attaching antigens that target tumor antibodies or other tumor markers, can also vastly improve current contrast agent standards.[61] These methods might also be able to provide biochemical information about tumor growth patterns that don't currently exist with CT, mammography, or tomosynthesis. Both of these approaches will be discussed in more detail later in this text.

1.1.4 Voxelization to Unstructured Mesh: MCNP's Role in Medical Sciences

The Monte Carlo method for radiation transport was created in 1946 by Los Alamos National Laboratory after it had been theoretisized by Stanislaw Ulam.[62] John von Neuman then created the first assembly of the computer code and made some assumptions about the particle transport. Although initial runs only contained 100 neutrons, it is estimated that each run had a computational time of 5 hours.[63] Robert Richtmyer suggested changes to the code that would allow for multiple fissionable materials as well as other changes; the code was finalized a year after it was first suggested. Shortly after, Enrico Fermi created a device, called Fermiac, that would trace neutron movements using the Monte Carlo method.[64] During the

1950s and 60s, several Monte Carlo codes for particle transport were developed; these contained new Monte Carlo methods for neutron and photon transport and were written in Fortran. Eventually, these codes were combined into a single code in 1977 creating the first version of MCNP. However, the code wasn't released until 1983 by RSICC as MCNP3. Since then, MCNP has been under continuous development and is currently in its sixth version. This last version, MCNP6, is a merger between MCNP5 and MCNPX (also developed by LANL).[65]

As the years went on, MCNP software was updated to implement changes capable with the modernization of computers. One of the first major improvements was the implementation of plotting graphics in 1988. This MCNP update, MCNP3B, included generalized sources, surface sources, and repeated structures (lattice) geometries.[66] The following update included electron transport and parallel multitasking. Three years later, MCNP4A introduced new photon libraries, ENDF-6, color graphics, dynamic memory allocation, and it contained enhanced statistical analysis. MCNP4B introduced enhanced photon physics, cross-section plotting, lattice universe mapping among other features. MCNPX was introduced in 1999 and it included mesh and radiography tallies, hence it was popularly used for medical applications. MCNP5 emerged in 2002 written in Fortran 90 and it included photonuclear collisions, superimposed mesh tallies, and Mac OSX support. Over the years, MCNP5 was developed to include more detectors and tallies (up to 10k tallies), lattice and fmesh tally enhancements, spontaneous fission sources, pulse height tallies, stochastic geometry, mesh tally plots, photon Doppler broadening, significant lattice enhancements, and much more. When MCNP5 and MCNPX were merged to create MCNP6, the most robust and comprehensive version of MCNP was created. MCNP6 includes the features described in MCNP5 and MCNPX as well as updates, such as protons and proton radiography, magnetic fields, unstructured meshes, high energy physics models, continuous testing models, and an abundance of other features. Because of this, MCNP is used as a reliable tool to conduct medical simulations with, including voxel modeling to simulate dose distributions, photon distributions in CT imaging, and much more.

One of the most common uses of MCNP for medical applications is determining the dose imparted on a patient during an imaging procedure. This is often done by replicating the human geometry/body

part(s) in MCNP with a series of voxels generated with MCNP's lattice capabilities. Voxels are essentially 3D pixels and in the late 1980s, the Visible Human Project was established to create extensive data on human anatomy by slicing a male cadaver into 1871 slices; these slices were later used to create 'Voxel-man.'[67,68] Voxel-man is one of many voxel models used to represent the human body during biomedical simulations. Visible Photographic Man (VIP-Man), Extended-cardiac Torso (XCAT), and Virtual Family models are voxel models of the human body created from segmented CT and MRI data.[69] Although voxel phantoms have been used over the last two decades to run biophysical MCNP simulations with, they are not the only type of computational phantoms used in MCNP. Mathematical phantoms are created from a series of equations defining organ boundaries and although they may not be as accurate as voxel phantoms, they require much less computational time. With the release of MCNP6, a new form of computational phantoms was introduced. Unstructured mesh phantoms have been found to improve accuracy and run time compared to voxel phantoms. **Figure 1** demonstrates the three different phantoms that can be modeled with MCNP software. These phantoms are capable of providing dose and flux information for each element in the phantom and the mesh can undergo multiphysics finite element analysis that can vastly improve current biophysical models.

(a)   (b)   (c)
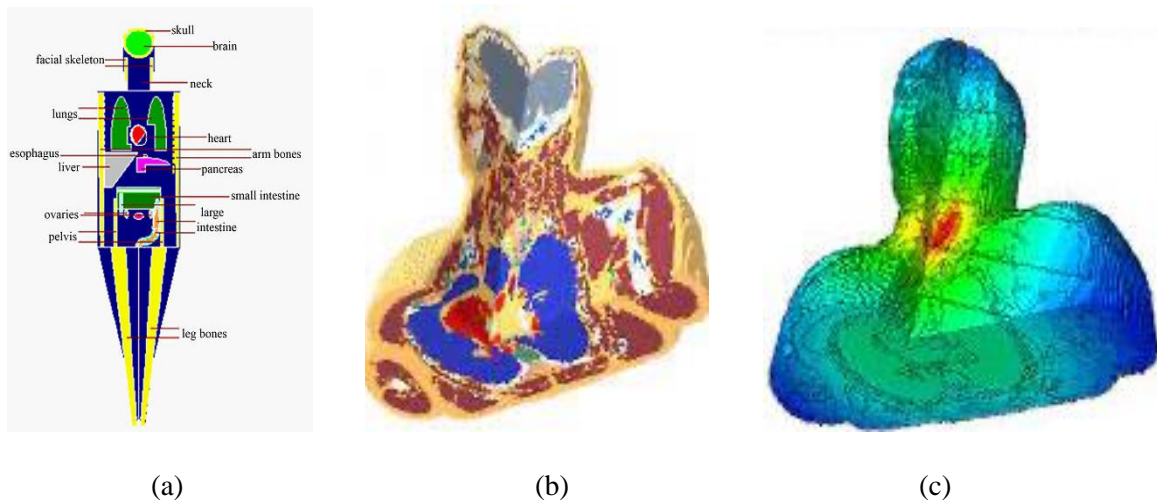
Figure 1:[70] The three different phantoms used in MCNP: (a) a computational phantom of the body constructed using a series of equations, (b) a torso reconstructed with voxel phantoms, (c) a torso reconstructed with mesh phantoms.

1.2 Significance

1.2.1 The Global Impact of Breast Cancer

Breast cancer is the leading cancer in women with an estimated 13% of women in the United States developing a form of invasive breast cancer in her lifetime.[71] In 2018 alone, there were 2 million new cases and a total of 627,000 deaths globally.[72] Although the 5 year survival rate is relatively high in developed countries, averaging at about 85%, the disease is nonetheless devastating.[73] Victims often suffer from severe anxiety and depression, pain, and financial burden, and it can also be a life changing. Breast cancer treatment options include radiation therapy, chemotherapy, hormonal therapy, and even mastectomy where the entire breast is removed to prevent the spread of cancer.[74] The intensity of the treatment depends on the severity of the disease and most women undergo unpleasant side effects during treatment. On top of that, survivors have to live with the fear of reoccurrence. Financial burden caused by cancer treatment was reported for 35% of breast cancer cases in 2018 with most of the same cases reporting reevaluation of treatment due to cost.[75] In the United States, the annual cost of breast cancer in 2020 exceeded 200 billion dollars and was one of the largest national medical service costs.[76] Because of the considerable impact that breast cancer has on victims and the country, preventative measures have become an important topic of conversation among women and their primary care doctors. Early detection of breast cancer can reduce the severity of treatment and has shown to improve the five-year survival rate.

The American Cancer Society estimates that early detection of breast cancer in the localized stage increases the breast cancer survival rate to 99%.[77] Early stages of breast cancer are asymptomatic therefore the cancer can remain unnoticed until it develops into a higher stage where the patient might begin to feel a lump under the skin along with irritation. Because early stages of breast cancer don't produce symptoms, the only way to detect it is with routine screenings with mammographic imaging. Studies have demonstrated the correlation between early detection and survival because survival is strongly associated with the stage at diagnosis.[78] If detected too late, there is a strong likelihood of lymph node invasion that can severely deteriorate one's chances of long-term survival.[79] Given its association with improved survival rates, screening programs have been implemented in a variety of countries, including most developed countries.

These countries have reported an approximate 25-30% reduction in breast cancer mortality due to these programs with some countries reporting a decreased mortality rate of up to 32%.[80] The positive impact of regular screening programs has motivated ongoing research to improve breast cancer detection rates to maximize the benefits of screening programs.

1.2.2 Challenges in Breast Imaging and the Impasse to Improved Detection

Mammography and other x-ray-based imaging techniques create images from differences in x-ray absorption, or attenuation, properties among the imaged materials. Materials with a high density or high atomic number are good at absorbing x-rays (which is why lead is often used as a shielding material). The relationship between material density and attenuation coefficient for most energies, including the energy range that breast imaging is conducted at, can be described by **equation 1**.

$$\mu = \frac{\rho Z^4}{AE^3} \quad (eq.\,1)$$

where μ is the attenuation coefficient, ρ is the material density, Z is the atomic number, A is the atomic mass, and E is the energy of the incident photon. The relationship between the atomic number and the attenuation coefficient allows for good contrast between tissues with slight differences in composition and density. At x-ray energies between 20 and 30 keV (produced from 30 kVp) where mammography is typically conducted at, adipose and glandular tissue are easily distinguishable due to differences in their density.
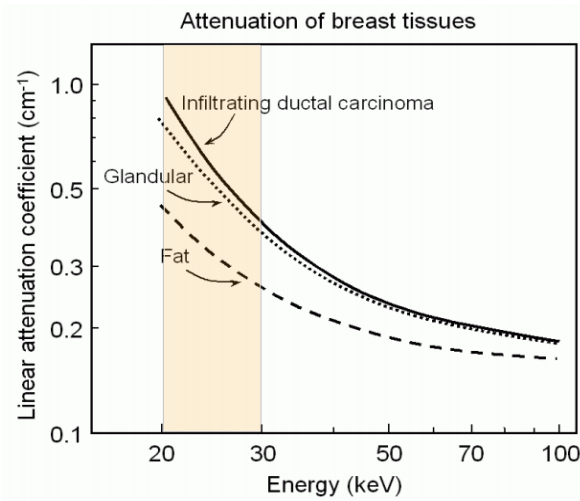
Figure 2: A graph demonstrating the relationship between linear attenuation coefficients and breast tissues as a function of energy. The highlight between 20 and 30 keV shows the attenuation expected during mammography.

However, most breast tumor tissues and glandular tissue share a very similar attenuation coefficient at energies above 20 keV due to similar densities. In **Figure 2**, the linear attenuation coefficients for glandular, adipose, and tumor tissue are shown; the figure demonstrates the close proximity between the glandular and tumor tissue alluding to the similarity between these two tissues during an imaging procedure.[81] For this reason, tumor tissue is difficult to differentiate from glandular tissue in non-enhanced mammography. Large quantities of glandular tissue in a breast can impose challenges in tumor detection, especially when the tumor mass is small.

Small tumor masses and a lack of calcifications can make it challenging to identify a malignancy during a screening procedure among women with large amounts of glandular tissue. The amount of glandular tissue a female has can be classified with the BI-RADS (Breast Imaging Reporting and Data System) scale. The BI-RADS category a woman belongs to can be determined by the following standards:[82]

- A: The breasts are almost entirely fatty (<20% glandularity by volume)

- B: There are scattered areas of fibroglandular tissue (20%-45% glandularity by volume)

- C: The breasts are heterogeneously dense, small masses might be obscured (45%-75% glandularity by volume)

- D: The breasts are extremely dense, which lowers the sensitivity of mammography (>75% glandularity by volume)

Women with breast density C and D experience a loss of sensitivity because the large presence of glandular tissue can obscure small masses. The efficacy of an imaging technique can be quantified by its *sensitivity, specificity,* and *accuracy* which are defined by **equations 2, 3** and **4**, respectively:

$$\text{Sensitivity} = \frac{\text{True Positives}}{\text{True Positives} + \text{False Negatives}} \quad (\text{eq. } 2)$$

$$\text{Specificity} = \frac{\text{True Negatives}}{\text{True Negatives} + \text{False Positives}} \quad (\text{eq. } 3)$$

$$\text{Accuracy} = \frac{\text{True Negatives} + \text{True Positives}}{\text{All Samples}} \quad (\text{eq. } 4)$$

Several studies have reported a strong correlation between dense breasts and low mammography sensitivity. The percent decline in sensitivity for women with BI-RADS category 3 and 4 varies per study but typically lies between 20 to 30% compared to the sensitivity reported for women with BI-RADS category 1 and 2. In a study that explored trends among the different breast densities from data gathered between 2012 and 2013, the sensitivity for women with BI-RADS category 4 was an abysmal 47%.[83] In addition to experiencing decreased sensitivity, women with dense breasts also experience an increase in breast cancer occurrence. The same data showed that the probability of developing breast cancer among women with dense breasts was 2.45 times higher than women with non-dense breasts. Because of the high occurrence of breast cancer and lowered sensitivity, it's important to create breast imaging techniques that don't deteriorate with high breast density.

Incorporating contrast agents into breast imaging has shown to increase sensitivity, especially in women with dense breasts. Studies with the highest improvement in sensitivity have reported sensitivities of 87.5%, 96.5%, and 97% with some studies reporting sensitivity increases of up to 40% compared to conventional mammography.[84,85,86] A study comparing contrast enhanced digital mammography versus conventional mammography found only a 6% increase in sensitivity.[87] Despite the margin of increase in sensitivity, contrast enhanced mammography has reliably shown better performance compared to conventional mammography, with the largest improvements observed among women with dense breasts. As mentioned previously, the current clinical contrast agents used in breast imaging are iodine-based.

Although these contrast agents are well established, there are issues associated with iodine-based contrast agents. Some patients might have adverse reactions due to an iodine allergy and other patients might experience renal toxicity and other potential health risks that have been reported for these type of contrast agents.[88] Another issue with these contrast agents is their relatively short clearance time; in breast imaging applications, images must be acquired within 10 minutes post injection. Because of the short clearance times, images will often show a decline in the contrast effect with each subsequent image. Iodine contrast agents also have relative low attenuation capabilities compared to other lanthanide contrast agents that have recently been proposed (Lusic 2012). Iodine has a k-edge at 33 keV, which sits right above the energy range typically used for mammography (20-30 keV). This means that the x-ray beam should remain at energies just above this energy to fully take advantage of the contrast agent's attenuation properties. This can be an issue because women with large breasts often require x-ray beams with slightly higher energies of about 30-40 keV, and so the contrast between the 'contrast region' and non-contrast region might be small. Finally, current x-ray-based contrast agents work by targeting the vasculature. The contrast agent infiltrates the vasculature around an organ or region of interest.[89] In breast imaging applications, the contrast will trickle down the breast vasculature into the glandular structure. Angiogenesis is a trait of tumor development and the increase in vasculature surrounding the malignant region means that the contrast agent will concentrate around the mass. While this is often effective, the efficacy depends on the tumor stage since novel and small masses won't have as much vasculature surrounding them, and it also depends on the tumor *type* since certain breast cancers, although rare, will have different vasculature growth rates. Consequently, improving contrast agents' targeting abilities can improve the ratio of contrast agent absorption in the region of interest relative to its surrounding tissue.

1.2.3 An Alternate Approach to Current Imaging Techniques

Current imaging techniques need to be further developed to improve the imaging sensitivity of women with dense breasts and the sensitivity of obscure cancers, such as those close to the chest wall as well as small tumors with poorly vascularized regions. The recent advancement of tomosynthesis has

created an avenue of new imaging techniques that have yet to be explored. Studies of non-enhanced tomosynthesis have reported a modest increase in sensitivity compared to full-field digital mammography with a more notable increase in sensitivity of up to 10% among women with dense breasts.[90] A study in 2021 involving 90 female patients reported a diagnostic accuracy of 97.7% for tomosynthesis, far exceeding digital mammography's diagnostic accuracy of 71.11%.[91] The specificity is also allegedly higher than that of digital mammography; a study involving 2,666 breast lesions found a 7% increase in the specificity with tomosynthesis versus digital mammography.[92] Because tomosynthesis incorporates the 'multi-view' feature that CT imaging features, masses obscured behind glandular tissue in mammography imaging are more likely to stand out in tomosynthesis without exposing the patient to a considerable radiation dose. Given the relatively high success of tomosynthesis in breast imaging, especially among women with dense breasts, future breast imaging development should focus on evolving this novel technique as a primary breast imaging system.

Another possible avenue to improve breast imaging sensitivity is to propose new contrast agents with higher effective-Z values or better targeting mechanisms to improve the contrast between the tissue of interest and the background. Although the Z-value for iodine is 53 – which is significantly higher than muscle's 7.71 – iodine contrast agents have a significantly lower effective Z.[93] This number is affected by the number of iodine particles per contrast agent molecule. Ioxaglate, for example, contains 6 iodine atoms per molecule in the chain repeat ($C_{31}H_{38}I_6N_6O_{13}$) while iohexol has 3 iodine atoms for a smaller molecule ($C_{19}H_{26}I_3N_2O_9$), both shown in **Figure 3**.[94]

(a)   (b)
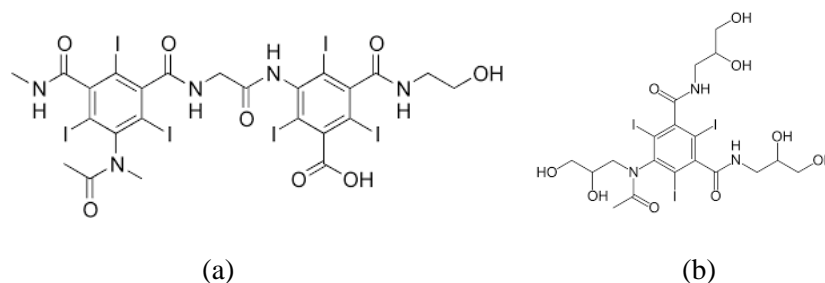
Figure 3: (a) The molecular structure of an Ioxaglate particle, (b) the molecular structure of iohexol.

The higher the amount of iodine per molar mass of contrast agent solution, the higher the effective Z. However, it is important to note that simply increasing the effective Z of the contrast agent by increasing the quantity of iodine in the molecule is not as easy task. The properties of the contrast agent must remain biologically favorable; this means the osmolarity, pH, viscosity, etc. must be compatible *in vivo*. Because this is not easily done with iodine-based contrast agents, other avenues to increase the effective Z of contrast agents are being explored. Heavy metals have become an attractive option as the primary attenuating particle in contrast agents because of their high density/high-Z and their higher k-edge compared to iodine. Silver, gold, bismuth, and other lanthanides are elements of interest because of their highly attenuating properties. Silver, with a Z-value lower than iodine's, has a density twice that of iodine's. Gold, on the other hand, has a density almost twice that of silver's and provides 3 times higher attenuation compared to iodine per unit weight.[95] With a k-edge at about 80 keV, gold contrast agents permit higher x-ray energies. However, because of the high cost implicated with gold, other heavy elements have also been researched for contrast agent applications.

Currently, there are no clinical applications of contrast enhanced tomosynthesis. Combining both tomosynthesis and contrast media provides 3D contrast enhancement which can provide improved lesion localization and characterization compared to contrast enhanced digital mammography. However, contrast-enhanced mammography requires a higher exposure dose compared to conventional digital mammography because of the dual-energies applied; a low-energy scan is performed below the k-edge while the higher-energy scan is conducted right above the k-edge. The images are then subtracted to identify the contrast-enhanced region. The same concept applies to tomosynthesis, though, tomosynthesis yields a higher exposure dose due to the multiple images acquired during a single scan. In a study with over 1,200 samples, the mean glandular dose for tomosynthesis was found to be 1.858 mGy whilst the dose for full-field digital mammography was found to be 1.374 mGy.[96] The shift from digital mammography to contrast enhanced mammography introduces a dose about 20-80% times higher than the former, therefore, it is expected that shifting from conventional tomosynthesis to contrast enhanced tomosynthesis will also induce a higher

dose.[97] Given the increase in exposure dose introduced by contrast enhanced tomosynthesis, there is hesitation in its clinical application. Moreover, if there is sufficient evidence proving that contrast enhanced tomosynthesis has the potential to drastically increase sensitivity, especially among women with dense breasts, then its clinical application might be encouraged.

1.3 Objectives

Cancer impacts a large percentage of adults worldwide. The stress, financial burden, and mortality rates are reduced with improved early detection. However, early detection is dependent on the sensitivity of breast imaging techniques and currently, the sensitivity is suboptimal for women with dense breasts and obscure cancers. Recently, studies have indicated that exploring new contrast agents can provide access to improved sensitivity because of their potential to increase the effective Z of the target tissue. Unfortunately, knowledge on novel contrast agents is limited; the modern idea of using lanthanides in contrast media is widely unexplored because of the complexity behind contrast agents and their biophysical interactions in the human body. Evidence supporting the exploration and use of novel contrast agents is scarce and physicists are less inclined to allocate resources researching their potential if there is little to no evidence supporting their utility. Furthermore, research demonstrating the efficacy of novel contrast agents in breast imaging is deficient and with little evidence supporting their use in improving sensitivity, progress incorporating this technique in a clinical setting is stagnant.

The long-term goal of this study is to help introduce feasible contrast agents that can improve breast imaging sensitivity, especially among groups that experience reduced sensitivity. To achieve this, there needs to be sufficient data, or evidence, supporting their efficacy. More specifically, the objective of this project is to find novel ways to improve the differentiation between tumor and glandular tissue by creating a realistic anthropomorphic model that not only considers the geometry of the breast but its physiological components as well. A realistic breast phantom can help incorporate elements that are often lacking in breast cancer studies, such as the inclusion of more cancer types, obscure locations, and large sample size. By incorporating these elements, the efficacy of potential contrast agents can be explored holistically. The

evidence provided by this work can provide indication on contrast agents that are worthwhile to pursue and provides assurance to other groups who wish to explore these contrast agents in a real environment. Because of the accurate particle physics provided by MCNP and the emulated biophysical environment of the breast, the results contributed by this project can serve as reliable evidence supporting the use of novel contrast agents in breast imaging. In addition, incorporating and exploring several variables, such as breast size, density, tumor location, and tumor type, provides affirmation that the proposed contrast agents have the potential to aid a wide range of patients.

Previous breast anthropomorphic phantoms that have been created for research purposes were often oversimplified. Oftentimes, breast phantoms, especially those used for exposure dose studies, only incorporated the material components of the breast, such as the glandular and fatty tissues, and often ignored other important aspects, such as the vasculature. Only recently did breast phantoms begin to incorporate other structural components of the breast, such as Cooper's ligaments, and skin. Because it is critical to understand the biophysical compatibility between the proposed contrast agents and the breast, incorporating the physiological characteristics of the breast is essential. Further, applying variability into the anthropomorphic breast model, i.e., varying breast size, is imperative to fully grasp the efficacy of the proposed contrast agents and exposes their limitations. Applying the physiological aspects to an MCNP anthropomorphic phantom is a novel idea, therefore there are some expected challenges. One of those challenges is poor phantom resolution determined by the mesh size. There is a trade-off between computational time and mesh size – a small mesh size takes much longer due to increased number of elements – and there is also a tradeoff between mesh size and accuracy since smaller meshes can provide finer details. In addition, biophysical assumptions are necessary to simplify the model, such as assuming laminal contrast agent and blood flow, in order to reduce the computational time. The effect of these challenges will be discussed towards the end of this paper

Currently, there are no clinical applications of contrast enhanced tomosynthesis. This project aims to combine tomosynthesis breast imaging methods with novel contrast agents to explore their efficacy and limitations. By creating a realistic tomosynthesis environment and an accurate breast mesh phantom in

MCNP, this technique can be explored without the need for costly resources. To achieve this, the project aims to:

- Create a realistic tomosynthesis environment by constructing a detailed Hologic tomosynthesis breast imaging machine, including the source, flat-panel detector, and support equipment, using MCNP

- Model a realistic breast phantom by considering the several structural components of the breast as well as the physiological components.

- Incorporate a time dependency using Python coding so that the biophysics of the elected contrast agents can be accurately studied.

- Improve the differentiation between glandular tissue and tumor tissue using a series of methods, primarily focusing on contrast enhancement.

- Test the efficacy of multiple contrast agents by quantifying tumor visibility as a function of breast size, density, tumor location, tumor stage, and tumor type.

- Generate clear and accurate radiographs demonstrating the structural components of the breast and the effects of contrast enhancement on any embedded tumors.

By accomplishing these objectives, the feasibility of using contrast enhanced breast imaging as a viable breast screening method can be disclosed. Although this project aims to explore novel contrast agents in breast imaging using tomosynthesis technology, ultimately the goal is to improve the differentiation between the glandular tissue and tumor tissue so that sensitivity can be improved, especially among women with dense breasts.

2 Related Work

2.1 Foundations of Breast Cancer

2.2.1 Characteristics of Breast Cancer and Physiological Changes in the Breast

To understand how breast cancer develops, it's important to understand the different components that make up the breast. The breast is comprised of adipose tissue, glandular tissue made up of ducts and lobes, Cooper's ligaments, the nipple, areola, the retromammary scape, and the chest wall. The lobes are composed of several lobules which are composed of clusters of alveoli that have the appearance of small sacs.[98] The alveoli produce and store milk, and they are the smallest constituent of glandular tissue. The breast also contains a complex vascular network that can be seen in **Figure 4** along with the multiple components of the breast. The breast contains several arteries, the internal thoracic vein, axillary vein, intercostal vein, intercostal nerves, superclavicular nerves, intercostal arteries, and pectoral axillary lymph nodes. As mentioned previously, glandular tissue is the 'dense' part of the breast. During pregnancy and lactation, the amount of glandular tissue increases because of increased demand for milk production. Studies have found that during this process, the number of acini, or alveoli, increase thus increasing the size of the lobes.[99] After the lactation period is over, involution occurs, and the breast epithelial tissue gradually decreases to reduce the breast glandularity. Involution also occurs with age which explains why the frequency of women with dense breasts decreases in older groups.[100] While the percent glandularity depends on age, genetics, and pregnancy, it is not dependent on breast size, as studies have found that women with large breasts often have large amounts of adipose tissue instead of glandular tissue.[101]

While the amount of glandular tissue in the breast might seem trivial, it can be an indication of a woman's likelihood of developing breast cancer since breast cancer often develops in the ducts or lobes. Depending on the type of cancer, the tumor can begin to grow along the epithelial cells of the ducts or lobes

.
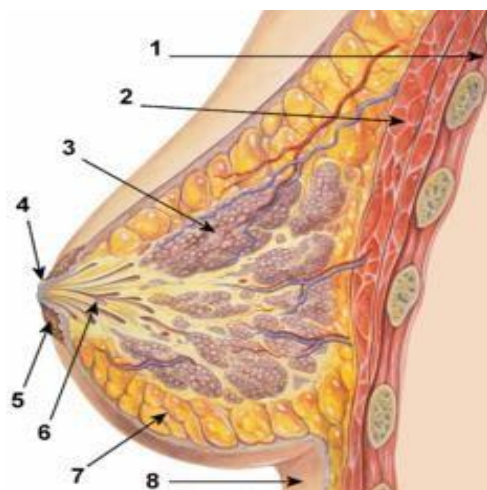
Figure 4: Cross-section of a human female mammary gland

1: Chest wall: the boundary between the thoracic cavity and the breast.

2: Pectoralis muscles: a series of chest muscles that lie behind the breast.

3: Lobules: small sac-like components that compose the lobes. They are connected by milk ducts.

4: Nipple: where the duct ends meet and where milk leaves the breast during lactation.

5: Areola: the area that surrounds the nipple

6: Milk duct: the ducts that carry out the milk from the lobes during lactation. They connect towards the nipple.

7: Fatty tissue: loose connective tissue composed of adipocytes, fibroblasts, preadipocytes, endothelial cells, and immune cells.

8: Skin: thin layers of skin surround the breast.

The amount of glandular tissue isn't the only risk factor associated with breast cancer. Obesity, ionizing radiation, hefty alcohol consumption, and genetics have all been associated with breast cancer; although, only about 5-10% of breast cancer cases are due to the inheritance of BRCA1 and BRCA 2 genes.[102] The relationship between genetic risk factors and breast cancer is well understood, however, the other risk factors associated with breast cancer are not well established and the development of breast tumors is quite arbitrary. Because most cases of breast cancer are unpredictable and abundant, it's important to locate malignancies when screenings are performed.

When a tumor develops in the breast, the breast undergoes several physiological changes. Symptomatic changes that serve as warning signs include the presence of lumps, changes in the breast size and or shape, pain and soreness, changes in the nipple or skin of the breast, and inversion on the nipple or other parts of the breast.[103] There are also other physiological changes that occur locally where the tumor

grows that can only be visible with imaging techniques or biopsies. Oftentimes, breast cancer begins when non-regulated unhealthy cells invade the cell lining of ducts or lobes (i.e. ductal carcinoma *in situ* and lobular carcinoma *in situ*) and continue to grow and spread until they eventually 'pour' out of the cell lining into the surrounding stromal tissue and became *invasive* (i.e. *invasive* ductal carcinoma).[104] In a biopsy, ducts infected with tumor cells will appear enlarged and often irregular thus providing indication of potential illness. Tumors have also been found to destroy surrounding healthy cells to make room for growth by depleting healthy cells of resources.[105] In doing so, fibrosis can be found surrounding the tumor in extreme cases. In addition to these local changes caused by tumor growth, tumors also have the ability to induce angiogenesis, or neovascularization.

Angiogenesis in tumors is widely believed to originate from hypoxia, or the lack of oxygen, inside the tumors due to their tightly packed structure caused by the rapid replication of cells.[106] The discovery of the hypoxia-inducible factor and the heterodimeric transcription factor HIF1-alpha has supported this theory because it has been found to stabilize in hypoxic conditions, thus allowing it to avoid interaction with the VHL (von Hippel-Lindau) protein.[107] This, in turn, allows the HIF1-alpha to induce genes that promote oxygen delivery. There is evidence supporting the theory that HIF1-alpha aids in tumor growth because it has been found in cancerous tumors but not benign tumors where prolific angiogenesis is absent. Stabilized HIF1-alpha in the tumor microenvironment causes an influx of signaling proteins that help induce localized vascularization, such as VEGF, or vascular endothelial growth factor. VEGF has been known as a powerful angiogenic growth factor responsible for the growth of vascular endothelial cells.[108] In tumors, VEGF is overexpressed compared to normal cells and in breast cancers, it has been found to be tremendously upregulated.[109] A study that used semi-quantitative RT-PCR analysis to quantify the expression of VEGR in breast tumors found that VEGF-A and VEGF-B are ubiquitous in all tumors analyzed.[110] VEGF-C expression was only found in node-positive tumors at a rate of 75% while VEGF-D was only found in inflammatory-type tumors at a rate of 33%. These findings are indicative of the association between VEGF expression and tumor growth patterns; there is a strong correlation between the quantity and type of VEGF proteins and the grade of angiogenesis present in a malignancy. In addition, the

presence of VEGF-C and VEGF-D in breast tumors provide an indication of the aggressivity of the tumor and its likelihood to metastasize.

There are other proteins that have also been found in breast cancer development, among the most common ones are Ki67, HER2, progesterone receptor (PR), and estrogen receptor (ER). Ki67 is a proliferation antigen that has been found to correlate with tumor cell proliferation and growth and can potentially serve as a predictive indicator of survival outcome. A study found that high expression of Ki67 is associated with high risk of recurrence and increased tumor size.[111] Ki67 was first discovered in 1983 when a group of people investigated the Hodgkin lymphoma cell line and since then, it has been defined as a proliferation marker responsible for cell growth.[112] While low levels of Ki67 exist in healthy breast tissue in ER negative cells, overexpression is extremely common in breast tumors; this can explain the rapid cell growth observed in breast tumors. Although studies that have studied the relation between Ki67 and other breast cancer related proteins, most have shown a poor prognosis associated with elevated values of Ki67, including a study with over 12,000 patients that found that high levels of Ki67 denote an increased risk of reoccurrence and worse prognosis with decreased survival rates.[113] Further, Ki67 index exceeding 15% has been found to correlate with high tumor grade.[114] Some studies have also found that high levels of Ki67 are correlated to ER-/PR- which leads to the belief that cancers that are not luminal A or B, such as triple negative breast cancers, are more aggressive and can be difficult to target with certain breast cancer therapies.

HER2, or human epidermal growth factor, is another growth-promoting protein, more specifically, a proto-oncogene, that is often overexpressed in breast cancer cells.[115] HER2 exists outside of normal breast cells but can be overexpressed in about 30% of breast cancers. A breast tumor is considered HER2+ when the levels of HER2 exceed those of normal breast tissue by at least 20%.[116] Similar to Ki67, high overexpression of HER2 is associated with quick tumor growth and progression.[117] In addition, it has also been found to hold an inverse relationship to ER and PR expression; studies have found a strong association between HER2 overexpression and ER-/PR- expression.[118] A theory behind this pattern is that HER2 expression is potentially suppressed by estrogen since it was discovered that removal of the hormone led to

unregulated HER2 expression.[119] This correlation between estrogen and HER2 has allowed for the development of HER2 targeting mechanisms that aid in treatment. Breast cancer with progesterone receptors, or estrogen receptors, or both, is the most common type of cancer with about 70-80% of breast cancers expressing at least one type of hormone receptor. Traditionally, women with hormone positive breast cancer experience a lower mortality risk compared to women with ER-/PR-.[120] Similarly to HER2, ER and PR expression allows treatment options with targeting mechanisms. Treatment specialists will often treat a breast cancer patient with medication that works through the hormone receptors to prevent tumor growth. In addition, because breast cancers that express hormone receptors often lack high HER2 expression, they grow slower and lead to better prognostics compared to women with ER-/PR- breast cancer. Interestingly, the lowest proliferating tumors also show higher rates of ER positivity.[121]

2.1.2 Subtypes of Breast Cancer; the Role of Tumor Heterogeneity in Breast Imaging

The type of proteins expressed in a breast tumor determine the tumor's molecular classification, or subtype. There are currently five different molecular subtypes of breast cancer, including luminal A, luminal B, HER2-enriched, triple-negative/basal-like, and normal-like.[122] Luminal A breast cancer includes those that are hormone receptor positive, either ER, PR, or both, HER2-, and also demonstrate low levels of Ki67. Because of the absence of Ki67 and HER2, these cancers grow slowly and are low-grade compared to the other subtypes; they also have the best prognosis. Luminal B on the other hand, are also hormone receptor positive but have high levels of Ki67 and can be either HER2 positive or negative; therefore, these cancer types grow a bit faster than luminal A type and they have a slightly worse prognosis. HER2-enriched cancers are hormone receptor negative and HER2 positive and these cancers grow faster than the luminal types and although they have a worse prognosis than the luminal types, they are often successfully treated with targeted therapy. Triple negative cancers are those with no hormone receptors or HER2 enrichment and because they can't be targeted like the other cancer types mentioned, they have a worse prognosis. These cancer types are usually aggressive and fast growing. This molecular subtype is more common in women with the BRCA gene mutation. Normal-like breast cancers are hormone receptor positive, HER2

negative, and have low levels of Ki67, similarly to luminal A breast cancers; however, they demonstrate a slightly worse prognosis than luminal A breast cancers.

HER2, ER, and PR have traditionally been used as breast cancer biomarkers and are often used to predict prognosis. A study predicted that ER is present in about 80% of breast cancer cases; because of its popularity, it is often used to predict the patient's response to endocrine therapy as well as overall survival and likelihood of reoccurrence.[123,124] Studies have estimated that about 40% of tumors that are ER+ are PR.[125] Tumors with this characteristic show abnormal growth factor signaling and are also typically less responsive to certain treatment than tumors that are PR+. HER2 is also used to predict poor prognosis. HER2 is predicted to be overexpressed in about 13-20% of invasive breast cancers with about half of those cases also being hormone receptor negative.[126] Triple negative breast cancers make up about 10-15% of breast cancers and currently, there is no targeted therapy available for these cancer types. The subsection of triple negative breast cancers that are basal-like have the worst prognosis out of any other molecular classification as they also express molecular weight cytokeratins. Although each of these biomarkers have been associated to different type of histological breast cancer subtypes, the basil-like molecular subtype has been found to have the greatest tumor diversity encompassing a range of tumors with different metastatic patterns, growth patterns, therapy response, and survival rates.[127] A study noted that predicting the behavior of a breast tumor can be a tricky tasks because there is overlap between the different tumor types.[128] The line between HER2 breast cancers and luminal B subtypes is blurry and tumors that lie in the HER2 category can also demonstrate behaviors found in the luminal B category. Furthermore, normal-like breast cancers have been found to demonstrate behavior found in normal breast tissue, but these findings are controversial since some theorize that this might be due to sample contamination.

Breast cancers are also described by their histological subtypes. The histological subtype of a breast tumor is determined by the tumor's growth patterns, such as its location, cell type, and tumor structure. Two broad histological categories are in situ and invasive tumors; in situ tumors are those that have only developed in their original location and have not spread anywhere outside of that location while invasive tumors are those that have spread beyond their original location or tissue and have infiltrated the

surrounding area. In situ tumors can be further subclassified into ductal and lobular tumors based on the whether the tumors developed in the ducts or the lobes, respectively. Ductal carcinoma in situ can be further subclassified into five different histological types of cancer, including comedo, cribriform, micropapillary, papillary, and solid type.[129] Invasive carcinoma breast cancers can be subclassified into six histological subtypes, including tubular, ductal lobular, infiltrating lobular, infiltrating ductal, mucinous, and medullary.[130] Infiltrating ductal carcinoma can be further divided into well differentiated, moderately differentiated, and poorly differentiated. Infiltrating lobular carcinoma can be subdivided into classical, apocrine, pleomorphic, alveolar, and solid type. Each of these subtypes are unique in their set of mutations, characteristics, and genomic differences.[131]

Infiltrating lobular carcinomas, ILC, make up about 8-14% of all breast cancers and have been found to have a limited ability to form palpable masses due to the loss of 'adhesion' molecules.[132] The four subtypes of ILC differ in their molecular subtype but often, ILC might be PR negative. An early study of ILC found that the cells in these cancers are small and round with small cytoplasm and they line the stroma in a single file.[133] ILC are subtle in their growth; they don't consume existing anatomical structures or connective tissue, but they are also difficult to find during breast imaging because they don't often form distinguishable masses. A study conducted found that ILC was difficult to detect in the early stages because of this.[134] A study that tracked the growth patterns of ILC compared to infiltrating ductal carcinoma, IDC, found that the size of ILC tumors exceeding 5 cm at the time of diagnosis occurred in about 14% of cases compared to 9.1% in IDC.[135] The study also found that the rate of lymph node metastasis was about the same for both ILC and IDC; however, it's more difficult to detect it for ILC given the subtle growth patterns observed with ILC. In addition, ILC was found to be hormone receptor positive more often than IDC and also less likely to contain overexpressed HER2 and p53. In fact, only about 5-10% of patients with ILC were found to be positive for HER2, endothelial growth factors, or p53 and it's been hypothesized that the small margin of ILC tumors found with these biological features might be due to a cancer variant and not just ILC, such as pleomorphic lobular carcinoma. Although ILC appears to contain less aggressive characteristics than other cancer types, its evasiveness during breast screenings and association with false

negative rates offsets these characteristics. Therefore, the prognostics for ILC are not that much different than for IDC.

Adenoid cystic carcinomas (ACC) are similar to ILC in that they are difficult to detect during an imaging procedure; in fact, they rarely present themselves as image-detected abnormalities.[136] ACC only account for about 0.1% of all breast carcinomas and they can present themselves with diverse morphological growth patterns, including cribriform, solid, reticular, glandular, and basalid. Despite being a triple negative cancer, ACC typically have excellent outcomes and are rarely aggressive. Another rare form of breast cancer is medullary carcinoma, which account for less than 1% of all invasive breast carcinomas. They are also similar to ACC in that morphologically, they are a triple negative type of carcinoma often associated with the BRCA1 gene, but they typically have favorable prognosis.[137] During screening, medullary carcinomas appear as masses with well-defined round, oval, or lobulated shape. During microscopic imaging, the cells of these masses are very distinct from normal cells with a syncytial growth pattern and a border surrounded with lymphoplasmacystic infiltrate.[138] Metaplastic carcinomas also account for less than 1% of breast carcinomas and they can display a variety of morphological characteristics, including spindle-celled, squamous, adenocarcinoma, and mesenclymal elements.[139] These carcinomas originate from those that have undergone sarcomatous neometaplasia. Studies have shown that during imaging, they often display microcalcifications and they appear as well-defined lesions with a firm and solid appearance. Metaplastic carcinomas have also been labeled as triple negative carcinomas due to the absence of ER, PR, and HER2 expression during studies. Their prognostic is dependent on their morphological characteristics and they can vary between low grade to high grade malignancies.

The pure form of micropapillary carcinoma is found in about 2% of breast cancer cases. These carcinomas are often well distinguished during breast screening because they present themselves as dense, irregular masses surrounded with microcalcifications and speculated margins. Breast imaging will also reveal the presence of lymphadenopathy associated with this malignancy.[140] Micropapillary tumors are often larger than other breast malignancies and they are also high-grade and are correlated with a poor prognosis. Further, 80% of micropapillary carcinomas are accompanied with lymph node metastasis and a

study conducted in the mid-90s found that the 5-year survival rate is only 50%.[141] Invasive cribriform carcinomas are well identified because of the cribriform patterns they display in breast tissue. During breast screening, these carcinomas appear as abnormalities surrounded with microcalcifications. Their shape often appears as a spiculated mass and the tumors are often free of metastasis.[142] Given that these carcinomas are luminal type, they often have good survival rates. Mucinous carcinomas are also luminal type and they are represented by extracellular mucin. During screenings, they appear as palpable masses and are often displayed as well-defined malignancies.[143] Because of their molecular classification, mucinous carcinomas often have favorable prognostics and women with these malignancies are often treated with breast conservation therapy.[144] Tubular carcinoma is found in 2% of breast cancer cases but can occur at higher rates among women who are mammographically screened.[145] During breast screenings, tubular carcinoma is easily identified with masses appearing as palpable masses and abnormalities. In a mammography, the tumor appears as a dense mass surrounded with macrocalcifications. The mass is often spiculated and ill-defined with grey-white color. Under a microscopy, the lesion cells appear round with a tubular configuration and do not display any signs of necrosis. Molecularly, tubular carcinomas are luminal type and are not aggressive compared to triple-negative carcinomas. Because of the positive prognosis associated with these carcinomas, breast conservation therapy is recommended for this cancer type.[146]

Neuroendocrine carcinomas make up about 0.5-5% of breast cancers.[147] In breast screening, the lesions appear as circumscribed tumors and palpable masses. This cancer type contains a few variants that determine the prognostics; however, this carcinoma is often associated with rapid growth. There is a variant - alveolar - that is similar to ILC, and there is another variant - small cell - that leads to poor prognosis. Because of the broad diversity entailed with neuroendocrine carcinoma, the best clinical approach for treatment is undetermined. Apocrine carcinomas make up a small fraction of breast cancer ranging between 0.3 to 4% and is often seen in postmenopausal women.[148] In imaging, apocrine carcinoma can be distinguished by the presence of apocrine differentiation throughout the entire tumor. Molecularly, apocrine carcinomas are classified as triple negative cancers and their treatment is no different than other triple negative cancers. IDC with osteoclastic giant cells is a very rare form of breast cancer. Its appearance can

be described as a well-circumscribed round mass likely surrounded with calcifications.[149] Typically, its mass is firm but spongey and when observed under a microscope, hypovascularized stroma is observed along with giant cells containing multiple nuclei. In addition, lymph node involvement is common with this cancer type. This carcinoma is generally classified as luminal-type and the five-year survival rate is about 70% thus matching those of other infiltrating ductal carcinomas.[150]

There are a few other rare breast cancers, such as secretory and glycogen-rich carcinomas, that also display unique characteristics. Because of the molecular variance among the different types of breast cancers, targeting strategies are difficult to optimize, especially among women with triple-negative breast cancer. Therefore, studying reliable biomarkers that can be used for tumor targeting is a daunting task, yet one that is worthwhile. In addition, lesion visibility during screening is important to be able to detect malignancies; because of this, breast cancer subtypes that do not form well-defined masses in early stages are difficult to identify during screening thus delaying treatment. For these reasons, exploring novel ways to improve tumor visibility for a broad range of breast cancers can improve sensitivity among populations that suffer from a decreased sensitivity. By experimenting with new imaging strategies that combine different techniques, there is less ambiguity between the limitations that depend on the different factors surrounding breast tumor visibility. Methods that can potentially improve sensitivity can be uncovered thus providing ample opportunities to explore these promising methods in a clinical setting.

2.2 Imaging Techniques for Breast Cancer

2.2.1 Strengths and Weaknesses of Breast Imaging Techniques

Breast imaging is performed with a range of imaging techniques, extending from non-radioactive techniques, such as ultrasound, to contrast-enhanced ones such as contrast-enhanced CT. These techniques vary in the energy they use, the type and angle of the beam, the signal processing tools, and robustness. The efficacy of the different imaging modalities can be quantified by their sensitivity, specificity, and accuracy and in situations where an imaging modality is not capable of providing enough information, it is supplemented with another imaging technique. The significance of the difference between the specificity,

sensitivity, and accuracy of different imaging techniques is often calculated using the p-value; a threshold of 0.05 is often used for the reliability of the results, therefore, results with a p-value below this value are labeled as 'significant.' The smaller the p-value, the stronger the evidence against the null hypothesis. The alternative hypothesis is then 'more evident' and this often suggests that the technique is worth looking into. In a later section, studies that compare the efficacy between different imaging techniques will be discussed.

The first dedicated imaging technique for breast imaging was mammography, shown in **Figure 5A**. This imaging technique involves using low-energy x-rays, typically below 30 keV, to locate calcifications or other signs of breast cancer. The procedure involves breast compression between two parallel plates to reduce motion while the image is acquired. The x-ray beam is located directly above the top compression plate while the film plate, or screen, is located below the bottom compression plate. Two images are gathered per breast; one is gathered in the cranio-caudal position (straight from above) and the other is gathered in the mediolateral oblique view (about a 45-degree angle from the top). Recently, film-screen mammography has been replaced with digital mammography which utilizes digital receptors to gather the signal and create images. This development has allowed radiologists to manipulate images to improve visibility and contrast between the lesion and surrounding tissue. Because mammography is used as a screening tool, other, more reliable imaging techniques are often used to further investigate a suspicious region found on a mammogram, such as an MRI scan, shown in **Figure 5B**. The benefit of using mammography over other imaging techniques is that it imparts a lower dose compared to other similar imaging techniques, such as CT, shown in **Figure 5C**. In a study conducted in 2013, 132 subjects were analyzed to evaluate the mean glandular dose imparted during a breast CT scan.[151] These measurements were then compared with the mean glandular dose obtained during a diagnostic mammogram. The calculations for dose were obtained by using normalized glandular dose coefficients in lieu of expensive simulations. The results demonstrated that the average mean glandular dose received from a CT was about 13.9 mGy with a standard deviation of 4.6 mGy while the dose for mammography averaged at 12.4 mGy with a standard deviation of 6.3 mGy for the same patients.

(a)

(b)

(c)

(d)
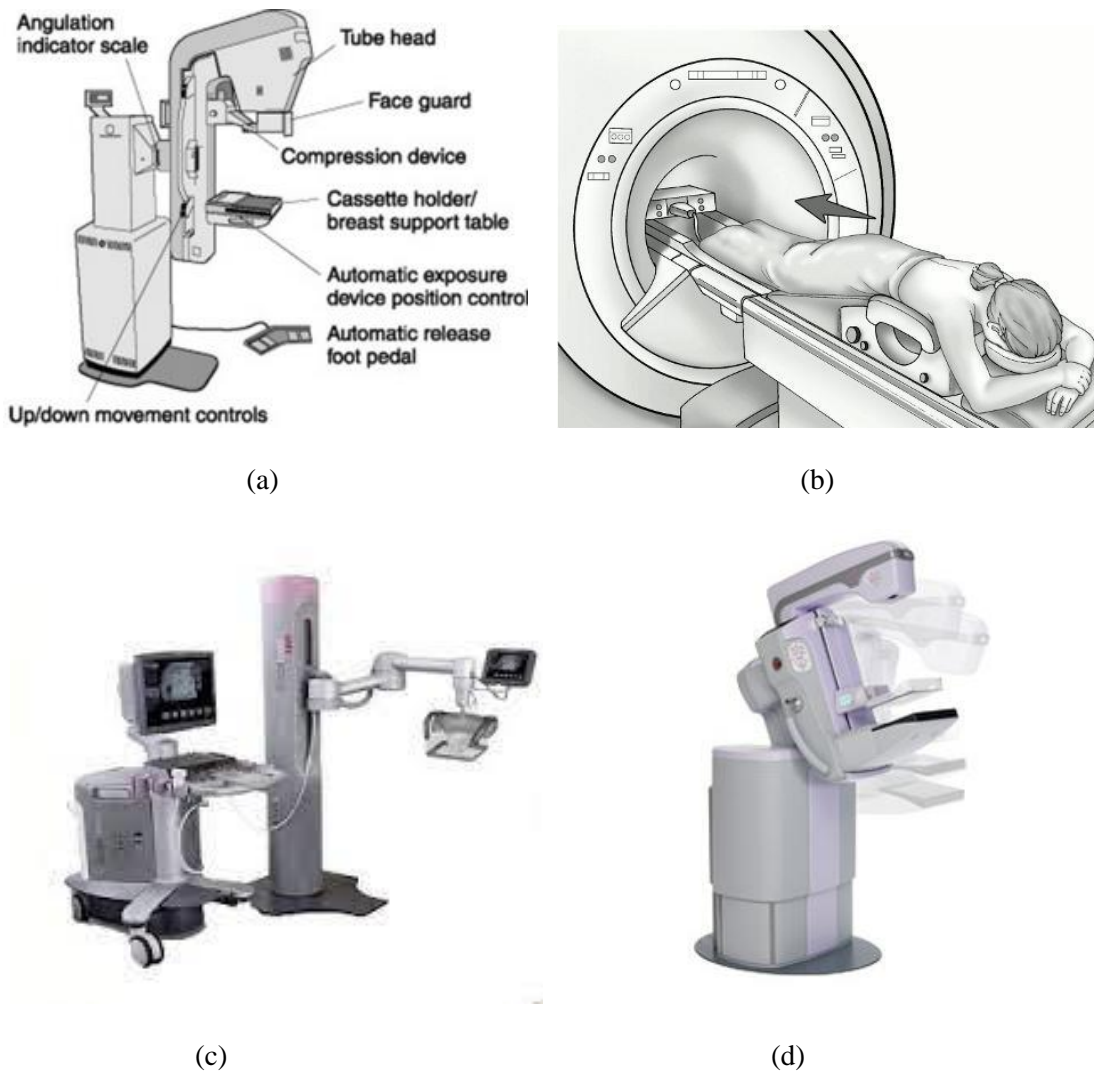
Figure 5:[152,153,154,155] Images of the various breast imaging techniques. (A) demonstrates a standard mammography unit, (b) shows a breast MRI procedure, (b) shows a breast ultrasound unit and (d) shows a tomosynthesis unit; it is similar to a mammography unit, except it has a rotating gantry.

The recent development of digital breast tomosynthesis, shown in **Figure 5D**, has introduced inquiries over its advantages and disadvantages over mammography, including dose. In a study conducted in 2018 a group conducted a large study to investigate the dose difference between full-field digital mammography and digital breast tomosynthesis.[156] The study involved over 1,200 women and each partook in both mammography and tomosynthesis screening. The trial utilized a computer software program that

calculated the glandularity present in each breast; this data was used along with exposure data to calculate the mean glandular dose. The results returned a statistically significant difference between the dose received per each screening method. The trial found that the mean glandular dose in the craniocaudal position for mammography was 1.366 mGy and 1.858 mGy for tomosynthesis. For the mediolateral oblique view, the mean glandular dose for mammography was 1.374 mGy and 1.877 mGy for tomosynthesis. Despite the larger dose given by tomosynthesis, the study implied that the increase in dose was minute and does not provide sufficient evidence to deter anyone from benefiting from the technology's clinical benefits. It's important to analyze and fully comprehend the dose administered by each technique. Minimizing the dose exposure during screening is of everyone's best interest because of potential detrimental effects. Although it has been proven that screening programs involving mammography are overall beneficial there has been controversy over higher cancer incidence among populations with screening programs.[157] However, it is also important to note that a wide range of factors influence breast cancer incidence, as well as detection. Countries with screening programs are more likely to detect breast cancer which can explain the higher rates. Although there is no solid evidence proving that radiation-inducing imaging techniques increase breast cancer incidence, it is best to exercise a conservative approach when using these imaging techniques.

A major disadvantage with mammography is that it struggles to differentiate tumor tissue from glandular tissue, especially among women with dense breasts. This leads to a high false-negative rate of at least ten percent.[158] A study conducted in 2017 organized over 25,000 mammographic examinations with 240 confirmed breast cancer cases. The study divided the cohort into groups based on their breast density classification determined by the BI-RADS scale. The group found that the overall sensitivity was 79.9%. However, when the sensitivity was analyzed along with the breast density, they found a dramatic decrease among women with high glandularity. The sensitivity for women with BI-RADS category 4 was calculated to be 50% which is significantly lower than the 79.4% observed among women with BI-RADS category 3.[159] A similar study conducted in Denmark in 2019 sought to analyze the decline in sensitivity among women with dense breasts. This study analyzed a year's-worth of full-field digital mammography data that included 285 confirmed breast cancer cases and over 55,000 total patients. The study found the overall

sensitivity to be 72% with a specificity of 98%. The highest sensitivity was observed among women with fatty breasts at a rate of 78% while the lowest sensitivity was observed among women with dense breasts averaging at about 47%. Meanwhile, the specificity varied very little between the different breast densities. Although women with BI-RADS category 4 typically compose a minority of the breast screening population (about 5%), it is paramount to have as high a sensitivity as possible, therefore, other imaging techniques have been developed to improve sensitivity among the most disadvantaged populations.

Another technique used for breast imaging is ultrasound medical imaging. With this technique, high-frequency broadband waves are emitted onto tissue which then reflect receipt sound waves off the surrounding anatomy to create an image of the differentiated tissues. The signal received from the receipt sound waves can be described by a set of transmission and reflection coefficients that are unique to each tissue structure.[160] Compared with other imaging techniques described here, ultrasound does not provide much anatomical detail and images often appear blurry to the viewer. However, it also doesn't use ionizing radiation unlike CT or mammography and minimizes the risk to the patient. In addition, it is relatively inexpensive, especially when compared to MRI. On the subject of sensitivity, breast ultrasound might be better or worse than that of mammography depending on breast density. In a study by Devolli-Disha et. al. that sought to compare the sensitivity between mammography and breast ultrasound, 547 women were screened with both imaging modalities (separately) to identify the sensitivity.[161] The study found that the sensitivity for women with fatty breasts was 82.2% while ultrasound provided a sensitivity of 71.1% for the same group of women. Meanwhile, the sensitivity among women with dense breasts was found to be 23.7% with mammography and 57% with breast ultrasound. These results imply that the sensitivity for ultrasound is more consistent and might be less density dependent than that of mammography. Because of its low risk and poor image quality, ultrasound breast imaging is often paired with mammography to supplement anatomical detail provided with mammography.[162] In a small study with 41 women, the accuracy between mammography and mammography supplemented with ultrasound was compared.[163] Berg et. al. found that the accuracy for mammography alone was 78%; however, supplementing mammography with ultrasound yielded an increased accuracy of 91%. They found that adding a single ultrasound scan to

a mammography screening session increased the number of detected lesions from 1.1 to 7.2 per 1000 high-risk women. However, they also found that the number of false positives increased significantly. Similar to MRI, there appears to be a trade-off between sensitivity and specificity with the ultrasound supplemented mammography technique.

To improve the accuracy, ultrasound can be enhanced with microbubbles. A current strategy to increase the contrast in ultrasound breast imaging is to bind the 'bubbles' to targeting ligands that can then bind to specific receptors that pertain to the disease of interest.[164] This technique has improved the differentiation between benign and malignant lesions because of its ability to provide metabolic information about the lesion of interest. A study conducted in 2016 by Luo et. al. experimented with contrast enhanced mammography to diagnose the stage of confirmed lesions.[165] They found that contrast-enhanced ultrasound was able to identify stage 4A cancer, as defined by BI-RADS, with a sensitivity of 85.4% and a sensitivity of 87.8%. The results demonstrated that this technique can be used to reduce biopsy rates. In a more recent study, Yan-Ran et. al. studied the differences observed between malignant and benign tumors during contrast-enhanced breast ultrasound.[166] They found that during screening, malignant tumors have an uneven enhanced intensity, the 'wash-in' speed was quicker than usual, and the surrounding vessels were enhanced. They found that contrast-enhanced ultrasound had a sensitivity of about 78.7% with a specificity of 84%, which were not much different than the sensitivity and specificity observed with non-enhanced ultrasound. However, the study noted that contrast-enhanced ultrasound was able to identify malignant tumors that conventional ultrasound had incorrectly identified as benign. Because contrast enhanced ultrasound can identify malignant lesions at a higher rate than conventional ultrasound, it can potentially improve the early diagnosis of breast cancers. Furthermore, studies have shown that ultrasound contrast agents have few adverse effects and are safer than radiocontrast agents, both in adults and children and currently, there are three FDA approved contrast-enhanced ultrasound techniques. Despite its safety, contrast-enhanced ultrasound still doesn't provide the anatomical detail that is crucial for localization and remains as a supplementary tool.

Magnetic resonance imaging, or MRI, is a non-radioactive imaging technique that utilizes magnetic fields to image organs, anatomical features, or physiological processes. With this technique, the induced magnetic field uses the hydrogen in the body to create a signal and discrepancies in the hydrogen concentration in a region are used to model the different tissues. Because MRI scans do not induce ionizing radiation, they have a very low risk associated with them compared to other imaging techniques listed here. In addition, imaging techniques that use x-ray/gamma beams to irradiate the body focus on highlighting the structural components of the body, such as the skeletal system and tissue structures, and while MRI also has these capabilities, it can also image metabolic functions, such as brain functions and injury. The type of MRI imaging performed varies based on the choice of sequence chosen. The MRI sequence is the setting that determines the radiofrequency pulses and the gradients used. In breast imaging, MRI has an advantage over the other techniques listed here because it has the highest sensitivity out of any other techniques clinically used. MRI has shown a substantial increase in tumor detection, especially when aided with contrast enhancement.[167] Typical values of MRI sensitivity in breast imaging range from 79%-98% along with an exceptional performance among high-risk groups compared to mammography.[168] In a study that sought to investigate MRI's ability to detect tumors in BRCA1 and BRCA2 carriers, 496 high-risk patients were analyzed to see if MRI's sensitivity was significantly lower for these groups.[169] The study also quantified the sensitivity for mammography using the same patients. The sensitivity for mammography was found to be 81% for the group with the BRCA1 mutation and 89% for the group with the BRCA2 mutation. Meanwhile, the sensitivity for MRI was found to be 99% for both groups. The significance of these results is that MRI is successful at locating tumors associated with more aggressive cancer types compared to mammography. Early detection of these cancer types can significantly improve prognosis due to the immediate treatment at early stages.

In a study conducted in 2019, 176 benign and malignant lesions were assessed with mammography and MRI to identify differences in imaging patterns observed between the two imaging techniques.[170] The patients used for this study were all depicted as women with dense breasts. Of all the lesions observed, mammography was only able to identify 67.6% of them while MRI was able to identify all of them. The

study also found that MRI was able to identify the lesion size more accurately than mammography among lesions smaller than 8mm. For the lesions missed with mammography, 47 were labeled as benign while the other 10 were labeled as malignant. The accuracy was found to be 78% and 94% for mammography and MRI, respectively. Meanwhile, the sensitivity was found to be 46% and 94% for mammography and MRI, respectively and the specificity was determined to be 99% and 78% for mammography and MRI, respectively. The sensitivity of MRI is reliably exceptional across a multitude of factors and continuously outperforms other breast imaging techniques. Recently, studies have explored techniques to extract useful metabolic information about tumor growth using MRI. A study conducted in 2021 explored kinetic features of breast cancer and sought ways to correlate these features with contrast uptake in contrast-enhanced MRI.[171] More specifically, the study analyzed contrast agent uptake through the microvasculature surrounding the lesion of interest. Trends observed by contrast enhanced MRI could then provide an indication of biomarkers that can be identified with this imaging technique. To assess the microvessel density per case, monoclonal antibody immunostaining was performed on the biopsy tissue samples. The results exhibited high signal enhancement ratios among lesions with high microvessel density. In addition, the signal wash-out rate was faster among tumors with high microvessel density than those with little angiogenesis. The findings in this study suggest that features observed with contrast enhanced MRI can help identify the stage of the identified lesion given the correlation between angiogenesis and tumor growth. Thus, the potential of MRI for novel tumor assessment clinical procedures is bountiful.

Unfortunately, there are a couple reasons why MRI isn't used as a widely adapted breast screening tool. For one, the specificity is low compared to mammography. The specificity for MRI has been reported to range between 37% and 97% with an average of about 70%.[172] While it is arguable that high sensitivity takes precedent over high specificity, it is less than ideal to use a system that continuously reports false positives. False positives lead to invasive and unnecessary distressing procedures. Another disadvantage of MRI is that it is very time consuming and uncomfortable to the patient. A single scan can last between 20-30 minutes while a mammogram only takes seconds to acquire and a contrast-enhanced mammography takes no more than 10 minutes.[173] During the scan, patients are discouraged from moving, therefore the

process can be uncomfortable. In addition, MRI isn't an option for patients who have a particular type of metal implant, such as stents made with certain materials, thus limiting the number of patients allowed to receive a scan. MRI is also far from cost effective. While mammograms cost between $75 to $250 to produce, MRIs can cost between $750 and $2500, sometimes more.[174] Furthermore, insurance companies will often dismiss coverage for an MRI unless the patient is at high risk for developing breast cancer, such as those with the BRCA genes, or abnormal findings have been found. With the development of improved breast screening techniques, there's a limited incentive to fund MRI as a breast screening tool. Unless the cost of MRI significantly decreases, the use of MRI as a routine breast examination tool is highly unlikely in the near future.

Computed Tomography, or CT, is an imaging technique that uses x-rays produced from a rotating gantry to create topographical images from multiple slices acquired over a scanned area. The digital processing that follows this procedure creates a 3D view of the interior of the body.[175] This imaging technique has become popular in clinical applications over the last couple of decades because of its ability to create very detailed, high resolution images. This imaging technique also has the ability to distinguish tissues that have density differences as low as 1%.[176] Because the density difference between lesions and glandular tissue is very slim, CT has an advantage over mammography when imaging dense breasts. In a recent study conducted by Wienbeck et. al., 112 lesions were analyzed and compared using non-contrast-enhanced CT and mammography.[177] In this study, two groups were created from the data; there was a low-density group for those with BI-RADS category A or B breasts, and a high-density group for those with category C or D. Two readers were used to analyze the data and the results were combined to compare the mammography results from the CT results. The readers found a sensitivity of 68% among both the low and high breast density groups with the mammography data. With the CT data, they found the sensitivity to be 91% for the low-density group and 88% for the high-density group. Although the sensitivity for CT was significantly higher than that of mammography, the specificity was significantly lower for the CT technique. The readers observed a decline in specificity of about 50% in CT compared to the mammography technique.

The sensitivity of CT often exceeds that of digital mammography because of its ability to distinguish the different tissues present in the breast. CT essentially creates a deconstructed model of the imaged breast that provides insight into the small details that surround the glandularity and breast vasculature. Meanwhile, the superimposition of breast tissue in mammography makes it challenging to distinguish between the different components present, potentially hiding tumors behind layers of glandular tissue. This issue is especially experienced among women with large quantities of glandular tissue. A study conducted a decade ago analyzed the benefits of using cone-beam CT by analyzing the image quality and sensitivity among 40 image sets. [178] A subject of interest in the study was to analyze the difference in coverage between breast CT and mammography. This includes the technique's ability to image obscure components of the breast, such as tissues close to the chest wall. The study found that the coverage of cone-beam CT for breast imaging in the lateral position was 92.5%, much higher than mammography's 12.5%. In the medial position, the coverage was 90% and 35% for CT and mammography, respectively. For the posterior position, the coverage for CT was also found to be 90% while that of mammography's was found to be 52.5%. All of these calculations were statistically significant. In addition, the presence of lymph nodes along the axillary was found for most CT scans with a coverage of 72%, but rarely found with mammography scans. On the subject of image quality, the study found the results between mammography and CT images comparable with both techniques identifying all calcifications above 1mm, all masses, and 85% of calcifications less than 1mm. An interesting finding that the study presented is that the image conspicuity was better for CT than mammography because of the lack of compression during the CT scans. Because the breasts weren't compressed for these scans, there was no observable distortion among the different tissues present and no structure overlap that could cause an erroneous estimation of the lesion location. The study also noted that vessels were more visible in the non-contrast-enhanced CT-produced images than the mammography images. However, some components were better visualized with mammography, such as the microcalcifications. These were better defined in mammography because in the CT images, the calcifications were subjected to beam hardening artifacts thus mildly distorting their appearance and potentially merging small clusters. Although CT demonstrated superiority in coverage and

image conspicuity over mammography, mammography was able to discern small details with better accuracy, such as calcifications. This leads to the conclusion that CT has utility in breast imaging, such as locating lesions in obscure locations, but the debate on whether or not it should replace mammography during screening operations is ongoing.

Unfortunately, CT scans deliver a substantial amount of radiation and are therefore overlooked as a technique for breast screening. This downside is one of the primary reasons why CT is unlikely to replace mammography for screening procedures anytime soon. In the study conducted by Wienbeck, the difference in dose between mammography and CT was over a two-fold. The glandular dose delivered by mammography ranged between 1.8 to 5.1 mGy with an average of 2.9 mGy for all the patients imaged. Meanwhile, the dose administered during CT ranged from 5.8 to 16.6 mGy with an average of 7.2 mGy. The gap in the average glandular dose between mammography and CT was also found to be density dependent with an average dose difference of 3.8 mGy and 5.5 mGy among women with dense breasts and non-dense breasts, respectively. The glandular dose is also said to increase in contrast-enhanced CT. A study evaluated the performance of contrast-enhanced, dedicated breast CT among 46 women with category 4 or 5 breast lesions.[179] In the study, all women underwent both non-enhanced CT and contrast-enhanced CT. It was estimated that women received between 4-16 mGy from mammography, and when they underwent contrast-enhanced CT, it was estimated that the dose received from this technique was an average of about 8-32 mGy. Acquiring a single breast CT image takes about 17 seconds and during screening, each breast is imaged individually thus yielding two images. However, contrast-enhanced CT requires two images; before the contrast media is administered, an unenhanced CT image of the breast is needed for image subtraction. Therefore, four images are needed during breast CT, thus essentially doubling the dose of non-enhanced CT. Although the increased dose delivered by CT compared to mammography seems trivial, it is estimated that fatal cancers caused by dedicated breast gamma imaging are about a 20-30-fold higher compared to mammography.[180] The study noted that lesion conspicuity was higher for contrast-enhanced CT and malignant calcifications were also better identified. In addition, the contrast of the lesion increased by 38 HU (Hounsfield Unit) and the HU difference between malignant and benign

lesions increased as well. Contrast-enhanced CT also offered a slightly increased specificity than non-enhanced CT, but the specificity for both techniques nonetheless trails behind that of mammography. A large decrease in specificity among breast CT data leads to the same problems seen in MRI; too many false positives lead to a large increase in unnecessary biopsies and wastes clinical resources.

Tomosynthesis is a recently emerging technique that offers aspects of high-resolution mammography and computer tomography. This technique was achieved with the development of the flat-panel digital detector which permits the high resolution obtained with mammography.[181] Tomosynthesis also has attributes similar to CT; this technique acquires 'slices' over a region of interest, but unlike CT, the slices span a limited angle instead of completing a full 180-degree rotation. Because of its limited angle, tomosynthesis has been tokened as the low-dose alternative to CT.[182] A typical range for tomosynthesis is about 50-60 degrees and can be as low as 15 degrees in breast imaging applications, therefore significantly reducing the glandular dose compared to CT.[183] In addition, tomosynthesis utilizes reconstruction algorithms similar to those used in CT, but since it does not obtain full anatomical slices, approximation algorithms are needed for full reconstruction. The two most commonly used reconstruction algorithms for tomosynthesis are filtered back projection and iterative, expectation-maximation.[184] The technology supporting tomosynthesis has been recently developed, therefore tomosynthesis is still undergoing continuous development. Early studies of the tomosynthesis technique for breast imaging demonstrated an unfruitful technique with very little to no improvement compared to mammography, but with ongoing research, studies began to find utility provided by tomosynthesis as a supplement to mammography.[185,186] When used as an extension to mammography, tomosynthesis has been proven to increase lesion detection rates with little increase in radiation dose. As radiologists become more experienced at reading tomosynthesis images, the possibility of using tomosynthesis as a non-supplemented imaging technique for routine breast screening is feasible.

The novelty of breast tomosynthesis requires in-depth experimentation and when it began emerging as a clinical tool, radiologists mostly thought of it as an extension to mammography because of its ability to enhance tumor analysis. An early study of tomosynthesis as an extension tool for mammography is the

TOMMY trial, conducted from 2011 to 2013 and supported by Hologic ©.[187] This large trial resulted in the analyses of 7060 cases making it one of the largest trials exploring the use of digital tomosynthesis in breast imaging. The procedure involved scanning each woman with a double-view 2D-digital mammography device and double-view tomosynthesis scan at the same time as a single procedure using Selenia Hologic equipment. The images were read by 26 professionals, including radiologists, advanced practitioners, and radiographers. The readers reviewed each case by analyzing either the 2D mammogram, the 2D mammogram + digital breast tomoynthesis, or the 2D synthetic mammogram + digital breast tomosynthesis. The readers were also unaware of the status or the outcome of the patient and no reader was given data from the center they were employed at. The sensitivity and specificity were calculated for each of the three methods and the data was divided into subgroups based on lesion size, lymph node status, breast density, etc.. The data included 1137 confirmed cancer cases and 5691 non-cancer cases. The results proved that adding breast tomosynthesis to 2D mammography increased the odds of detecting cancer by 34% while simultaneously increasing the specificity and reducing the odds of non-cancer recall by 56%. The results also showed a higher area-under-the-curve for the receiver operations analysis (ROC) curve for both techniques that included tomosynthesis compared to the mammography alone. There was a noticeable improvement in the ROC curve among women with dense breasts and a minute improvement among women whose lesion radiologic finding was microcalcifications. The sensitivity varied drastically among the different subgroups of women with an average improvement of about 1-2% with the two techniques that incorporated tomosynthesis compared to mammography alone. However, there was a more drastic improvement in the sensitivity among the dense breast group and among the group with invasive lesions 1-2cm in size (93% versus 86% for 2D mammography + tomosynthesis versus mammography). Sensitivity was also improved among the group with grade-2 lesions and drastically improved among groups with a mass as the primary radiologic feature. There was little to no difference in the sensitivity between the synthetic and non-synthetic groups that also incorporated tomosynthesis. The study concludes that the addition of tomosynthesis to mammography improves tumor visibility, reduces false-positive rate, and overall improves the accuracy of breast screening. The strength of the study was its large cohort size which

included a diverse lot of lesion varieties. However, given how recent tomosynthesis technology was at the time of the study, the readers were relatively inexperienced and had to take short training courses to become accustomed to the images while they had over ten years of experience reading mammographic images. This caused a bias in favor of mammogram data over tomosynthesis data. Analyzing the potential of tomosynthesis as a singular screening tool requires readers that are experienced at reading tomosynthesis images and as the technology is further developed and researched, the true potential of tomosynthesis may be uncovered.

A comparative study conducted in 2018 found that digital breast tomosynthesis, or DBT, has an improved sensitivity over 2-D digital mammography and can improve the assessment of tumor size.[188] In the study, Michell and Batohi note that the 'flattened' images produced by mammography contain overlapping components that can make it challenging to differentiate between the different structural components of the breast and can obscure lesions under layers of glandular tissue. Therefore, a major advantage provided by tomosynthesis is the 3D reconstructed view of the breast that provides accessibility to the breast constituents. The stack of images obtained over the limited-angle projections are rendered to create the 3D view and does not include superimposition of multiple tissues as seen in mammography and neither does it contain features from adjacent layers, as observed in computed tomography. A study conducted in 2016 sought to quantify the differences between DBT and full-field digital mammography by assessing the sensitivity, specificity, and BI-RADS category assessment in both techniques.[189] The study included 319 patients with 337 malignant lesions and 42 benign lesions. Prior to the study, the women chosen for the study had BI-RADS lesion scores of 4 or 5, which includes women with *suspected* lesion as well as women with a BI-RADS score of 6, which includes those with newly diagnosed lesions. Full-field digital mammography images were acquired in both the craniocaudal and mediolateral oblique views, but digital breast tomosynthesis images were only acquired in the mediolateral position. There were 15 tomosynthesis images acquired per scan over a 40-degree angle and the images were reconstructed with a custom algebraic iterative technique. The dose was equivalent for both techniques. The sensitivity was calculated for each technique based on their ability to identify the glandularity level (breast density), tumor

type (invasive vs. non-invasive), and tumor size. The specificity was calculated from the density type and non-cancer data %. The ability to correctly identify the breasts' density for both techniques was comparable but slightly better among the tomosynthesis technique with a sensitivity of 88.4% among dense breasts, which was about 10% higher than that of mammography. Tomosynthesis was also better at identifying the tumor invasiveness with sensitivity comparison of 70% versus 53.3% for mammography among non-invasive lesions. Among the invasive lesions, tomosynthesis and mammography had a sensitivity of 90.6% and 83.4%, respectively. Tumor size assessment sensitivity was also higher for tomosynthesis, outperforming mammography for both lesions smaller and larger than 2cm. The overall specificity was slightly higher for full-field digital mammography by less than 1%. The study concludes that the accuracy of digital breast tomosynthesis was higher than that of full-field digital mammography and provides evidence that breast tomosynthesis may improve lesion detection and characterization. However, the study states that it is worthwhile to expand the study since the subjects used in the study may not be generalizable and representative of a larger population. The lesions were also unclassified, therefore, there was no information provided on whether or not the results are subjective to certain tumor types.

In a later study conducted in 2020, data for 488,099 patients with almost 14,000 breast cancers was analyzed to evaluate the performance of breast tomosynthesis, breast tomosynthesis combined with digital mammography, and mammography alone.[190] The objective of the study was to quantify the performance of tomosynthesis because of the evidence provided by other literature stating the potential of the technique; however, small cohort size has often been the limiting factors in the other studies conducted. The data was gathered from numerous studies and studies with bias in their data were excluded from this study. The sensitivity, specificity, and ROC curves were calculated with a confidence interval of 95%. The results returned equal values for sensitivity for both techniques that utilized tomosynthesis and a sensitivity of 79% for digital mammography alone. The specificity was higher for tomosynthesis alone with a value of 84% compared to 81% for tomosynthesis combined with digital mammography. Mammography alone returned as specificity value of 79%. The AUC for the ROC curves were 0.93, 0.92, and 0.85 for tomosynthesis, tomosynthesis and digital mammography, and mammography alone. Overall, the results demonstrated that

both techniques that use tomosynthesis have a higher accuracy than digital mammography alone while the difference between tomosynthesis and tomosynthesis combined with mammography are not significant. These findings are momentous because they provide reliable evidence that tomosynthesis can be used as a sole imaging technique and provides adequate lesion detection without the need for a secondary imaging technique. As a concluding remark, the study mentioned that it is worthwhile to explore these findings further with subclassification, that is, comparing the difference in the accuracy of the different techniques listed among different groups of women, such as those with asymptomatic lesions. Given the relative novelty of tomosynthesis as a breast imaging technique, such analysis will occur over time.

As previously mentioned, tomosynthesis technology is fairly recent and is under continuous development. A downside to this is that the lack of experienced readers can have a severe impact on the sensitivity and overall accuracy of the imaging system. This creates a discrepancy between the accuracy in comparative studies which imparts a challenge on determining the accuracy and full potential of tomosynthesis as a breast imaging technique. A comparative study conducted in 2017 sought to identify a relationship, if any, between reader experience and breast tomosynthesis sensitivity.[191] The members of the study noted that breast tomosynthesis trials reported inconsistent findings in their quantitative analysis and the sensitivity and accuracy of tomosynthesis was challenging to determine due to the inconsistency of the readers' experience. The main question that surrounds tomosynthesis technology in breast imaging is whether or not it improves tumor identification and assessment during routine screening. This question is difficult to answer with inconsistent results reported from multiple studies. Therefore, assessing the role of reader experience in sensitivity findings can lead to a better understanding of the novel technology and its accuracy. The study points out that the diagnostic accuracy of 2D mammography is affected by the years of experience readers have as well as the amount of 2D mammograms read each year. To quantify the association between reader experience and breast tomosynthesis accuracy, the study analyzed 7060 screening cases along with the data demonstrating the readers' experience. Interestingly, the study found that breast tomosynthesis sensitivity was higher for readers who had less experience reading 2D mammography images, and among these readers, tomosynthesis was a great addition to 2D mammography.

While the sensitivity in the tomosynthesis technique compared to 2D mammography increased among 80% of readers, the highest increase was observed among readers with less than ten years of experience. This trend may be caused by more equally proportionate exposure to tomosynthesis images and 2D mammograms while those with more years of experience are more accustomed to 2D mammograms. This may pose a challenge to older readers who are unaccustomed to tomosynthesis images if tomosynthesis becomes a widespread screening tool.

A main concern associated with transition to digital breast tomosynthesis is the glandular dose increase from digital mammography. The increase in glandular dose can be dependent on several factors, such as the equipment used, breast density, and breast thickness. A recent study conducted in 2018 compared the average glandular dose between 2D digital mammography and digital breast tomosynthesis.[192] In the study, DICOM data from 3819 woman was used and analysis was performed with and without breast density stratification. Both the craniocaudal and mediolateral oblique views were acquired for both techniques. The overall average glandular dose was found to be 1.4 mGy for mammography and 2.1 mGy for tomosynthesis. The difference in glandular dose was higher among women with fatty breasts, with an average of 1.74 mGy and 2.27 mGy for mammography and tomosynthesis, respectively. However, the average glandular dose was very similar among women with dense breasts between the two techniques with an average of 1.73 mGy for mammography and 1.79 for breast tomosynthesis. For breasts with similar compression thickness, the breast density played a larger role in mammography's average glandular dose than it did with tomosynthesis demonstrating an increase in the dose with mammography but not tomosynthesis. The ratio between mammography's and tomosynthesis' average glandular dose was close to 1 for dense breasts and the highest observed was 1.33 for fatty breasts and the overall average ratio was 1.24. These results demonstrate that although the dose is higher for breast tomosynthesis, it is not a substantial increase, and is in fact minimal among the population that would most benefit from tomosynthesis as a screening tool.

2.2.2 Sensitivity and its Barriers

The sensitivity of a breast imaging system is an invaluable way to measure its efficacy as well as the trustworthiness of the results. A system with a high sensitivity is more likely to reduce cancer mortality by detecting tumors early before any symptoms appear. Therefore, it's crucial to prioritize sensitivity in an imaging system. For this reason, sensitivity is often seen as the limiting factor in many imaging systems, including those outside of breast imaging. The main motivation behind several novel imaging techniques is to improve sensitivity so that tumors or other diseases can be detected early. If a system has inadequate sensitivity, the system can either be improved, or an entirely new system may be suggested. In breast imaging applications, both strategies have been used; contrast agents have been incorporated into mammography to improve the system and entirely new systems, such as breast CT, have been developed in hopes of improving the sensitivity.

In breast imaging, the widespread limiting factor is the interdependence of glandular tissue and tumor tissue, which can appear inseparable in breasts with high glandular content and in cancers with no well-defined masses. As previously mentioned, the reason for this interdependence is the nearly identical attenuation and density between the two tissue types. Consequentially, the two tissue types can be indistinguishable in x-ray-based imaging techniques. This is especially true in mammography where superimposition of glandular tissue can create the illusion that a cancerous mass is located in the breast causing an increase in false positives. The opposite can also be true, where superimposition of breast tissue can obscure a tumor mass which causes an increase in false negatives. Strategies to offset the challenges set by high breast density include 3D imaging, such as CT and tomosynthesis, to improve the appearance of superimposed tissue. Although these methods have demonstrated an increase in sensitivity, the sensitivity is still limited by the fact that the attenuation of the glandular and tumor tissue are very similar. Therefore, tumors that aren't presented as well-defined masses can be mistaken as glandular tissue. Because of the similarities between glandular tissue and tumor tissue in x-ray-based imaging techniques, strategies that highlight their differences outside of density provide much utility. MRI's ability to depict small differences in hydrogen content has earned it the best sensitivity out of any other imaging technique. Likewise, ultrasound has provided a boost in sensitivity with its ability to differentiate tissue composition from

recipient sound waves, but because of its lack of structural information, it isn't often used as a standalone procedure.

Another limiting factor in the sensitivity is the electronics used in breast imaging. This includes detector panels, digital processing techniques, and any component of the image processing chain that follows breast irradiation. While there has been a vast improvement in imaging systems, including the switch from film to digital technology, limited resolution can obscure microcalcifications, which are often used to identify regions with a potential malignancy. A limited resolution also restricts vasculature visibility, especially the small vessels that surround a tumor. Small details that accentuate the difference between a malignant region and a healthy region are often lost in an imaging technique with poor resolution. For this reason, it's important to continuously develop the detectors and electronics that contribute to breast imaging.

A challenge with improving the sensitivity of a breast imaging system is preventing the system from becoming 'overly sensitive.' An increase in false positive leads to a decreased specificity, as seen with MRI, which often has a specificity lower than that of mammography's. Systems similar to MRI tend to increase the overall number of positives thus leading to an overestimation of malignancies. Although high specificity isn't as sought after as high sensitivity, poor specificity can lead to a loss of resources as patients find themselves undergoing unnecessary biopsies to confirm the state of a finding. Therefore, aiming for a high accuracy in any imaging system benefits the clinical setting as well as patients undergoing screening procedures.

2.2.3 Proposed Pathways on Improving Sensitivity

A pathway that has been proposed for breast imaging that has not been listed in this paper is single-photon emission computed tomography, or SPECT. This imaging technique involves using an internal source of radiation, such as a contrast agent conjugated with radioparticles, to target specific tissues and create a 3D image of the target region. The radioparticles are gamma emitters, such as Tc-99m, and the contrast media typically includes targeting antigens as vehicles to drive the radioparticles into the tissue of

interest. This imaging technique is similar to MRI in that in can measure metabolic functions, such as myocardial perfusion.[193] Compared to CT, the resolution of SPECT is quite poor, and while collimators are used to improve the spatial resolution, they significantly reduce the efficiency. Breast specific gamma imaging systems, or BSGI, incorporate SPECT into mammography-like systems to image the breast with gamma cameras.[194] In a meta-analysis study that investigated the use of SPECT as an adjunct tool to mammography, SPECT provided a high sensitivity of 95% in high-risk settings with an adequate specificity of 80%.[195] Cancers smaller than 1cm in length demonstrated a lower sensitivity of 84% and ductal carcinoma *in situ* had a sensitivity of 88%.[196] A large prospective study that included 936 women found that incorporating BSGI into breast imaging can increase the sensitivity from 27% to 91% and can increase the rate of cancer detection by 7.5 per 1,000 women.[197] The limitation with this technique is the undeniably large increase in dose imparted by the radiocontrast used. The dose from the Tc-99m-sestamibi contrast currently used is estimated to impart a dose of about 6.5 mSv, which is about a 9-fold higher than the 0.7 mSv estimated for mammography. Because of its associated high dose, BSGI isn't considered a viable option for breast screening. However, studies investigating the effectiveness and performance of a reduced-dose radiocontrast are currently underway.

A fairly recent imaging technique that has been proposed for breast imaging is spectral mammography. This technique originates from spectral CT, which is dependent on energy-sensitive photon counting detectors that enable the system to differentiate between the variegated photon energies that are impinged upon the detector.[198] The number of bins in a system vary per utility, but systems with about 4-5 bins have been widely experimented with. The bin limits are typically placed right above the k-edge of the different materials of interest; this allows for clear differentiation between the different materials present. **Figure 6** demonstrates spectral CT images compared to a conventional CT image. The five images below demonstrate the segmented images produced from the different materials present in the phantom by using distinct energy bins during image acquisition. All components can be easily distinguished with this method.
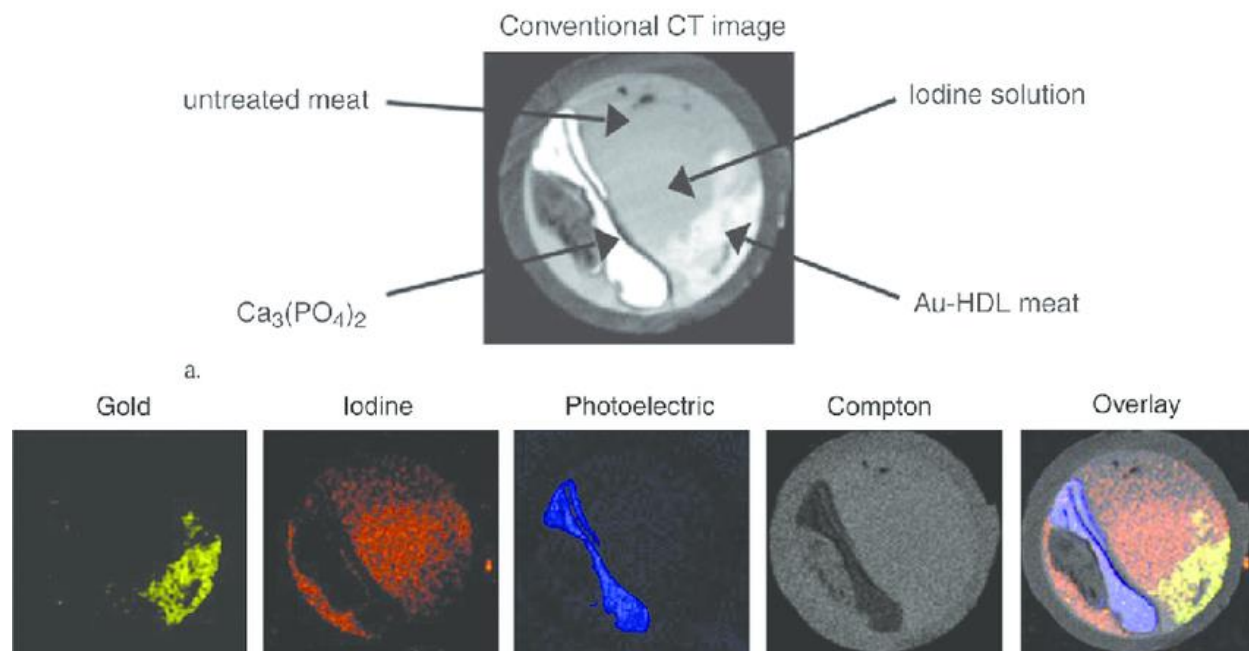
Figure 6:[199] An image comparing conventional CT with spectral CT. The bottom images demonstrate the segmented CT based on the different signals received for each energy bin used during a spectral CT scan.

A study conducted in 2010 sought to investigate the use of spectral CT to determine the probability of a heart attack based on the amount of plaque identified in an imaging session.[200] In this study, mice were injected with two different contrast agents; an iodine-based contrast agent was used to visualize the vasculature in the mice while a gold nanoparticle lipoprotein contrast agent was used to target macrophage burden caused by atherosclerotic plaque. The energy thresholds for the detector system were placed at 25, 34, 51, 80, 90, and 110 keV which considered the iodine k-edge of 33.2 keV and the gold k-edge of 80.7 keV. The resulting images were decomposed into the material constituents with an image representing gold contrast agent update, another representing iodine uptake, an image representing calcium, and another representing tissue. The results demonstrated that the gold images showed a clear and well-defined aorta with an outlined region representing the gold uptake in the surrounding plaque. The iodine images demonstrated a clear representation of the mice vasculature and the calcium images demonstrated the mice skeletal systems with little to no cross-contamination of contrast agents. The study had two important takeaways. The first is that gold nanoparticles provide utility in imaging and can significantly increase the

attenuation of an area of interest. Its conjugation with a targeting agent, such as liposomes, can significantly improve contrast localization which improves the contrast between the background and the tissue of interest. The second takeaway is that spectral CT is very successful at differentiating between the different components in a region as long as the energy bins are chosen to maximize efficiency. The utility of spectral CT vastly improves with the use of contrast media; therefore, it is highly encouraged to incorporate at least one contrast agent in spectral CT imaging.

A niche application of this technique is contrast enhanced spectral mammography, or CESM, which falls under the scope of spectral *molecular* imaging, or SMI. SMI techniques include the addition of contrast agents to further differentiate between the organ, feature, or tissues of interest and the surrounding region. Although CESM is very similar to dual-energy contrast-enhanced mammography and dual-energy CT, it's different in that it uses separate energy bins whereas the other two techniques use fast voltage switching, and the high energy beam cannot be fully filtered, thus causing an overlap in the source spectrum.[201] Separate energy bins allows for clearer differentiation between the different materials present, therefore highlighting regions affected by the contrast media further than with other techniques. In a study conducted in 2017, Fallenberg et. al. aimed to compare the diagnostic performance of CESM with digital mammography and MRI, since the former is the most widely used screening technique and the latter is the breast imaging technique with the highest sensitivity.[202] The study included 187 women with invasive breast cancer and or ductal carcinoma *in situ*. Four techniques were used to generate images that were then analyzed by a group of radiologists; these included, digital mammography, CESM, digital mammography + CESM, and MRI. The ROC curves generated from each of the techniques were used for quantitative assessment of their performance. The average sensitivity was calculated for each technique and the results demonstrated a comparable sensitivity between MRI and the techniques that used CESM. The sensitivity for MRI was found to be 0.95 and 0.94 for CESM and CESM + digital mammography while digital mammography alone produced a sensitivity of 0.81. The specificity was the lowest among for MRI, with an average of 0.88, and highest for digital mammography with an average of 0.95. The average specificity for CESM and CESM + digital mammography was 0.92 for both techniques. The area under the curve for

the ROC curves was the lowest for mammography with a value of 0.76 while the area under the curve was comparable for MRI, CESM, and CESM + mammography with values of 0.85, 0.84, and 0.83, respectively. When analyzing the ROCs for women with dense breasts, they found that CESM alone and MRI performed very similarly, showing no significant differences between the two techniques, proving to be the most beneficial techniques for women with sense breasts. In addition, CESM provided the most inter-reader agreement than the other techniques, and it also demonstrated improved lesion size estimation compared to the other techniques listed. The results shown in this study agree with other studies that have examined and compared CESM with other clinical techniques to evaluate its performance.[203,204] Unfortunately, the study only involved patients with confirmed breast lesions, both benign and malignant, which introduces bias into the data. It's important to evaluate the performance of CESM in a realistic setting, one where lesion-free women are included to measure its accuracy among a diverse dataset. The study size is also relatively small and doesn't provide enough details on the lesion characteristics that can impact visibility, such as location and stage. Nonetheless, these promising results demonstrate that there is a potential future for CESM in a clinical screening setting.

MRI has been tokened as the 'gold standard' for breast imaging due to its high sensitivity without imparting ionizing radiation onto receiving patients. However, given its high cost, and long scan times, using MRI as a screening tool is impractical. Promising techniques, such as CESM, tomosynthesis, and other SMI techniques have the potential to provide as high a sensitivity as MRI in a clinical setting without requiring high costs or high scan times. The inclusion of contrast agents in imaging techniques has proven to improve the sensitivity in traditional techniques, such as CT, MRI, and mammography. Further, their role in breast imaging can be further explored in novel imaging techniques. CESM and other SMI studies have widely demonstrated a high efficacy in these imaging techniques; therefore, the role of contrast agents in breast imaging techniques should be extensively adopted. In addition, multi-energy techniques that increase the utility of contrast agents by improving sensitivity might be the future of breast imaging with further clinical research. With the numerous breast imaging techniques and tools that have been proposed and explored in the recent years, the options available to improve sensitivity are numerous and several

comparison studies need to be conducted to find techniques that can reproducibly surpass the clinical utility and facility that mammography offers.

Further work is still needed for imaging techniques mentioned in this paper. Imaging techniques that use energy discrimination can surpass tissue differentiation of other dual-energy techniques, largely due to the energy-sensitive detectors used. To optimize these detectors and improve their spatial or energy resolution, the detectors must employ an ideal combination of pixel pitch, size, and semiconductor layer thickness. Distance between pixels can also impact image quality and artifacts caused by their size may be removed with charge processing techniques.[205] Other work that is still needed includes contrast agent exploration. The role of contrast agents in breast imaging is promising but more research is needed to explore contrast agents that are the most promising in a clinical setting. A wide range of novel contrast agents have been proposed for a variety of imaging techniques, including breast screening. Feasible contrast agents need to employ a balance of high contrast enhancement, biocompatibility, and cost effectiveness, among other features. In addition, tomosynthesis is a well-performing imaging technique that has demonstrated high sensitivity and promise with further development; moreover, a tomosynthesis technique that utilizes contrast enhancement has yet to be employed in a clinical setting. Given the efficacy improvement that contrast agents have provided in a variety of imaging techniques, tomosynthesis can also potentially benefit from contrast enhancement. In the next section, the future of contrast agents will be discussed.

2.3 Contrast Agents for Breast Imaging

2.3.1 A New Approach to Breast Imaging Contrast Agents: Materials

Contrast agents are used to enhance the visibility of tumors and other areas of interest by highlining features unique to the target tissue, such as excessive vasculature. Exploring and improving contrast agents in medical imaging is an ongoing process and there are several factors to consider while developing contrast agents, including, does the contrast agent produce a comparably higher effective Z in the target tissue than in the surrounding tissue? Is the contrast agent compatible with a specific imaging technique? Does the

contrast agent have a stronger affinity for the tissue of interest relative to other tissues present? With these questions in mind, researchers have sought out ways to improve tumor visibility in various imaging techniques. In a review conducted by Caschera et. al., the performance of various contrast agents spanning a range of imaging techniques is evaluated.[206] The study recognizes three important physiochemical properties of contrast agents that need to be considered during creation, including concentration, viscosity, and osmolality. In CT and other forms of x-ray-based imaging techniques, the contrast agents function by increasing the absorption of x-ray radiation in the target organ, lesion, or blood vessels. Currently, iodine is the most common element used for these imaging techniques because of its K-shell binding energy of 33.2, which is around the average energy used for medical diagnostic imaging. In their study, Caschera et. al. estimate that the average increase in attenuation caused by each mg of iodine per ml of blood or cubic centimeter of tissue is 25 Hounsfield units (HU).[207] Meanwhile, contrast agents for ultrasound imaging techniques allow for tissue perfusion imaging in addition to the 'live action' information on vascularization provided by the Doppler technique. Elementary contrast agents for ultrasound imaging were presented as encapsulated air microbubbles, but because they dissolved before reaching the vascular network, they were evolved to contain phospholipids, which provided structural stability.[208] These contrast agents work by increasing the radio frequency of the vasculature section they are located in, and since their development, they have been used for the characterization and assessment of lesion detection and treatment response. Contrast agents for MRI function by increasing proton relaxation rates in the area of interests which shortens the relaxivity (T1 and T2). Contrast agent utility in MRI is represented by the T1 and T2 ratio; T1 specific contrast agents are composed of paramagnetic complexes while T2 specific contrast agents are primarily composed of super paramagnetic ions. MRI contrast agents vary based on their application and can be used to highlight different regions of the target tissue. It's important to note that no matter the imaging technique, the chelating compounds attached to the contrast molecules are important to consider because they control the delivery of the contrast agent.

In this paper, the contrast agents of interest are those that play a role in x-ray-based imaging techniques. A current approach to increase the efficacy of contrast agents for x-ray-based imaging

techniques is to increase the effective-Z of the target tissue by increasing the effective-Z of the contrast agent. This can be achieved by increasing the concentration of the main element, such as iodine, per unit contrast solution, or by introducing heavier elements into the solution. The problem with increasing the number of contrast particles per solution is that the viscosity and osmolality might cause discomfort or biologically incompatible for clinical use. Heavy elements that are currently being considered for novel contrast agents are lanthanides. Lanthanides have high atomic numbers and are relatively dense; however, free lanthanide ions are extremely toxic. This is partially due to their tendency to mimic other elements that humans need, such as calcium, and can disrupt biological processes. Fortunately, several lanthanides can form highly stable bonds with acid chelates.[209] A method for incorporating lanthanides into contrast agents is by attaching a lanthanide chelating ligand, such as one with Gd, Eu, or Tb, to a macrocyclic amine and a covalently attached antenna along with calcium-binding aminodiacetate arms.[210] A more popular application of lanthanides in contrast agents is the use of macromolecular and nanoparticle lanthanide structures for CT contrast enhancement.

A lanthanide macromolecule currently under development is a DTPA-conjugated dextran polymer that uses either Gd or Dy and can be used to image vasculature or lesions with CT. In a study that analyzed the biocompatibility of lanthanide nanoparticles, a Dextran solution with a molecular weight of 40,000 g/mol was conjugated with 0.5 Dy atoms per glucose as a viable contrast solution. The paper states that Dextran is an excellent choice as a host macromolecule because it has a molecular weight low enough for renal filtration and a size large enough for longer retention times. It also allows for a large number of reporters, such as Gd and Dy. Interestingly, the molecule can be altered to contain a molecular weight appropriate for optimal imaging performance. The Dextran molecule was approximately 8.8 nanometers in diameter and had an average molecular weight of 101,537 g/mol. The results demonstrated no acute toxic effects and a half-life of about 8 minutes. Qualitatively, the inferior vena cava that was used as baseline remained enhanced (bright) throughout all CT scans. Quantitatively, the solid part of the liver tumors they imaged were enhanced by about 5-10 Hounsfield Units. A concluding remark of the study was that the contrast agent had an increased viscosity relative to other marketable contrast solutions. High viscosity

introduces challenges during injection, and it can be unsafe to inject large quantities of a highly viscous solution. The study noted that other molecular configurations might work better in imaging applications, however, they noted that retention time is 3-fold longer than standard contrast media makes these type of contrast agents worth looking into. Further studies should be conducted to optimize their biocompatibility as well as improve their attenuation. Although the attenuation of the nanoparticles didn't demonstrate a remarkable improvement from current iodine-based contrast agents, research investigating the optimization of lanthanide placement is ongoing.[211]

A different nanoparticle type that is currently undergoing investigation is AuNPs, or gold nanoparticles. These nanoparticles are favored among other contending contrast particles because they have ideal features; gold has a high density, it is nontoxic in small quantities, and it has a high atomic number. On average, gold has been found to increase contrast by 2.7 times per unit weight compared to iodine.[212] Because AuNPs has favorable synthesis properties, have modifiable surfaces, and can be manufactured with a controlled size, AuNPs have been thoroughly researched in various applications, including applications outside of medical imaging. Their modifiable surfaces allow researchers to incorporate a range of biocompatible particles, such as targeting ligands, that can transport the nanoparticles to a target region with efficient delivery. **Figure 7** demonstrates how a gold core is surrounded with PEG; the surface is then further modified by incorporating targeting antibodies.
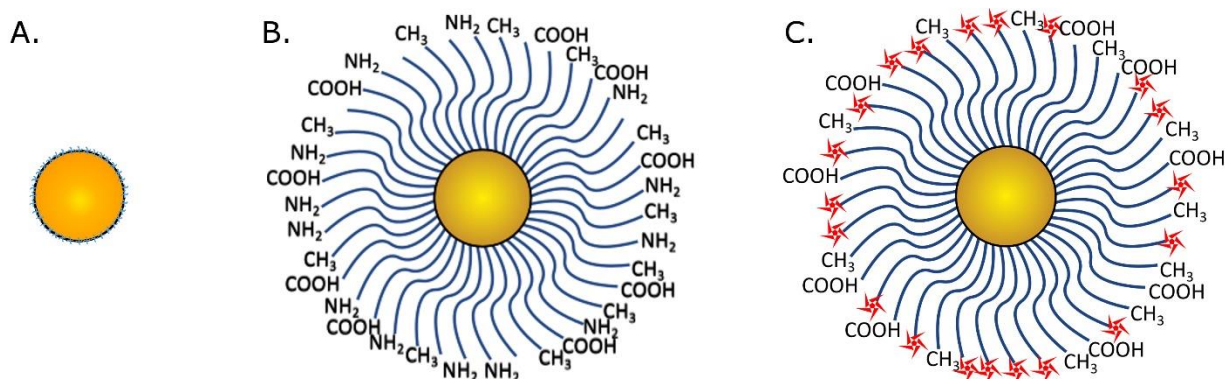
Figure 7: A visual representation of AuNP conjugation with (b) PEG and (c) targeting antibodies.

A simple AuNPs design used for contrast media is PEGylated AuNPs; these are AuNPs attached with PEG, or polyethylene glycol, that have long blood circulation times, are biocompatible, and are comparatively large particles.[213] A study conducted in 2016 analyzed the behavior of PEGylated AuNPs modified with targeting ligands for CT imaging using mice. The AuNPs were modified with entrapped branched polyethylenimine which exhibit biochemistry similar to animated dendrimers.[214] The study hypothesized that these modified AuNPs can successfully and efficiently accumulate in cancer cells. The study reviews several aspects of the potential contrast agents. To assure biocompatibility of the modified AuNPs, cell viability assay was conducted with cell morphology observation. Targeting specificity of the AuNPs among the cancer cells was quantified with flow cytometry as well as confocal microscopy. Staining studies were conducted to assess the *in vivo* AuNP biodistribution using hematoxylin and eosin. The x-ray attenuation properties of the AuNPs were analyzed by comparing the contrast of the particles to Omnipaque. An observation made during the study is the brightness of AuNPs exceeded that of Omnipaque at the same element concentration, thus agreeing with previous studies.[215] The cytotoxicity analyses conducted with the AuNPs demonstrated that the toxicity depends on the molecular configuration of the nanoparticles; gold concentrations exceeding 400 uM demonstrated cell viability below 80% with a certain configuration but concentration could exceed 800 uM with cell viability exceeding 80% with a second configuration. The concentration studies analyzing the uptake of the AuNPs among cancer cells found that the concentration of AuNPs was significantly higher in the cancer cells expressing the receptors of interest than the cells without them, thus providing critical information on the AuNPs' capability to specifically target the cells of interest. Quantitative analysis of contrast enhancement demonstrated significant increase in contrast among tumors affected with AuNPs compared to those affected with Omnipaque. In addition, the study found that higher concentrations of the contrast agent yielded higher contrast which demonstrates a confirmed correlation between contrast uptake and 'brightness.' The study also found that the maximum AuNPs concentration was achieved 2.5 hours post injection but can take up to 6 hours with a different molecular configuration. In conclusion, the study found that tumor-targeting particles can be attached to AuNPs for CT imaging for improved contrast enhancement while remaining biocompatible. This study was

one of the first reported studies that used AuNPs synthesized with PEG for the purpose of x-ray imaging. Because this was an early application of tumor targeting PEGylated AuNPs, areas that need further development are highlighted. Small changes to AuNPs can affect distribution time, cell viability, and uptake, therefore, specific applications of AuNPs need to be studied extensively to assure their compatibility with the tumors or tissues and application of interest

Several subsequent studies reported utility in surface modification strategies used to create targeted contrast agents with AuNPs. A study that explored AuNPs modified with 2-deoxy-D-glucose reported high resolution anatomical and metabolic information can be obtained with the contrast agent using CT imaging.[216] A different study reported a targeting stringy using UM-A9 antibodies to target squamous cell carcinoma *in vitro* using CT imaging.[217] The study reported that the 45 nm-length AuNPs provided much higher contrast to the region of interest compared to regions with normal cells or in images obtained without targeting strategies. A similar study targeted squamous cells in live mice using AuNPs modified with EGFR antibodies with an average length of 45 nm.[218] The study found that squamous cells took up the EGFR-modified AuNPs at concentrations 130 times higher than in parallel cells in the control mice given the same quantity of contrast agent. No toxicity was observed 7 days post injection. Other studies have described alternative nanoparticle coatings outside of polymer coatings that can provide favorable biochemical characteristics that can aid in the delivery or metabolism of the contrast agents. A study described a strategy to improve biological stability and controllable particle size with silica coatings as an alternative to polymer coatings.[219] The versatility of AuNPs makes them a favorable candidate to a broad spectrum of clinical techniques, including breast cancer imaging. Targeting strategies for breast carcinoma are discussed in the next section.

Unfortunately, the high market cost of gold disincentivizes its use in contrast agents, and other high-density metals are being considered. A potential candidate to substitute gold with is silver. Silver has a high atomic number of 79 and a density over twice that of iodine's. A study conducted in 2016 created silver nanoparticles with silica encapsulation surrounded with PEG coating to experiment the nanoparticle's use as a contrast agent in dual-energy mammography.[220] A primary reason why silver was chosen in the

study is due to silver's low k-edge of 25.5 keV. At this energy, the anatomical detail of soft tissue is clearly visible. This energy also provides extended flexibility between the low and high energy spectra used during dual energy mammography. Another reason why silver is a potential contender for clinical nanoparticles is due to its improved signal to noise ratio compared to iodine; in optimal dual-energy imaging conditions, silver has provided a signal to noise ratio up to 43% higher than iodine's.[221] The study utilized mice to study the biocompatibility, organ contrast enhancement, and performance compared to saline and gold nanoparticles. The study did not mention the use of any targeting mechanism in the nanoparticles. The average size of the silver nanoparticles was measured to be about 102 nm and the clearance characteristics demonstrated a half-life in the blood stream of about 15 minutes. Thereafter, the particles were mostly distributed to the liver, lymph nodes, and spleen where they were mostly metabolized and excreted in about 24 hours after injection.

When compared to the saline and AuNPs, silver demonstrated superior contrast performance in dual-energy applications. The AuNPs demonstrated significant enhancement in both the low and high energy images; however, because the k-edge of gold is above the energy range used (29-49 keV), there is no significant difference in the gold contrast. Therefore, when the images are subtracted, there is little residual enhancement seen in the final image. Saline provided insignificant to no enhancement in any images. In the low energy image, the silver contrast is faintly observed and appears much more prominent in the high energy image. When the images are subtracted, the final image demonstrates significant enhancement where the silver nanoparticle reside. The study noted that the silica shell and PEG coating creates a stable and highly biocompatible nanoparticle that can be used intravenously. An important takeaway of the study is that the structure of the nanoparticle needs further review. A reason for this is the relatively low amount of silver per unit weight; only one silver particle is used per nanoparticle center, therefore each particle only contains 19% silver by weight. The bulk of the weight was due to the silica shell which provides no contrast enhancement. For this reason, the nanoparticle should be modified to have a reduced shell thickness which would increase the amount of silver by weight. The nanoparticle should also be modified to include more PEG, which was concluded after the vascular half-life was found to be

insufficiently short. Increasing the amount of PEG can provide more favorable pharmacokinetics and accumulation in the liver, spleen, and lymph nodes is less likely to occur.[222] Overall, silver nanoparticles have favorable qualities that can improve dual energy mammography and provide utility in other clinical applications as well.

Another potential replacement for AuNPs is tantalum oxide nanoparticles, or TaONPs. These nanoparticles have shown promise in *in vivo* and *in vitro* applications and have been found to increase x-ray attenuation in CT imaging compared to iodine-based contrast agents.[223] Like other nanoparticles, the size of TaONPs can be easily modified and can range between 5 and 15 nm. TaONPs with PEG have been found to function as a useful contrast media for multimodal imaging, including CT and fluorescence imaging in rats.[224] In addition, studies monitoring toxicity up to 2 weeks post injection concluded that no significant toxicity was produced by these nanoparticles. Iron-platinum nanoparticles, FePtNPs, also have desirable properties observed with AuNPs without the high cost. Analogous to other nanoparticles described in this paper, FePtNPs can be manufactured with a controlled size, albeit typically on the smaller scale with sizes ranging from 3-12 nm and can also be modified to control tumor targeting antibodies.[225] These particles exhibit relative long retentions times and it can take up to a week to fully clear the contrast solution from the body. These nanoparticles have no observable toxicity at concentrations exceeding 10 mM of iron and demonstrate overall good biocompatibility.

The use of nanoparticles in contrast solutions is a recent technique and is currently being thoroughly researched. There are several factors to consider while creating these nanoparticle solutions and some of them are due to the fact that small changes in the nanoparticle structure can impact their biocompatibility, retention time, and other biochemical interactions in the body. Because small differences in the nanoparticles can impact the utility and role of the contrast agent, numerous experiments and research needs to be conducted to make sure the contrast agent provides utility to the imaging technique of interest, can target the organ or tumor of interest, and has biochemical properties that are compatible with humans. AuNPs have been the most thoroughly researched of all the other nanoparticles listed in this paper, however, given their high cost, it is critical to find other heavy metals that can replace gold. Given the current status

of ongoing research, it is very likely that nanoparticles with the same contrast enhancement potential as AuNPs will be developed at a cheaper cost. The nanoparticle configuration possibilities are numerous with a broad range of potential heavy metals, shell type, and targeting mechanism, hence nanoparticles might be the future of contrast agents.

2.3.2 A New Approach to Breast Imaging Contrast Agents: Targeting Mechanisms

Contrast agents, including those under current development, can provide an improved signal to noise ratio in a region of interest by providing a boost in the attenuation. While contrast solutions function properly through the vasculature, they are most effective when specific targeting mechanisms are included and provide the highest boost in the signal to noise ratio. Oftentimes, a targeting mechanism is included by conjugating a specific ligand or bioparticle to a contrast particle, such as a nanoparticle, however, other methods have been used. Particles with an affinity to certain organs can be used, such as iodine for thyroid imaging, or calcium for skeletal structures. Other methods include controlling the contrast particle size to favor the biophysical properties of a region of interest. In the interest of breast imaging, particle size can be manipulated to take advantage of the porous, or *leaky*, vasculature that surrounds breast tumors. Investigating the efficacy and utility of a variety of targeting mechanisms can provide the key to improving contrast agents which can, in turn, increase the sensitivity and accuracy of breast imaging systems.

A method to target breast tumors is to take advantage of the hyper-porous characteristics of tumor vasculature. As described earlier in this paper, tumors develop rapidly and require a quickly built vascular system to accommodate tumor growth. Tumors are known to have high concentrations of vascular endothelial growth factors, VEGF, in order to develop the vessel networks required to supply the tumors with nutrients. These factors are also signaled due to the hypoxic environment created inside a tumor during the early stages of development. Meanwhile, VEGF and VPF, vascular permeability factor, can increase the permeability of these microvessels in order to increase the transport of plasma proteins to the tumor site.[226] In fact, it is crucial for tumors to be hyperpermeable because they permit the transport of fibrinogen and plasma proteins to initiate clotting; transport of these protein rich fluids allows tumors to activate the

clotting system by creating the extravascular fibrin gel matrix, which is the primary step in stroma generation.[227] An early study conducted in 2000 explored taking advantage of the leaky vasculature surrounding solid tumors to explore the transport of macromolecules for therapeutic purposes.[228]
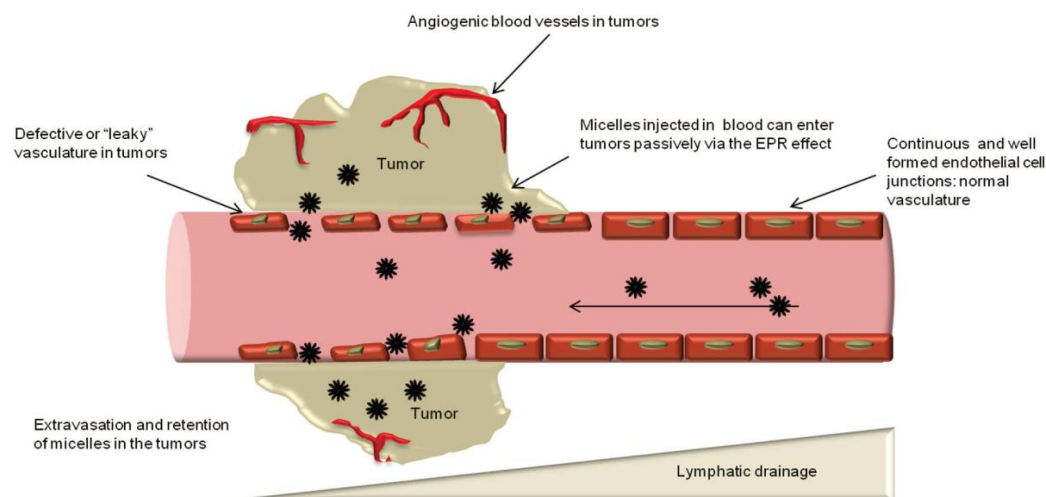
Figure 8:[229] A visualization of the leaky vasculature that surrounds tumors.

Enhanced permeability and retention, EPR, is a tumor specific characteristic, shown in **Figure 8**, that can be exploited for tumor-targeted particle delivery and the term was coined after several observations noted that high concentrations of macromolecules could be retained in tumors for up to 100 hours. This effect is especially dependent on the size of the molecules; studies have observed the relationship between size and retention and found that low-weight molecules return to blood circulation through diffusion.[230] The EPR effect has been explored in several tumor types which has led to extensive research in macromolecules that favor tumors in lieu of surrounding tissue.[231]

This tumor targeting method extends to breast tumors where nanoparticles have been explored as a viable treatment. An early application of macroparticles in breast tumor pathology was the development of 100 nm macromolecules to improve the delivery of therapeutics to the tumor site in breast cancer.[232] The study utilized treatment macroparticles, ABI-007, approximately 100 nm in size that had PEG coating and the treatment efficacy observed from these macroparticle were compared with standard, unmodified

paclitaxel. The results from this study demonstrated that the 100nm liposome PEG particles have favorable properties with improved therapeutic delivery in addition to reduced off-target delivery. In other words, the treatment's efficacy increased with the improvement of targeted delivery. The study also observed shorter delivery times with the nanoparticles and the use of corticosteroid premedication was also unnecessary. Because patients were not preexposed to steroid treatment, they experienced improved quality of treatment. The overall treatment response was improved for the nanoparticle-bound paclitaxel which provided a promising gateway to improved therapeutics for breast cancer. This improvement was widespread across other pharmaceuticals that experimented with nanoparticles in cancer therapeutics. The same mechanisms that have been applied to improving treatment targeting have also been experimentally applied to contrast agents. An early application of this is observed with iodinated nanoparticle contrast agents that have been created from micellar, liposomal, and polymeric configurations.[233] A study comparing the different iodinated nanoparticle types noted that despite the configuration used, all nanoparticles display prolonged circulations times which improve flexibility in a clinical setting.[234] The study noted that micellar nanoparticles exhibit high stability which allows for large iodine payloads of up to 130 mgI/ml thus improving the contrast per unit contrast solution. The circulation half-life of about 3h is also a consequence of the particles' high stability. Meanwhile, polymeric contrast agents exhibit their own advantages.[235] These particles contain a robust covalent bond between the benzoic acid and the polymers which prevents the iodine from leaking out of the particles. In addition, the polymers allow for the modification of the surface which provides multifunctionality, such as ligand-based targeting. Liposomal contrast agents are unique in that they can transport both hydrophilic agents inside aqueous cores as well as hydrophobic agents in the lipid bilayers. They also have easily modifiable surfaces that introduces multifunctionality into the solution.[236] The average circulation half-life observed with these particles is 3.5 hours. Among the different nanoparticles that have undergone clinical investigation, including those not listed here, such as those with metal cores, have demonstrated advantageous circulation times and have displayed favorability towards the leaky vasculature that surrounds tumors.

More specialized targeting mechanisms include those that exercise the use of biological ligands that are geared towards targeting regions that express biological molecules of interest. An example of this is contrast solutions that use the HER2 antibody to target upregulated HER2 in breast cancer.[237] In an early explorative study of HER2 antibody labeled contrast agents, FePt nanoparticles ranging between 3 and 12 nm in diameter were used in CT/MRI multimodal imaging. The contrast solutions were injected into mice infected with MBT2 intravenously. The study observed long circulations times and most of the particles were cleared within a week post injection. The study delivered two important observations; the first is that HER2 antibody labeled nanoparticles displayed high affinity towards the lesion site, and the second observation was that the results were the most promising for the contrast solution with the largest nanoparticles. There was an observed relationship between nanoparticle residence, including both circulation time and lesion affinity, and particle size. The study found that the smallest nanoparticles, which were those 3nm in length, easily permeated the blood-brain barriers; therefore, although these particles were not the most helpful in breast imaging applications, they might serve a purpose in future brain imaging. In addition to these results, the contrast solution did not cause any observable toxicity at concentrations exceeding 10 mM of iron. These results have since been replicated in other studies that have utilized variations of HER2 antibody labeled contrast particles, including a HER2 dendrimer conjugated gold nanoparticle. [238]

HER2 is overexpressed in only about 15-30% of breast cancers, therefore, these results are not generalizable to all breast cancer patients.[239] ER+ breast cancers make up about 80% of all breast cancer cases.[240] Therefore, targeting estrogen receptors in breast cancer provides more utility that targeting HER2 from a screening standpoint. A study was conducted in 2016 to investigate the utility of targeting ER in MRI imaging.[241] The contrast solution used composed of pyridine-tera-acetate-Gd particles conjugated to either estradiol (ER targeting mechanism) or tamoxifen (no ER targeting mechanism) and the mice used were infected with either ER+ or ER- breast cancer. After conducting *in vivo* MRI imaging, the study found that the MRI longitudinal relativity was superior in the mice with ER+ cancer cells. In addition, studies that were done to quantify the dynamic contrast found that the estradiol had an augmented signal compared to

the tamoxifen in the ER+ mice. Meanwhile, the tamoxifen did not demonstrate enhancement of the MRI signal between the ER+ and ER- tumors therefore proving the interaction between the estradiol and the ER in the tumors. The estradiol also demonstrated specificity in *in vivo* imaging. In conclusion, the study found that the ER-targeting estradiol is capable of targeting ER+ tumor cells compared to other cell types and the study establishes the potential behind this targeting mechanism as a contrast agent.

The purpose of contrast-enhanced breast screening is to improve the likelihood of identifying cancer. Because of the ambiguity surrounding breast screening, using HER2, ER, or PR targeting mechanisms ignores triple-negative breast cancers; therefore, the targeting mechanism needs to consider as many breast cancers subtypes as possible. This means that the contrast solution should target biomarkers that are widely present across most, if not all, breast cancers. Ki67 is a breast cancer prognostic factor that is upregulated in malignant tissue; it is representative of cell proliferation and breast tumors, which have higher cell proliferation that healthy tissue and express higher levels of ki67 than surrounding healthy tissue.[242] A review study reporting the role of ki67 in a clinical sense determined the use of ki67 as a targeting protein in breast cancer therapy.[243] The study reports that antisense oligodeoxynucleotides, ASOs, attached with ki67 antibodies have been found to inhibit the proliferation of tumor growth. However, these molecules tend to suffer from nuclease degradation. On the other hand, ki67 antibodies conjugated with peptide nucleic acids demonstrate increased stability compared to ASOs conjugated with ki67 antibodies.[244] These molecules were found to impersonate DNA that targets tumor cell DNA and RNA with high affinity and specificity and outperform ki67-ASOs as targeting agents.[245] The study highlights how ki67 peptide nucleic acids have been found to reliably target tumors in therapeutic applications among multiple studies.[246,247] Furthermore, investigation of ki67 as a feasible targeting protein is still ongoing and studies focusing on its targeting application in contrast agents are unheard of.[248]

A barrier with using ki67 antibodies as targeting agents is the lack of stability between ki67 expression and breast cancer. Ki67 is undoubtedly overexpressed in several breast cancer cases; however, its expression is correlated with tumor grade and high ki67 expression is associated with worse prognostics. Therefore, ki67 is used a prognostic factor to indicate the severity of the tumor and likelihood of survival.[249]

Unfortunately, the variability in ki67 expression among breast tumors imposes challenges with standardization of ki67 assessment, and currently, there is no standard operating procedure that defines the cutoff for ki67 expression that separated healthy from unhealthy tissue.[250] Although the expression of ki67 is very low in healthy tissue, displaying concentrations below 3%, its expression in healthy tissue obscures the threshold between healthy and unhealthy tissue.[251] Nonetheless, ki67 can still serve as a targeting marker given its success in therapeutic applications; however, several studies need to be conducted to assess it as a proper targeting agents in contrast agent applications.

A semi-common feature of breast cancer is the p53 gene mutation that is present in about 30-35% if all breast cancer cases but present in about 80% of triple negative breast cancers.[252] This indicates p53 targeting as a favorable technique among triple negative breast cancers that are otherwise difficult to target, but an inefficient technique in broad scope applications. Therefore, targeting p53 might have a future role in triple-negative targeting in therapeutic applications, but it is otherwise ineffective in breast screening applications. Because of the broad range of breast cancer subtypes, targeting breast cancer through means of protein expression is difficult. The different breast cancer subtypes have been found to express different receptors and proteins and choosing a single specific targeting antibody might not be inclusive of all the breast cancer types. This introduces 'blind spots' in screening applications where some breast tumors might be missed simply because they do not express the protein that the contrast solution is searching for. Further investigation on breast cancer biomarkers is needed to find markers that are ubiquitous across all subtypes of breast cancer.

2.4 MCNP Simulations

2.4.1 MCNP and Dose Models

MCNP is a powerful simulation program that is used to simulate various clinical scenarios and for decades, it has been used to create computational anthropomorphic phantoms capable of simulating the interactions between radiation and the human body. With the development of MCNPX and subsequent MCNP6, the ability to replicate a clinical environment improved as features were incorporated into MCNP

to improve the accuracy of the radio-human interactions. Early applications of these MCNP developments were dose calculations ranging from workplace exposure to medical exposure. In breast imaging applications, a topic of interest is dose imparted during an imaging procedure. Therefore, when MCNP allowed for accurate simulation of a clinical environment, several studies investigated the dose imparted during breast imaging using MCNP simulations. This was achieved through a series of anthropometric and anthropomorphic phantoms that sought to replicate the human breast in a computer environment. Before MCNP6 and the addition of mesh phantom, anthropometric and anthropometric phantoms were achieved either mathematically or with voxels. Mathematically, phantoms can be created by defining a series of equations that work together to form the geometry of the breast. However, more accurate calculations can be achieved with voxel phantoms. Repeated structures were introduced in MCNP in the 1980s and with the introduction of MCNPX, dose calculations with voxel phantom in medical applications was popularized, including glandular dose calculations.

A study conducted in 2005 by Dance et. al. experimented with high-resolution voxel phantoms to calculate the glandular dose received during x-ray mammography, with a particular interest in device optimization to reduce the dose while improving image quality.[253] Because it is believed that dose to the glandular tissue is the main reason for radiation-induced breast carcinogenesis, the study specifically measured the dose imparted to the glandular tissue.[254] In the study, MCNP is used to model the multiple components of an x-ray mammography system, including the x-ray beam, the compression plate, the image receptor, and the collimator. Two voxel models were used to calculate the glandular dose; the first model used structural phantoms to construct the breast in three separate components, and the second model used a new method tokened 'unstructured' voxel building that essentially created a model from unstructured voxel structure instead of from segmented components; both phantom types can be seen in **Figure 9**.[255]
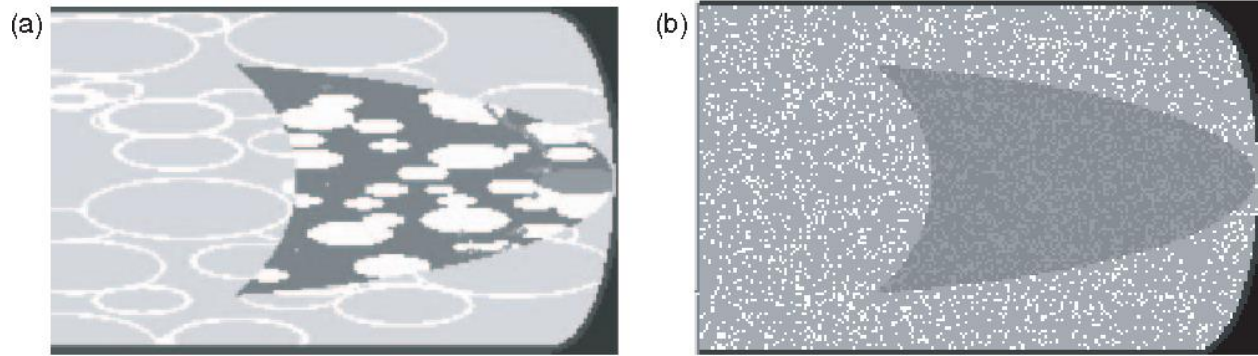
Figure 9: A visualization of a breast phantom created from (a) structured voxels and (b) unstructured voxels.

Multiple phantoms were created using these methods and they ranged in breast thickness and glandularity. The results demonstrated increasing disagreement between the two models with increasing breast thickness and glandularity. A difference of up to 48% was observed between the first and second voxel methods. This demonstrates that the way the glandular distribution is modeled in the voxel phantom impacts the dose approximation, which further proves that antiquated methods used to calculate the glandular dose might be inaccurate due to the oversimplification of the breast structure. Furthermore, the study proves that current dose calculations for breast mammography have limitations. However, the study itself also contains limitations. For one, the models were built from 2D glandular distributions instead of 3D distributions, which limits the accuracy of the model. In addition, the models were oversimplified and did not accurately represent the complex glandular structure inside the breast; there was also no mentioned of skin consideration in the model. In conclusion, the study points out the importance of accurate breast structure representation and admits that further development is needed.

A different study sought to improve the accuracy of breast phantoms by incorporating more accurate glandular tissue distribution compared to other models used.[256] The study, conducted by Alghamdi et. al., emphasizes that existing breast phantoms for dose simulations contain homogenous composition distribution where it is assumed that the glandular and adipose tissue are uniformly distributed throughout the breast. However, the study emphasizes that this should not be the case and incorporating anatomical details can provide more accurate dose estimations. The geometrical model was created with an in-house

software program that created the anatomical features of the breast, including the breast shape, ducts, skin, lactiferous ducts, Cooper's ligaments, and chest muscles. The shape of the breast was created with a series of equations, primarily a semi-ellipsoid and one-sheet hyperbola. The inner anatomical details were also described with equations but the glandularity was modeled from Gaussian noise in areas with no anatomical detail. To construct a phantom, the mathematical model was voxelized and then converted into a lattice file that is usable for MCNP. The fraction of the imparted dose that comprises the mean glandular dose was derived from an equation considers the ratio of the attenuation of both the glands and the adipose tissue, as well as the percent glandularity. A radiograph tally was used to simulate a resulting mammogram from the phantom used. A series of MCNP simulations were carried out that included both the heterogenous phantoms and the newly developed phantoms and the simulations were also performed on both the craniocaudal position and the mediolateral oblique.

The study aimed to analyze the accuracy of dose estimations from the newly developed phantom as well as to validate the dose estimations obtained from an oversimplified breast model. It also anticipated to calculate the error caused by image reconstruction. The study found that the dose estimations among the homogenous phantom in the craniocaudal and mediolateral oblique position varied by less than 2%, despite the difference in their shape. Meanwhile, the dose for the newly developed phantom was estimated to be 22% higher than that of the homogenous phantom in the mediolateral oblique position, despite their similar shapes. This leads to the conclusion that the anatomical structure of the breast plays a role in the accuracy of dose estimation. Their results coincide with other studies that have found that differences in the glandular distribution lead to differences in dose estimation; however, this study claims that their model is different from those used in other studies. In the produced radiograph, a coarse breast imaging is presented with a much poorer resolution than that observed in mammograms. In addition, the study did not present the error in image reconstruction and admitted that more work in needed in the future. This leads to the conclusion that these simulations need to be conducted with 3D imaging devices, such as CT or tomosynthesis. These imaging modalities also provide a different amount of dose compared to 2D imaging. Overall, this study was seemingly rudimentary with no information on the glandularity used and no information indicating the

differences in error between the two phantoms as a function of glandularity. A more holistic approach to the data collection would vastly improve the reliability of the results and would allow for an exploration of the differences in dose error estimation as a function of glandularity.

A very similar study conducted in 2018 also used MCNP to validate the differences between homogenous and anthropomorphic breast phantoms in dose estimations in a clinical setting.[257] In this study, both breast phantoms were compared with experimental results obtained with a digital mammography unit. The experimental results were obtained for both a homogenous and heterogenous breast phantom implanted with thermoluminescent dosimeters to obtains local dose deposition. In conjunction with these dosimeters, metal oxide semiconductor dosimeters and GafChromic films were also used. For the MCNP simulations, a semicylindrical phantom as used to represent the homogenous model while the anthropomorphic phantom was created from patient data that was deconstructed and reconstructed into a voxel phantom. The homogenous computational phantom had 50% glandularity while the anthropomorphic phantom had 10.9% glandularity. MCNP tallies were used to replicate the dosimeter placement in the real phantoms. The dosimeters had to be calibrated to fix errors caused by the heel effect and other artifacts caused by an uneven beam distribution. The beam was also replicated in MCNP. The study aimed to verify the validity of MCNP dose estimations as well as to provide insight on the ongoing development of improved breast models for dose estimations. The results found good agreement between the dosimeter results and the MCNP-acquired results, but higher error was observed with the Galchromic dosimeters. The study also observed the drastic increase in dose that occurs with breast thickness; an increase of about 93% was observed which coincided with previous studies.[258] This was observed with both MCNP and the experimental setup. When comparing the homogenous and anthropomorphic phantoms, they found that the difference in dose was 10% for a breast glandularity of 10.9%, which was in accordance with literature. Unfortunately, the study didn't use any other anthropomorphic phantoms with different glandularity, therefore the results found were only for low density breasts. An observation that was made during this comparison is that the position of the glandular tissue in the breast plays an important role in dose estimation because the beam strength decreases with thickness due to attenuation. Glandular tissue located on the upper section of the breast will receive

more dose than if it were located by the bottom half. This confirms the importance of accurate breast representation in dose studies. In conclusion, the study found that MCNP is capable of accurately replicating experimental studies, at least for breasts with low glandularity. The study also mentions that the experiment should be replicated with 3D imaging techniques.

These different dose studies openly discuss the utility that MCNP provides. MCNP has been found to be an accurate tool for anthropomorphic phantom development and it is robust enough to provide the physics needed to run clinical simulations with. With the recent addition of unstructured meshes in MCNP, dose studies can be replicated with even more precision and faster run times. The studies mentioned above did not experiment with a wide variety of breast sizes or glandularity, which is important in order to be able to assess the relationship between these variables and calculation error. New breast models developed for dose estimations should consider the diversity of breast composition and include any necessary correction factors that are needed to correct for dose estimations.

2.4.2 MCNP as an Imaging Tool

MCNP's tally capabilities make the program a powerful tool for detection studies. The broad range of tallies available allow users to choose counting methods that are specific to their needs. With the development of MCNPX and MCNP6, radiograph tallies have been introduced specifically for imaging simulation. Hence, MCNP can be used to simulate a variety of imaging systems, including mammography and tomosynthesis units. By simulating imaging systems, studies can validate anthropomorphic phantoms and explore ways to optimize detection methods. Further, several studies have focused on exploring MCNP's imaging capabilities and have sought out ways to replicate existing imaging units as accurately as possible. This following section focuses on discussing the findings of those studies including any limitations encountered.

Over two decades ago, studies exploring the capabilities of digital mammography units were conducted along with other proposed breast imaging methods. Peplow and Verghese explored the differences between a synchrotron mammography unit and a next-generation mammography system with

digital detector and slot geometry, with a focus on comparing their scattering properties.[259] To quantify the degree of scattering observed with each imaging unit, an MCNP code was developed that simulated the properties of both detectors and simulated accurate images produced by each system. The study emphasizes the importance of accurate imaging physics to maintain clinical relevance, therefore full-field imaging simulations were conducted with a realistic pixel size. Due to long simulation times required for such images, multiple variance reduction techniques were implemented. To compare the two systems, two common mammography phantoms were used; these included the contrast detail phantom and the phantom developed by the American College of Radiologists. Neither of these phantoms are anthropomorphic but they help provide information on a system's limitations and capabilities. In addition, because they are standard phantoms that are used across various studies, the results presented from imaging these phantoms can be compared with other results outside of this study. To properly simulate the imaging properties of each imaging modality, the properties of each were thoroughly investigated and every detail was incorporated into the code, including the exact energy of the beams used in the experimental set-up, collimators used, detector resolution, and relative noise. The images were further 'smeared' with the modulations transfer function to reflect the energy 'smearing' – which occurs when the energy deposited in one pixel is deposited into nearby pixels - that is observed in real systems. Finally, the images produced with MCNP were compared with results produced from each respective imaging device to validate the accuracy of MCNP's imaging capabilities.

The initial findings demonstrated cleaner images produced by the simulated mammography systems compared to the experimentally derived images. This was due to the lack of experimental artifacts in the image plate and the monochromators. The findings for the second technique were different. The synchrotron imaging technique is nearly scatter-free, therefore the MCNP code used to simulate this technique analytically demonstrated sufficiently similar images compared to the empirically obtained ones. A small deviation is that the MCNP images are a bit more uniform with less visible artifacts compared to the synchrotron obtained images. The same differences are observed among the mammography-acquired images and the MCNP simulated images; the artifacts are more obvious in the empirical data than in the

theoretical one. More specifically, the images obtained with the mammography unit contain 'stripes' caused by the collimator that are not visible in the MCNP simulations. A primary difference observed between the empirically obtained mammography images and the MCNP simulated images is that the contrast in the empirical images is nonuniform. The cause behind the nonuniformity is not explained in the study. However, it is noted that without applying the MTF to the MCNP simulated images, the contrast among the MCNP images is higher than that of the mammography empirical images. The reason behind the contrast degradation in the empirical mammography data is that the scatter contribution is 9%. Once the MTF is applied to the MCNP simulated system, the contrast is parallel to that of the empirical environment. This implies that incorporating a scatter component is necessary in MCNP simulations in order to achieve a similar system. In conclusion, the study notes that the more accurate method to simulate an empirical system with MCNP would be to incorporate every component that causes noise in an imaging system, because images produced by these systems contain noise and artifacts that are produced at different steps along the imaging process. However, including these 'steps' in MCNP diligently and meticulously would require tremendous imaging capabilities that are simply not feasible within a reasonable time frame. Thus, applying the MTF along with simplified noise can help produce an image as close as possible to real images.

The study was conducted nearly a decade before the release of MCNPX and a few years before the release of MCNP5. Since then, radiograph capabilities have been introduced and their inclusion in MCNP simulations have vastly improved the simulation of imaging systems. A study conducted shortly after the release of MCNPX describes using the code to simulate imaging detectors to determine the scatter to primary ratios in radiology.[260] In the study, three methods are explored – a method that uses the radiograph tally, another that uses an energy integrating detector, and a detector based on energy absorbed in the target material. To validate the different methods, the scatter-to-primary ratios obtained with the simulation were compared with experimentally acquired values. To simulate the three different detector systems in MCNP, the study used the recently added F5 tally, or radiograph tally, and the F1 and *F1 tallies, which measure the current integrated over a surface in units of particles and energy, respectively, essentially representing energy integrating detectors. A main difference between the radiograph tally and the energy integrating

tallies is that the radiograph tally can be customized to mimic a detector panel that considers collimation, energy gating, and scattering contributions and these settings need to be fine-tuned to accurately simulate a system. Meanwhile, the F1-type tallies are stochastic, and the only contributions made to the 'detector' are from particles that cross the detection surface. The *F1 tallies are different from the other two in that they consider the spectral sensitivity of the programmed material. For image simulation purposes, the tallies were relatively small to permit the view of clinically relevant details; however, to balance long computational times and clinical relevance, the resolution is coarsened to calculate the scattering contribution of the geometry in question without compromising the accuracy of the calculations. Therefore, the pixel size was increased from 0.1 x 0.1 mm^2 to 5 x 5 mm^2. The tallies were also modified to include the properties of the detector used in the experimental equipment, which was a 500 um-thick CsBrEu phosphor plate. To create images with the three systems, two separate images are acquired; the first image is that of the low-resolution scattering and the second image is the high-resolution primary one. These images are then combined to create the final image.

To validate the MCNP-simulated images, the results were compared with previously published MCNP data.[261,262] The MCNP results were further validated by comparing the results with experimentally acquired scatter to primary ratios. The phantom used in these experimental calculations was composed of PMMA. The experimental calculations and the MCNO-acquired calculations were compared by measuring the percent difference between the two measurement types. When comparing the MCNP-acquired results with previously published results of the scatter to primary ratios, the results demonstrated close agreement in the data among the perfect energy integrating detector (F1), and varying agreement among the data created by the radiograph tally with percent difference ranging between 5.4% and 44.4%. For the energy absorbed detector, there was close agreement between the MCNP-acquired data and previously published results of scatter to primary ratios with absorbed energy detectors, but again, poor agreement compared to the radiograph tally results. For the experientially acquired scatter to primary ratios, comparison of the data with the radiograph tally results demonstrated that the radiograph tally overestimated the measured ratios with differences as high as 45.5%. The perfect energy integrating detector demonstrated similar results to

the experimentally acquired ones with ratios about 4.7% lower, on average, that the experimental ones. The absorbed energy detector model demonstrated the best performance with differences of about 1.3% compared to the experimental results. This might be due to the tally's ability to consider the spectral sensitivity of the target material. In conclusion, the study demonstrated that the best tools for image simulation are those that closely resemble the physics behind image detection systems. Although the radiograph tally was created to facilitate image simulation, it might not readily consider the noise and scattering that is observed in a real imaging system. Therefore, it is important to be diligent and understand the particle physics that play a role in the image acquisition.

Creating imaging systems in MCNP requires considering the different components that are needed to create an image. The source, setup, and detector/image acquisition tool need to be incorporated in the simulation to create a realistic imaging environment. A study conducted by Long et. al. recreated a tomosynthesis imaging system in MCNP to validate organ studies.[263] The study simulated the Siemens Sensation 16 multi-detector CT scanner with a 52-degree fan beam. The simulated system included beam filtration, appropriate energy range, pitch, and beam collimation. Information on the x-ray beam for this specific system was used to create the x-ray beam used in the MCNPX source input deck. Weighing factors used in the MCNPX source dependent on the angular distribution were determined by the extent of the heel effect in the experimental setup. To calibrate the plastic scintillator dosimetry system, head and body acrylic CTDI phantoms were used. The results of the phantom were scaled to tissue kerma using mass energy absorption coefficient ratios. Dose measurements were conducted on a pair of phantoms – one corresponded to a reference adult male and the second corresponded to a 9-month-old male – and these phantoms were available as physical phantoms and MCNPX voxel phantoms. The dose was calculated in MCNPX using F6 kerma approximation tallies, which offer an adequate approximation of average organ dose.[264] The results of these tallies were then converted into units of mGy using methods provided in previous studies.[265]

The differences in the calculated dose between the simulated and experimental environment for the adult male phantom were within 5% for 5 out of the 16 organs, and within 15% for 15 out of the 16 organs for the axial scans. For the helical scans, the dose differences were within 5% for 3 out of the 15 organs and

within 15% for 14 out of the 15 organs. For the infant phantom, the dose calculations were more in agreement with all doses differing less than 15%. The reason why the dose measurements were more accurate for the infant phantom is because the infant is wholly covered by the beams; therefore, the entire phantom is scanned in a single measurement whereas the male body is measured with anatomical landmarks. This introduces artifacts to the adult scans that are not seen with the much smaller infant phantom. Artifacts due to the lateral beam are absent in the smaller phantom but need to be accounted for in the adult phantom; therefore, larger differences in the dose calculations are seen. The study noted that the largest sources of error among the MCNPX generated dose calculations were the lack of knowledge of the beam starting angle and the tally errors. Meanwhile, calibration of the dose was found to be challenging in the experimental setup due to several sources of error, including uncertainty of the ion chamber measurements, energy dependence, and the use of acrylic instead of soft tissue equivalent material. The uncertainty errors associated with these measurements are then said to exceed those of the MCNPX results. The study concluded that the organ dose calculations were generally in agreement between the experimentally derived results and the MCNPX simulated results and emphasized that minor geometrical errors should be accounted for to match the systems as closely as possible.

2.4.3 MCNP's Anthropomorphic Capabilities

MCNP can be used to simulate an imaging procedure that begins from the x-ray source and ends at the image receptor. The versatility and robustness of this simulation tools allows researchers to explore alternative pathways to solve imaging or other clinical problems. For decades, MCNP has been used to validate dose measurements, x-ray scattering properties, imaging receptors, and numerous particle physics scenarios with high accuracy. Several studies have validated the precision of MCNP in radiographic applications and have expressed the utility of such simulations.[266,267] With attention to detail, the error between MCNP simulated results and empirical results can be made minimal and with further advancements in the MCNP program, clinical simulations are quicker and more accurate than in previous

versions of the code. With the addition of unstructured mesh capabilities in MCNP6, anthropomorphic simulations in MCNP have greatly evolved.

A study that reviewed the advancements of anthropomorphic studies and simulations with MCNP reported the differences between the different simulation methods available in MCNP.[268] The paper was published shortly after the release of MCNP6 and includes a thorough discussion on the recently added mesh capabilities. The study compares three main phantoms – the Snyder head, the Zubal head, and the VIP-Man phantoms – which have been previously modeled and tested with MCNP and recreates the phantoms with unstructured meshes to quantitatively compare the results with previously used phantom-building methods. The use of anthropomorphic phantoms has been around for decades, and the complexity of the phantoms has evolved with computational advancements. Early phantoms were developed in the 60s and 70s for radiation dosimetry and they followed the MIRD, or Medical Internal Radiation Dose, guidelines. These early phantoms relied on the use of mathematical equations to build the computational phantoms with. The equations outline rudimentary shapes that represented the different organs present in the human body and the tissue data is selected from the ICRP 'Reference Man' documentation.[269] The Snyder head and the Zubal head are both examples of mathematical phantoms built with MCNP. They are each represented by a set of ellipsoidal equations.[270] The issue with using mathematical phantoms is that they often misrepresent human anatomy and instead describe an oversimplified version of it. The National Library of Medicine helped improve anthropomorphic phantoms by providing a detailed 3D representation of both male and female human bodies in a project known as the Visible Human Project.[271] Voxelized models of these bodies emerged as studies began using these in clinical research. The resolution of the voxels in MCNP models ranged between 0.33mm to 4mm with the tradeoff between computational efficiency and accuracy being the main deciding factor on which resolution to use. The Snyder head and the Zubal head were also remodeled as voxel phantoms in MCNP decades after they were originally developed as mathematical phantoms, then later developed into mesh phantoms with the latest MCNP development.[272]

The unstructured mesh versions of the three phantoms were developed with meshing tools in Abaqus/CAE and the mesh size used was a standard hexahedra mesh. The study used a Python script that generated Abaqus input files from lattice data found in MCNP voxel phantom files. The group then used Abaqus built-in capabilities to create a mesh input file for MCNP. This process facilitated the conversion of existing voxel phantoms into unstructured mesh phantoms. Converting the files took several hours and the largest lattice tested took approximately 3 days to generate. To test source accuracy, the study used unstructured mesh models of the lungs in the VIP-man and the Snyder head phantom. The phantoms were given an Iodine source and 100 million histories were used. The results demonstrated that both unstructured mesh phantoms displayed computational improvements compared to their voxalized counterparts. The mesh lungs took about half of the simulation time it took for the voxel lung model to run in MCNP and the mesh Snyder head was also faster and more geometrically accurate compared to the voxel Snyder head. An observation made during the study is that the computational accuracy declined with high element quantity. As the resolution improved (i.e 0.3mm instead of 4mm), more elements were needed to fill in the phantom; this resulted in longer computational time and higher statistical error. What this means is that even though smaller, more abundant elements represent a more accurate phantom geometry, more resources are needed to reduce the error, otherwise, the computational accuracy is poor. The study concluded that unstructured meshes provide an accurate alternative to hand-calculated measurements and they have demonstrated promising results that are indicative of their use as the next type of anthropomorphic phantoms.

A more recent study used MCNP's unstructured mesh capabilities to study the decay of radioactive contaminants in human lungs.[273] In the study, Taalat et. al. are interested in the deposit of radionuclides in the lung-mouth system, therefore, these are modeled as physiologically realistically as possible to simulate the airflow responsible for the particle transport in the lungs. The study notes that previous models of the respiratory system simplify the air distribution by dividing the sections into compartments that neglect the fine details that describe the accurate distribution of air and particles. By limiting the regions of the lungs to 3-10 models, the compartment method neglects to include anatomical details that are essential for accurate simulations. Instead of depending on compartments to determine the distribution of particles in

the lungs and airway, the study used computational fluid-dynamics to map out the probabilities of particle deposition in the different regions of the lungs. By incorporating fluid-dynamics into the study, the impact of particle size can also be considered which can provide a better assessment of the severity of accidental inhalation. The study then aimed to couple the results of the fluid dynamic simulations with the MCNP simulations to provide a model that considers both the physiological and radiophysical interactions of the inhaled particles. In the MCNP simulations, the study used the beta spectra of multiple sources because beta spectra model a distribution of energy that is representative of the energy emission expected from the radioactive material present in the lungs after inhalation. The different source types allowed the group to analyze the results for different energies that can help validate the model for different radionuclide depositions. A drawback of the study is that the dose results are only representative of freshly inhaled contaminants because the code does not consider the biokinetics of particle transportation after it has reached the lungs. The particle transport pathways after the contaminates have reached the lungs are not included, therefore, the dose to other organs only includes the dose emitted from the lungs and not the dose emitted from particle absorption. In addition, the dose caused by particle accumulation is not included as a result of the limited biophysics.

An initial finding of the study was that the lungs contain both laminar and turbulent flow. The velocity profiles are impacted by several factors, including flow type, branch length, and branch diameter; therefore, the distribution of particles can vary significantly across the different regions of the lungs. This proves that an oversimplified model fails to provide an accurate representation of the dose distribution and can have dire consequences. The results demonstrated similar distribution of particles regardless of particle size during inhalation; however, during exhalation, the particles larger in size were cleared at a faster rate. Meanwhile, the MCNP simulations ran for 100 million histories and the relative errors associated with the gamma dose was below 2%. Regions further away from the lungs received fewer gammas, therefore, the error associated with the dose in these regions was higher (~20%). The fmesh tally used to calculate the fluence of the particles in the lungs demonstrated 'hot spots' in the throat and the parenchyma surrounding the lungs. The results also demonstrated a strong relationship between the fluence and the medium that the

particles travel through, which is consistent with literature. An important takeaway from the study is that including anatomical details on the respiratory tract improved the inhalation estimates and dose calculations, thus highlighting the importance of accurate geometry and details. The study also pointed out that assumptions and oversimplifications made during the study potentially reduced the accuracy of the results. One of these was reduced particle histories. Because the phantom contained a complex geometry, the run time was impossible to keep reasonable with high history count. A compromise was to keep the number of histories at 100 million to achieve a reasonably low error while maintaining a reasonable run time. Another drawback was phantom processing. The study struggled to convert the geometry of respiratory system into a mesh phantom without using too much computer memory. This highlights the importance of additional research that explores the efficient use of mesh phantoms. Because this technique is recent and unfamiliar, findings ways to improve the integration of mesh phantoms into MCNP is an exploratory process.

A different study explored the utility of MCNP's mesh capabilities by validating dose measurements calculated between mesh phantoms and voxel phantoms.[274] The 'high-quality' mesh phantom constructed was modeled after the adult reference provided by ICRP *Publication 110* and includes high level details that negate the need for supplementary stylized models, such as a program that simulates the respiratory airways. The quality and accuracy of the mesh phantom was quantitatively measured by comparing internal and external exposure dose gathered from MCNP simulations and comparing the measurements with reference values provided in ICRP *Publication 116* and *133*. In addition to those dose calculations, the mesh phantom was also used to estimate dose coefficients for industrial radiograph sources placed near the body. The study notes that mesh phantoms exhibit versatility over voxelized phantoms because they can be easily deformed to represent different body types stemming from a single model; this allows for personalized dose models that can be useful after accidental exposure. Meanwhile, the rigidity of voxel phantoms disallows geometry manipulations that would allow such capabilities. A principal goal of the study is to analyze the full extent of mesh phantoms for dose calculations so that *reference humans* modeled with voxel phantoms can be used for dose estimates during an emergency.

The mesh phantoms were converted from the voxel-type reference phantoms through a series of 3D surface rendering and refinement procedures and features that were too small to be modeled through this process were modelled separately. To model the blood vessels, a program known as BioDigital was used to produce the 3D distribution of blood in the body. The detailed eye model was developed a decade prior by Behrens et. al. and was adopted to calculate the dose factors in the mesh phantom.[275] The model was made as detailed as possible and included micron-thick targets to ensure accurate dose calculations in the skin and the respiratory system as well as other organs with fine details, which can be seen in **Figure 10**. The final model was revised by an anatomist to ensure accuracy and the final masses of the components were found to be within 0.1% of the reference values. The finalized male model contained 8.2 million tetrahedrons while the finalized female model had 8.6 million tetrahedrons. The mesh model was found to be compatible with major Monte Carlo codes, including Geant4, MCNP6, and PHITS and both the memory usage and the computation speed were measured with all the Monte Carlo-based programs used. The phantoms were irradiated with an isotropic source consisting of gammas and electrons with particle energy ranging from 10^{-2} to10^4 MeV as well as neutrons with energy ranging from 10^{-8} to 10^4 MeV and helium ions ranging from 1 to 10^5 MeV.
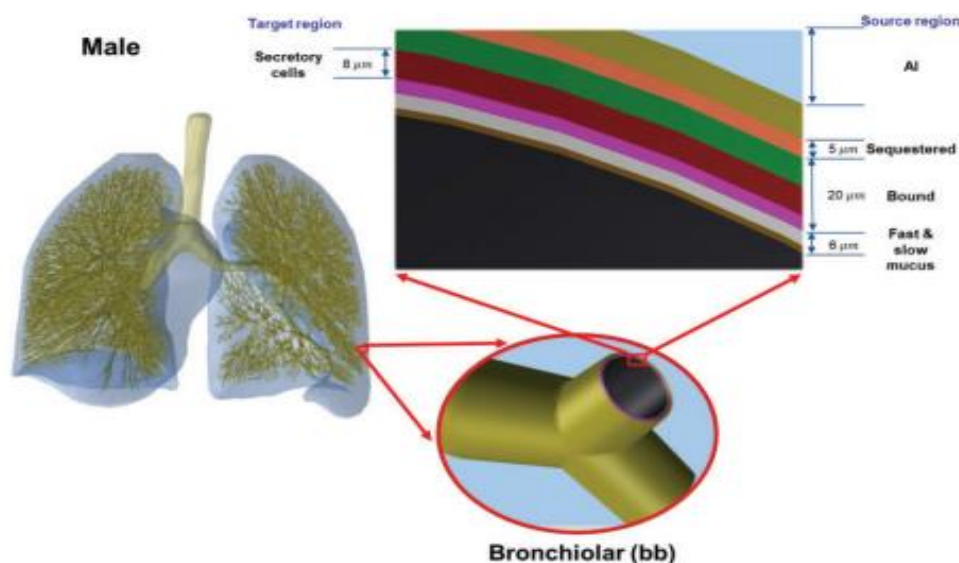

Figure 10: An image gathered from the work described by Kim et. al. The micron-thick targets can be seen here.

The memory usage between Geant4, MCNP6, and PHITS was found to be 11, 14, and 1.2 GB, respectively. The computational speeds varied depending on the particle type and energy and ranged from several hours to tens of hours. The dose coefficients were gathered separately for external and internal exposures as well as for different energy ranges. For external exposures, the dose coefficients were calculated in terms of effective dose per fluence for monoenergetic beams separated by particle type. For internal exposures, the effective dose was calculated per emission for cortical bone, liver, lungs, and thyroid. The dose calculations were found with statistical errors below 0.5%. The results demonstrated agreement for neutron and gamma dose calculations for all three programs used, for both the internal and external dose calculations. More specifically, the percent error for the external dose calculations were within 5% of the reference values and the internal dose calculations were within 2% of the reference values. The dose calculations for neutrons varied much more between the different programs due to differences pertaining to how each program conducts its Monte Carlo calculations; however, the differences in dose were within 10%. Dose calculations from charged particles had the largest differences for internal exposures but the error was within 5% for external calculations. There was also an energy-error relationship between the dose coefficient calculations and the particle energy. For particle energies exceeding 1 MeV, the dose coefficient calculations agreed with those in the reference while those with energies below 1 MeV displayed increasing differences with decreasing energy. The highest differences among low energy particles were seen for the skin dose calculations. The study states that the mesh model differs from the voxel reference model in that it includes um-thick layers which are not included in the voxel model because the voxels have a resolution on the mm-scale, and these differences are likely the reason why the dose calculations vary to such a high extent.

The group also investigated the dose coefficients for exposure caused by industrial radiography sources. Two additional types of phantoms were used for these calculations; one of the phantoms represented a 10th percentile body type while the other represented a 90th percentile body type. Including these two phantoms into their work allowed the group to explore dose discrepancies caused by differences in the geometry. Interestingly, the dose coefficients were smaller in the 90th percentile phantom than those

calculated for the 10th percentile phantom. The dose coefficients were up to 40% larger for the 10th percentile phantom thus demonstrating the considerable differences between the phantoms. This validates the need to develop diverse phantoms that can accurately estimate the dose for the assortment of body types that represent humans. The study concludes that the calculations performed with the mesh phantom closely resemble those in the reference values. This evidence serves as precedent establishing the accuracy of mesh phantoms and their potential use in other clinical applications. The mesh phantoms also demonstrated flexibility and versatility, which hints at their ability to mimic more flexible geometric structures. The study demonstrated the utility of mesh phantoms for dose calculations, and it established a rudimentary process to use these phantoms for applications outside of dose coefficient validation. After confirming their accuracy, the study suggested that their application serve several purposes in clinical applications, such as those that experiment with different body structures.

MCNP's anthropomorphic capabilities have served a multitude of researchers. With the evolution of these capabilities, anthropomorphic structures have become increasingly complex as improved computational power and accuracy have allowed researchers to run simulations with millions of elements. Much of the work highlighted in this section focuses on MCNP's use for dose calculations. There is evidence validating the recently developed mesh phantom ability in MCNP but there is little to no work highlighting its use in imaging applications. MCNP has been proven to accurately model imaging systems, including the source and detectors, anthropomorphic models, and various settings. However, because the mesh capability is a fairly recent addition to MCNP, there is no work suggesting its use for imaging solutions. Nevertheless, mesh phantoms provide advantages over voxel phantoms in both flexibility and speed, and their utility in imaging applications should be explored.

3 Project Overview

This project aims to facilitate the search for practical contrast agents that can improve sensitivity during breast imaging. Advancements in MCNP have allowed for the creation of mesh phantoms that can

be used to create realistic and accurate models for problems researchers are trying to solve in a cost-effective manner. This project applies MCNP techniques because it permits the flexibility needed to study the scope of potential contrast agents. To accurately assess the efficacy of proposed contrast agents, the phantom needs to exhibit the same properties as a human breast, including vasculature, glandular structure, and lesion patterns. Therefore, much of this project focuses on phantom building with MCNP and other tools to achieve a phantom that can provide reliable results. Several phantoms will be created so that the limitations of each proposed contrast agent can be explored, and these phantoms will vary in size, glandularity, and other factors that impact lesion visibility. These phantoms will employ biophysical kinetics that impact contrast agent delivery, such as vascular flow, and the relationship between contrast agent properties, including viscosity and particle size. Employing these kinetics provides a model that demonstrates the biocompatibility and practicality of the proposed contrast agents. The contrast agents that will be explored will vary in their effective Z, density, and particle size. Although antigen-labeled contrast agents are promising in clinical applications, the biological modeling that is needed to study them exceeds the scope of this project. The data acquired with this project will provide insight into materials that can improve existing imaging techniques. Although it is not guaranteed that a contrast agent solution will be found with this project, the data gathered here will provide acumen on the use of anthropomorphic phantoms for imaging exploration as well as the limiting factors that exist in breast imaging techniques.

The first step to execute this project is to develop a biologically accurate breast phantom that can replicate various breast types. Because the biophysics need to be considered, python scripts will be used to integrate biophysical factors into the model. Python scripts will also be used to develop varying breast mesh phantoms from the provided variables. In addition, MCNP mesh phantoms are Abaqus compatible, therefore, python scripts are used to translate mesh geometries created with Python scripts into Abaqus-type files. Once the Abaqus-type files are created describing the geometry of the breast, the files will be pre-processed with an MCNP pre-processing program that aids in the conversion of Abaqus-type files into usable MCNP files. The Hologic tomosyntheses imaging environment is also replicated in MCNP. The source is developed by reproducing the Hologic x-ray beam in MCNP, and the source specifics for the x-

ray beam are gathered from the Hologic user manual and technical specifics sheet, including the beam hardening mechanics used. A pulse-height tally is used to measure the x-ray spectrum that is created with an initial electron source from the cathode in the x-ray tube. This x-ray spectrum is then used to create an x-ray source that emulates the x-ray tube at much faster computational speeds compared to the electron-based source. The rotation of the source follows the rotation specified on the Hologic manual. The flat panel detector is replicated with the appropriate tally and every significant component of the image acquisition process is included, including the bucky table. The contrast agent properties are acquired from literature and are used to determine speed of delivery, clearance time, tumor affinity, and attenuation. Images are acquired to assess the efficacy of the different contrast agents used. All of these steps are discussed in detail in the **Methods** section.

The project described in this paper highlights a novel approach to explore potential contrast agents. Traditionally, contrast agents are explored with a series of trials that originate from new ideas that materialize into animal studies that further seek their potential if the idea develops into fruition. However, this process is time consuming and costly. By outsourcing the investigative aspect of contrast agent proposition, time and resources can be preserved. In addition, studies that investigate breast imaging techniques often lack diversity and fail to acknowledge the role of breast cancer type, breast size, and lesion location in lesion visibility. Constructing a simulated system that can incorporate diversity into the data with ease can expand our understanding on the relationship between these different factors and tumor visibility. Further, a simulated breast imaging system that emulates contrast agent distribution has never been done before and this project helps establish guidelines for similar future projects. Although the goal of this project is to propose potential contrast agents that serve a clinical purpose, the results generated from this project will manifest the major barriers and limitations that are preventing adequate sensitivity, especially among women with dense breasts and women with obscure lesion regions. Moreover, the results will expose the utility and limitation of a simulated environment for breast imaging studies.

Part 2: Materials and Methods

4 Materials

4.1 References

The set of breast phantoms generated in this project are designed to provide an accurate representation of real breasts to deliver accurate biophysical data of contrast agent behavior and efficacy in tomosynthesis imaging. Furthermore, to conceive accurate breast phantoms, a considerable number of resources were used to acquire holistic information on breast structure, breast cancer behavior, breast macro and micro vasculature and tomosynthesis technology. These resources ranged from scholar articles to textbooks with topics ranging from tumor growth patterns to capillary action. While searching for these different resources provide to be time consuming, an extensive literature search was necessary for the sake of validity and accuracy.

The tomosynthesis equipment emulated in this project replicates Hologic's Selenia® Dimensions® mammography system. Technical information on this system was gathered from Hologic's website, where system manuals, information sheets, and other resources on the technology were readily available.[276] The guides available through the Hologic website provided information on the system's rotating gantry, X-ray beam generation, dimensions and materials, and amorphous selenium detector. To properly implement the breast tomosynthesis system in MCNP, the MCNP User's Manual was referenced.[277] Specific material data, such as atomic composition and density was gathered from the NIST *Standard Reference Materials* website.[278]

NIST material data was also used to find the composition of the adipose, skin, and cortical bone. Glandular tissue composition information was collected from ICRP *Publication 103* while Cooper ligament information was collected from ICRU *Technical Report 46*.[279,280] Information on breast carcinoma composition was challenging to find given the expanse diversity of breast cancer. An article that investigated the composition of breast carcinoma and sarcoma using multimodality imaging was used to

gather information on the atomic composition of breast cancer.[281] Information regarding breast structure, including fundamental components and positional information, was primarily gathered from Netter's *Atlas of Human Anatomy*.[282] This anatomy reference provides extensive information on human anatomy ranging from muscle structures to vasculature networks. To establish a relationship between breast volume parameters and size, a standard breast sizing guide was used.[283] The sizing guide provided information on the volume of each breast size, which was used to extrapolate functions that could model each individual breast size. Specific information regarding glandular structure, ranging from information on the average diameter and length of the main ducts to the size and shape of the terminal ductal lobular units (TDLUs), was gathered from multiple resources, including a mammography reference book and scholar articles.[284,285,286,287] These references were also used to acquire information on Cooper ligaments, including their structure and size.

Vasculature information was also extracted from multiple sources. General macro vasculature structure information, that is, information regarding main arteries and veins, was obtained from the *Atlas of Human Anatomy*. Specific vascular data, such as vessel diameter and flow dynamics in the regions of interest, was acquired primarily from scholar articles.[288,289,290,291] Rudimentary contrast agent information regarding clinical practices and expectations was acquired from a textbook that focuses on contrast enhanced mammography.[292] Ample information on capillary exchange was collected from multiple sources to understand the multiple factors involved in contrast agent dynamics, such as the rate of diffusion and residence time and how these are affected by the characteristics of contrast media. Fundamental knowledge on capillary exchange was gathered from reference texts while specific information regarding capillary behavior in tumors was gathered through scholar articles.[293,294,295,296] To implement specific contrast agents into the breast phantoms, relevant details on the physiological properties of each contrast agent was gathered from multiple scholar articles. The physiological properties of interest are those that directly impact their distribution, such as viscosity, particle size, and osmolarity. Because contrast solutions often include buffer solutions to suspend the contrast particles in, such as gold nanoparticles in a phosphate buffered saline solution, the properties of those were investigated as well.

Breast cancer information was obtained from several sources that discussed tumor behavior and growth patterns, such as lesion characteristics at different cancer stages and vasculature characteristics surrounding the lesion.[297,298] Information regarding specific characteristics for the different types of breast cancer was gathered from scholar articles that focused on definite breast cancer types.[299,300,301] Multiple sources were used to verify information gathered to ensure validity. The two lesion types studied in this project are infiltrating lobular and infiltrating ductal carcinoma, both of which encompass multiple subtypes of cancer. Because most breast cancer cases are either infiltrating lobular or infiltrating ductal carcinoma, these two lesion types were incorporated into the model before the others.

4.2 Software

The primary focus of this project is to reproduce a clinical environment into a simulated environment. To achieve this, robust software is necessary to mimic accurate radiation physics and breast geometry. As mentioned, the radioparticle simulations are all conducted in an MCNP environment. Other aspects of this project, including phantom generation and data processing, were conducted using Python and ImageJ where the former served as a scripting tool for phantom building and information storage and the latter provided aid in image processing. Because of Python's robustness, all breast components were built with Python scripts; Python was also used to create scripts for contrast agent simulation as well as file writing automation.

Several Python packages were used to achieve a realistic breast phantom. The package *pygmsh* was used to create mesh models of the different breast components while *meshio* was used to process the resulting mesh geometries. Python offers multiple mesh-building packages, but *pygmsh* was chosen over the others because it can build 3D geometries from rudimentary geometrical structures, such as cylinders, cones, and ellipsoids. After these tools were used, *trimesh* aided in geometry processing, such as mesh merging and overlap processing and the post processed meshes were converted back into Abaqus-style mesh files with *pygalmesh*, which is a different mesh-building package capable of creating meshes from

numpy arrays. Other Python packages used in this project are those that are built-in, including packages used for image processing and algorithm development.

ImageJ provided a visual interface for the "detector" data created by processing the MCNP tally files. Although Python was used to extract and convert raw MCNP tally data into Hounsfield Unit arrays, ImageJ was used to acquire histograms at different regions of the resulting images with ease; this is due to the fact that ImageJ provides a snipping tool that can be used to analyze specific regions in an image. ImageJ also allows the user to import a stack of images thus facilitating the image processing procedure, since tomosynthesis data exists as a stack of images at different projections. ImageJ also provides tools that can be used to manipulate an image, such as Gaussian filtering, noise de-speckling, and contrast enhancement. It also offers tools to acquire metrics, such as the average signal over a region. Data acquired with ImageJ, such as background and foreground pixel values and standard deviation, was processed with Python to quantify the validity and quality of the simulated images. Ultimately, Python provided considerable utility in the data and statistical analysis conducted in this project.

5 Methods

5.1 Building the MCNP environment

The first object created in the MCNP environment was the tomosynthesis equipment; because the simulated system is presumed to be an exact replica of a real tomosynthesis system, ensuring a high fidelity in the MCNP environment was the priority. This entails replicating the real tomosynthesis system in every relevant aspect, starting with the x-ray tube and ending with the photon-collecting detector. Every component between two points was included into the simulated environment to mimic x-ray interactions expected in the real system.

X-ray creation begins after electrons exiting the cathode collide against the rotating anode, creating a cascade of X-rays from the different electron interactions that occur in the target material. The cathode emitting the electrons is modeled as a thin tungsten cylinder representing the tungsten filament used in

clinical X-ray tubes. The Hologic tomosynthesis equipment is dual-focal; this means the target anode houses two different angles – 10 and 16 degrees – to provide two distinct beam sizes. To replicate this anode type, the anode is built from a set of cones with varying opening angles that are connected with a set of 'rings' at the different steps, shown in **Figure 11a**. The anode is also assigned the tungsten material to replicate the Hologic model.

<div align="center">(a)   (b)   (c)</div>
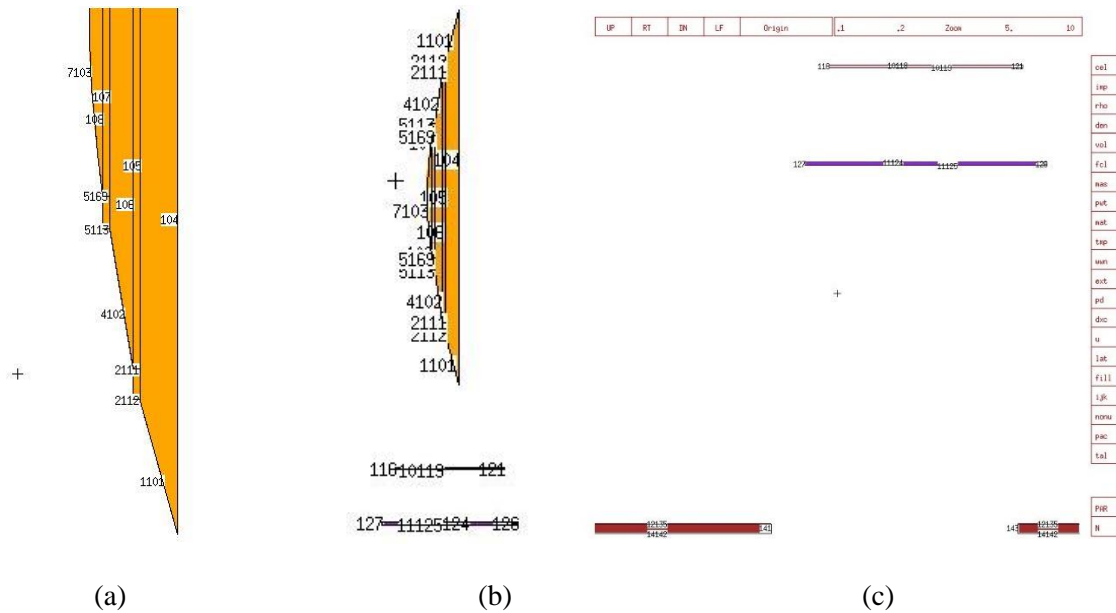
Figure 11: A set of images created with MCNP's interactive plotter (IP) tool demonstrating the beam geometry created in MCNP. Figure (a) pictures the multiple components that make up the anode while (b) pictures the location of the anode relative to the beryllium window (lilac) and aluminum filter (purple) and (c) pictures the beryllium window and aluminum filter relative to the lead collimator (burgundy).

Next, the beryllium window is created as a small, thin rectangular prism with the same dimensions as the one used in the Hologic equipment, which is shown as a thin lilac rectangle in **Figure 11b**. The aluminum filter, which provides filtration for low-energy x-rays, is placed about two centimeters below the beryllium window and was assigned a thickness of 0.07 cm, as shown in **Figure 11b**, where it is represented as a thin purple rectangle. The beam is collimated into a rectangular shape following filtration; therefore, a lead, 4-blade collimator is placed below the aluminum filter, demonstrated in **Figure 11c** as a set of burgundy rectangles. The collimator blades intersect to shape the beam, which isn't shown in the figure

since the figure only demonstrates a 2D cross-section at x=0 of the beam set-up. The Hologic collimator can be expanded and contracted to accommodate different beam sizes, but the one used in the MCNP environment was created with a 5.8 inch by 4.9 inch window to ensure the beam expands to the size of the detector plate when the X-rays reach the Bucky table.

The compression paddle follows the collimator and is composed of plastic meant to provide minimal attenuation of the beam as it reaches the target. The paddle dimensions match those of the bucky table to reduce edge artifacts that might appear in the images. The Bucky table follows the compression paddle and is composed of a 0.12 cm-thick carbon fiber panel. The table houses a modest, 1.5 cm - thick space before the detector screen is reached. This space is meant to house an anti-scatter grid in the Hologic equipment but was emitted in this simulation for reason explained later in this paper. The detector screen is modeled as the amorphous selenium detector (AmSe) that is used in Hologic's tomosynthesis system. This detector is a direct-conversion type; therefore, no photodiodes are needed to convert the X-rays into light. This means the detector can be modeled as a thin slab of amorphous selenium material representing the multitude of pixel arrays used in a clinical setting. To emulate the AmSe detector that Hologic uses, the thickness of the slab is set to 0.025 cm. The material assigned to the detector object matched that of clinical AmSe detectors, with 99.5% of the detector composing of selenium, 0.5% composing of Arsenic, and 10 ppm composing of chlorine.

After the geometry was configured in MCNP, the source was created. The source was first created as a monoenergetic electron source with an MCNP data card. The data card specified the energy of the electrons, the weight of the source, which is equivalent to the number of source particle emitted (approximately 4.2×10^{17} electrons for Hologic's tomosynthesis device), the location of origin, the beam shape, and the beam direction. The electron source was aimed at the anode to create the polyenergetic X-ray source and it was kept as a pencil beam with a small radius equivalent to the one used in Hologic's equipment. To ensure the electron source was working properly, an MCNP trial run was conducted with 5 million histories. This initial run lasted about an hour, demonstrating that running a full simulation with

over 1 billion particles would be impossible, given the fact that a tomosynthesis scan requires 15 total images, equating to a total run time of about 15,000 hours.

To reduce the run time, the source was exchanged for an X-ray source that not only reduced the number of particles needed, but also significantly decreased the run time. When electrons collide with the anode, about 1% of the electron energy is converted into X-rays and the rest is converted into heat.[302] This means that most electrons that interact with the anode will become obsolete for the purpose of the simulation. To extract an exact number of photons created from the electron beam source, an FMESH-type tally was used directly under the anode. The polyenergetic beam extracted from this process for a tube voltage of 40 kVp is shown in **Figure 12a**. In MCNP, tally cards function similarly to detectors; their purpose is to quantify the observable interactions that occur in a specified region, such as energy deposited into a volume, the particle flux over a region in space, and much more. More specifically, the FMESH tally is meant to function similarly to a detector panel with arrays of "pixels" with dimensions specified by the user. The tally measures the flux over each specified pixel volume and the tally offers several options that allows the user to filter out interactions that don't meet specified criteria, such as a non-perpendicular angle, unmet energy requirements, or wrong particle type. The tally can also discriminate between different energies with boundaries estimated by the user to create 'bins' of the different energies observed in the interactions. This functionality allows users to observe energy patterns in the beam's spatial distribution. This tally type is often used in imaging simulations and is used in this project to replicate the system's detector panel, which is also discussed in this section.

The tally was placed at various locations to assess the number of photons that remained along the different stages of the beam creation as well as the changes in energy that occurred after particles were filtered by the beryllium window, aluminum filter, and lead collimator. Tallies were also placed close to the Bucky table to observe the extent of beam broadening, shown in **Figure 12b.**
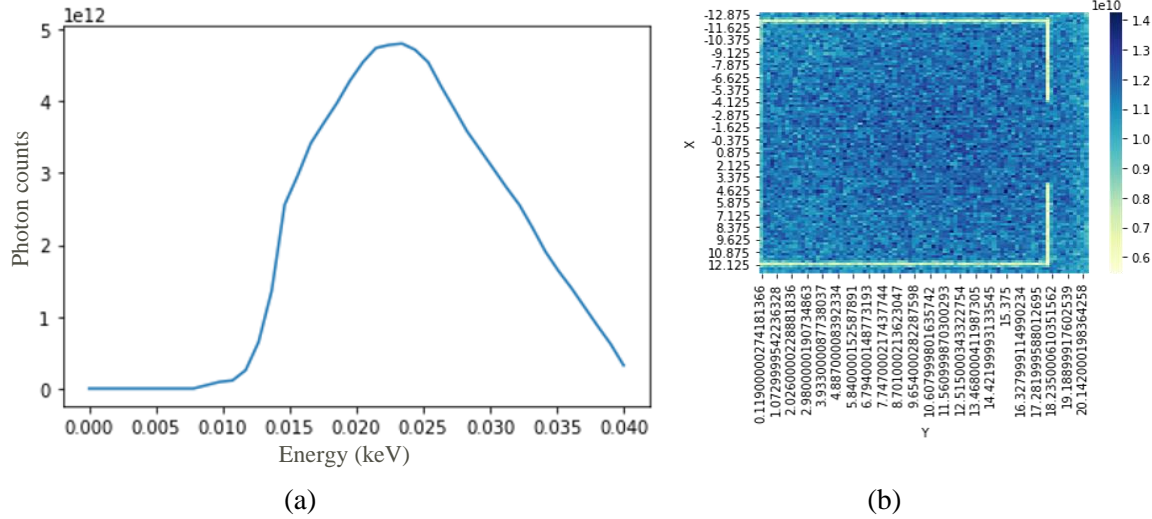
Figure 12: (a) demonstrates the tally results for photon that were generated from an electron beam accelerated at 40 kVp with a quantity of approximately 4.2x10^17 electrons as a distribution of energy. (b) demonstrates the spatial distribution of the resulting beam at the bucky table. The artifact shown in the image represents the compression paddle.

The results of the tallies demonstrated low-energy filtration following the aluminum filter and proper beam shaping following the lead collimator. Furthermore, the tallies provided an exact energy distribution of the polyenergetic X-ray beam and once the results of the tally were normalized, the percent probability at each energy bin was obtained. This energy distribution was used to formulate the X-ray source in MCNP to replace the electron source, whose energy is specified as a distribution with different probabilities at each energy bin. Because the energy distribution changes with electron energy, this process was replicated for all beam energies used in Hologic's tomosynthesis equipment, ranging from 21 kV to 40 kV, in increments of 1 kV. The origin of the source was moved to about half a centimeter below the collimator because at this location, the rectangular shape of the beam can be easily replicated in the MCNP source card. The source was also given a small angle of distribution to represent the beam broadening that occurs as the beam exits the collimator and approaches the Bucky table. The source weight was also changed to $4.4x10^{14}$, which is the approximate quantity of photons that remain from the original electron source at the new source location. At this new location, only 1/1000th of the original histories that were used to simulate the electron source are needed to achieve the same uncertainty statistics.

An FMESH data card is used to represent the flat panel detector. As mentioned, the FMESH tally easily replicates a panel of pixel detectors with a resolution chosen by the user. The tally is embedded into the cell representing the AmSe block to emulate the Hologic flat panel detector with the thickness of the FMESH tally established as the same thickness of the AmSe block. The resolution of the flat panel detector that Hologic equipment uses is 70 microns and for a detector panel with an active imaging area of 18 cm x 24 cm for tomosynthesis, over $8.8x10^6$ cells are needed. Using an FMESH with such small resolution would significantly increase run time as more histories would be needed to maintain a reasonable uncertainty at each detector element. Therefore, the resolution of the simulated system is coarsened to 250 microns, which still achieves a reasonable resolution.

Breast tomosynthesis requires a rotating gantry to move the source along an arc to produce a set of projections. Hologic's tomosynthesis system uses a rotating gantry that rotates from -7 degrees to 7 degrees in 1-angle increments to produce a total of 15 projections. As this occurs, the detector remains stationary. To emulate the rotating gantry, a rotation data card (TR) is used for each different projection angle along the rotating arc; therefore, 14 total rotation cards are used but only one is enacted per simulation. The rotation cards are used to rotate specific cells – the volume cells that shape the gantry – with the "TRCL" argument and the source is also rotated along with the volume cells with the "TR" argument. Four different rotation angles are shown in **Figure 13**. The images demonstrate how only the gantry components are rotated; the yellow circle represents a cross section of the anode, and the bottom component represents the bucky table with the compression paddle a few centimeters above it. The filter and the collimator blades are also shown but are obscured by the surface card labeling.
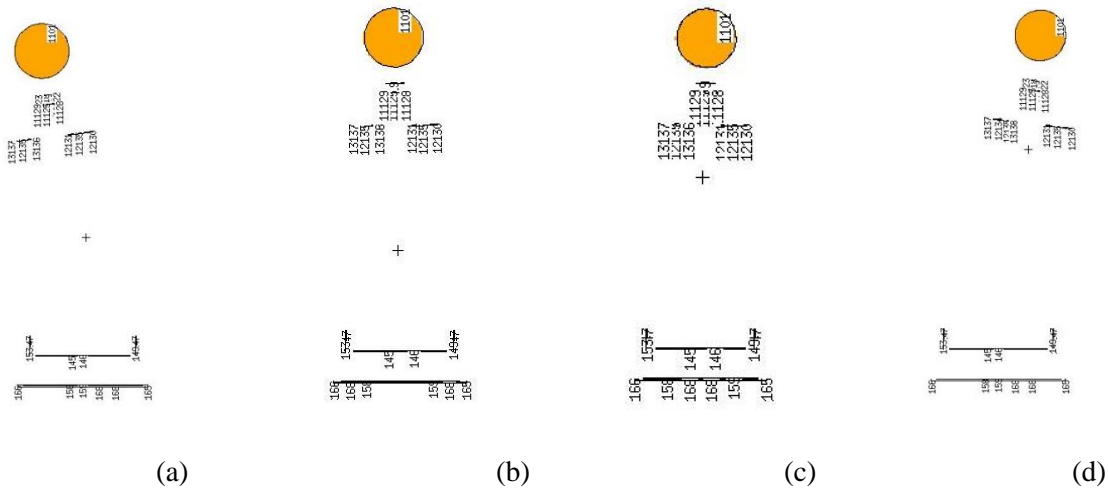
Figure 13: images of the positioning of the gantry at different rotations. The angles of rotation shown are (a) 7, (b) 1, (c) -1, and (d) -7.

5.2 Building the Breast Model

After the tomosynthesis system was completed, the breast phantom was built. Several aspects were considered when constructing the breast phantom, ranging from material specification to changes in volume with breast size. Because the breast phantom considers the biophysics of contrast agent delivery, the vasculature is also meticulously configured into the model. Model versatility is an important aspect of the breast phantom and is a core factor in the Python scripts that were created to generate the breast phantoms. The different components of the breast are meant to vary depending on user requirements, including vascular consideration. In the following sections, the creation of the breast components is discussed in detail.

5.2.1 Breast Components

The breast contains four main components: the skin, glandular tissue, adipose tissue, and Cooper ligaments. The glandular tissue can be broken up into multiple sections starting at the main ducts and ending with the miniscule terminal ductal lobular units (TDLUs) that form the lobules. Since the phantoms are meant to be versatile, no patient CT data was used to build the breast components. Instead, every component is built with a set of Python algorithms that determine the dimensions and shape of the different breast

components based on user input. This allows the user to control the creation of the phantom from the ground up. In addition, Python offers multiple mesh-converting packages that were considered in this project to supersede the use of the Abaqus program. This creates a more streamlines phantom building process that is easier to work with.

The first component created is the skin; the skin provides a precedent for the other components that reside inside of its boundaries. The breast size and shape are controlled by the skin boundary and once these are determined, the spatial distribution of the other components can be determined as well. A set of relationships were extracted from the breast sizes, volume, and dimensions with the assumption that these breasts can be modeled by a set of ellipsoid functions. Because the breast is compressed during tomosynthesis, the breasts are modeled as an ellipsoid sandwiched between two parallel planes. The resulting structures can be seen in **Figure 14.**

| (a) | (b) | (c) |
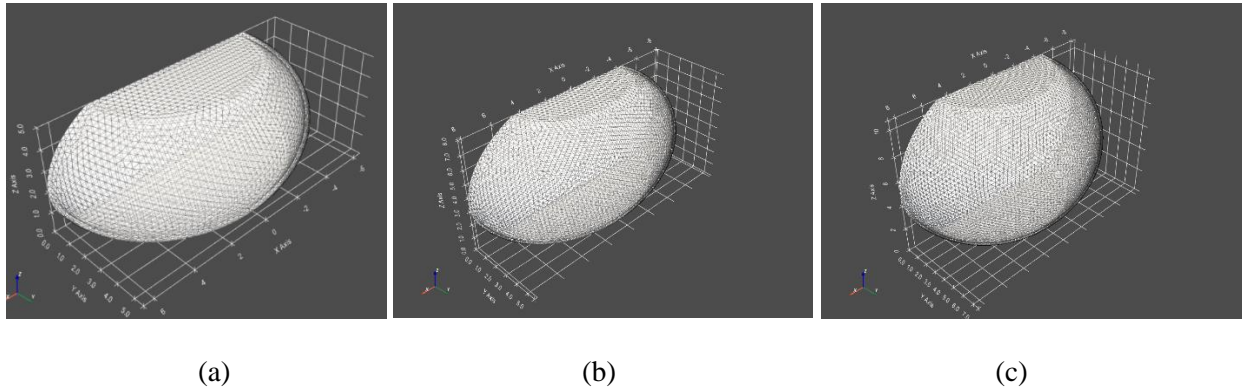
Figure 14: A set of figures demonstrating different meshes representing the skin surrounding the breast. (a) represents a breast sized 32A, (b) represents a breast sized 38A, and breast (c) represents a breast of size 38D.

The relationships between breast size and dimensions are stored in a dictionary and determine the *a, b,* and *c* parameters of the ellipsoid volume as well as the placement of the parallel planes. When the user provides the desired breast size, the breast size is used as a dictionary key to retrieve dimensional data and the corresponding items are extracted to create the skin with the matching parameters.

These parameters are placed inside a Python function that generates the skin mesh. The function randomly generates a skin thickness between 1.5 mm and 2.2 mm with Python's *random* package. Then, a set of *pygmsh* 3D geometrical objects are generated from the skin parameters. An ellipsoid is generated from *a, b,* and *c* and then a box with the same dimensions is generated and halved from negative *b* to y=0. The box geometry is then subtracted from the ellipsoid; this removes half of the ellipsoid, and a semi-ellipsoid remains. Next, a set of rectangular prisms are created spanning from +*c* to the height of the top parallel plane, *z2*, and from -*c* to the height of the bottom parallel plane, *z1*. The pair of rectangular prisms are subtracted from the semi-ellipsoid and a "compressed" semi-ellipsoid remains. Then, the process is repeated with the skin thickness subtracted from the parameters. This generates a slightly smaller compressed semi-ellipsoid, which is then subtracted from the full-sized semi-ellipsoid so that a skin shell remains. This shell is also elevated so that the center is above the origin so that the lowest point of the skin is at z=0; this places the breast directly on top of the bucky table. Finally, the skin geometry is converted into an unstructured mesh object that can be stored as an Abaqus-type mesh file with Python's *mehsio* package.

A separate function generates the glandular components. The function uses the breast size, the predetermined skin thickness, and the user-provided glandularity to generate components that meet the required criteria. The function discretizes the % glandularity into bins to determine the number of main ducts that are needed based on the glandularity provided; the minimum number of ducts used is 5 and the maximum is 10. The resulting number of main ducts needed are then spatially distributed around a central point, which is where the nipple is assumed to reside, chosen to be at the *x*-axis centerline and the maximum *y*-value. The first duct is placed at the center point and the ducts proceeding it are equally distributed 60 degrees apart counterclockwise around the center point. The following ducts, up to duct number 7, are all equidistant from the center, with the distance randomly chosen from a gaussian distribution. The depth of the main ducts is also chosen from a gaussian distribution and is kept the same for all the main ducts. Because the main ducts are modeled as a set of cylinders, they are assigned a shared radius from a gaussian distribution. All of the parameters chosen to model the ducts are chosen from a range of values that were

chosen from literature. Because breast components vary in size, incorporating randomness into the model is an important step that highlights diversity in the data.

The main ducts are created as a set of three components. The main ducts contain a sinus that lies around the center of the duct; therefore, the first main duct components are proceeded by an ellipsoid that represents the sinus. The sinus dimensions are also randomized but kept within a small range to ensure no geometry overlap. The sinuses are also rotated so that the back portion of each point away from the center, except for the first sinus located at the central point. This introduces as outward direction in the ducts to bias the glandularity and fill out the breast volume. At the back end of the sinus, a secondary portion to the main duct is attached. The secondary portion is also described by a cylinder with the same radius as the front portion of the main ducts; the difference between the two is that the secondary portion is angled by the same degree as the sinus preceding it. Following the secondary portion of the main duct lies the secondary ducts.

The secondary ducts represent the ducts that extend throughout the breast. They vary in depth and thickness and their quantity depends on the breast glandularity. Each main ducts attaches two or three secondary ducts, depending on whether the main duct is labeled as an odd or even number, respectively. The secondary ducts are given a random length, although the parameters ensure that the length is no less than 2 cm and no more than the remaining depth before the chest wall is reached. If the main duct is attached two secondary ducts, the ducts are uniformly separated by an angle away from the sinus angle, forming a Y-shape, in a random direction but within a predetermined margin to prevent geometry overlap. If the main duct connects to three secondary ducts, the 'central' secondary duct is given the longest length and its angle follows that of the main duct that it is attached to. The remaining ducts are given a random angle away from the center line but within a predetermined margin. **Figure 15** demonstrates the ductal system after all components have been assembled. The figure demonstrates the 3D geometries used to model each component of the ductal system.

(a)   (b)
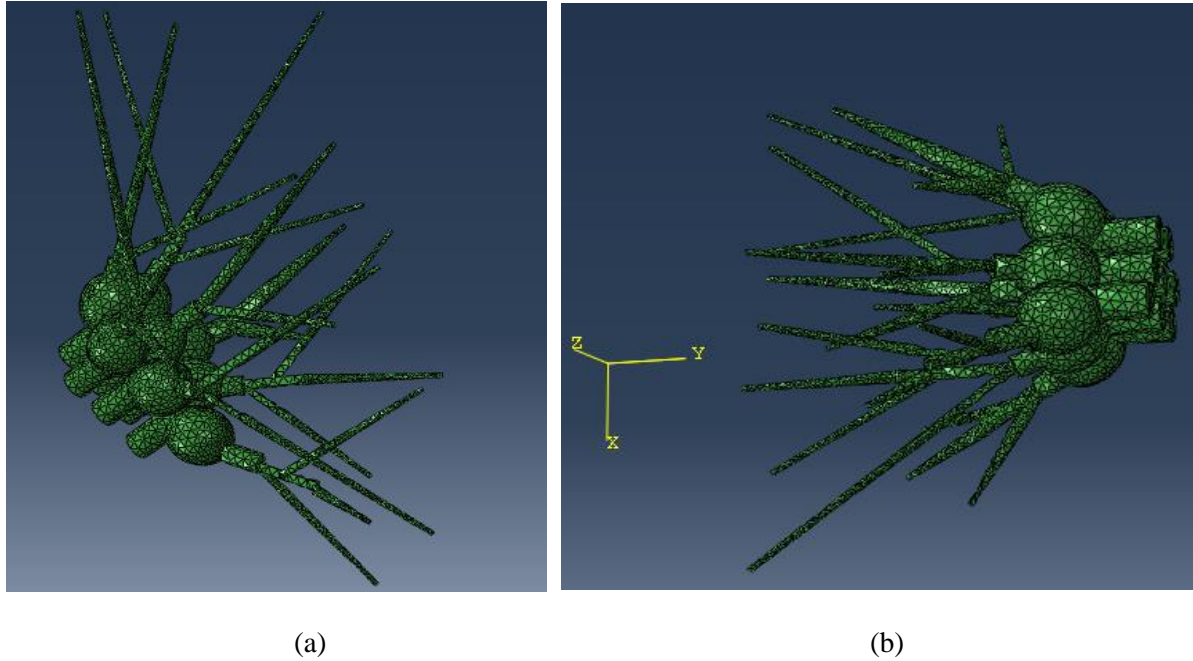
Figure 15: A set of images demonstrating the structure of the ductal system before the lobules are attached. Both (a) and (b) picture the same ductal system but at different views.

After all the ductal components have been defined, the Cooper ligaments are created. First, an algorithm is used to create the main Cooper ligaments; these are the ligaments that surround the main ducts and sinuses. Similar to the main ducts, these Cooper ligaments are symmetrically placed about the center point and their dimensions are determined by the dimensions of the main ducts. The Cooper ligaments are responsible for providing the breast with support; thus, they create a network that surrounds the glandularity and attaches to the skin shown in **Figure 16a**. The thickness of the ligaments is kept at 0.2 mm, which adheres to the average thickness of these ligaments. The main ligament data is stored into a dictionary that keeps track of positioning and dimensional information of all the ligaments. This data is then accessed by a secondary set of algorithms that creates the 'secondary' Cooper ligaments.
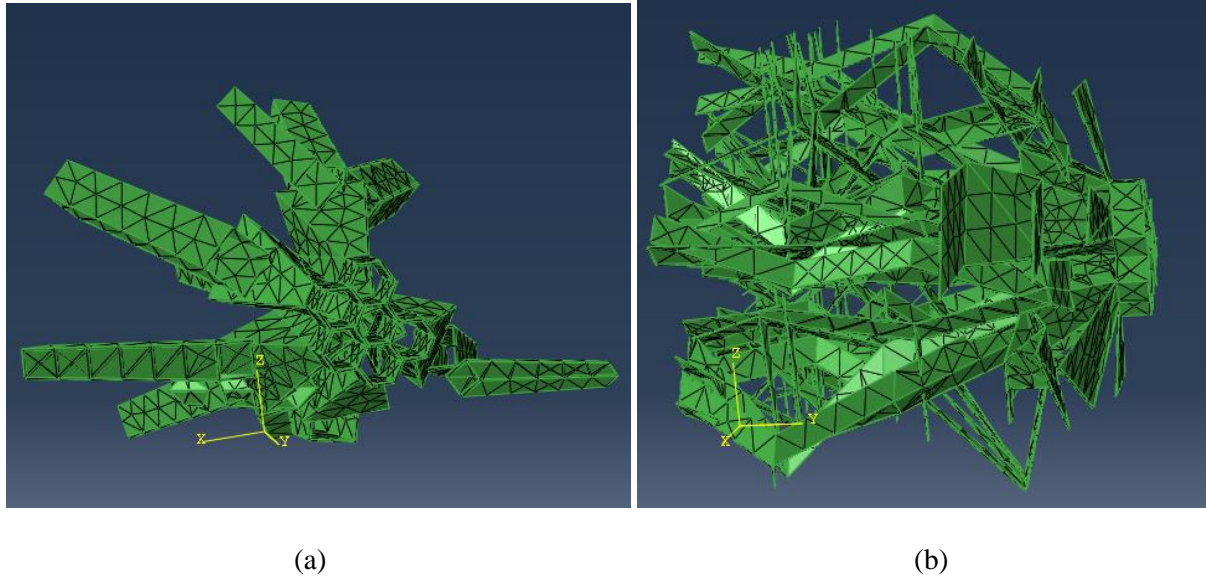
Figure 16: The Cooper ligaments at different stages in the construction process. (a) demonstrates the first stage, when the ligaments are built surrounding the main ducts and (b) demonstrates the addition of the secondary ligaments.

Secondary Cooper Ligaments are those that attach the main ligaments to the rest of the breast until the chest wall is reached. They surround the secondary ducts and they 'fill out' the rest of the breast tissue. The algorithms used to create the secondary Cooper ligaments check the positional data of the main ligaments and attaches the new ligaments to the existing structure. The new ligaments create a network that attaches to the surrounding skin until the chest wall is reached. A different function is applied that ensures that the dimensions and position of each ligament does not exceed the boundary imposed by the skin. The new positional and dimensional data is stored onto a second dictionary. After the secondary Cooper ligaments are created, a different set of algorithms use the *pygmsh* package to create mesh geometries from the two Cooper ligament dictionaries. The dictionary containing the main Cooper ligament data is processed first; each item in the dictionary is converted into a 'box' item and rotated by a predetermined angle (that is also stored in the dictionary) to position the ligament into the correct location, then stored into a list. Once all the dictionary items have been processed, the list items are joined together to form one large structure. The structure is converted into a mesh object and stored into an Abaqus *.inp* file. The final version of the Cooper ligament geometry is shown in **Figure 16b**. The dictionary with the secondary Cooper ligaments is

more difficult to process due to geometry errors that often arise in this process. Because *pygmsh* is a program built with C++ roots for a Python engine, the program can be challenging to work with. To avoid geometry errors, each ligament was joined one at a time into a master structure and converted into a mesh object within a *Try-Except* loop inside the Python algorithm. If an exception was made during execution, the item was removed from the dictionary. After the loop finishes executing, the remaining dictionary items are converted into a mesh object and stored into an Abaqus *.inp* file.

After the ducts and Cooper ligaments are created, a volume check is performed to calculate the total volume of the glandular components created so far; this allocates the remaining volume onto the lobular objects so that the requested glandular density is fulfilled. Although Cooper ligaments aren't always considered glandular components, their density and attenuation are comparable to that of glandular tissue and the two tissue items are often grouped together in mammographic images. In this project, the glandular tissue and the Cooper ligaments are stored in separate files because they are assigned different materials in the MCNP file.

Once the total lobule volume is calculated, average parameters are assigned. The breast size and percent glandularity are used to determine the amount and the size of the lobules that reside along the ducts while the volume is used to carefully balance the two variables. The number of lobules assigned per duct is quantified in units of lobules per unit distance, since longer ducts should contain a higher lobule count. A small margin of uncertainty is assigned to each lobule as it is positioned along the ducts as well as in its parameters to introduce randomness into the glandularity. It's important to prevent uniformity and predictable patterns, as this is unrealistic in a real human breast. The lobules are created as ellipsoids with two parameters sharing the same dimension while the other dimension is about twice of the other two dimensions; this is to create a prolate appearance that is often observed in a lobule. All lobules are attached normal to the surface of the duct they are adhered to; however, they are each tilted towards the chest wall by a random degree between 30 and 60 degrees. The same function that is used to verify that the Cooper ligaments do not exceed the skin boundary is applied to the lobules to ensure that they are placed within the skin boundary. If the lobule exceeds the boundary, it is repositioned. The data for each lobule, including

its ellipsoid parameters and positional information, is stored into the same dictionary that stores the ductal information. Each main duct is stored as a dictionary key and every glandular object within its path starting at the nipple and ending at the last lobule along the secondary duct is stored within that dictionary key as an individual item.

When the function and all its glandular-tissue-generating algorithms finish executing, the dictionary containing all the glandular data is passed onto a separate function that converts the dictionary data into mesh objects. The function iterates through each dictionary key, that is, each main duct and its path. First, the front component of the main duct is unpacked; coordinate and dimensional data is used to create a cylinder object with *pygmsh*. The next item along the main duct path is the sinus; this sinus is modeled as an ellipsoid with the predetermined dimensions. The sinus is also rotated with the predetermined angle. The sinus and the front part of the main duct are joined with a *pygmsh* Boolean operator and stored as a new item within the function. The back component of the main duct is also created as a cylinder and rotated by the same degree as the sinus preceding it. After its creation, it's joined with the preceding items. The resulting geometry is stored as a new object. The next set of items in the sub dictionary are the secondary ducts. The function iterates through the small duct list as well as each lobule stored that lies along the path of each corresponding secondary duct. The duct in the path is first created into a cone object with *pygmsh*. The function iterates through the list of lobules attached to the duct and uses the parameters associated with each lobule to create a *pygmsh* ellipsoid for each item. As each lobule is created, it is stored into a list. When the function is finished iterating through all the lobule items in a sub dictionary, the function joins them as a singular object using a *pygmsh* Boolean operator. The resulting item is then joined with the cone representing the secondary duct and stored as a new item. After each secondary duct connected to a corresponding main duct is converted into a *pygmsh* item, the entire pathway is joined as a single item and placed into a list until the function finishes iterating through each dictionary key. Once complete, the final geometry is converted into a mesh object and stored into an Abaqus-type *.inp* file. The images shown in **Figure 17** demonstrate the geometry that is stored as the complete glandularity, which includes the ducts and the lobules. The image in **Figure 17a** represents the fibroglandular tissue inside a

32A-sized breast with a glandular density of 20% while the image in **Figure 17b** demonstrates a similarly

sized breats with a glandular density of 30%.

(a)   (b)
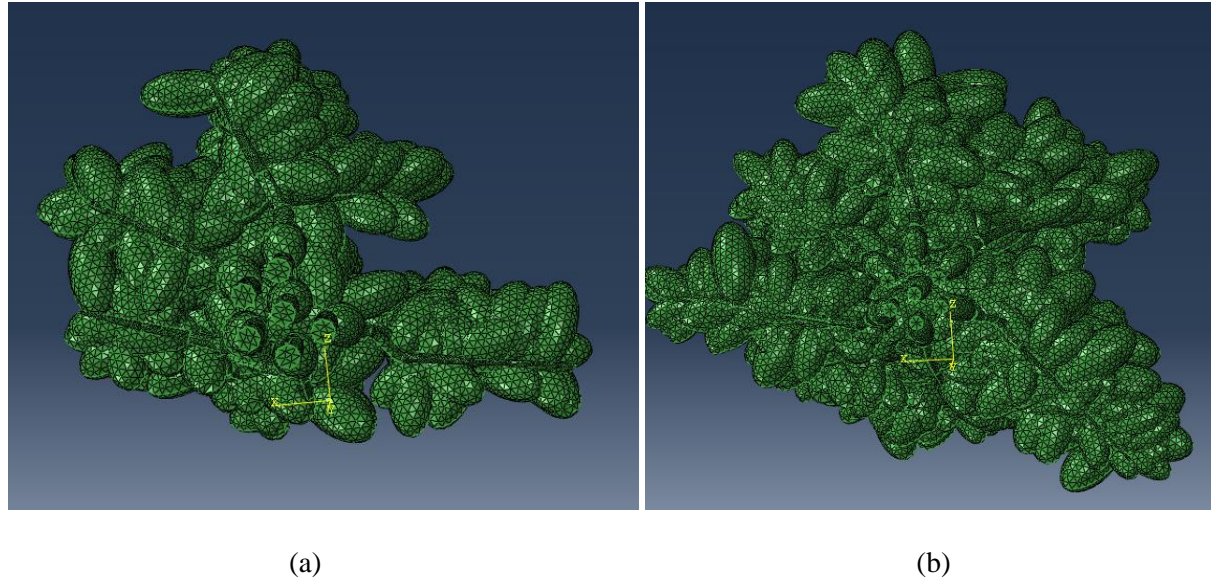
Figure 17: The mesh geometries of completes glandular structures. (a) depicts a glandular structure pertaining to a breast sized 32A with 20% glandularity while (b) depicts a similarly sized breast with 30% glandularity.

A separate function is utilized to run the previous function to ensure that no errors occur that could

discontinue the run. What this means is that the glandular components are created inside a *while-loop* that

ensure the geometry is created without issues. To satisfy the condition of the loop, the function that creates

the glandularity must complete execution. If the function does not complete execution, a marker indicating

failure is used so that the loop reruns. Each marker is counted and if five failed executions are marked, the

while-loop will stop executing and the function will end, alerting the user that there are structural problems

in the geometry that need to be addressed that are preventing the code from executing properly. If the loop

is successful, the file generated for the glandular tissue is stored and the user will be notified that the

function ran successfully.

Finally, the adipose tissue is created by using the parameters that define the 'hollowed' component

of the skin geometry. The adipose is created in a similar fashion as the skin, except it is kept as an entire

solid component. The mesh is saved as a separate file given its composition is different than that of the glandular tissue. The adipose will be processed later to remove the tissue overlapped by the Cooper ligaments and the glandular tissue. There are additional chest wall components that can be created in the same script; however, they're not essential to craniocaudal breast imaging and the user is free to choose whether or not they would like to generate mesh files for the chest components. The chest wall components include ribs, the intercostal muscle, the pectoral muscle, and a thin fascia layer that lies between the breast and the pectoral muscle. Although these components are independent of breast glandularity, the breast size is used to some extent to determine the length of the ribs along the axial plane. These components are also created with a margin of uncertainty to introduce randomness.

5.2.2 Vasculature

The vasculature was modeled using multiple scripts, given the complexity of the vascular system. The vascular system is first modeled as a macro-system, that is, the veins and arteries that run along the site of injection, into and out of the heart, and up until the subbranches of the breast are reached. The script that creates the macrovasculature models the vascular system starting at the median cubital vein (MCV), where contrast agent solution is typically injected. The contrast agent then travels to the basilic vein once the MCV and the basilic vein meet. The brachial veins connect with the venular branch, and the vein converts into the axillary vein. At this point, the radius of the vein increases, and the flow rate also increases. A few smaller veins connect to this vein along the way and the vein develops into the subclavian vein. As the contrast agent traverses the subclavian vein, the external, vertebral, internal jugular, and dorsal scapular vein connect to the subclavian vein. The subclavian vein then converts into the brachiocephalic vein and receives blood flow from the internal thoracic vein, also known as the internal mammary vein. The inferior thyroid vein also joins the subclavian vein before the veins from the right and left side of the body join to create the superior vena cava. Before the superior vena cava reaches the heart, the Azygos vein connects a small distance above the heart before the vein reaches the right atrium.

The data storing systems implemented into the code consider the amount of time that the blood and contrast agent spend in the heart and the lungs. Because capillary exchange that occurs in the pulmonary alveoli does not result in the loss of contrast agent or blood, the ratio of contrast agent to blood at these stages does not change and the volumetric flow rate exiting the heart should equate the volumetric flow rate entering the heart. The blood and contrast agent exit the heart via the aorta at a high velocity before the aortic branch distributes part of the blood flow through its top three connected branches and before the rest of the flow is transported through the thoracic aorta. The aortic arch contains the right brachiocephalic artery, the left common carotid artery, and the left brachiocephalic vein. Because the right brachiocephalic artery contains the right common carotid artery along its path, the volumetric flow exiting through the right brachiocephalic artery is equivalent to the sum of the volumetric flow exiting through the left common carotid and the left brachiocephalic artery. There are a few other discrepancies between the left and right side of the vascular system, such as small differences in branch length. The script considers these differences, and the user is instructed to specify the arm that the contrast agent was injected in as well as the breast that the system is imaging.

The contrast agent travels through the subclavian artery and eventually through the axillary artery. As it travels through these main arteries, the contrast agent is distributed through the connecting branches along the way, including the internal, superior, and lateral thoracic arteries. These three branches are the principal suppliers of blood flow to the breast. Furthermore, the internal thoracic artery contains three branches at each intercostal space, two of which supply blood to the breast. The perforating and anterior intercostal branches distribute blood flow to different regions within the same intercostal space. The superior thoracic artery contains limited branches that reside within intercostal spaces two through four. The lateral thoracic branch also contains a limited number of branches, and these are typically found within intercostal spaces two through 6. The blood supply flowing through the perforating and anterior thoracic branches exceeds that of the superior and lateral branches and they contain subbranches that protrude out of each branch along the intercostal space. These subbranches and the branches connected to the superior and lateral thoracic arteries are considered terminal branches, that is, they don't subdivide into any other

known branches before they transform into arterioles. Once these terminal branches are reaches, the microvasculature script is enacted.

As the contrast agent travels through the different junctions along the venular system, changes in flow rate, blood velocity, and cross-sectional area are accounted for. Murray's law is used to calculate the change in vessel radius as the connecting branches join the into the main pathway, shown in **equation 5**, where r is the resulting radius, r_1 is the main vessel, and r_2 is the connecting vessel.

$$r^3 = r_1^3 + r_2^3 \quad (\text{eq.} 5)$$

Using conservation of mass, the flow rate through the resulting vessel is the sum of the main vessel and the connecting vessel. To estimate the velocity of the blood through the resulting branch, the flow rate, given in cm^3/s, is divided by the cross-sectional area, given in cm^2, to produce the velocity in cm/s. This biokinetics data is stored into a dictionary where each key is a pathway along the microvasculature route, such as the brachiocephalic pathway or the axillary pathway. A separate dictionary stores the length data associated with each pathway and the time, in seconds, that it will take the contrast agent at a specified point to traverse the pathway, which is calculated by dividing the pathlength by the velocity and is given in seconds.

The microvascular script is responsible for simulating the delivery of contrast agent into the breast tissue. This involves simulating the transport of the contrast agent through the arterioles and into the capillaries. It also calculates the diffusion of the contrast agent through the capillary walls and into the interstitial fluid through capillary action. The script contains two dictionaries pertaining to the characteristics of the arterioles at different dimensions, including the diameter and length at each dimension; one of the dictionaries contains this information for the vasculature pertaining to healthy tissue while the other dictionary houses the information for tumor tissue. It's important to account for the differences in the characteristics for each vascular type since these differences create the contrast gradient between healthy

and tumor tissue. The script also assigns randomized general capillary characteristics, such as average capillary diameter and average number of capillaries per capillary bed.

The script imports dictionary data from other scripts, including the vessel characteristics from the macrovasculature script and the glandular data created from the script that creates the mesh geometry for the breast components. The script also contains multiple function that are responsible for mapping out the distribution of the microvasculature, such as assigning microvasculature branches to specific regions in the breast and compartmentalizing the microvasculature based on the volumetric distribution of the breast. A function in this script is responsible for assigning capillary density – and overall vascular density – to each component in the breast. The glandularity and adipose capillary densities differ, and the function assigns these differences as a function of glandularity. In addition, if a tumor is embedded in the geometry, the capillary density assigned to the tumor is dependent on the tumor stage, since smaller tumors require a high vascular density and larger stage tumors exhibit necrotic, hypoxic regions. Finally, the script also assigns a specific number of capillaries to each component in the glandular system as well as any embedded tumors that is dependent on the capillary density and the volume of the component. By calculating the capillary quantity at each region in the breast from the amount of glandular and tumor tissue present, the blood flow demand at each labeled region can be calculated.

Several other functions are generated to create data structures to keep track of the different vascular components that need to be accounted for, such as the flow dynamics and the minimum amount of time needed for the contrast agent to reach each region. One of these functions accounts for the change in contrast agent percentage flowing through the vessels as it recirculates the heart and it also considers how the injection time impacts the amount of contrast agent that circulates through the vascular system. A different function keeps track of an imaginary timer that is responsible for terminating the simulation once the requested time has passed.

The capillary action is simulated by a function that enacts the pharmacokinetics of the chosen contrast agent to estimate the distribution of the contrast into the interstitial fluid. The information pertaining to each contrast agent is stored in a dictionary in a separate script. This dictionary can be imported

into the microvasculature script to enable access to the data for the contrast agent of interest. The same script that holds the contrast agent dictionary also stores the functions used to calculate the pharmacokinetic constants used to estimate the contrast agent diffusion across the capillary wall. This is to avoid cluttering in the microvasculature script and they can be accessed with ease the same way that the dictionary information can be accessed.

The function first calculates the hydraulic conductivity, which is a function of fluid viscosity and capillary characteristics, which varies depending on the capillary type. The osmotic reflection coefficient is also calculated, which is a function of particle size and capillary cleft or pore size. The diffusion and permeability coefficients are also calculated. Then, the Starling equations are used to estimate two quantities; the first is the bulk flow across the capillary, given in ml/s and shown in **equation 6**, and the second is the molar flow, given in mol/s and shown in **equation 7**.[303]

$$Q_v = L_p * SA * \left([P_c - P_i] - \sigma[\pi_p - \pi_i] \right) \quad \text{(eq. 6)}$$

$$Q_S = -SA * \omega * \Delta C \quad \text{(eq. 7)}$$

In the first equation, L_p is the hydraulic permeability, SA is the surface area of the capillary, P is the oncotic pressure, σ is the osmotic reflection coefficient, and π is the osmotic pressure. In the second equation, ω is the permeability and ΔC is the difference in solute concentration between the capillary and the interstitial fluid. Although both of these quantities depend on the hydraulic conductivity and capillary pressure gradients, the molar flow also depends on the difference in solute concentration between the capillary fluid and the interstitial fluid. Therefore, the concentration of the contrast agent diffusing through a capillary wall can vary. The function estimates the remaining contrast solution in the capillary as the blood flow exits as well as the flow rate. These quantities and a few other metrics are output by the function and used by a different function that keeps track of the concentration of the contrast agents in the interstitial fluid with each iteration.

There are a few key differences between tumor capillaries and healthy breast tissue capillaries. Healthy capillaries in muscle tissue contain small clefts where the endothelial cells meet. These are usually 5 - 15 nm in size and they permit bulk fluid transport. Meanwhile, capillaries surrounding tumor tissue are much leakier; this feature is meant to facilitate nutrient transport during tumor growth. This "leakiness" manifests itself through several mechanisms, including the presence of fenestrae, large holes, and large clefts with widths about ten times greater than healthy clefts.[304,305] The distribution density for each of these capillary artifacts is described in detail in available scholar articles. The frequency of each artifact was accounted for when implementing the severity of the "leakiness" found in tumor capillaries and ultimately, these artifacts determine the difference in contrast agent concentration in the interstitial fluid surrounding tumors and healthy tissue. The oncotic pressure also varies in tumor tissue and is reportedly less than in healthy tissue. As a result, the pressure gradient created in tumor capillaries varies from that of healthy tissues. Because oncotic pressure is a principal component in the Starling equations, the bulk flow and contrast agent delivery across the capillary walls will vary drastically between the tumor and healthy tissue. Again, it's important to account for these differences to fully encompass the differences in contrast agent uptake between the tumor tissue and healthy tissue, which ultimately creates the difference in attenuation between tumors and glandular tissue.

Because a capillary bed contains several capillaries arranged in a mesh, capillary exchange is calculated through a series of iterations as the contrast agent travels through different generations within the capillary bed, with each generation receiving the blood flow and contrast agent concentration calculated for the capillary generation before it. Simultaneously, a dictionary keeps track of the contrast agent present at each capillary generation; this is an important metric to keep track of because the contrast agent difference between the blood flow and the interstitial fluid determines the amount of contrast agent that diffuses through the capillary wall. As this occurs, a different function keeps track of the contrast agent that flows out of the arterioles into the capillary bed. This function utilizes the dictionary that stores information on the overall contrast agent residence time in the microvasculature dependent on injection time. This process functions to keep track of the contrast agent quantity flowing into the first-generation capillaries in the

capillary beds. These different functions are used in tandem until the allocated simulation time is reached, at which point the resulting contrast agent concentration in the interstitial fluid is stored into a dictionary and output by the function to be used in the next step along the assembly line.

The next step in the microvasculature is to distribute the contrast agent concentrations to each respective tissue. The previous function calculates the contrast agent distribution through the different individual pathways, that is, through each terminal branch from the internal, superior, and lateral thoracic arteries. Because these are each coupled with specific regions in the breast volume, the distribution of contrast to specific breast tissues is also estimated. This holds true for both the healthy and tumor tissues that may share a region; the script identifies tumor tissue if there is a marker for it in a breast region and the contrast agent distribution for tumor tissue is used to estimate the contrast agent in the tumor interstitial fluid. To calculate the specific contrast agent concentration at each breast region, the contrast agent in the interstitial fluid must be summed for the total number of capillaries within a unit of volume. Each capillary pathway contains the amount of contrast agent that has diffused across the capillary wall for each capillary generation starting at the arteriolar end of the capillary and ending at the venular end. The script sums the concentration of the contrast agent for each generation and that number is then multiplied by the number of capillaries across the entire width of the capillary bed, shown in **equation 8**.

$$\text{mols of CA per capillary} = \left(\sum_{x}^{i=generations} CA\ mols_x \right) * \text{capillary width} \quad (eq.\ 8)$$

The calculation yields the estimated amount of contrast agent in the interstitial fluid surrounding a single capillary bed. Then, the calculation is multiplied by the capillary density to calculate the amount of contrast agent in the interstitial fluid in units of inverse volume, shown in **equation 9**.

$$\text{mols of CA per volume of tissue} = \left(\sum_{x}^{i=generations} CA\ mols_x \right) * \text{capillary width} * \text{capillary density} \quad (eq.\ 9)$$

Finally, this number is multiplied by the volume of tissue to calculate the total contrast agent in each tissue type in each different breast region. Because adipose, glandular, and tumor tissue each have different capillary densities, the contrast agent distribution for each tissue type must be calculated separately. The final calculation is to convert the contrast agent quantity into a ratio to estimate the amount of contrast agent in relation to the other elemental components present in the tissue. The final quantity of contrast agent in a region is presented as a weight ratio. This step is to make sure the format of the contrast agent distribution is compatible with the MCNP code.

5.2.3 Tumors

There are two primary types of breast cancers: invasive ductal carcinoma and invasive lobular carcinoma, each named after the region they originate in. Invasive ductal carcinoma, IDC, occurs about four times more frequently than invasive lobular carcinoma and there are several rare breast cancers that fall into this category. Invasive lobular carcinoma, ILC, on the other hand, has higher prognostics, especially when detected early, since this type of breast cancer is usually non-aggressive. A few other rare cancers can be classified as ILC special type, but most ILC cases are normal type. An important distinguishing factor between IDC and ILC, beside their location of origin, is the structure of the lesions they form. While IDC tends to form solid masses with varying shape, ILC does not; because ILC forms 'strings' and 'sheets' of cancerous cells instead of solid masses, ILC can be difficult to identify during breast imaging. This poses a great challenge that can be overcome with contrast imaging.

Given that most breast cancers are normal type IDC and ILC, these where the first breast tumors that were programmed into a Python script. The Python script is responsible for identifying regions in the breast to embed the tumor in, depending on the breast cancer type, and it was also responsible for lesion sizing, which is dependent on the cancer stage. The script is also responsible for creating lesion geometries that are representative of the breast cancer they are emulating. The user also has the option to specify a particular region in the breast they would like to embed the tumor in. For example, because IDC can appear

anywhere along the breast ducts, the user has to option to embed the tumor in the main ducts, or the secondary ducts. If the user would like to embed the lesion towards the chest wall, there are available options for that.

IDC lesions, which can be described as solid masses, can take on four different forms: irregular, spherical, segmental, or discoidal. The maximum dimension is referred to the lesion's diameter and is dependent on the lesion stage chosen. To assign a lesion shape, a probability function is used. The randomly assigned lesion geometry is used to create the lesion shape, which is described using a conjunction of ellipsoids with dimensions determined by the chosen shape. ILC lesions, on the other hand, does not form solid masses and instead forms strings and sheets of cancer cells. Because of its sporadic volume, ILC lesions must be created differently compared to IDC lesions. Instead of modeling ILC lesions as solid masses, a series of geometrical figures are combined to create the textured appearance that mimics ILC lesions. The size of the lesion is also dependent on the lesion stage with the maximum dimensions equivalent to the 'diameter' established within the boundaries of the defined lesion stage sizes. The geometries defining the lesions are converted into mesh geometries and their information is saved into a json file that can be imported into the microvasculature script. The json file contains information pertaining to the lesion volume, position, size, and stage; this is information that is used to determine the extent of lesion vasculature.

Any lesions that are created are imported into the script that manipulates the geometry to ensure there is no overlap. The lesion geometry takes priority over the other tissues that may be present, therefore, any tissue that is in the vicinity of the lesion tumor will be displaced by the tumor mesh. Because embedding a lesion is an optional argument in the scripting process, the final Abaqus mesh input file can be created to contain or be absent of a lesion object. If a lesion is embedded, the MCNP input file is modified to include the lesion object.

5.3 File Automation

The breast phantoms are created to incorporate data variability and are meant to allow the user to explore the limitations of contrast agents by incorporating multiple variables into the geometry. To run the simulations efficiently, the script building process is automated; this reduces the errors produced during input file development due to typos and improves the synergy between the creation of the geometry and the input file. The mesh files are converted into Abaqus-compatible input files with a script that accounts for the different mesh components present. A different script automates the MCNP input file building; it requires a few user-specified details, such as the detector resolution and beam voltage, but the script lines are carefully written by Python.

It's critical that the mesh files be in an Abaqus-compatible format; this is the only unstructured mesh format that MCNP accepts, beside 'mcnpum.' After the glandular components are created with the main script, there is minor overlap between the Cooper ligaments and the glandular tissue. Further, the adipose tissue is first created as a solid piece that fills-in the cavity of the skin. In reality, the adipose tissue surrounds the glandular and Cooper ligament tissue; thus, the Cooper ligament and glandular volumes need to be removed from the adipose tissue and create cavities where they will be placed once the geometry is combined in the final mesh file building stage. To achieve this, the mesh geometries are 'preprocessed' before they are converted into an Abaqus file. The meshes, which include the adipose, glandular, Cooper ligament, and if applicable, the tumor tissue, are imported into a script with a Python package called *trimesh*. This package allows the user to convert meshes into numpy arrays that can easily manipulated and it provides useful information on the mesh properties, such as mesh volume, and bounding coordinates. The script takes note of important properties pertaining to each mesh in order to keep track of its position, given this information is lost once the meshes are converted into numpy arrays.

Reformatting the meshes as numpy arrays to perform edits serves several advantages. This format is computationally fast to work with because the data is stored in contiguous memory locations. Python processes data from numpy arrays parallelly, significantly improving the run time. There are also several operations that can be performed with numpy arrays, such as *numpy.pad*, that allows the user to 'pad' the array with a chosen value to reformat an array into a desired size. This is useful if the user wishes to add
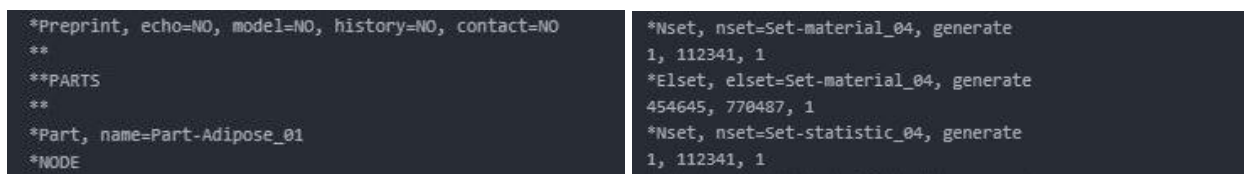
two or more arrays with different dimensions. In this script, the pad operation is used to resize the arrays to reposition the individual volumes so that they are correctly aligned within the adipose tissue, which houses all of the other breast components. The operation *numpy.where* is also used in this script to replace non-1 values that might arise after performing mathematical operations on the arrays. A few other numpy tools are used.

Mathematical operations are performed on the numpy arrays to remove overlapping parts. The tumor tissue is given priority because it is assumed that as the lesion grows, it displaces surrounding tissue. Then, glandular tissue is prioritized over Cooper ligament tissue since Cooper ligaments offer support and form around the glandular components. Therefore, the glandular array is subtracted from the Cooper ligament array to remove overlapping elements. In places where only glandular tissue lies, negative values are created; these are replaced with 0 to imply empty space in the Cooper ligament array. Adipose tissue is assumed to be where everything else is not, that is, it fills the empty space between the breast components and the skin. Thus, the adipose tissue is what remains after the other tissues are subtracted from the adipose array. After the numpy arrays are finalized, they are reconverted back into meshes with *pygalmesh*, which is a package similar to *pygmsh*, but it allows users to create meshes from numpy arrays. After the meshes are created, they are stored as .inp files with *meshio*.

Meshio will store vertex data into a file, but it will not create the header lines, nor will it create the material information that is created in a true Abaqus file. For this reason, mesh files created with *meshio* need to be reformatted into a true Abaqus format to be compatible with MCNP. Up to this point, the different meshes are stored in separate mesh files because they are each comprised of different materials and *pygmsh* nor *meshio* can create meshes with distinguishable components. However, Abaqus files will contain different parts with distinguishable features that can each be individually assigned material properties. To be compatible with MCNP, the different components need to be stored in the same mesh file as separate parts. The components can be differentiated by assigning them different materials and part names. A script is instructed to generate a 'master' mesh file from the different components present; it is given a list of the different components that need to be mapped in the mesh environment. The breast

components present cannot be automatically assumed because the breast geometry will not always contain a lesion and the user might want to include chest wall components. The script also needs to be provided a list of materials that correlate to the different breast components it receives and the list must contain the materials in the same order that the breast components are in. The same is true for the list of densities it must be provided. As the script interprets every input component and its associated mesh file, the script assigns header lines that give the part a name, such as 'Part-01' for the first part in the list. It's important that each component is assigned a different name or MCNP will not be able to properly distinguish the part that is associated with each material information given in the data block. The script automatically assigns part names sequentially to avoid this problem.

Mesh files created with *meshio* will often contain triangle and line elements that do not contribute to the 3D structure of the mesh; these are removed from the mesh file because MCNP requires that unstructured meshes have only one element type, such as tetrahedra in this case. This process also helps reduce the file size, since these extra elements contribute to a significant amount of memory. The remaining tetrahedra data is stored into the master mesh file. Once the mesh elements are stored into the master file, the material information along with elset and nset data lines are added into the file to mimic an Abaqus input file. An example of this strategy is demonstrated in **Figure 18** below, where header lines are included to establish the beginning of a part and elset and nset lines are added at the end of a part to establish the nodes and elements pertaining to a part.

```
*Preprint, echo=NO, model=NO, history=NO, contact=NO        *Nset, nset=Set-material_04, generate
**                                                          1, 112341, 1
**PARTS                                                     *Elset, elset=Set-material_04, generate
**                                                          454645, 770487, 1
*Part, name=Part-Adipose_01                                 *Nset, nset=Set-statistic_04, generate
*NODE                                                       1, 112341, 1
```

Figure 18: Example header lines added to the meshio *mesh files by the Python script to imitate an Abaqus-written mesh file.*

After the lines are added, the script moves onto the next item in the component list and restarts the process where all the information is stored in the same master file. When the script finishes processing all the breast

components, the Abaqus file information is stored onto a text file and is assigned a file name that can be assigned by the user or is created by the script based on the different components that were conglomerated. This file can now be embedded into an MCNP input file

The next step is to create an MCNP input file. While most of the tomosynthesis environment remains stationary, there are a few components that require user input. The x-ray source is placed on a rotating gantry that rotates from -7 to 7 degrees, thus one of the user inputs is to specify the angle of rotation between this range with 15 total options. The user is also asked to specify the energy of the beam, which should lie between the range of 21 to 40 kV. To create the compression paddle, which is placed directly on top of the breast phantom, the user needs to provide the height of the breast; this quantity is used to calculate the height of the paddle. The script also needs to know if there is a tumor embedded so that an extra cell card can be assigned to it. This also ensures that the number of cell and material cards provided by MCNP equate the number of parts and materials listed in the embedded Abaqus file. The user is also instructed to provide the name of the embedded unstructured mesh file as well as the type of embedded file. Although Abaqus mesh files are the only type of 3rd party mesh files accepted by MCNP, the user has the option to 'preprocess' the Abaqus mesh using an MCNP utility program called *um_pre_op* to convert the file into an mcnpum file type. By doing so, MCNP won't have to process the mesh file while processing the MCNP input file and convert it into a final format that is readable by the MCNP code. Because the geometry of the phantom doesn't change with source rotation, the user can save time by converting the Abaqus input file into a mcnpum file during the first simulation and then use the new file format in the proceeding 14 simulations. In the Python script, the user has the option to specify the resolution of the AmSe detector. Although a coarser mesh reduces lesion visibility, the number of histories needed to minimize the error at each pixel element decreases, resulting in a faster run time. It's up to the user to select the balance between the resolution and run time tradeoff. Finally, the user can choose the number of histories they would like to run in the simulation. Currently, 10 billion histories result in a reasonable error while maintaining the run time within a few hours for a resolution of 0.25 mm.

5.4 Sample Collection

      A full Hologic tomosynthesis scan requires image acquisition at 15 different projections. This stack of images is further processed by the Hologic software by undergoing filtered back projection. This process creates a larger stack of images through a process of interpolation that creates 'in-between' images. To replicate this process with the simulated images, a script processes the tally data output by MCNP. The raw tally data output by MCNP is located in a text file that compartmentalizes the tally data by location within a grid. Each individual tally 'bin' is accompanied by its coordinate data; therefore, the tally file must be parsed to extract useful tally information.

      The first step in the parsing process is identifying the appropriate column and row data allocated for each dimension. The Python package *pandas* is used to sort the data from the text file into a table that can be reorganized with ease. While sorting the data, the information for each bin is converted from a string format into float data. Each tally file created from the full rotation (15 total files) undergoes this process and the data for each file is stacked into an array. The end result of the parsing process is a three-dimensional array; the first and second dimensions pertain to spatial distributions along the AmSe detector while the third dimension pertains to the angle of rotation. Once the image stack is complete, the script proceeds to process the images by removing the background noise. This is done by applying Otsu thresholding with Python's *skimage* package, which is a package that focuses on providing image processing utilities. This creates a binary mask that is then applied to the original array to remove the background. Then, the background value is set to its average value.

      The stack is then processed with a different function that converts the pixel values, which are originally in units of flux per unit volume, to units of HU (Houndsfied Units), which is currently the standard unit in CT imaging. The HU of each pixel can be calculated with **equation 10.**

$$HU = 1000 * \frac{\mu - \mu_{water}}{\mu_{water} - \mu_{air}} \quad (eq.\,10)$$

In this equation, μ is the attenuation coefficient of the region of interest. The equation expects the given value to be in units of attenuation. Therefore, in the process of calculating the HU for each pixel, the attenuation at each pixel is calculated first. The attenuation coefficient for the tissue depicted in each pixel is estimated using an algorithm that calculates a raw attenuation coefficient using the expected intensity equation. Then, the distance between the source and the detector and the distance between the source and the top of the breast are considered to calculate a rough approximation of the attenuation coefficient of the breast. The algorithm that converts each pixel value into units of HU is vectorized to apply the function simultaneously to all the pixel values in a single array.

The next step is to apply a filter to reduce noise and or unwanted artifact. The Wiener filter is an excellent filter to reduce noise by reducing the mean squared error. The filter is applied to the stack using the Wiener filter image processing tool available with Python's *scipy* package. A filter size of 3 is used to avoid excessive blurring effects in the final images. After the filter is applied, the user is given the option to interpolate between the projections to generate a fuller stack. Essentially, this process interpolates between each set of pixels to estimate in-between values and the number of in-between values is also chosen by the user. The user can generate half-angle projections by interpolating once between every projection; this would generate 29 total images. The number of interpolations is unlimited but typically, a Hologic tomosynthesis scan provides about 40-60 total images. The final stack is saved as a series of text files instead of bitmap files so the data can be preserved as accurately as possible.

5.5 Data Interpretation

Metrics gathered to quantify the performance of the simulated system should be consistent with current standard metrics used in real clinical settings. Comparison of Hounsfield Units and attenuation coefficient values between the simulated breast tissue and reference values from online repositories is a good metric to quantify its performance compared to a real breast. Standard metrics used in medical imaging are the contrast to noise (CNR) and signal to noise (SNR) ratios shown in **equation 11** and **12**, respectively.

$$CNR = \frac{\text{Average signal ROI} - \text{Average background ROI}}{\text{background standard deviation}} \quad (\text{eq. } 11)$$

$$SNR = \frac{\text{Average signal ROI}}{\text{Signal standard deviation}} \quad (\text{eq. } 12)$$

The CNR is a good metric to quantify the visibility of an object amongst a background and is often used to judge the performance of a contrast agent. The SNR is a different metric that is used to evaluate the strength of the desired signal compared to the background noise.

Measuring the contrast resolution, 'C,' is similar to measuring the CNR because it quantifies the difference in signal between two regions; however, in the contrast resolution, this quantity is relative to a signal reference rather than the standard deviation, shown in **equation 13** below.

$$C = \frac{|\text{Signal}_A - \text{Signal}_B|}{\text{Signal}_{\text{reference}}} \quad (\text{eq. } 13)$$

There are no strict requirements on what the reference signal should be as long as it is indicative of the target tissue signal strength. A good reference signal to use is the expected difference between two objects in an optimized setting. That way, enhancement contributed by contrast agent in a tumor can be quantified relative to an expected value of enhancement. Finally, calculating receiver operating characteristics, or ROC, curves provide an illustrative view of a system's performance during binary classification given a varied threshold. That is, ROC curves demonstrate the relationship between the sensitivity and the false positive rate. In this application, the binary classification is whether or not a tumor is present. Therefore, the varying threshold determines whether or not a tumor is enhanced enough compared to surrounding tissue to raise a positive response.

To apply these metrics to the tomosynthesis results, the processed projection images are loaded into ImageJ. ImageJ allows users to sample specific regions in an image to acquire statistics in a region of

interest. The images shown in **Figure 19** demonstrate how ImageJ is used to acquire the average signal and the standard deviation at different locations in an image.
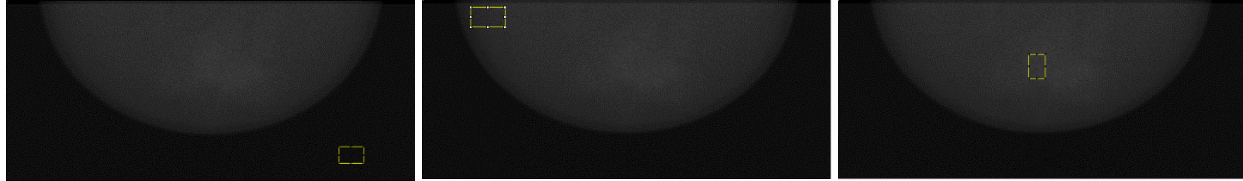
Figure 19: images demonstrating the sampling regions chosen for (a) the background, (b) the adipose tissue, and (c) the glandular tissue.

ImageJ provides a histogram of the selected region, which includes information on the standard deviation, the mean value at that region, and the maximum and minimum values. These values are used to calculate the CNR and the SNR for each set of images. The attenuation coefficients at these regions are calculated using the script that converts the tally data into Hounsfield units, since converting the flux data into units of attenuation is already part of the HU calculation process. To improve the visibility by enhancing the contrast, the window and level are adjusted using the built-in 'Window/Level' functionality in ImageJ; this allows user to adjust the visibility of the contrast gradient without affecting the pixel values. Outlier values are also removed from the images using the built in 'Remove Noise' functionality under the 'Noise' tab. This removes excessively bright or dark values that might arise in the data due to counting errors in the FMESH tally.

The performance of the phantom is evaluated by calculating the attenuation coefficients and comparing them with reference values to make sure that the radiophysics is accurately modeled by MCNP. The glandular tissue is expected to behave similarly to water while adipose tissue is slightly less attenuating than glandular tissue due to its lower density. Therefore, the attenuation curves for the glandular and adipose tissue should be similar to that of water. The attenuation coefficient at each pixel is estimated in the same function that is used to calculate the HU. Because there are multiple tissues overlapping at a single pixel point, the attenuation coefficient calculated at each value is a combination of the tissue ratios at that value.

The calculated attenuation coefficient at a location predominantly composed of adipose tissue includes about 3 mm of skin tissue, therefore, the attenuation coefficient does not reflect 100% adipose tissue. Similarly, the attenuation coefficients calculated at regions composed primarily of glandular tissue will also include attenuation contributed by adipose tissue along the vertical path of the beam.

The contrast agents are evaluated differently. The primary function of a contrast agent is to enhance an area of interest, that is, increase the visibility of an object of interest within the foreground. Therefore, the metric used to evaluate the efficacy is the CNR, since it denotes the contrast between an object of interest and its surrounding environment while also considering the effect of noise. Using the set of tomosynthesis images ranging from -7 to 7 degrees, the mean signal is collected for the lesion alongside the standard deviation of the signal. This is repeated for the surrounding tissue to calculate the CNR for each contrast agent at different conditions. The data was stored in a *Pandas* table with Python so it could be easily accessible for data analysis. The first five entries of this data structure can be seen in **Table 1**. The columns demonstrate the different variables that are considered when building a phantom. These different variables, except for the CNR, have an impact on the visibility of a lesion, and with enough data, the role that each play on lesion visibility can be quantified. The data was collected from the projection that most clearly depicted the lesion which is, uncoincidentally, the same projection with the least amount of tissue superimposition.

	Size	Glandularity	Energy (keV)	Lesion type	Lesion stage	C.A. type	CNR
0	30B	15	27	IDC	T1a	Iohexol350	2.37
1	30B	15	34	IDC	T1a	Iohexol350	1.98
2	30B	15	27	IDC	T1a	None	0.76
3	30B	15	27	IDC	T1a	IohexLipo	2.08

	Size	Glandularity	Energy (keV)	Lesion type	Lesion stage	C.A. type	CNR
4	30B	15	34	IDC	T1a	IohexLipo	1.55

Table 1: The data storage system created with Python's Pandas *package. Size, glandularity, lesion type, lesion stage, and contrast agent type are believed to impact the visibility of a lesion in a breast imaging system*

Furthermore, the data in the table is used to perform statistical analysis on the variables studied. The first variable of interest is the contrast agent, specifically, how much does each contrast agent impact lesion visibility? To answer this question, a logistic model is used to quantify the probability of an event occurring (1 or 0) given the linear combination of one or more independent variables. This model, represented by a sigmoid function, is shown in **equation 14**. Here, the $p(x)$ is the probability that the dependent variable will occur given the value of the predictor, x, while β_0 is the intercept of the linear regression equation and β_1 is the regression coefficient.

$$p(x) = \sigma(t) = \frac{1}{1 + e^{-(\beta_0 + \beta_1 x)}} \quad \text{(eq. 14)}$$

The independent variables can be presented as discrete or continuous variables. In this application, the dependent variable is whether or not a lesion can be detected; if a lesion is detected, the event is labeled as 1 and if the lesion is not detected, the event is labeled as 0. Logistic regression solely works on binary models, that is, with results that are represented by either a 1 or 0. If the results are quantified by a continuous model, such as a scale ranging from 0 to 10, then a regression analysis should be performed instead. Although the CNR is presented as a continuous variable, the CNR is used to evaluate whether or not the visibility of the lesion surpasses a given threshold. If the CNR meets the threshold criteria, the lesion is deemed visible, and the event is labeled as 1.

The threshold for the CNR should be greater than 1, since anything below 1 indicates that the standard deviation surpasses the difference in contrast and any difference in signal is hidden by the noise.

Therefore, the initial threshold is set to 1.5 where cases with a CNR surpassing this value indicate lesion visibility. Ideally, the CNR threshold should be set to 2 since a difference in signal greater than two standard deviations depicts two discernable ROIs. However, because the number of histories used is much smaller than the number of photons emitted during a real tomosynthesis scan, higher levels of noise compared to a clinical system are inevitable. With enough data, the threshold can be varied to create receiver operating curves, or ROCs, to demonstrate the diagnostic ability of this binary classifier. Because ROCs measure the relationship between the specificity and the sensitivity as the threshold varies, both lesion-included and non-lesion-included images need to be simulated with parallel variables. This requires a large data set composed of images with and without lesions that would require a long period of time to accumulate given that each simulation takes several hours to generate.

Furthermore, to compare the performance within the contrast agent variable, a Chi-Squared test is performed to evaluate the performance of each contrast agent relative to one another. This test identifies whether there is a statically significant difference between the expected outcome versus an observed outcome of a dependent variable in one or more categories within a contingency table. The test computes the chi-squared frequency distribution between expected and observed values to determine whether or not the null hypothesis is true. The distribution function in shown in **equation 15**, where x_i are the expected numbers and m_i are the observed numbers.

$$\chi^2 = \sum_{i=1}^{k} \frac{(x_i - m_i)^2}{m_i} \quad (\text{eq. } 15)$$

In this application, the frequency of lesion detection is compared among the different contrast agents to determine which contrast agents deviate from this frequency by a significant margin. This allows highly effective contrast agents to stand out among the rest of the lot.

Both of these tests can be performed to evaluate the other variables present in the data set. Logistic regression can consider multiple variables and this test can evaluate which variables play the biggest roles

in lesion visibility by ranking the contribution that each variable plays on visibility. Furthermore, the inclusion of interaction terms in the logistic regression test provides information on the effect that each class within a single variable has on the results. This is particularly useful when considering both the breast glandularity and the contrast agent used, since the efficacy of the contrast agent is likely to change with glandularity. With enough data, the relationships that each variable has with lesion visibility as well as how this relationship changes based on other factors, can be estimated.

Part 3: Results

6 Phantom Performance

The goal of this project is to develop a set of complex breast phantoms that consider the biokinetics of contrast agents so that they can be studied in a simulated setting. The phantoms are also meant to consider a wide variety of variables that can influence lesion visibility so that the limitation of each contrast agent can be studied wholistically, including breast density and size. The phantom should also include different forms of breast lesions, since these too play a role in visibility; smaller lesions are easier to obscure than large lesions and some lesions, such as infiltrating lobular carcinoma, do not form solid masses and are therefore challenging to discriminate. This following section focuses on the phantom's capability to replicate these different variables into a set of breast models that can be used to study the performance of contrast agents.

An important relationship to study is that between breast glandularity and lesion visibility, since sensitivity decreases with increased glandularity; therefore, it's critical for the phantom to be able to replicate a wide variety of breast glandularities. Currently, the Python script that is responsible for creating the breast components, including the glandular structure and the Cooper ligaments, can model breast glandularity, or breast density, ranging from 5% to 90%. As the glandularity increases, the number of components in the glandular structure are expected to increase to meet the volumetric demands of the

glandularity. To verify this, a breast sized 32A was created with 20, 40, and 60% glandularity. The images

in **Figure 20a – c** demonstrate how the glandular structure adapts to the different glandularities.

(a)   (b)   (c)

(d)   (e)   (f)

(g)   (h)   (i)
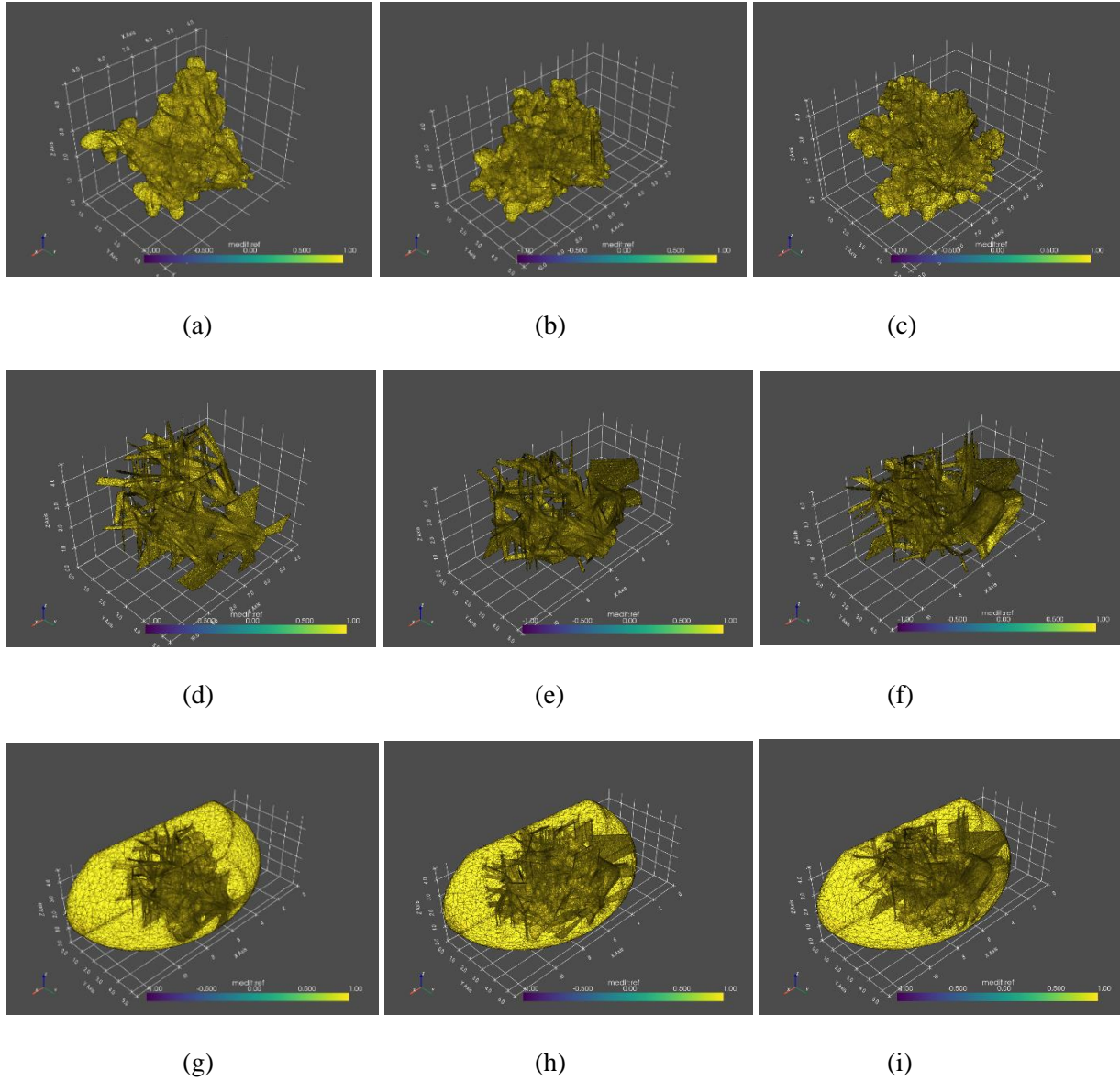
Figure 20: A set of images showcasing the meshes created in Python to replicate different components of the breast. Figures (a-c) depict the change in glandular structure with a breast glandularity of 20, 40, and 60%. Figures (d-f) depict the corresponding Cooper ligaments surrounding the glandular structures shown in (a-c), respectively. Figures (g-i) depict the adipose tissue surrounding the glandularity and Cooper ligaments shown in (a-c) and (d-f), respectively.

As the glandularity increases, the number of main ducts also increases as well as the lobular density. The Cooper ligaments also adapt to changes in glandularity, as demonstrates in **Figures 20 d – f**. In these images, the Cooper ligament structure changes to envelop the added glandular structure. The adipose tissue in **Figures 20 g – i** also changes as its volume decreases to accommodate the increase in glandular volume.

The lesion also provides variability in the model. Currently, the model considers two types of lesions, should the user decide to include a lesion into the breast model. These are infiltrating ductal and infiltrating lobular carcinoma. These two lesion types compose the majority of all breast cancers and rare forms of breast cancer are usually a subtype of one of these cancer types. Infiltrating ductal carcinoma grows in the ductal system while lobular carcinoma grows in the lobules surrounding the ducts; this difference is considered by the Python script that is responsible for modeling the breast cancer geometry. These lesions also differ in that ductal carcinoma tends to form solid masses while lobular carcinoma forms strings or sheets of lined cancer cells that don't form a solid mass.[306] The lack of structure poses a challenge in identifying the lesion during imaging scans; therefore, it is critical to distinguish the characteristics between the two lesion types in the breast models. Furthermore, ductal carcinoma exists in four main structures: spherical, segmental, discoidal, and irregular, all shown in **Figure 21** as T1c-stage lesions. The figures include views of the lesions in the x-y plane and the z-x plane, labeled as 1 or 2, respectively. The shape impacts the visibility of the lesion as some shapes blend in with the glandular structure and can be more difficult to distinguish.

(a1)   (b1)

(a2)   (b2)

0 cm   5 cm 0 cm   5 cm

(c1)   (d1)

(c2)   (d2)
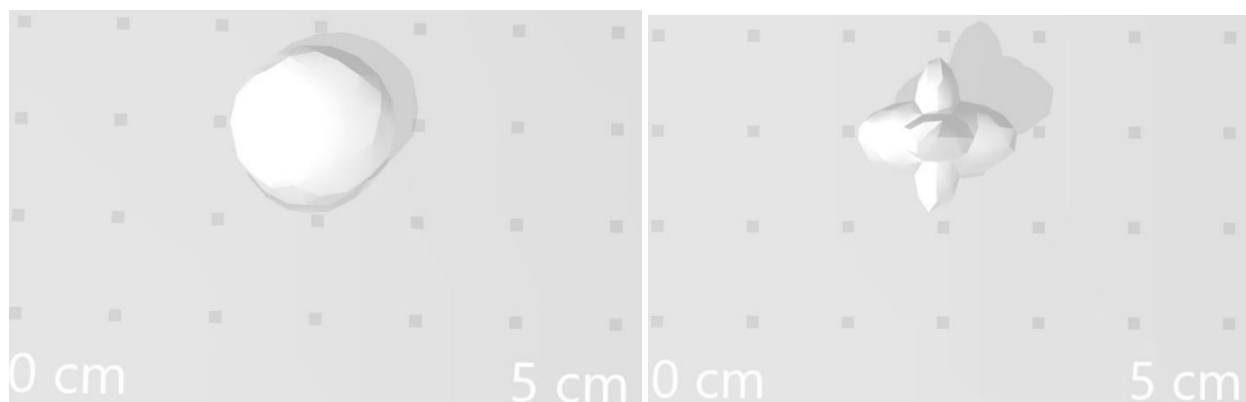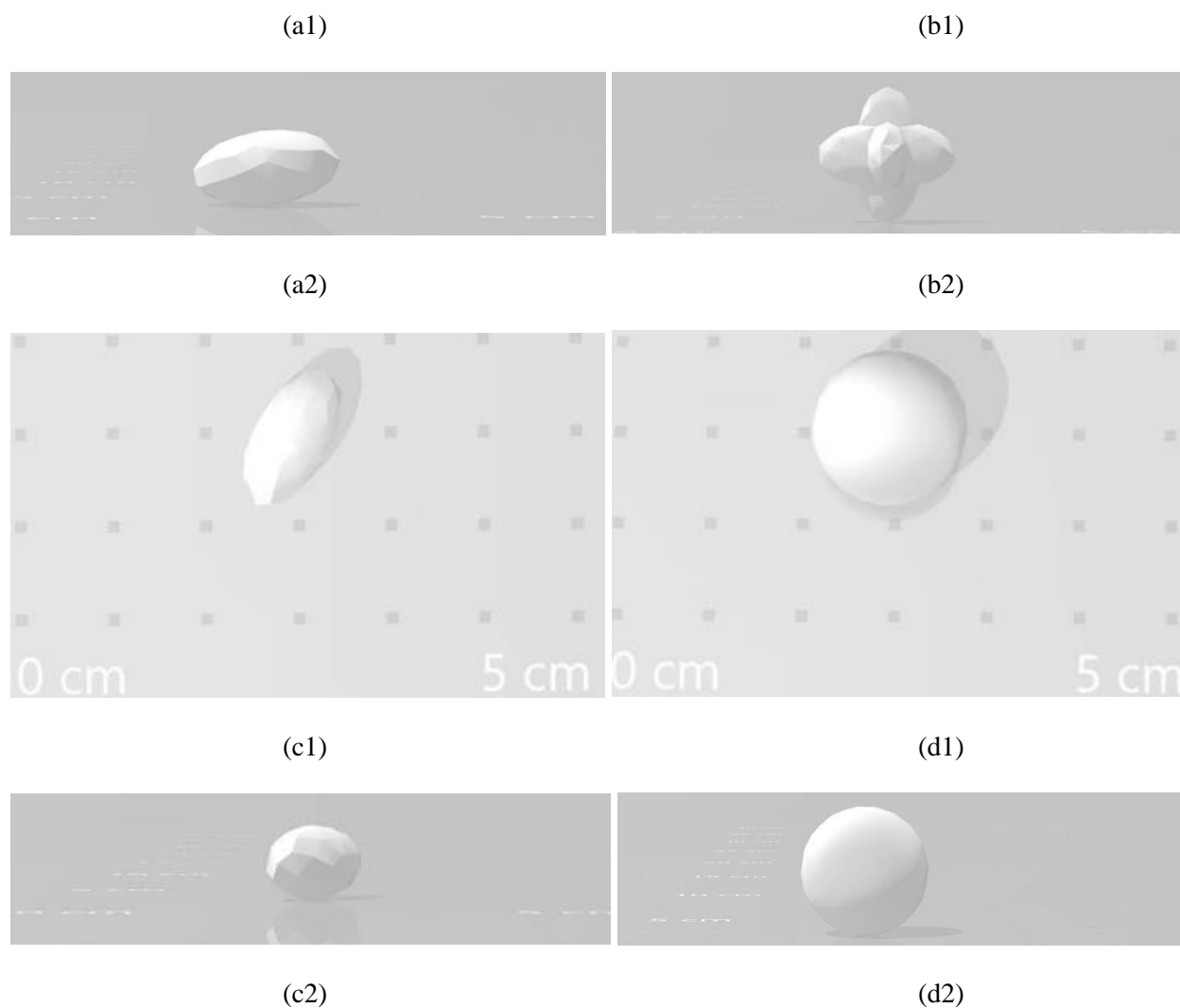
Figure 21: Images of the four geometries that can be created for infiltrating ductal carcinoma lesions with top and side views. (a) demonstrates the discoidal formation, (b) pictures irregular lesions, (c) pictures segmental lesions and (d) shows a spherical lesion.

The size of the lesion is also an important factor to consider, given that smaller lesions are more conspicuous and can be hidden with ease with or without tissue superimposition. The model considers five different stages of breast tumors, each associated with a difference size range. A T1a lesion that falls between 1 and 5 mm in its longest dimension is far more difficult to identify than a T3 lesion that is over 5 cm in size in its longest dimension. By incorporating different lesion stage options into the model, the user can explore the limitations imposed by the size of the lesion. The images shown in **Figure 22** demonstrate the difference in sizing between four different lesion sizes; the first stage, shown in **Figure 22a**, is a T1a-

stage lesion and is less than 1mm in size at its widest dimension while **Figure 22d** shows a T2-stage lesion and is between 2 to 5 cm in size at its widest dimension. All of the lesions shown in the figure pertain to a segmental type infiltrating ductal carcinoma lesion. Meanwhile, **Figure 23** pictures infiltrating lobular carcinoma at different stages, starting with stage T1a on **Figure 23a**, and ending with stage T2, as seen on **Figure 23d**. As previously stated, infiltrating lobular carcinoma doesn't quite form solid masses compared to infiltrating ductal carcinoma, thus explaining the gaps observed in the figures. As the lesion expands at the different stages, these gaps become more obvious, as shown in **Figure 23d.**

(a1)	(b1)	(c1)	(d1)

(a2)	(b2)	(c2)	(d2)
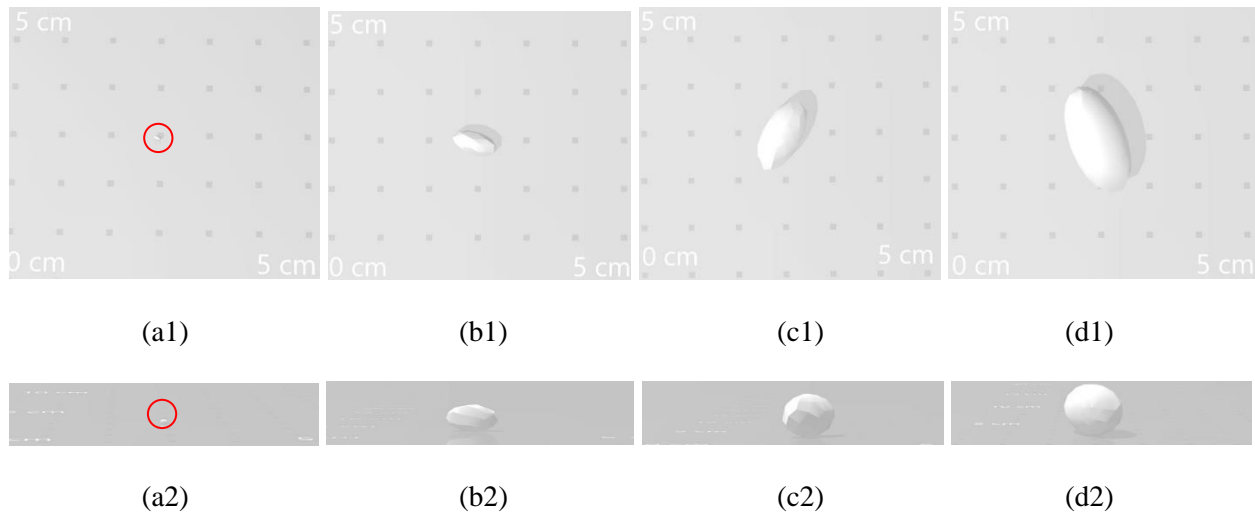
Figure 22: Images showcasing the difference in lesions size for a segmental-type infiltrating ductal carcinoma lesion between the different stages available with the tumor- creating script. Figure (a) demonstrates a T1a-stage lesion, (b) demonstrates a T1b-stage lesion, while (c) demonstrates a T1c-stage lesion, and (d) demonstrates a T2-stage lesion. The first row is a top view of the lesions while the bottom row is a side view of the same lesions.

(a)	(b)	(c)	(d)
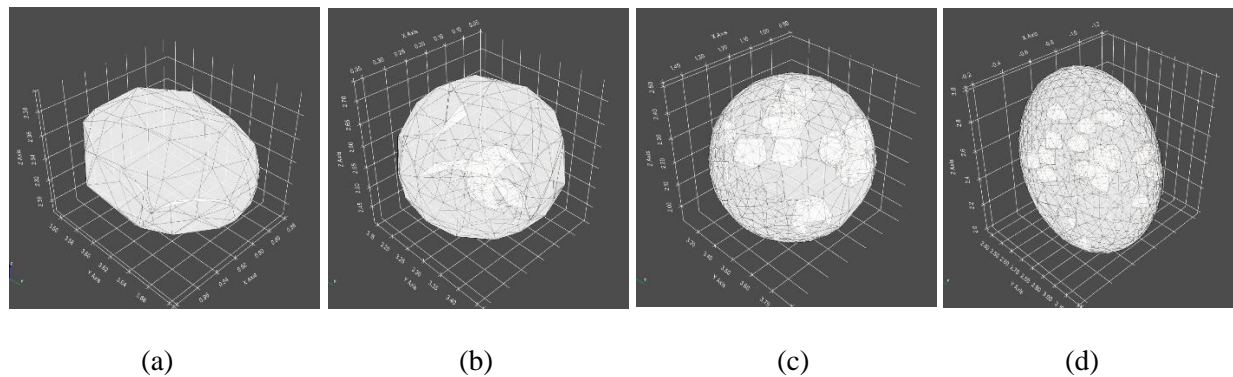
Figure 23: Images of the different stages for infiltrating ductal carcinoma. Figure (a) shows a T1a-stage lesion, (b) pictures a T1b-stage lesion, (c) pictures a T1c-stage lesion, and (d) pictures a T2-stage lesion.

Before contrast agents can be modeled with the phantom, the performance of the phantom needs to be evaluated first. The first full tomosynthesis set of images were collected for a phantom of size 32A with 15% glandularity and no embedded lesion. No contrast agent was included in the first phantom created because the attenuation coefficient values need to be verified for 'unenhanced' breast tissue to verify that the coefficient are within the range of reference values. A total of 15 meshes were collected from MCNP simulations; these were processed with an image reconstruction script and another 14 in-between slices were interpolated from the data creating a total of 29 images. These images can be observed in **Figure 24**. The images with units of Hounsfield and the images with units of attenuation coefficient were then imported into ImageJ as a set of text images.

Samples were collected for the adipose and glandular tissue as well as the background using the lasso tool in ImageJ. The mean value at each of these samples was used to estimate the Hounsfield value of the given tissue; the collected values are shown in **Table 2**. The table also contains reference values for each tissue so that the calculated values can be compared. A range is provided for the adipose and glandular tissue since these values differ across several conducted studied. There are several factors that can cause variance in the Hounsfield units, such as additional attenuation caused by external components, including the Bucky table and compression paddle, that are unaccounted for. Furthermore, the Hounsfield units for fibro glandular tissue can vary due to superimposition of adipose tissue that can lower this value. In this case, a breast with 15% glandularity is comprised primarily of adipose tissue and even in regions of high glandular content, overlapping adipose tissue is inevitable. Since adipose tissue has a lower attenuation coefficient than glandular tissue, the Hounsfield units estimated for regions of high glandular tissue are lower than expected.
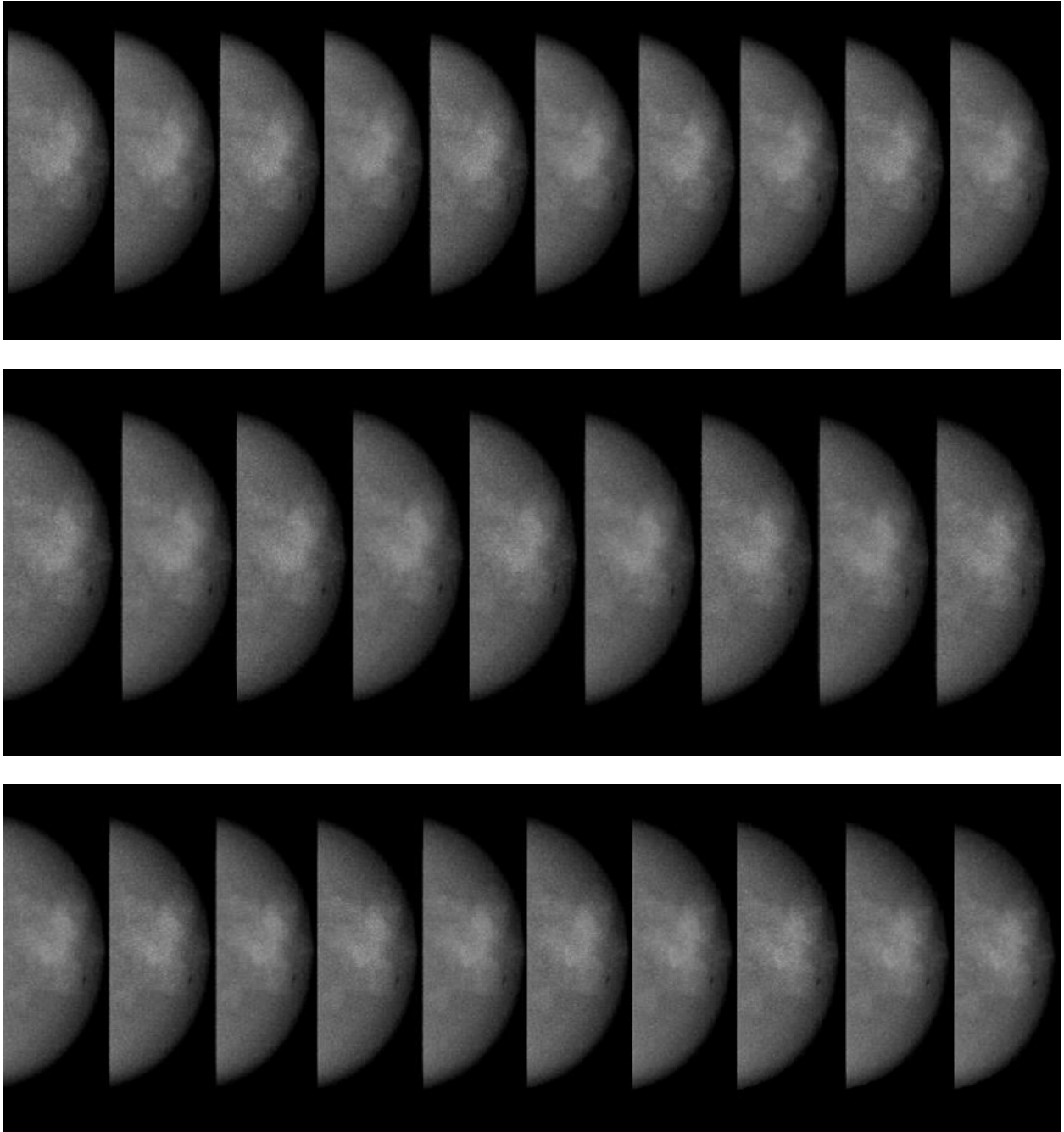
Figure 24: The first set of tomosynthesis images simulated with MCNP and processed with Python.

Region	Simulation Attenuation (HU)	Reference Attenuation (HU)
Adipose	-55	-120 to -30
Glandular	15	10 to 80

Air	-812	-1000
Iodine C.A.	28.3 HU per mgI/ml @ ~ 27 kVp	25-35 HU per mgI/ml @ ~ 100 kVp

Table 2: Comparison of the Hounsfield units calculated in the simulated images versus reference values.[307,308]

It's important to verify that the attenuating properties of the breast scale properly with beam energy. By verifying that the attenuation coefficients scale logarithmically with energy, the phantom demonstrates that it is properly simulating the behavior of real tissue. To study the attenuating properties of the breast tissues as a function of energy, linear attenuation coefficients for adipose and fibroglandular tissue were gathered across multiple energies between 21 and 33 keV, shown in **Figure 25**. These values were collected from sampling the images with units of attenuation coefficient, similarly to how the Hounsfield unit data was collected. The mean and standard deviation for both tissues at different energies were collected and plotted along with the attenuation of water at the same energies to compare the values. The results are shown in **Figure 26a** where the attenuation of the glandular and adipose tissue are plotted along with the attenuation of water for comparison.

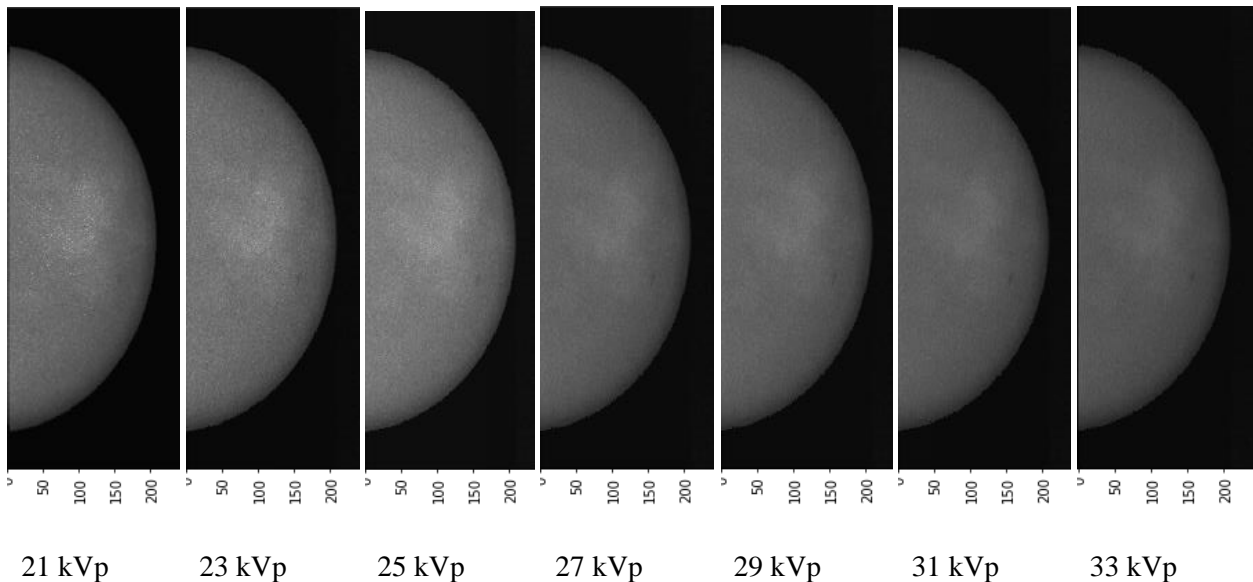21 kVp   23 kVp   25 kVp   27 kVp   29 kVp   31 kVp   33 kVp

Figure 25: Images of a 32A-sized breast with no embedded tumor at different beam energies. The pixels of each image have units of attenuation coefficient.
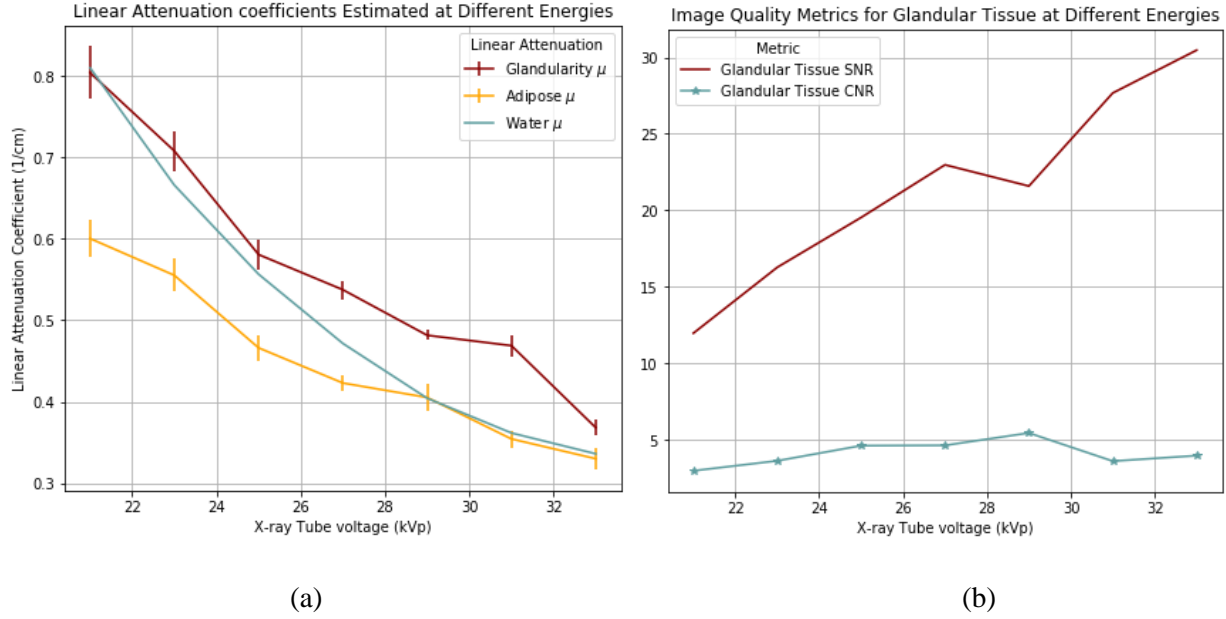
Figure 26: (a) A plot of the linear attenuation coefficients gathered for the adipose and fibroglandular tissue at different energies for comparison. (b) A plot of the SNR and CNR values at different energies where the SNR and CNR values are calculated using the Hounsfield Unit images and the fibroglandular tissue signal is compared with the adipose signal.

The attenuation coefficients are compared with that of water due to their similarity. Oftentimes, glandular, and other soft tissues are simulated with a composition of water due to their similar density. However, since glandular tissue is slightly denser than water, it is expected for its attenuation to be slightly higher than that of water. Adipose tissue is only about 0.08 g/cm^3 less dense than water, therefore, it should also have attenuating behavior similar to that of water but with coefficients slightly below those of water, which is shown in the graph in **Figure 26a**.

As previously mentioned, the CNR and the SNR are often used as image quality metrics in X-ray imaging. They allow technicians to quantify the quality of an imaging system and the extent of noise interference. These metrics can also be used to validate the behavior of the phantom by providing insight on the observable changes between contrast and noise with increasing energy. As the energy increases, the attenuation decreases. Because attenuation is proportional to interaction with matter, it is expected that the beam will interact less with the breast as the energy increases. Due to the decrease in interaction, less scattering occurs in the media which leads to less noise in the image. Additionally, as the energy increases,

the difference in attenuation between the adipose and fibroglandular tissue decreases, as seen in **Figure 26a**. Thus, differences in signal between adipose and glandular tissue become less apparent as the beam energy increases and the contrast between the two tissues decreases. The signal to noise ratio is simply the ratio between the signal strength, which is given in Hounsfield units in this application, and the noise. Hounsfield units do not vary much with changes in energy because they are calculated dependent of the attenuation relative to water and air. For this reason, the SNR is expected to increase with energy as the noise decreases due to decreasing scattering. This trend is shown in **Figure 26b**. This figure also demonstrates the relationship between the CNR and the energy, depicted by the bottom line in the graph. Both the contrast and the noise decrease with increasing energy, which explains why the ratio stays relatively similar throughout the different energies used in the simulations.

7 Contrast Agent Performance

7.1 Contrast Agent Absorption in Different Tissues

After each breast phantom is generated by a Python script, the next step is to simulate contrast distribution in the breast tissue. This capability is a critical component of the breast phantom because the purpose of the phantom is to provide a means to wholistically study contrast agents with different breast variables. There are three main tissues in the breast: tumor, glandular, and adipose tissue. Each of these vary in their vascular density and tumor tissue contains a different vascular structure and permeability than the other two tissue types. Therefore, difference in contrast agent absorption between the different tissues is expected.

The extent in the difference in contrast agent absorption between a lesion and its surrounding tissue plays a critical role in lesion visibility because a higher absorption of contrast agent in the lesion implies a higher difference in signal. On top of differences in contrast agent absorption due to differences in the vasculature between lesion and healthy tissue, the properties of contrast agent can also impact its rate of

absorption at different tissue. Furthermore, the difference in absorption in the tissue is also time dependent as some contrast agents absorb more readily than others. This also means the residence time of contrast agents varies. To observe these differences, the absorption of two different contrast agents were observed as a function of time. Iohexol350 and tantalum oxide nanoparticles, TaONPs, were compared because Iohexol350 was readily absorbed into the breast tissue while TaONPs exhibited delayed absorption. The comparison between the absorption of the two contrast agents for the three different tissues is shown in **Figure 27**. The graphs display the absorption of the contrast media in units of mgCA/cc, which quantifies the mass of the attenuating particle per unit volume of tissue; for Iodine, the units are in mgI/cc.

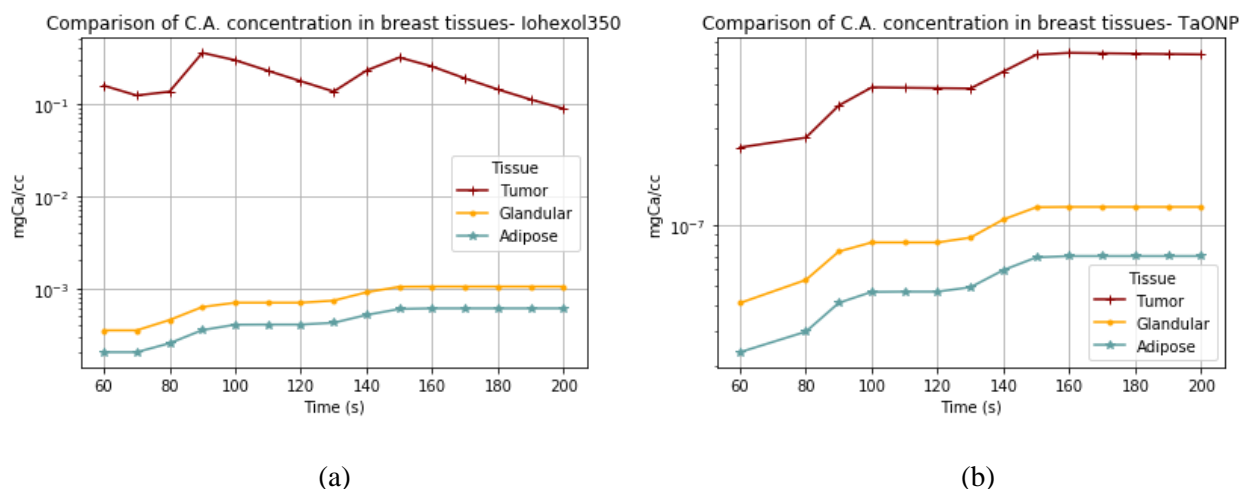(a)   (b)

Figure 27: Graphs demonstrating the relationship between absorption in the interstitial fluid at different tissues as a function of time. The graph shown in Figure (a) depicts absorption trends for Iohexol350 while the graph shown in Figure (b) depicts absorption trends for Tantalum Oxide Nanoparticles.

The absorption is calculated over time, which is provided in units of seconds starting at the time of injection, not the time post injection. The absorption quantities were gathered for a breast sized 34A with 15% glandularity and a lesion stage of T1c. The contrast agent was administered into the left arm and the injection rate was 3 ml of solution per second with a total of 60 ml of solution administered over a period of 20 second.

The ratio of contrast agent absorption in the tumor tissue relative to the amount injected is another important observation in contrast agent behavior because it demonstrates desirable distribution. If only a small portion of the injected contrast agent navigates into the desired region, then most of the solution provides no utility. This can significantly drive-up costs as more contrast solution is needed to achieve a concentration in the tumor tissue to achieve desirable signal enhancement. A comparison of the absorption concentration at the tumor tissue of the 5 different contrast agents studied as ratios of injected contrast concentration is shown n **Figure 28**. The quantities for the absorption of the contrast agent were collected for a breast of size 34A with an embedded lesion of stage T1c. The quantities were collected at a time of 140 seconds with an injection rate of 3 ml of solution per second and a total of 60 ml of solution for a total injection time of 20 second. Therefore, the quantities represent the concentration of the contrast agents in the tumor tissue 120 seconds after injection of the media in the left arm. While the graph only depicts the concentration at a single time stamp, it is important to note that time after injection has great impact on the distribution of the contrast agent in the tissue, as seen in **Figure 27**. Thus, the bar graph is very likely to appear differently at different time stamps.
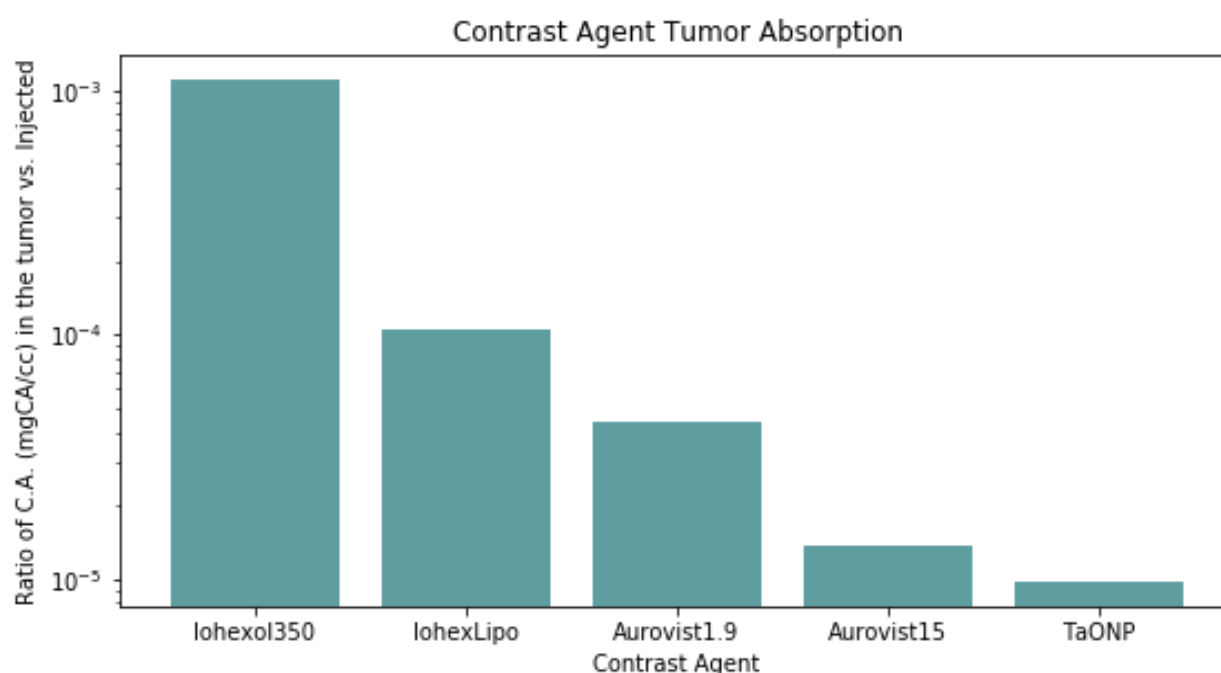
Figure 28: A bar graph demonstrating the difference in contrast agent absorption for the different contrast agents relative to the contrast agent concentration injected.

7.2 Contrast Agent Impact on Lesion Visibility

The purpose of using contrast media in imaging is to accentuate a region of interest, such as lesions in this application; hence it's important to evaluate the performance of the contrast media relative to enhanced signal. As mentioned in the **Materials and Methods** section, the signal in CT imaging is quantified in Hounsfield Units, which are derived from estimated attenuation coefficients at each pixel. Incorporating a highly attenuating material into a tissue should results in an overall increase in the effective attenuation of that tissue which should result in an increase in the Hounsfield Units in the region of interest. To gather performance data of the different contrast agent studied, average Hounsfield Units were acquired for the lesion and its surrounding tissue along with the associated standard deviation using ImageJ. This was repeated for all of the samples available, which ranged in lesion stage, breast size, and contrast agent used.

Sample images collected from ImageJ are shown in **Figures 29** and **30** where embedded infiltrating ductal carcinoma lesions are included into the breast geometry. The images in **Figure 29** depict a breast sized 30B with 15% glandularity. The lesion embedded in the geometry is of spherical shape and is a stage T1c lesion with a volume of about 1.5 cm^3. The lesion is located in the "front" part of the secondary ducts where the lesion is less likely to be surrounded and obscured by the breast lobules. The first image, **Figure 29a**, no contrast is included in the vasculature, and the figure was obtained with a 27 kVp beam. The next image demonstrates the same breast geometry but with an aggregated TaONP contrast solution and a 22 kVp energy beam. The geometry was captured at several projections, but the figure depicts the breast geometry at a projection angle of -5 degrees. The image on the right pictures the same conditions as the figure in **Figure 29b**, but with a projection angle of 5 degrees. The figures were all captured with a detector resolution of 0.5mm.

The next set of images, shown in **Figure 30**, picture a breast sized 34A, which has a larger volume than the 30B-sized breast and the glandularity is still 15%, but because the breast is larger, there is more glandular volume in this breast geometry. Similarly to the images shown in **Figure 29**, the images include an embedded lesion of stage T1c; however, the lesion is segmental and has a volume of 0.46 cm^3.

(a)   (b)   (c)
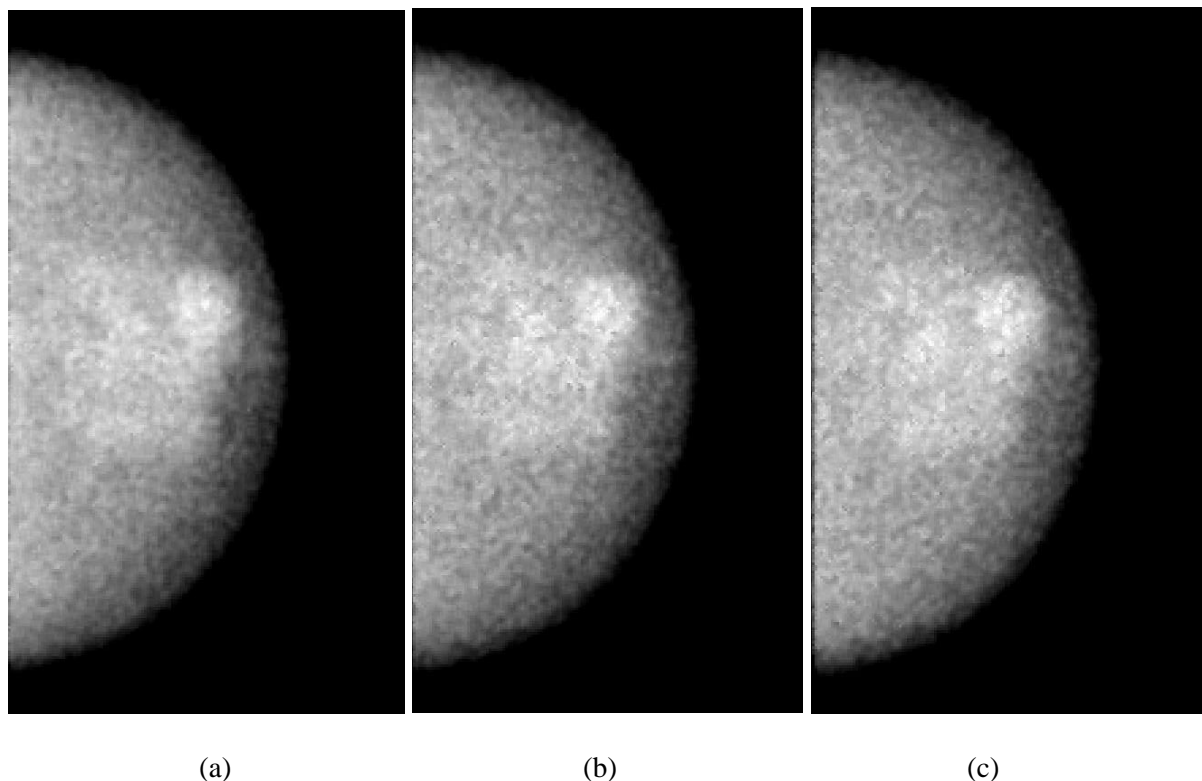
Figure 29: A spherical T1c-stage lesion with (a) no contrast, (b) TaONP contrast solution at -5 degrees, and (c) TaONP contrast solution at 5 degrees.

The images in **Figure 30** also demonstrate the geometry with no contrast solution included, **a**, TaONP contrast solution included at a projection angle of -5 degrees, **b**, and contrast solution included at a projection angle of 5 degrees, **c**. The lesions are outlined by a red oval because they are more obscure in appearance compared to those shown in **Figure 29**. The figures were also acquired with a detector resolution of 0.5mm and the energies of the beam are the same as those used in **Figure 29**.

(a)   (b)   (c)
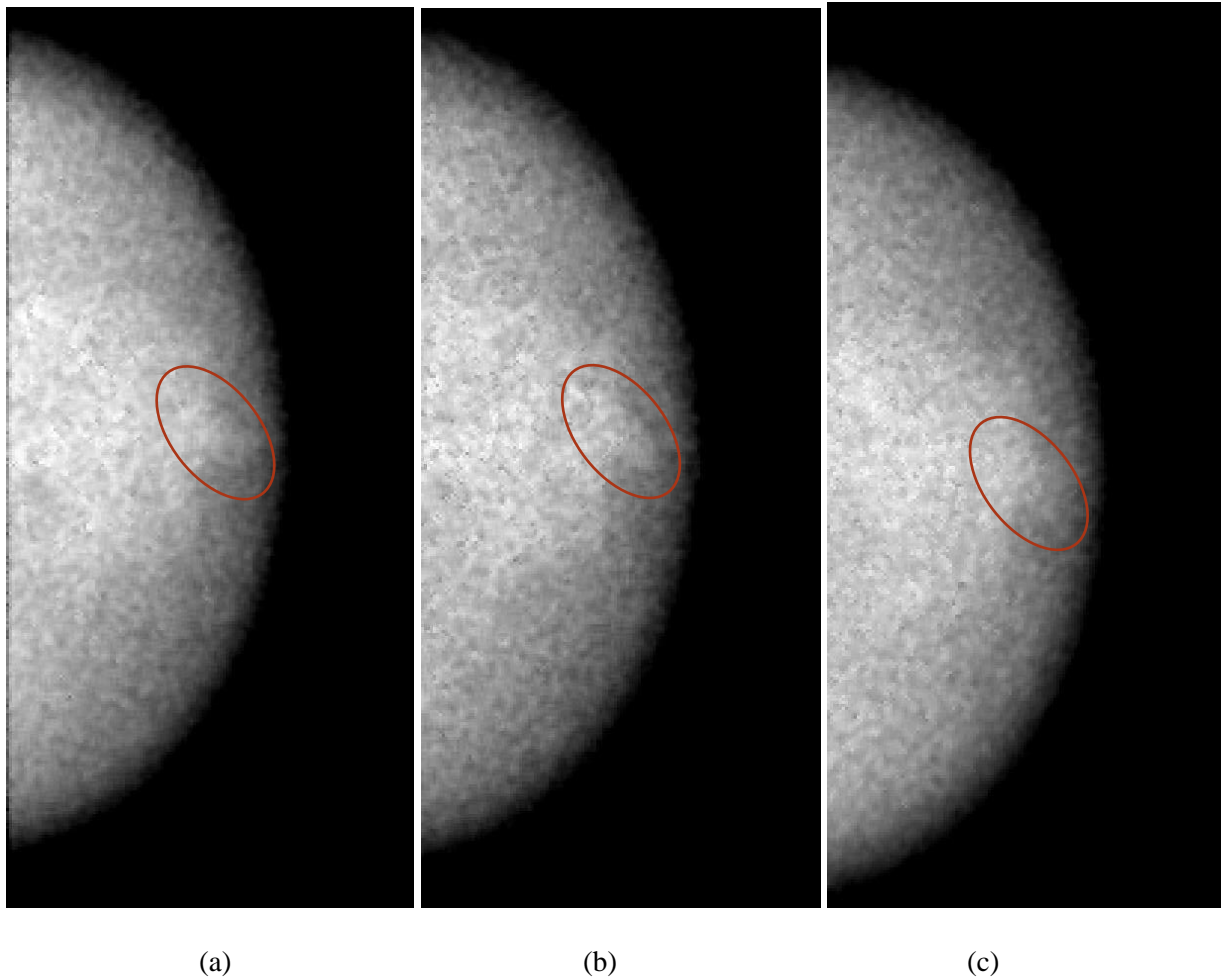
Figure 30: images demonstrating an embedded segmental T1c-staged lesion with (a) no contrast solution, (b) TaONP contrast solution at -5 degrees, and (c) TaONP contrast solution at 5 degrees.

The attenuation coefficient is dependent on the atomic number, density, and the energy of the incident beam. Heavy metals are expected to attenuate more than organic materials and explains why gold nanoparticles are currently proposed as a potential contrast agent over Iodine. Hence, it is expected for metallic contrast agents to attenuate more than non-metallic contrast agents at the same concentrations. To verify this, the average Hounsfield signal difference between the lesion tissue and the surrounding tissue was quantified as a ratio relative to contrast agent concentration at the lesion. The concentration was measured in units of mgCa per cubic centimeter of tissue. The results of this method are shown in **Figure 31** where the five different contrast agents are compared to one another. The bar graph demonstrates the relative impact that each contrast agent has on the signal. It solely considers the absorption of the contrast

media at the region of the interest and excludes the difference in concentration between the lesion and the surrounding tissue.
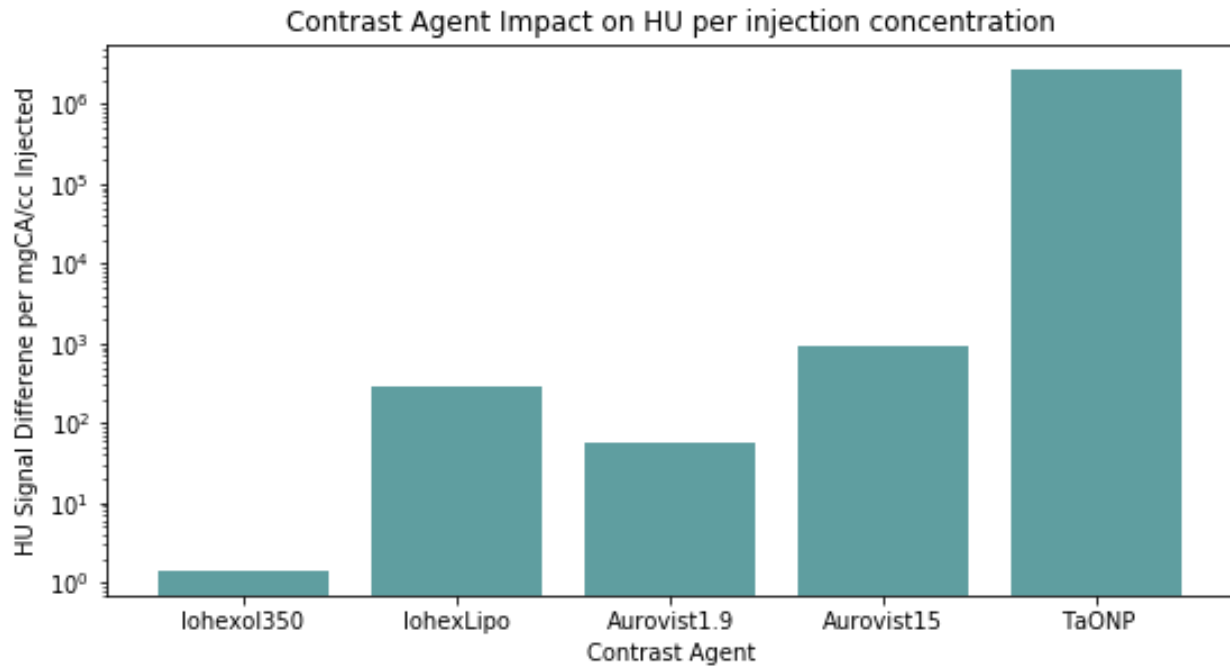

Figure 31: A bar graph comparing the difference in signal relative to the concentration of the contrast media in the tumor tissue for the different contrast agents studied.

In a clinical setting, a trained radiologists evaluates the presence of a lesion. A lesion is more likely to be visible if it has a high contrast to noise ratio relative to the surrounding tissue and as the glandularity increases, the contrast between the lesion and the surrounding tissue decreases and the lesion becomes difficult to detect. To combat this, contrast agents can increase the contrast between the lesion; therefore, a valuable contrast agent is one that increases the contrast to noise ratio in a lesion to improve its detectability. As an objective way to measure the 'visibility' of lesions as a function of contrast agent type, a CNR threshold was established, as described in the **Materials and Methods** section. The threshold was set to 1.5 because the difference in signal needs to be higher than the standard deviation to create two discernable peaks in the signal while also considering that the simulated system is a bit noisier than the clinical system

due to the lack of collimation and decrease in photon 'events.' This threshold is used to create the binary system that is discussed in the statistical analysis portion of this paper.

The difference in signal between the lesion and the surrounding tissue was divided by the standard deviation of the lesion to calculate the CNR for each case studied. The cases were separated by contrast agent type to study differences in the CNR between them. The results of this technique are shown in **Figure 32** where five contrast agents and cases with no contrast agents are compared. The graph also displays differences in the lesion stage, since there is an obvious relationship between lesion stage and lesion visibility, discussed further in *section 7.3*. The relationship between lesion stage, contrast agent type, and CNR can be studied in detail with a larger data set. Each data point in the graph represents an individual case. All the cases studied so far have embedded tumors and a glandularity of 15% and a consistent injection rate of 3 ml per second with a total of 60ml of contrast media. The time is also consistent for all of the contrast agents, which is set to 140, which is equivalent to two minutes post injection. Although this timing does not maximize the contrast potential for all of the contrast agents studied here, as shown in **Figure 27b**, the timing was kept consistent to avoid introducing variables into this portion of the study. By reducing the variables, more consistent results can be acquired. The variables introduced in the data studied in this portion include the contrast agent type, lesion stage, and breast size, although only two breast sizes are used – 30B and 34A – with different volumes. Furthermore, the energy of the beam also varies but this is not considered a variable because the energy of the beam was chosen to optimize the results of each individual contrast agent as well the breast volume.
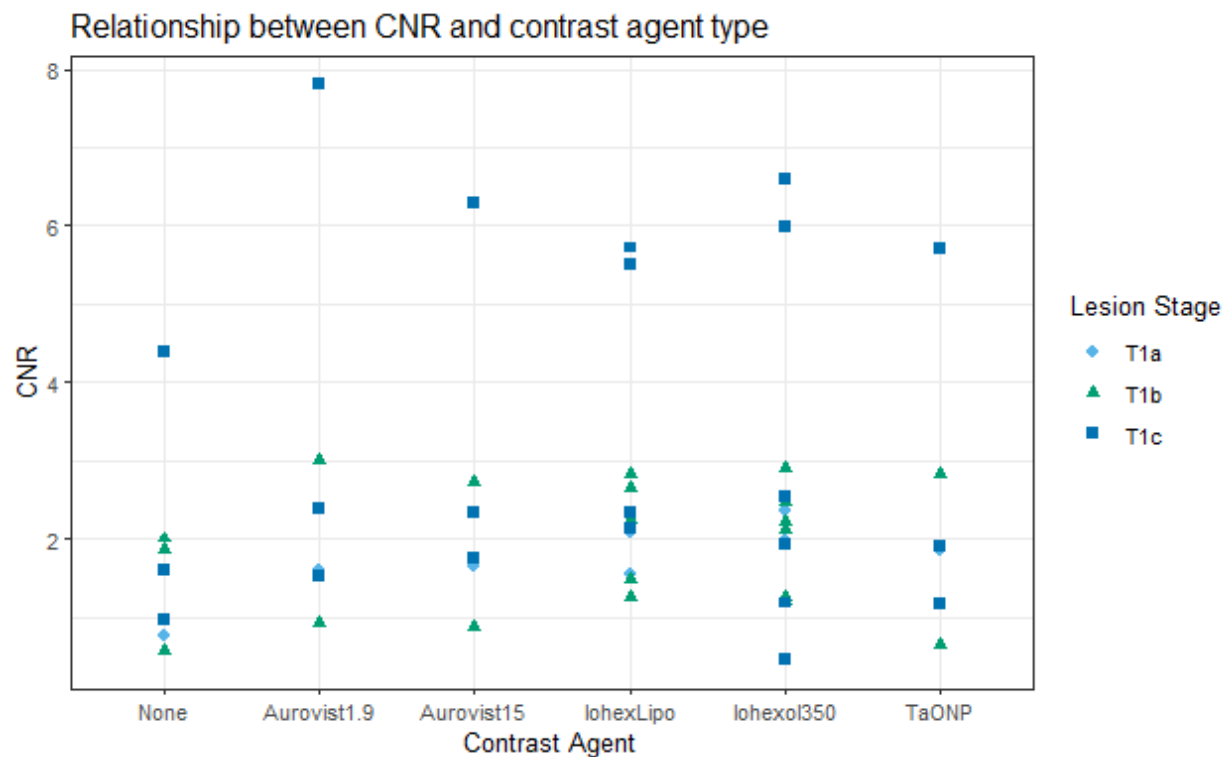
Figure 32: A graph demonstrating the relationship between contrast agent, CNR, and lesion stage.

7.3 Effect of Different Variables on Lesion Visibility

The small sample size prohibits an extensive view of the relationships between the different variables available with the breast phantoms. While the sample size is too small to analyze all the variables included in the breast phantom, the lesion stage was one of the few variables included in the data and can be analyzed in more detail. The data displayed on **Figure 32** implies a relationship between CNR and lesion stage; this is expected since lesions are more difficult to detect when they are small due to tissue imposition that can easily obscure small geometries. To explore this trend, the CNR was plotted as a function of lesion stage, as shown in **Figure 33**. This graph pictures the same data displayed in **Figure 32** but arranged differently so that the CNR in relation to lesion stage can be analyzed while still considering the role of the contrast agent used. The amount of data used to create the graphic is limited, but the difference in the CNR for each lesion stage is still obvious.
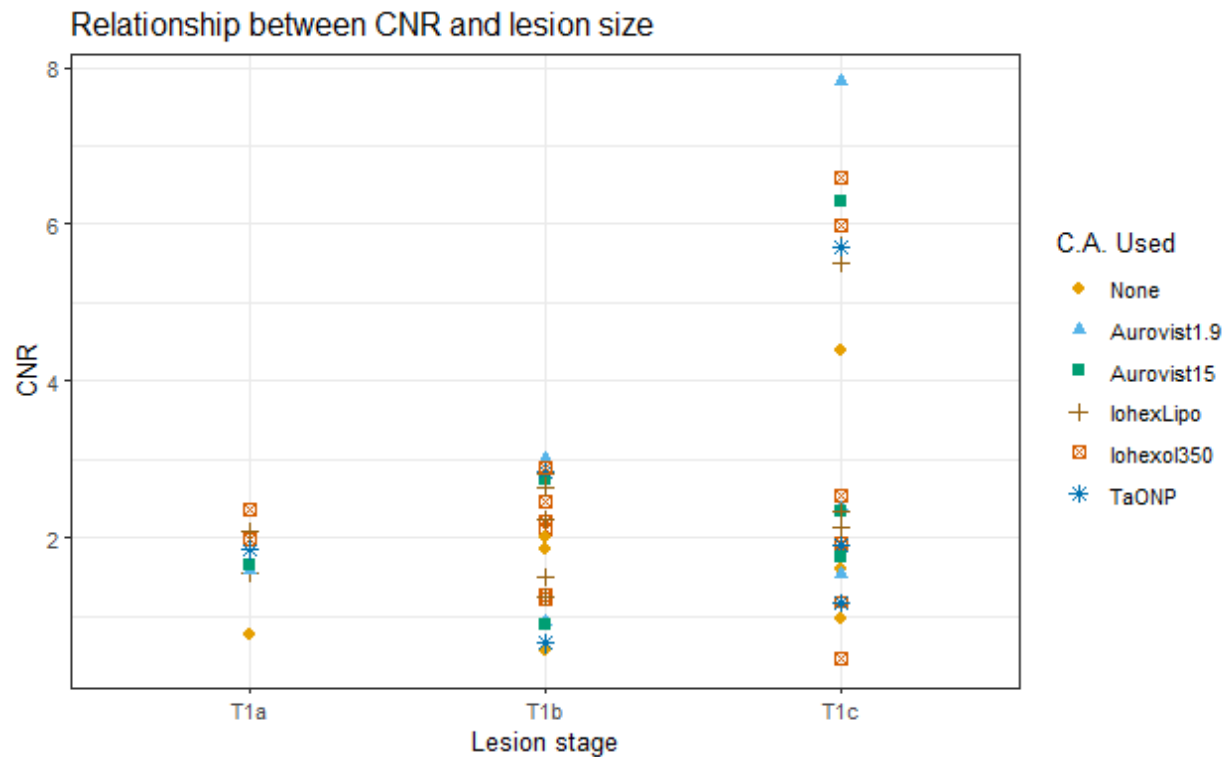
Figure 33: A graph created with RStudio demonstrating the relationship between the CNR and the lesion stage while also showcasing the contrast agent used at each data point.

There are other factors pertaining to lesion characteristics that contribute to lesion visibility outside of lesion stage. The lesion shape and type can contribute to visibility; hence it is critical to incorporate these characteristics into the phantom. While the lesion stage appears to be a determining factor in lesion visibility, lesion volume is more considerate of the impact that shape plays on visibility. For example, the lesion geometries shown in **Figures 29** and **30** are both stage T1c lesions; however, the segmented structure of the second lesions reduces its volume and its volume only measures about a third of the first lesion depicted. As a result, the CNR for the segmented lesion is much lower and is only deemed "visible" in a couple of cases. A more comprehensive view of the CNR relationship with lesion size is shown in **Figure 32** where the CNR is plotted in relation to the lesion volume. The graph highlights the lesions that pertain to each breast size and glandularity used, which also play a role in lesion visibility. The black horizontal line that strikes through the plot demonstrated the "visibility" threshold established for the binary data

collection. By plotting the lesion size and CNR this way, the categorical variable is replaced by a continuous variable that can be used to formulate an exact relationship with the CNR.
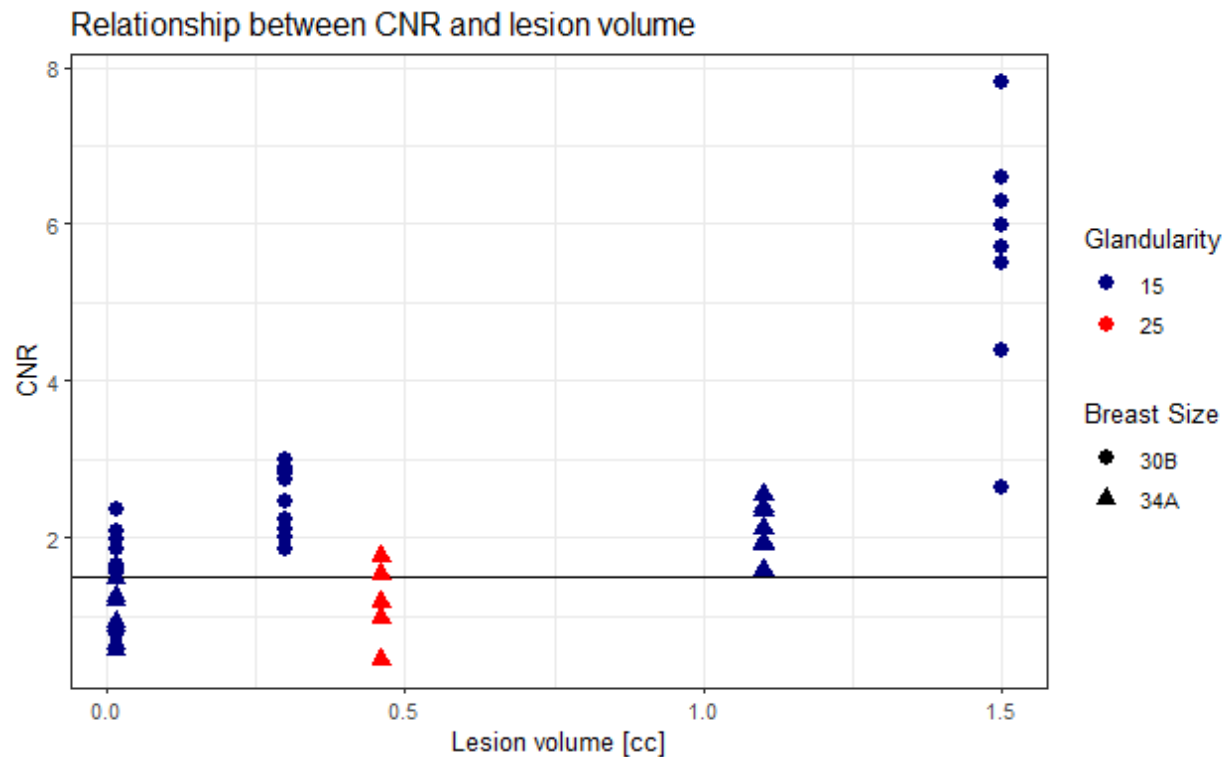

Figure 34: A graph demonstrating the relationship between the CNR and the lesion volume alongside the glandularity and breast size.

A different graph that plots the same variables but depicts contrast agents instead of glandularity and breast size is shown in **Figure 35**. The plot it meant to demonstrate any correlation between the contrast agents and the contrast to noise ratio at different volumes to see if their performance is dependent on the volume size. With limited data, the continuity of the lesion volume isn't really shown in the graph and the data points are restricted to a few locations. However, the data appears similarly to that shown in **Figure 33** but with a bit more dimension due to the fact that the lesion stage can be further analyzed into the specific volume formed with it.
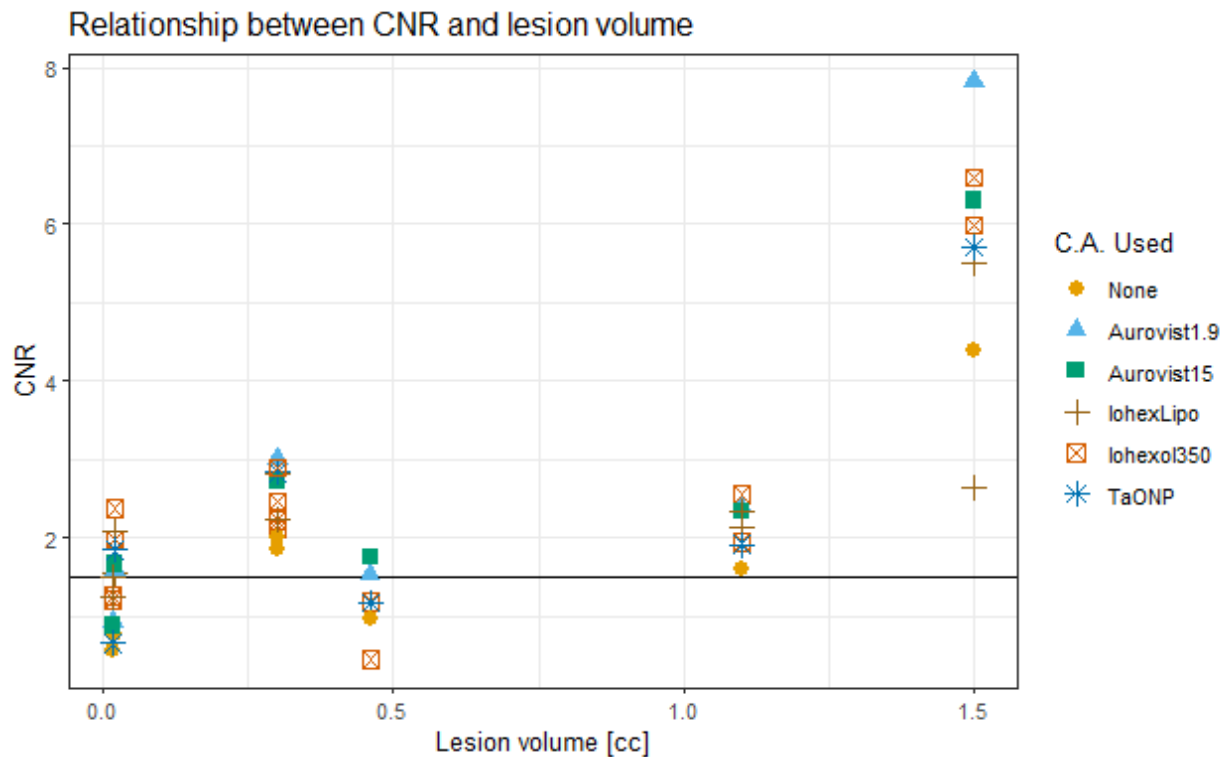
Figure 35: A graph plotting the lesion volume versus the contrast noise alongside the contrast agents used to study the impact that each contrast agent plays on lesion visibility.

7.4 Statistical Analysis

The amount of time required to run a single case, that is, a case with unique variables, exceeds several hours given that each tomosynthesis scan requires several projections to build a complete stack of images. Given this information, a small sample size is expected. Unfortunately, with a small size, it is unfeasible to closely analyze the relationship between contrast agent efficacy and multiple individual variables, such as, comprehending the decline in lesion visibility with increasing glandularity while using a particular contrast agent. Fortunately, the sample size is large enough to study the performance of each contrast agent included in the analysis in a broad sense.

The goal of exploring novel contrast agents is to identify at least one that significantly increases the contrast to noise ratio compared to others. To study the performance of the contrast agent relative to each other and to the lesion stage, as depicted in **Figure 33** and **Figure 33**, a two-way ANOVA test, or

analysis of variance test, is conducted in R to examine the difference in means between contrast agent types and the lesion stage in relation to the contrast to noise ratio; the results are shown in **Figure 36** below.

```
              Df Sum Sq Mean Sq F value  Pr(>F)
lesion_stage  2  64.10   32.05  19.278 6.3e-06 ***
c_a_type      5  13.04    2.61   1.569   0.202
Residuals    27  44.89    1.66
---
Signif. codes:  0 '***' 0.001 '**' 0.01 '*' 0.05 '.' 0.1 ' ' 1
```

Figure 36: A two-way ANOVA test conducted with R comparing two independent variables and lesion visibility. The results demonstrate the significance of the results in the last column.

This test uses an F-test to verify if the variability between the means of the groups studied exceeds the variability of the observations found within the groups. The F value is shown in **Figure 36** and is defined by **equation 16** below:

$$\text{F value} = \frac{(\text{variance of the group means})}{\text{mean of the within group variances}} \quad (\text{eq. }16)$$

A large F value indicates that the variance of the group is larger than that of the group and signifies an association between the group and the results. In addition, the p-value shown in the last column in the table indicates whether or not the results are significant, that is, whether or not the null hypothesis should be rejected. In this application, the null hypothesis is that there are no variables that affects the contrast to noise ratio while the alternative hypothesis is that there is a relationship between the variables and the contrast to noise ratio.

From the table in **Figure 36**, the F value for the lesion stage is large and indicates variation in the group means compared to the means of the whole lot. Furthermore, the p-value associated with this result is below the 0.05 significance threshold, ergo the results are significant. This means the lesion stage plays a role in CNR and consequently, the extent of lesion visibility. The test also considers the contrast agent type. Meanwhile, the F value for the contrast agent type is much smaller than that of lesion type and the p-

value exceeds 0.05; therefore, there is no indication that the contrast agent type plays a role in lesion visibility. To study this further, a one-way ANOVA was conducted on the contrast agent data alone to study solely the relationship between the contrast agent type and lesion visibility; the results are shown in **Figure 37**.

```
            Df Sum Sq Mean Sq F value Pr(>F)
c_a_type     5    6.7   1.340   0.337  0.886
Residuals   29  115.3   3.977
```

Figure 37: A table demonstrating the results of a one-way ANOVA test conducted in R. The test is conducted on contrast agent type and the contrast to noise ratio results.

The table delivers the same results as **Figure 36**; there is no indication that the contrast agent type influences the contrast to noise ratio. The F value is lower than that in the two-way ANOVA for contrast agent type; this might be due to a small perturbation in the results detected when considering the lesion stage that is not observed when the contrast agent type is analyzed by itself.

The lesion stage can be further analyzed as lesion volume to consider the impact of lesion type. When the lesion stage is replaced by lesion volume in the two-way ANOVA test that compares it against the contrast to noise ratio alongside the contrast agent type, the same, but more drastic results are found, as shown in **Figure 38**. The test shows no change in significance with the contrast agent type, which means the contrast agent type plays no influence on the contrast to noise ratio results, and it also shows that the lesion size plays a significant role in the contrast to noise ratio and in turn, visibility.

```
            Df Sum Sq Mean Sq F value    Pr(>F)
c_a_type     5   5.59    1.12   0.805    0.552
lvol         1  78.99   78.99  56.929 2.11e-09 ***
Residuals   43  59.67    1.39
---
Signif. codes:  0 '***' 0.001 '**' 0.01 '*' 0.05 '.' 0.1 ' ' 1
```

Figure 38: A table demonstrating the results of a two-way ANOVA test conducted in R. The test compares the two variables, contrast agent type and lesion volume, to the contrast to noise ratio.

The p-value is lower than that for the lesion stage which implies a more drastic significance for the lesion volume variable.

While the contrast to noise ratio is seemingly unaffected by the contrast agent type, the data displayed by **Figure 31** indicates that there might still be a relationship between the contrast agent type and the level of enhancement per unit contrast agent. To test this theory, another two-way ANOVA test was conducted for both the contrast agent type and the lesion stage while testing for the log of the difference in contrast between the lesion and surrounding tissue per mg of contrast agent per cubic cm of tissue. Essentially, the test is seeing if there is an associated between the lesion stage, contrast agent type, and the extent of enhancement per unit contrast in the tissue. The noise is not accounted for. The log of the extent of enhancement per unit contrast agent in the tissue is used to analyze the data because the concentration of the contrast agents in the tissue varies vastly; this is also reflected by the fact that the graph shown in **Figure 31** uses a log-scale in the y-axis. The concentration of Iohexol350 is several orders of magnitude greater than the tantalum oxide nanoparticles, hence the data is moved to a log scale. The results of this two-way ANOVA test are shown in **Figure 39**. In this test, both the lesion stage and the contrast agent type are accounted for as the test finds an associated between those two variables and the extent of enhancement per unit contrast agent in the tissue. Interestingly, the F value for both the lesion stage and the contrast agent type is elevated with a higher elevation observed for the contrast agent type.

```
              Df Sum Sq Mean Sq F value  Pr(>F)
lesion_stage   2  21.46   10.73   7.897 0.00245 **
c_a_type       4 232.24   58.06  42.738 2.5e-10 ***
Residuals     23  31.25    1.36
---
Signif. codes:  0 '***' 0.001 '**' 0.01 '*' 0.05 '.' 0.1 ' ' 1
```

Figure 39: A two-way ANOVA test comparing two independent variables with the log of the HU enhancement per unit contrast agent concentration in the tissue.

The p-value for both variables is below 0.05; hence the results are deemed significant. This means that both variables studied influence the extent of enhancement in the signal per unit of contrast agent concentration

in the lesion. The graphs pictured in **Figure 40** also demonstrate a clear relationship between both the contrast agent type and the lesion stage and the extent of enhancement that each contrast agent provides. The graph shown in **Figure 40b** displays similar data to the bar graph shown in **Figure 31**; the difference is that the former displays the distribution of the data in relation to the lesion stage.

(a)   (b)
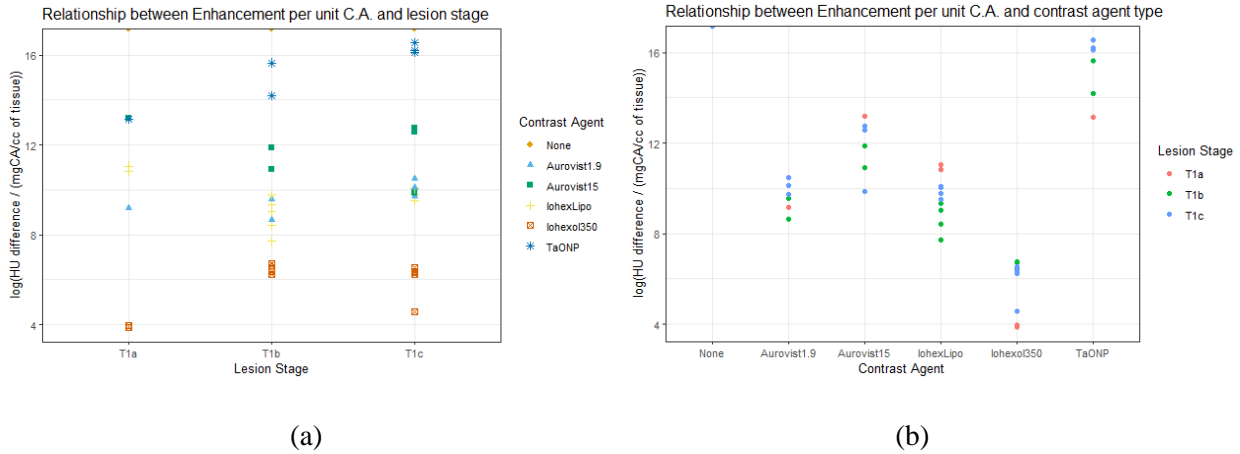
Figure 40: graphs demonstrating the impact that (a) lesion stage and (a) contrast agent type have on the extent of enhancement in the lesion per unit contrast agent.

As mentioned, the CNR threshold of 1.5 is used to create a binary system that classifies lesions as visible or not visible. Each case that was studied in this project underwent this classification system to extract a trend between the visibility of a lesion and the contrast agent used. The binary data collected was used to run a logistic regression model on both the contrast agent type and the lesion stage. The results of this logistic regression model collected from R for data pertaining to a breast sized 30B are shown in **Figure 41**. The results shown in the table indicate that there are no discernable contrast agents that affect the lesion visibility. The p-value is below the significance threshold for all the factors analyzed indicating that the performance in terms of lesion visibility is the same throughout all the contrast agent studies and the lesion types. In this model, the variables are tested around the 'None' type data, that is, data collected from cases where no contrast agent was used. The model was also offset by '1' to eliminate the use of one of the factors, such as the T1a, as the 'y-intercept' of the model. This was to gather the significance of the different

cases without excluding a data type. With more data, a more exact model can be created and perhaps some

significant results might be observed.

```
Call:
glm(formula = detect_flg ~ lesion_stage + c_a_type - 1, family = binomial(),
    data = df)

Deviance Residuals:
    Min       1Q   Median       3Q      Max
-1.7034  -0.5155   0.4776   0.7308   1.3312

Coefficients:
                    Estimate Std. Error z value Pr(>|z|)
lesion_stageT1a       1.1700     1.4165   0.826    0.409
lesion_stageT1b      -0.3545     1.0759  -0.330    0.742
lesion_stageT1c      18.0213  2880.4484   0.006    0.995
c_a_typeAurovist1.9   0.6381     1.6547   0.386    0.700
c_a_typeAurovist15    0.6381     1.6547   0.386    0.700
c_a_typeIohexLipo     0.9435     1.3610   0.693    0.488
c_a_typeIohexol350    1.5383     1.3294   1.157    0.247
c_a_typeTaONP         0.6381     1.6547   0.386    0.700

(Dispersion parameter for binomial family taken to be 1)

    Null deviance: 48.520  on 35  degrees of freedom
Residual deviance: 33.329  on 27  degrees of freedom
AIC: 49.329

Number of Fisher Scoring iterations: 17
```

Figure 41: The results of the logistic regression model conducted on the binary data collected for the lesion stage and the contrast agent type from the data collected for a breast sized 30B. The binary data indicates whether or not a lesion is deemed visible or not visible. The results were gathered from R.

```
Call:
glm(formula = detect_flg ~ lesion_stage + c_a_type - 1, family = binomial(),
    data = df)

Deviance Residuals:
    Min       1Q   Median       3Q      Max
-1.8182  -0.6586   0.4914   0.8141   1.3545

Coefficients:
                    Estimate Std. Error z value Pr(>|z|)
lesion_stageT1a       1.1668     1.2915   0.903    0.366
lesion_stageT1b      -0.4073     0.8847  -0.460    0.645
lesion_stageT1c       0.7518     0.9036   0.832    0.405
c_a_typeAurovist1.9   1.3012     1.3845   0.940    0.347
c_a_typeAurovist15    1.3012     1.3845   0.940    0.347
c_a_typeIohexLipo     1.3414     1.1446   1.172    0.241
c_a_typeIohexol350    0.6886     1.0137   0.679    0.497
c_a_typeTaONP         0.3144     1.2098   0.260    0.795

(Dispersion parameter for binomial family taken to be 1)

    Null deviance: 69.315  on 50  degrees of freedom
Residual deviance: 51.635  on 42  degrees of freedom
AIC: 67.635

Number of Fisher Scoring iterations: 4
```

Figure 42: The results of the logistic regression model conducted on the binary data collected for the lesion stage and the contrast agent type from the data collected for all cases.

The results of the logistic regression model shown in **Figure 42** were gathered from all of the cases studied. The results are similar to those shown in **Figure 41** but with a lower standard error. While there is no change is significance between the contrast agent used, the lesion stage, and the visibility, the standard error decreases for the more wholistic model. This is expected because more data is included into the model and should continue to decrease with added cases. This further reinforces the conclusion that more data is needed to create a more predictive logistic regression model. More data would decrease the error and provide more reliable results.

Part 4: Discussion

8 Expectations and Outcomes

At the start of this project, there were two major goals established; the first was to build a new type of phantom that would include the recently developed unstructured mesh capability in MCNP, and the second goal was to use this new type of phantom to study contrast agents in a simulated setting. The phantom created in this project is built from rudimentary components that amalgamate to create a highly customizable phantom that can be used to study several variables that might contribute to sensitivity during breast imaging. The phantom includes vasculature-like dynamics that emulate contrast agent delivery during contrast enhanced breast imaging. These vascular dynamics include the macro and micro vasculature involved in contrast agent delivery and they can be used to study a broad range of contrast agent solutions excluding those with ligand attachments. The breast phantom and vasculature dynamics were used to study 5 different contrast solutions (and a "control" phantom) to validate the phantom and provide insight on the differences observed between the different contrast solutions studied.

The contrast agent dictionary created for this project includes more than the 5 contrast solutions studied in this project, but due to the fact that data acquisition is time consuming, only 5 contrast solutions were studied to collect enough data for each. Additionally, several factors contribute to lesion visibility

during breast imaging but only a few variables were considered during data acquisition. The data collected was then used to extract relationships observed, primarily those pertaining to the contrast to noise ratio. The data collected is displayed using data visualization and multiple ANOVA tests were conducted to obtain statistical information the data collected. The following section discusses the information gathered from the data presented.

8.1 Breast Phantom Expectations and Outcomes

An advantage to using unstructured mesh phantoms is that they provide faster run times compared to voxel phantoms. Although there was no comparison study between voxel and unstructured mesh phantoms done in conjunction with the work done in this paper, the unstructured meshes had unexpectedly long run times in MCNP, even with dozens of cores running simultaneously. Part of the reason for this is the small resolution needed to replicate breast imaging systems. A small detector resolution requires a large number of histories to keep counting statistical errors low. The other reason for long run times is the complexity of the breast models; dozens of thousands of elements are needed to create the breast geometry. For a small volumed breast, such as a 32A – sized breast, the number of histories needed to represent the Cooper ligaments alone is about 50,000. For the adipose, the number of elements needed is about less than half this quantity due to the fact that the adipose has coarse mesh regions where detail is unnecessary. In addition, Cooper ligaments make up a minuscule fraction of the total breast volume while adipose tissue comprises a much larger volume, depending on the glandularity of the breast. Furthermore, certain components of the breast model should be restructured to minimize the number of elements needed to represent them.

In addition to long MCNP run times, the unstructured mesh phantoms took several hours to generate. The lung unstructured mesh phantom created by Anderson et. al. took about 24 hours to generate from voxel data, hence long phantom generation times are expected. The generation time scaled nonlinearly with element quantity; a small breast with 15 % glandularity took about an hour to generate while a breast with 40% glandularity took about 4 hours to generate. This is due to the fact that as the glandular volume

increases, more geometries and elements are needed to complete the structure. This increases the probability of overlap in the model, and the function that removes and fixes overlap spends more time correcting these mistakes with larger volumes contrast to smaller ones.

The glandular components created by the Python script show appropriate scaling with breast density, as shown in **Figure 20 a-c**. As the density increases, the number of elements increases, and the distribution of the glandular structure expands to fill the volume of the breast. The direction biasing implemented in the system motivates the glandularity to expand towards the unoccupied volume of the breast post compression to avoid overlap with the skin boundary. The effects of this can also be observed in **Figure 20c** where the glandular volume expands upwards as the glandularity increases and the image in **Figure 20i** also demonstrates how there is no overlap between the glandular structure and the skin boundary. All breast components are kept within the skin boundary, surrounded by adipose tissue, thus providing evidence that measures implemented to prevent skin boundary crossing are functioning as they should.

There are a few issues with the Cooper ligament structure where some ligaments expand beyond the dimensions of a realistic ligament. Typically, Cooper ligaments are about 0.2 mm thick, about a few mm wide, and 1-3 cm long. While the Python script implements techniques to ensure the Cooper ligaments are created with realistic boundaries, there are a few misshapen ligaments that are not filtered out from the ligament system. The effects of this can be observed in **Figure 20 e-f** where a few ligaments exceed the typically width. As of yet, there are no observable artifacts created with such erroneous ligaments and there is no evidence that the ligaments impact the appearance of the phantom in simulated images. However, these ligaments should still be corrected to improve the validity of the model.

Beside the fundamental breast components, it is also critical for the lesions to be modeled accurately in the mesh phantom. The lesion geometry should be an accurate representation of real breast tumors because the shape can greatly impact its visibility during breast imaging. Different geometrical types of infiltrating ductal carcinomas were considered and included as a user-specified option to study the visibility of its variations. Users are also given the option to vary the size of the lesion by assigning a stage to the

lesion model. The size of the lesion is determined from a set of parameters that fall within the stage boundaries and the exact size is randomized. The lesions are also created with randomly assigned angles to rotate the lesion in a random direction. Again, this is to include randomness into the model to prevent the model from appearing predictable. The different lesion types for infiltrating ductal carcinoma are seen in **Figure 21** with the lesions assigned randomized rotations. The discoidal shape, shown in **Figure 21a**, is slightly tilted in the y-x plane and the shift can only be observed from the second image. The other lesion shapes shown in the same figure encapsulate the different possibilities that can be generated with the Python script for an IDC breast tumor.

The images shown in the following figure, **Figure 22**, depict the wide range in sizes that the lesion can be modeled with. The smallest lesion shown measures about 2 mm in size at its longest dimension, which is smaller than the average size of the lobules created for a breast of size 30B with a glandularity of 15%. From this figure, it's easy to see why early-stage lesions can be difficult to detect. The lesion, which is a T2-stage lesion, shown in **Figure 22d** on the far-right measures about 2 cm at its longest dimension and about 1 cm in the other two dimensions. Because the lesion is of the discoidal type, the smaller two dimensions reduce the overall volume of the lesion and the lesion can appear less obvious than a spherical shape lesion, where the dimension is about the same throughout and its volume exceeds that of the other lesion types for the same lesion stage.

The model is also capable of including infiltrating lobular carcinoma, which possesses different properties than IDC. To reflect these changes, the model induces 'porosity' in the geometry that reflects the lesions' inability to form solid masses. The appearance of ILC lesions at the different stages is shown in **Figure 23** where four lesion stages are shown. The lesions are also modeled with randomness, such as a randomized rotation and elongated dimensions, but the ILC lesions included in the model do not contain as much variation as the IDC lesions. The figures demonstrate how the 'porosity' changes with lesion stage with the effects becoming more obvious at later stages. To induce the same level of detail on the smaller lesions, the element size would have to be decreased. A miniscule element resolution might not be compatible with the rest of the geometry of the breast, and it might also increase the run time of the mesh

creation while not contributing to a significant difference in the imaging results. Hence, it is not worthwhile to reduce the element size in the ILC lesions. While the ILC mesh geometries shown in **Figure 23** are not represented by 'sheets' or 'lines' of tumor cells, the structure used in lieu of creating infinitely small element sizes to replicate these 'sheets' still introduces the barrier in ILC imaging that creates challenges in lesion identification during clinical breast imaging.

Once all the components of the breast were conglomerated into the final breast phantom, tomosynthesis trials were conducted with a total of 15 images acquired for each breast. The 'signal' processing imitated with Python creates a collection of images that seeks to replicate clinical results; however, there are certain algorithms missing from this process that would adequately process the mages, such as the MLEM algorithm. Despite this discrepancy between the simulated results and clinical results, the projections show in **Figure 24** demonstrate the phantom is performing adequately. The Python script interpolates between the projection images to create a fuller stack. The phantom used to create the set of images does not include an embedded lesion nor does it include contrast solution; the phantom was created as a baseline to establish expectations of the imaging results. The images depict the glandularity among the adipose tissue and areas with high glandular content are depicted as lighter colored areas. Visually, the phantom is performing adequately, and the randomness of the glandular structure prevents the formation of predictable patterns that are indicative of a false breast.

The Hounsfield unit measurements available in **Table 1** prove that the MCNP simulations are running as expected. The beam physics are replicated within a clinical standard to produce attenuation results that closely resemble those of a real setting. The measured attenuation of the air is not -1000 HU because there are objects that lie between the beam and the detector panel that contribute to added attenuation. The bucky table and the compression paddle lie along the beam path and contribute to mild beam absorption, therefore, the pixels depicting 'air' include the attenuation of these supplementary items. In addition, because the glandularity is only 15%, the HU for the glandular tissue is on the lower end of the clinical range due to the added adipose tissue that lies in the beam path. At a higher glandularity, it is

expected for the estimated HU to increase for the glandular regions as there is less adipose tissue padding the glandular tissue.

Hounsfield units are the standard units used in computed tomography and are derived from the linear attenuation of a material relative to air and water.[309] Tomosynthesis acquires 2-dimensional data over multiple projections, hence the 3D attenuation is computed.[310] However, because tomosynthesis uses a limited angle, the attenuation can only be estimated from approximation mathematical algorithms. Furthermore, tomosynthesis does not use a standard greyscale metric similar to CT but HU were used as the standard metric in this project because of the similarity between tomosynthesis and CT and because the data produced from the simulated projection images can be compared with reference values produced from CT imaging. While the images could have been presented in units of attenuation so that the tissues could be compared with attenuation values presented in the NIST reference tables, transforming the data into HU provides some advantages.

By converting attenuation values into HU, the energy dependency is removed. Instead, the data is converted into a value that is relative to water and air that scales with energy. The contrast agents studied in this project have varying L and K edge energies, hence the beam energy differed for each case accordingly. In doing so, the attenuation values gathered from the projection mages are expected to vary because of the exponential relationship between attenuation and energy. If two cases containing Iohexol350 were conducted at 20 and 30 kVp, the case conducted at 20 kVp would yield higher attenuation values for the iodine-enhanced tissue solely due to the fact that the attenuation coefficients are all expected to be higher at 20 kVp. Therefore, by converting the measured attenuation values into Hounsfield units, the enhancement of the different contrast agents can be compared independent of energy. Instead, the performance of the contrast agents can be judged on a scale that normalizes the data for easy comparison. In addition, by converting the data into HU, the performance of the tomosynthesis can be compared with the performance of CT. In **Table 2**, the performance of iodine enhancement in this project is compared with a reference value obtained from CT imaging. The reference value is provided in units of iodine concentration and does not require any further calculations.

To better map out the distribution of attenuation as a function of energy, fitted curves were created for both the adipose and the glandular tissue. These fitted curves were compared with water because they share similar properties. The results shown in **Figure 26a** demonstrate adequate behavior between the adipose and the glandular tissue with both the curves performing similarly to that of water. The images associated with the different attenuation measurement are shown in **Figure 25** with energies ranging from 21 keV to 33 keV. The figures demonstrate how the contrast and the noise change with energy; the contrast and the noise decrease with increasing energy as the attenuation between the different tissues converge with increasing energy while the scattering decreases. These results are expected, and the curves shown in **Figure 26a** representing the associated CNR and SNR at different beam energies serve to validate the beam physics simulated with MCNP. The CNR curve is expected to stay consistent as both the contrast and the noise decrease with increasing energy while the SNR curve is expected to increase as the signal, measured in HU, remains consistent with increasing energy while the noise decreases, which causes the ratio to increase.

8.2 Contrast Agent Testing Expectations and Outcomes

A disadvantage to studying contrast enhanced tomosynthesis with the breast phantoms created in this project is that this imaging method requires several projection images. The purpose of breast tomosynthesis is to view the breast from multiple angles to avoid tissue superimposition that obscures lesions in 2D mammography. The Hologic tomosynthesis equipment acquires 15 images at 15 different angles, ergo, images of the breast phantoms were acquired at 15 different angles. This means that each different model requires several hours of run time. In the exploratory phase of contrast agent testing, it might make more sense to limit the number of projections needed to quantify the performance of each contrast agent. The initial step towards evaluating a contrast agent is to quantify its performance compared to no contrast enhancement and clinically used Iodine contrast enhancement. These initial trials would only use a couple of projection images because a boost in performance should be observable within a single image. By investigating the novel contrast agents within established parameters, its performance can be

evaluated from a first principle's perspective: is this contrast agent seemingly performing better than currently used contrast agents? Is it increasing lesion visibility within reason? Is it worthwhile to pursue clinical applications of this contrast agent?

If the novel contrast agent passes these initial checks, then it can be progressed into a stage where full tomosynthesis images are acquired. By moving it to this stage, their performance in a tomosynthesis setting can be validated: does it perform notably better in a tomosynthesis setting compared to 2D mammography? Is lesion visibility still limited by tissue superimposition in tomosynthesis despite enhancement provided by the novel contrast agent? In addition, once a novel contrast agent proves to provide utility in the initial stage, its full performance can be verified. What this means is, its performance in a variety of geometries can be evaluated. Does its efficacy significantly decrease with increasing glandularity? Does tomosynthesis ameliorate this issue? Is enhancement optimized at a certain time post injection? Does it provide much needed utility in cases with high breast density? By validating the contrast agents through different stages of testing, time allocated towards those worthwhile pursuing is optimized while minimizing allotted time towards those that do not provide utility.

Projection images were acquired for five different contrast solutions in conjunction with a "None" type baseline to compare the extent of enhancement relative to no enhancement. The images shown in **Figures 29** and **30** vary greatly from those shown in **Figure 25**. These images included embedded lesions while **Figure 25** does not include any lesions. Furthermore, because the lesions embedded in **Figures 29** and **30** are on the larger side, the resolution was coarsened to reduce run-time. These images include T1c-stage lesions, but they differ in the shape; **Figure 29** has a spherical lesion embedded into the geometry while **Figure 30** has a segmented lesion included. The difference in lesion visibility is clearly depicted when the two sets of images are compared. The spherical T1c-stage lesion is clearly visible on all images, including the case where contrast solution is omitted. Meanwhile, the segmented lesion shown in **Figure 30** is much less visible. The lesion is visible with the TaONP enhancement at a projection of -5 degrees but becomes invisible at other projections, such as at 5 degrees as depicted in **Figure 30c**. The lesion is not

visible with no contrast enhancement at any projections, and this is the case will all but two contrast agents studied.

These results are not unexpected, since the cases used to create the images in **Figure 30** contain a lesion that is about a third of the size of the lesion seen in **Figure 29**. In addition, the cases consist of a breast larger in volume than that used in **Figure 29**. The added volume increases the thickness of the breast volume and the overall attenuation observed in the model. This reduces the signal and increases the noise as a larger fraction of the beam is scattered. The added noise further reduces the lesion visibility. In a clinical setting, the beam energy is increased for larger breasts because of the increase in attenuation from the added volume; however, the energy was only differed across the different contrast agent cases to accentuate the K or L edges specific to each contrast agent. Increasing the beam energy for the larger breast phantom would have decreased the scattering but might have decreased the contrast between the different tissues. A study analyzing the role that beam energy plays for each contrast agent studied can provide insight on ways to maximize the visibility provided by each contrast solution. Furthermore, this would allow users to choose beam energies that best fit the model used.

The lowest beam energy used is 22 kVp and it's used in conjunction with cases "injected" with the TaONP contrast solution and the highest energy beam used is 34 kVp for the cases with Iodine-containing contrast solutions. It has been mentioned that the beam energy was chosen to maximize the K or L edge of each attenuating element; however, the energy of the beam affects the noise because of the relationship between energy and attenuation. Cases with TaONP and Aurovist contrast agents received beam energies of 22 and 23 kVp, respectively, and they delivered an average standard deviation of 40 HU at the lesion site. Meanwhile, Iodine-containing cases received beam energies of 27 and 34 kVp and the average standard deviation is about 35 HU at the lesion site. The graph displayed in **Figure 32** demonstrates similarity between the different contrast agents relative to contrast to noise ratio. This means that although the standard deviation is typically higher for cases with lower beam energy, the contrast between the lesion and the surrounding tissue is higher to compensate for the gap in standard deviation. It is unclear if the difference

in contrast is due to lower beam energy or better attenuating power of tantalum and gold, hence varying the beam energy for each contrast solution can provide insight on this observation.

In the statistical analysis portion of the results, the two-way ANOVA test comparing the effect of lesion stage and contrast agent type on the lesion contrast shows that the contrast to noise ratio is significantly impacted by the lesion stage, but not the contrast agent type. These results do not necessarily indicate that contrast agent type does not affect lesion visibility; they simply indicate that there is not enough evidence to reject the null hypothesis. The data used to run this test uses five types of contrast agents and the 'None' type, summing the total of number of options to six. Meanwhile, only three types of lesion stages are included (T1a, T1b, and T1c). This means there are more data points supporting the findings for the lesion stage compared to the contrast agent type. The graph shown in **Figure 33** compares CNR versus the lesion stage demonstrates the 'None' type of contrast agent as underperforming compared to the other types analyzed, given by the fact that it ranks the lowest among the other type of contrast agents plotted in the same graph for the same breast geometries. This indicates that the use of *some* contrast agent improves lesion visibility by increasing the CNR compared to the baseline; however, there is not enough data available to support this theory.

A factor that might influence the contrast agent performance in the data collected is the timing used. Iodine-based contrast agents, such as Iohexol and Iopamidol, have short retention times and display maximum enhancement at around two minutes post injection. While only one of these type of contrast agents is included in the data, Iohexol350, the rest of the contrast agents included in the data are nanoparticle based. These contrast agents are advantageous because they offer longer retention times and provide imaging flexibility and consistency. They also absorb less readily than iodine-based contrast solution because of their large size. These two facts provide evidence that the timing used in the study, 140 seconds, largely benefits Iohexol350 analysis but does not benefit the other nanoparticle-based contrast agents. At this time stamp, the nanoparticles are still accumulating in the interstitial fluid, as seen in **Figure 27** where the absorptions of Iohexol350 and TaONP are compared. If the data was acquired at a longer time stamp, the concentration of the Iohexol350 at the interstitial fluid would be significantly reduced but the

concentration of the other contrast agents would increase, which would cause a shift in the extent of contrast observed for each contrast agent. The results gathered for the contrast solutions do not highlight the full potential of most of the contrast agents used and it would be beneficial to run more cases where the timing is adjusted to maximize the amount of contrast agent in the interstitial fluid for each contrast solution analyzed.

An observation made from **Figure 33** is that the T1c cases have a broad CNR distribution. Some cases perform below the 1.5 threshold while most perform highly above it. While lesion stage is a large contributing factor to lesion volume, the volume is also affected by the lesion shape. Hence, the CNR relative to the lesion volume was plotted as shown in **Figure 34**. The graph includes insight on the breast glandularity and breast volume for each case include in the data. Only a few breast geometries were included in the data since each geometry was "reused" for each contrast agent and explains why the continuous variable appears categorical. The graph demonstrates that generally, the CNR increases with lesion volume but decreases with breast volume. This finding is supported by the two-way ANOVA test that compares the lesion volume and the contrast agent type with the contrast to noise ratio results, shown in **Figure 38**. The table shown in **Figure 38** demonstrates a significant relationship between the lesion volume and the contrast to noise ratio and it also demonstrates that the volume of the lesion might have a higher influence on the CNR compared to the lesion stage. In **Figure 34**, the third and fourth groups of data shown in the graph were extracted from cases with a larger breast volume which explains why the CNR decreases following the previous set of data. By adding dimensions to the graph, the impact that each variable has on lesion visibility can be displayed and demonstrates the complexity behind breast imaging.

The same graph is shown in **Figure 35,** but the third dimension is replaced by contrast agent type to further inspect any possible interaction between contrast agent type and lesion visibility. Because the data set is small, definite conclusions cannot be drawn from the data displayed. This is supported by the ANOVA table in **Figure 38** which shows no significant impact between contrast agent type and contrast to noise ratio. However, the graph in **Figure 35** demonstrates the Aurovist1.9 as a reliably high performing contrast agent and the "None" type as a consistently low performing contrast agent. While Aurovist15 and

Aurovist1.9 contain the same concentration of gold in their formula, Aurovist1.9 contains nanoparticles that are 1.9nm in diameter while Aurovist15 contains nanoparticles 15nm in diameter. The difference in diameter impacts the rate of absorption in the interstitial fluid; the smaller particles are more readily absorbed in the interstitial fluid while the larger particles require a longer time span to absorb. Because the cases are analyzed 2 minutes post injection, it is very likely that the time stamp is not optimized for the Aurovist15 contrast solution. This is supported by the graph shown in **Figure 27** where the contrast solution concentration in the interstitial fluid increases over time for larger particles. Again, optimizing the time stamp for each contrast solution is a worthwhile task that will expose the potential of each contrast agent studied.

So far, no data has proved a definite distinction between the performance of each contrast agent studied relative to the contrast to noise ratio. The results do, however, demonstrate that contrast agent type significantly affects the Hounsfield unit enhancement per mg of contrast agent per unit of tissue, as proven by the two-way ANOVA test shown in **Figure 39** that compares the contrast agent type and lesion type with the log of HU enhancement per unit contrast agent. The evidence shown in the bar graph displayed in **Figure 31** also demonstrates a clear difference in the enhancement observed for each contrast agent when each contrast agent is normalized as a concentration. A more detailed view of the contrast agent relationship with the extent of HU enhancement is displayed in **Figure 40b** where the contrast agent is plotted relative to the observed HU enhancement per unit contrast agent. The graph also includes the lesion stage associated with each data point to demonstrate how the extent of enhancement is also affected by the lesion stage. The results demonstrate that the contrast agents enhance the tissue differently. The contrast to noise ratio was similar enough between all the different contrast agents studied which prevented the two-way ANOVA test from identifying any outliers; however, the amount of contrast present at the lesion varied widely for all the contrast agents present. Because there is evidence showing that the level of enhancement varies per contrast agent, it is likely that adjusting the contrast agent concentration in the tissue to create uniform distribution among all the contrast agents used will result in more distinguishable differences in the contrast to noise

ratio. Again, choosing a time stamp that maximizes the concentration of each unique contrast agent in the lesion is likely to return differences in the CNR.

The results also demonstrate a significant relationship between the lesion type and the level of enhancement per unit contrast agent. This relationship can be seen in **Figure 40a** where the lesion stage is plotted relative to the log of the HU enhancement per unit contrast agent concentration. This can be explained by the decrease in tissue superimposition as the lesion grows larger. At small sizes, lesions are padded by glandular tissue that obscure the signal. At larger sizes, the lesion tissue becomes increasingly dominant and is less affected by superimposition during breast imaging. As mentioned in the **Materials and Methods** section, the Hounsfield units calculated at each pixel is proportional to the attenuation, which provides an estimate of the effective-Z of the tissue that lies along the pixel route. With a larger size, there is more tumor tissue that lies along this tissue path and the effective-Z shifts towards the properties of the tumor resulting in an attenuation that is more representative of the tumor. Because the tissue is embedded with contrast solution, a larger tumor size would permit the contrast solution to affect the attenuation of the lesion to a greater extent.

Furthermore, the results of the logistic regression model found no associations between contrast agent type, the lesion type and lesion detection. The binary classifier used in the logistic regression model compressed the contrast to noise ratios to either a 1/true or a 0/false where a 1 indicates a tumor flag and 0 indicates that there are no identifiable tumors in the image. Therefore, information on the extent of lesion visibility is lost when using this logistic regression model. There are only a few cases studied per contrast agent used and the lesions included were either highly visible, such as large T1c-staged lesions, or not visible, hence the contrast agents performed similarly in that aspect. The large T1c lesions are obvious in appearance and can even be identified without the use of any contrast agent and no T1b lesions located towards the back of the ducts with heavy amounts of tissue superimposition were visible by any means. The T1b and T1a lesions placed towards the main ducts were all visible except for a case with no added contrast solution because there are no lobules by this region that can obscure lesions. Because the data was

equally polarized across all of the contrast agents studied, there were no discernable differences among them, especially since the model does not consider differences in CNR between them.

The same logic applies to the lesion stage; almost all cases were deemed 'visible' by the binary model except for T1b lesions located towards the back of the glandularity and some smaller T1c lesions. With the small amount of data, no conclusions can be drawn for the logistic regression model. With the two-way ANOVA test, the lesion stage was identified as a significant contributor to CNR because the test found a correlation between the lesion stage and the extent of contrast. However, this model lumps all cases with a CNR higher than 1.5 as having the same performance, hence no lesion stage is markedly different from the rest. The logistic regression model does not provide much utility unless there is a large amount of data that includes a wide range of lesions at different locations and stages, since both of these factors impact the visibility. Including semi visible lesions than can easily be undetected without contrast would allow segregation among contrast agents that can aid in these situations. A gradient in performance among each contrast agent would provide the necessary information needed to run a logistic regression model that can provide definitive information on the difference among the contrast agents studied.

The logistic regression model failed to identify potential contrast agents that achieve higher lesion visibility compared to currently used iodine contrast agents. This is attributed to the lack of data and the results might change once more cases are explored, but no definite conclusions about each contrast agents' contribution to lesion visibility can be made. The first logistic regression model, shown in **Figure 41**, was created from the data solely pertaining to cases with a breast size of 30B. The second logistic regression model, shown in **Figure 42**, was created from all the data analyzed. Both models demonstrate that no contrast solution nor breast stage can definitely predict the visibility of a lesion. An observation made from the two logistic regression models is that the error decreases for the more wholistic model that includes all the data acquired. The decrease in error provides evidence that increasing the data can provide more definite results. While it is a premature assumption that including more data might uncover a highly performing contrast solution, including more data can uncover more definite relationships between visibility and each variable studied, not just for the contrast agents included in the data. The other metrics shown in the results

section provide evidence that some contrast agents perform better than others when narrowed down to attenuation capabilities. Retention times also appear to vary between the contrast agents; longer retention times can provide benefits in a clinical setting. Therefore, although the logistic regression model did not yield positive results, there is a possibility that the contrast agents studied here can differ in lesion enhancement if studied further.

The ANOVA tests conducted to study the effects of the different variables included in the data provided valuable insight on the contributions that each variable had on the collected metrics. ANOVA testing can be performed on both categorical and continuous variables and can provide metrics to weigh the quality of the results, such as the p-value which indicates the likelihood that the null hypothesis can be rejected. It is important to note that while ANOVA provides valuable information on the data, it should not be overused. This is true for all methods of comparison testing. In statistical hypothesis testing, the results are deemed significant if the evidence for supporting the null hypothesis is low. However, if multiple hypotheses are tested, such as conducting several ANOVA tests, the probability of finding evidence to reject the null hypothesis increases regardless of whether or not the null hypothesis should actually be rejected. Hence, the probability of Type 1 errors increases with each additional test conducted.[311] If the use of several hypothesis testing is necessary, a Bonferroni correction can be applied to compensate for false 'significance' in the data.

9 Future Work

9.1 Further Phantom Development

The work done on this project sets precedent to the use of customizable unstructured mesh models. The results delivered demonstrate proof-of-concept that a clinical setting can be replicated by considering the basic physics that contribute to an empirical system. Furthermore, by proving that such a setting can be built, there is evidence that this type of model can be further developed to increase accuracy and incorporate more dynamics into the system. The model thus far provides wide options for phantom glandular density

and breast size, but the lesion library can be expanded. In addition, lesion growth patterns should also be further explored to include lesions with multifocality, lesions that have expanded to the chest wall, and lesions with microcalcifications.

Currently, the model considers two types of breast cancer: general infiltrating ductal carcinoma and general infiltrating lobular carcinoma. However, there are over a dozen subtypes of breast cancer, many of which fall under the umbrella of IDC and ILC carcinoma. These subtypes vary into their growth patterns and their tendency to metastasize. These characteristics impact lesion visibility during breast imaging; therefore, it is important to model the different types of breast cancer to better understand the relationship between lesion type and probability of identifying it during breast imaging. This also allows for the exploration of contrast agents that are best suited for identifying lesions that would otherwise be difficult to identify without enhancement or with Iodine-based contrast solution.

The model should also consider benign lesions. Although benign lesions do not pose a threat to the patient, they can be incorporated into the model to study the specificity of the system. By studying the interaction between contrast agents and benign lesions, the specificity of certain contrast agents can be studied, and the likelihood of false positives can be better understood. This is important when evaluating the utility of a contrast agent; while it is important to correctly identify the presence of breast cancer, it is also important to avoid false positives, which can lead to costly and time-consuming unnecessary procedures.

The lesions can be further developed by including calcifications that often serve as tumor indicators. Breast calcifications are common artifacts observed in breast imaging, especially among older women; however, their patterns can provide indication of the presence of malignancies. This is especially true among IDC where most early-stage IDC lesions are first detected by the presence of calcifications and a total of 55% of nonpalpable breast lesions are detected by the presence of microcalcifications.[312] It is also often the case that microcalcifications are the only indication of breast cancer, especially in the early stages of development. It is also important to note that approximately 80% of microcalcifications are benign.[313] For this reason, it's critical to consider the minute details in microcalcification patterns that are associated

with malignant breast lesions, such as miniscule clusters or line formations that are often an indication of breast cancer. If these differences are not accounted for, the inclusion of microcalcifications in the breast model might increase the rate of false positives, thus reducing the specificity and accuracy of proposed imaging methods.

The model can also be improved by increasing the accuracy of the contrast agent delivery system into a more sophisticated model. Currently, the model quantifies the amount of contrast agent delivered to the tissue via capillary action. The rate of capillary diffusion depends on several factors, including media viscosity and osmolarity. The Python script that estimates the amount of contrast agent at a given tissue and specified time stamp keeps track of the contrast agent in the interstitial fluid and simulates the contrast agent entering the interstitial fluid as well as the contrast agent that exists the interstitial fluid due to changes in the concentration gradient and pressure along the capillary network. However, there is another mechanism that eliminates the contrast agent in the interstitial fluid outside of capillary action, and that is transport via the lymphatic system. Bulk flow in the capillary system is driven by pressure, which is dependent on the magnitude of both the hydrostatic and osmotic pressure. Generally, the hydrostatic pressure exceeds the osmotic pressure towards the arteriolar end of the capillary mesh while the osmotic pressure exceeds the hydrostatic pressure towards the venular end. Therefore, bulk flow is in the outward direction towards the interstitial fluid at the start of the capillary meshes and inward at the venular end where deoxygenated blood returns to the heart. At the arteriolar end, the net pressure is about +10 mmHg but -7 mmHg at the venular end.[314] This discrepancy in pressure indicates that more fluid is entering the interstitial fluid than is leaving it. Excess interstitial fluid is removed by the lymphatic system where it is then drained into the lymphatic ducts. These lymphatic ducts drain into the subclavian veins where the fluid reenters the circulatory system. Lymphatic drainage is an important mechanism to include in the model because it removes contrast agent that is otherwise assumed to pool in the interstitial fluid and contribute to signal enhancement. Additionally, the rate of lymphatic drainage is dependent on multiple factors that can vary across different contrast agents.

Furthermore, this leads to another means of removal that should be included in the vascular model, which is glomerular filtration in the renal system. The glomerulus is responsible for removing waste from the vascular system through means similar to capillary diffusion but with capillaries more porous than those surrounding muscle and soft tissue. The fenestrae in these capillaries are about 50-100 nanometers in diameter, making them about a 10-fold larger than the clefts in muscle and soft tissue.[315] There are key differences that distinguishes between tissue capillaries and glomerulus capillaries and these differences are demonstrates in the Starling equation used to model the filtration rate, shown in **equation 16**.

$$GFR = K_f \left(\left(P_{gc} - P_{bc}\right) - \left(\pi_{gc} - \pi_{bc}\right) \right) \quad \text{eq. 16}$$

In this equation, GFR is the glomerulus filtration rate, or the rate at which waste product is removed from the blood, K_f is the filtration coefficient, P_{gc} is the glomerular capillary hydrostatic pressure, P_{bc} is the Bowman's capsule hydrostatic pressure, and π is the oncotic pressure of the respective components. The filtration coefficient is calculated by taking the product of the permeability of the capillary and the filtration area of the capillary membrane. The permeability is dependent on particle size and charge; permselectivity is a term used to the capillary's ability to discriminate between anions and cations in the blood. Due to the presence of negatively charged proteoglycans along the capillary membrane, the capillaries exhibit aversion to negatively charged particles traveling in the blood while showing favoritism to positively charged particles.[316] This translates to longer filtration times for negatively charged particles and faster filtration times for positively charged particles. While glomerular filtration is negligible for short time stamps, its significance increases over time as contrast agent begins to filter out of the blood stream with the passage of time. When longer time stamps are included in the data to explore contrast agent optimization, the impact of glomerular filtration will become obvious.

Because permselectivity extends to particle size and configuration, the unique properties of each contrast agent will determine the rate of filtration at the glomerulus and the residence time in the blood.

Iodine contrast agents, such as Iohexol and Iodixanol, are small molecules about half a nanometer in length while nanoparticles can range from a few to dozens of nanometers in size. This difference is why iodine-based contrast agents have very short clearance times while nanoparticles can reside in blood for several hours. By incorporating the glomerulus filtration rate into the simulated vascular system, the length of observable contrast in a lesion due to contrast agent enhancement can be studied and compared among the different contrast agents. Residence time is a key feature in contrast agent imaging, and a longer residence time allows radiologists to work with greater flexibility. A longer residence time also delivers more consistent images since contrast agents with very short residence times often exhibit a diminishing signal in an area of interest with the passage of time.

9.2 Acquiring More Data

A set back to simulating tomosynthesis images is that it requires the acquisition of several images at different projections to create the illusion of a rotating gantry. Replicating the Hologic tomosynthesis system requires image acquisition at 15 degrees. In addition, the resolution of the images is inversely proportional to run time; by halving the resolution from 0.5mm to 0.25mm, the number of histories needed to achieve the same counting statistics quadruples. Furthermore, do reduce the noise in an FMESH tally with a resolution of 0.25mm to tolerable levels requires about 10 billion histories. This requires a run time of about 4 hours for a small breast geometry. This means it takes over two days to gather images for a full tomosynthesis scan and about 5 days to gather enough data for an iodine-based imaging scan where images are acquires below and above the iodine K-edge. A few measures were implemented to reduce the run time, such as coarsening the resolution to 0.5mm for images with lesions at stages above T1b and biasing the beam towards the region with the breast geometry, since the active area of the flat panel detector is much larger than the area needed to image a breast, especially one with a smaller volume.

Despite these efforts to minimize the run time needed to collect images for a single case, not enough cases were simulated to build a full library of breast imaging data to fully understand the relationships between the different variables studied. This includes running multiple simulations of different versions of

the same case, such as 38D sized breast with a T1b lesion placed at different locations along the ductal system and with different geometries, to fully understand the challenges in breast imaging and the limitations in each contrast agent studied. This extends to different lesion types, glandular densities, breast size, and lesion size. Hundreds of images would need to be simulated to build a wholistic data library that can be used to explore different contrast agents.

With enough data, ROC curves can be generated. ROC curves help evaluate the diagnostic ability of a binary classifier and this is done by varying the threshold of the classifying system, such as varying the minimum CNR ratio needed to classify a lesion as 'visible.' With enough data, ROC curves can be created for the different variables used to quantify the impact that each variable has on the accuracy of the system. This in-depth analysis would provide a better insight on the performance of the contrast agents and the variables that interfere with improved lesion visibility.

9.3 Validating the Phantom

An important step in phantom development is validation. A system needs to be validated to verify that it provides adequate measurements by ensuring that it can accurately replicate an empirical system. This is typically done by taking measurements at varying conditions and verifying that the measurements of the simulated system match the empirical system within a margin of error. Because the purpose of this phantom is to explore novel contrast agents, comparison between simulated and empirical results is not always possible because there is no reference data available for newly proposed contrast agents, such as TaONPs. Fortunately, enough data exists on Iodine-based contrast agents to validate the simulated results with existing data to verify that the simulated system is adequate. While this strategy provides some validation on the system's performance, eventually, the system should be validated for multiple variables. This requires exploring the performance of the contrast agents with different breast sizes and different breast densities to ensure that the measurements are within an established margin of error compared to the empirical results. This requires the collection of a large repository of sample clinical images that have properties that match the breast phantoms for accurate comparison.

The most robust method to validate a phantom would be to collect empirical measurements alongside the simulated trials; this would ensure the collection of parallel data for the two systems. This method can be implemented for existing iodine-based contrast agent but is limited by the experimentation of novel contrast agents, given that some are still being tested for patient safety. Validation with Iodine-based contrast agents should still provide enough validation that the system is running as it should. If the results of Iodine enhancement are equivalent between a simulated and empirical setting, then there is proof that the simulated system is able to replicate the delivery of the contrast agent into the breast tissue and the particle physics are properly simulated. With this information, the results collected for other contrast agents should provide enough insight on their efficacy in a clinical setting, albeit might not be 100% representative of empirically collected results. With that said, the results found with this simulated setting still provide information on the performance and efficacy of contrast agents compared to one another and still provide an indication of contrast agents that have the potential to improve sensitivity in breast imaging. By creating a simulated clinical breast imaging system with proof-of-concept techniques, the efficacy of each contrast agent can be studied from a fundamentalist perspective. Therefore, the results collected with these phantoms provide insight on the utility of proposed contrast agents.

Part 5: Conclusion

There are several computational breast phantoms available, some more sophisticated than others. These computational phantoms vary in their construction methods with recent models adapting unstructured mesh geometries while others are constructed from traditionally used voxels. Antiquated phantoms with oversimplified geometry, such as those constructed by Dance et. al., have evolved to include more complex structures including distinguishable glandular components and Cooper ligaments.[317,318] Some groups have created breast models using algorithms to introduce areas of glandular tissue among adipose tissue, such as seeding algorithm used in the UPENN phantom, created by the University of Pennsylvania.[319] This method establishes regions of glandular tissue with Cooper ligaments placed along the boundaries of each region.

The phantoms created from the seeding algorithm are built with voxels ranging from 25 to 1000 um in size. Example phantoms created using this method can be seen in **Figure 43a** with the simulated imaging results shown in **Figure 43b**; the phantoms vary in volume, but all have the same glandularity.

(a)   (b)
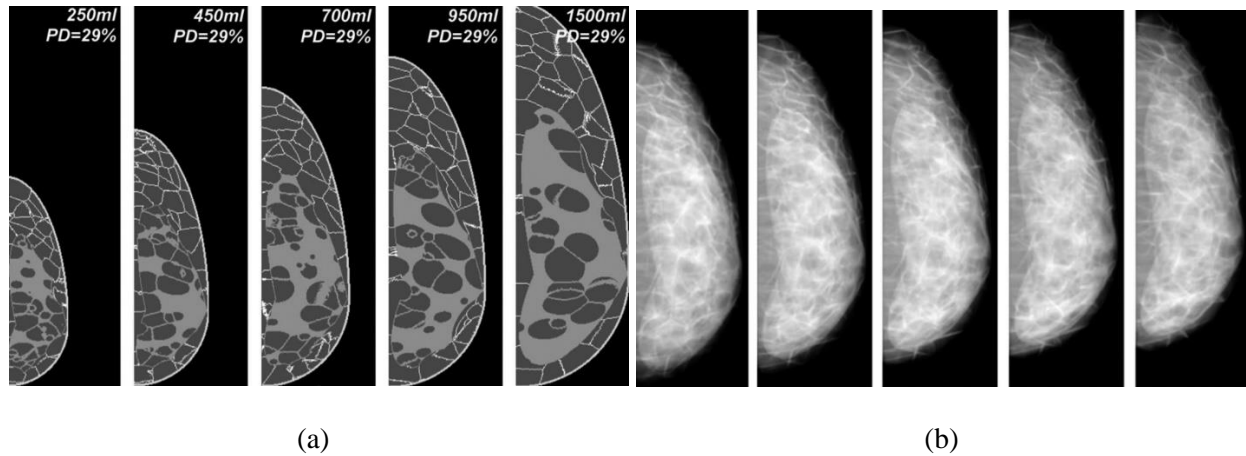
Figure 43: Phantoms created by the University of Pennsylvania using a seeding algorithm. Figure (a) demonstrates the placement of glandular tissue (light grey) among the adipose tissue while the boundaries form the Cooper ligaments (white). Meanwhile, (b) pictures the mammograms created with the phantoms.

The breast images created with the UPENN phantoms are an improvement from oversimplified models but still lack the realism that is needed to emulate clinical studies.

Some studies have created realistic breast phantoms using existing patient data, such as the phantoms created by the University of California, Davis.[320] The phantoms created by UC Davis were built from segmented breast CT images where multiple tissue classes were assigned in the images using a 3D bias-corrected fuzzy C-means clustering algorithm. These individual tissues were converted into voxels with voxel sizes ranging from 194 to 407 um in size. The resulting voxel phantom created using this method are shown in **Figure 44a** where 15 different breast models are displayed. The images vary in the glandular content, which is represented by the lightly colored regions, and clear boundaries between the glandular and adipose tissue are shown.
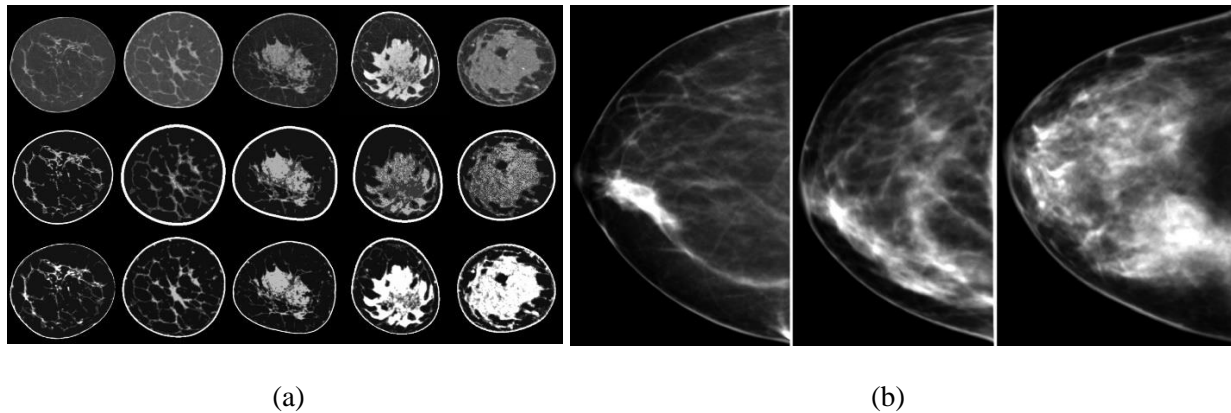
Figure 44: Phantoms created by UC Davis using patient CT data. Figure (a) pictures 15 different models created using the segmentation method and (b) pictures the mammograms resulting from the breast phantoms.

The set of images shown in **Figure 44b** picture the mammographs created with the breast phantoms, each with a different glandularity. The disadvantage to using this method, as stated by the authors, is that they are limited by the patient data available. In their study, only BI-RADS category 4 and 5 (high suspicion) images were used because they were the only images available. This imposes a challenge when introducing flexibility in the variables for patient-specific applications. Furthermore, the group aims to expand their phantom library by creating a set of basis images from the CT data that can be used as "eigenbreasts" to create new synthetic breast phantoms. There are other similarly created phantoms that vary in execution and data used.[321]

The computational phantom created in this study is unique from other phantoms in that it creates diverse models from fundamental breast components. These breast components have been studied in detail to implement as much realism and structural integrity as possible. The ductal and glandular distribution implemented in the phantoms was created from observable patterns in real breasts instead of using algorithms or Gaussian noise to imitate the appearance of glandular tissue.[322] The lack of predictable patterns used in the building methods described in this paper creates models that contain a randomized glandular structure free of symmetry. The effects of this are observed in **Figure 45** where a tomosynthesis image created from a 30B-sized breast with 15% glandularity and a T1c-staged embedded tumor constructed in this study, shown in **Figure 45b**, is compared with a mammogram of the DeBRA phantom,

shown in **Figure 45a**, and a real breast mammogram, shown in **Figure 45c**. Compared to the DeBRA

phantom, the 30B-sized breast created in this study is much less predictable and has no obvious symmetrical

patterns that are giveaway signs of a breast phantom. The image is more closely related to the real

mammogram shown in **Figure 45c**.

| (a) | (b) | (c) |
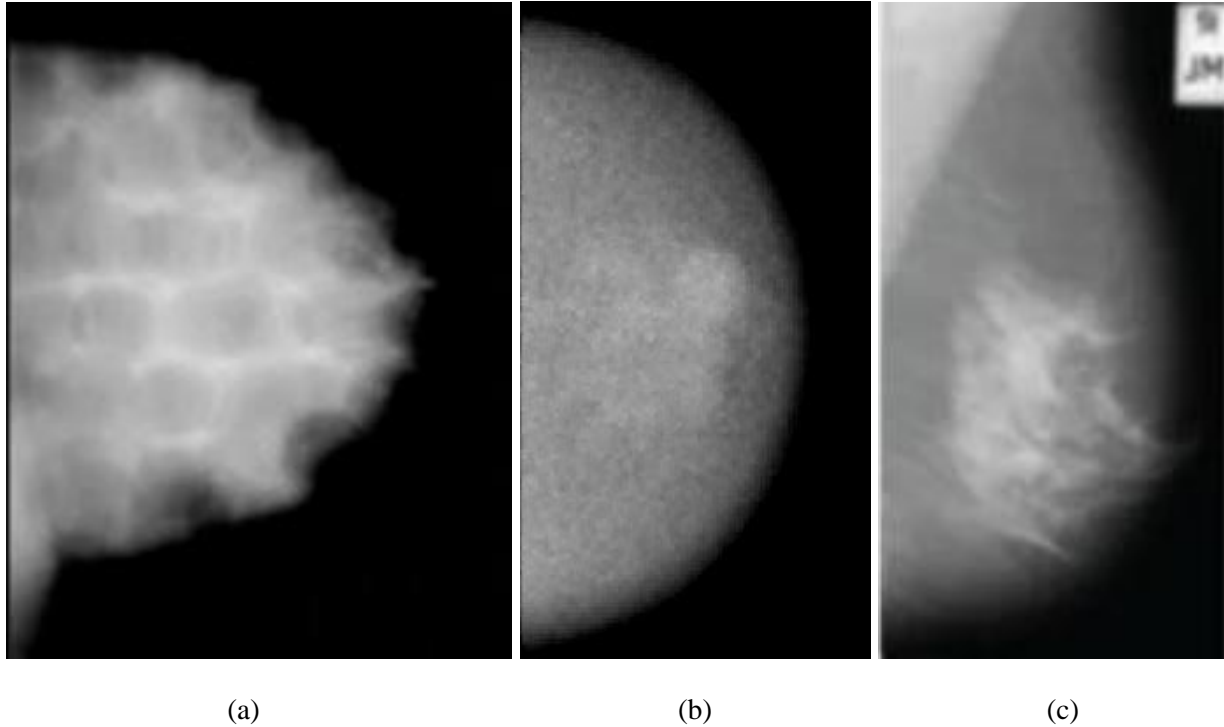
Figure 45: Comparative images of mammograms. Figure (a) depicts a simulated mammogram created with the DeBRA phantom, (b) pictures a simulated tomosynthesis slice from a 30B-sized breast with 15% glandularity created with the methods described in this paper and (c) pictures a mammogram of a real breast categorized as a BI-RADS 2 breast.

On top of creating realistic breast images, building the phantom from fundamental components

instead of segmented CT data provides the advantage of controlling every aspect of the model. This is

useful when investigating the limitations of an imaging techniques. Models built from existing patient data

have to depend on available data; studies would need to parse through thousands of images to find a

geometry that fits their specific needs, especially when investigating rare forms of breast cancer. With the

methods highlighted in this paper, the lesion can be embedded into a specific region in the breast with a

specified glandular density and a specified breast size. By controlling these different aspects of the model, the user is free to investigate imaging systems with a wide array of breast geometries that would otherwise be difficult to acquire. This phantom building method allows researchers to work with large samples sizes that are unique and incorporate the different scenarios that can be encountered during breast imaging, such as obscured breast lesions located towards the chest wall, every lesion size embedded in a wide range of breast glandularities, and various irregularly shaped lesions. Researchers can create wholistic breast phantom libraries that can be used to explore novel imaging techniques.

The phantoms are also built using unstructured meshes which provide several advantages to voxel phantoms. While they are meant to be a faster and less computationally expensive alternative to voxel meshes, they also provide flexibility in the model resolution. Voxel phantoms are restrictive in element size; if a model requires small details, the resolution needs to be small enough to accommodate these small details which means that every component built within the voxel lattice must also be created with small voxel elements. This can be computationally expensive, especially when building large phantoms. While coarsening the size of the voxels reduces run time, it also reduces the resolution of fine details that might not be accurately represented with a large voxel element size. With unstructured meshes, different mesh resolutions can exist within the same universe. Even within a geometry, the resolution of the mesh can be specified as a range instead of a specific value. This is particularly useful when creating a large shape with small details, such as a box with small holes or a cone with a small angle. In this application, the resolution of the unstructured meshes ranges from 0.08 cm to 0.5 cm which optimizes the number of elements needed to model large spaces of surrounding adipose tissue and Cooper ligaments. The unstructured meshes also provide smooth curved surfaces, something that is not quite achievable with voxel phantoms. Because the lobular components are created using a series of ellipsoids and the ducts are created using cylinders and cones, smooth curved surfaces are essential. By modeling realistic, curved surfaces, unstructured meshes replicate tissue geometries more accurately than voxel phantoms. Although it is outside the scope of this project, unstructured meshes would provide a more accurate estimate of dose imparted on glandular tissue

during breast imaging and their implementation would allow users to perform finite element analysis during post processing to comprehensively analyze dose distribution in the breast.

Finally, the breast phantoms created in this project explored a novel method to implement contrast enhancement in breast imaging, and this was achieved by implementing a vascular system that delivers contrast agent based on physiological functions. Other research groups, such as those outlined in Glick et. al., have implemented techniques to incorporate contrast enhancement during simulated breast imaging. This is done by estimating a contrast agent concentration from empirical data. They reviewed images with contrast enhanced lesions to estimate the difference in Hounsfield units before and after contrast enhancement to extrapolate a contrast agent concentration in the lesion. This requires prior knowledge on the attenuation of the contrast medium to calculate the distribution of the medium in the lesion and surrounding tissue. The limitation to this technique is that it is not robust enough to study novel contrast agents. Its utility extends to imaging applications that utilize contrast media with available reference data and with controlled settings, such as strict post injection times, since the settings in the simulated environment need to match those of the empirical environment to deliver the same contrast enhancement results.

By simulating the delivery of contrast agents from a physiological standpoint, the different factors that impact contrast agent enhancement can be studied, such as finding optimized post-injection imaging times and minimum injection volume needed to meet a visibility threshold. This also allows researchers to evaluate the performance of a contrast agent without knowing the expected results. Unlike other methods used where specific results are anticipated in their breast models, this method allows researchers to blind test new techniques without introducing biases into the data. This method also allows users to examinate an important aspect of contrast agent delivery, and that is contrast agent affinity towards lesions. Typically, iodine-based contrast solutions are assumed to have an affinity towards lesions due to the high microvascular density and capillary porosity that surrounds tumors. While this is true, the expected uptake in contrast solution does not scale linearly with lesion size. Furthermore, contrast agent distribution in the surrounding tissue is dependent on several factors, such as particle size, solution viscosity, solution

osmolality, and even composition. Factoring in the impact that each of these solution properties has on solution uptake creates a much more dependable model compared to a model that assumes contrast agent movement in the breast is static. Even iodine-based contrast agents have a very short residence time and the time at which the image is acquired post injection can play a role on the extent of observed enhancement. While some aspects of the contrast agent delivery system in this model can be improved for further accuracy, differences between contrast agent concentration between the glandular, lesion, and adipose tissue vary from in each case studied. This further proves that contrast agent enhancement can be impacted by an array of variables and accounting for those differences creates a more accurate and dependable breast model.

On top of with working with a complex breast phantom, it's critical to use the model in a highly sophisticated simulation setting to properly emulate every aspect of breast imaging. Coupling complex breast phantoms with MCNP simulations creates a highly robust environment that incorporates realistic particle physics that are observed in a clinical setting. While most critical components of Hologic's tomosynthesis system were incorporated into the simulated tomosynthesis system, there are a couple aspects of the simulated system that are lacking in performance. The tally mesh used to represent the amorphous selenium flat panel detector has a much coarser resolution compared to the real detector. Hologic's digital image receptor boasts a pixel size of 70 microns. Implementing this pixel size in MCNP would require a tally with about 14 million mesh elements. A mesh this size would require an impossibly large number of histories to reduce counting statistics to a reasonable quantity at each mesh element. It would also take a long time to process each image since the arrays resulting from such a large data set need to be parsed. Therefore, the mesh was coarsened to 250 to 500 microns, depending on the size of the lesion. The user is free to increase the resolution of the tally, but it is not recommended to do so unless a large number of histories is also incorporated into the script.

Moreover, the MCNP simulations were conducted with billions of particle histories. While these histories produced long run times, they were a compromise between fast simulations and a realistic beam density, which would have required a number of histories 5 orders of magnitude greater than the number

used in these simulations, even with beam optimization. Hence, it was expected that that the resulting images would be noisier than clinical images. Despite this limitation, the resulting mages still provided adequate CNR and SNR measurements and the standard deviation calculated for each image is within reason. Furthermore, because the number of histories used in each simulation is already at a bare minimum, an anti-scatter grid was not included in the images. Hologic uses a High Transmission Cellular (HTC) grid to reduce scattering noise in their images. While this device would have been easy to incorporate by implementing an FMESH requirement to only count photons that intercept the mesh at an angle normal to the surface, doing so would significantly reduce the efficiency of the system. This would increase the number of required histories needed to keep counting statistics within an acceptable degree. Eventually, when variance reduction techniques are implemented and faster run times can be achieved, an anti-scatter grid should be implemented to replicate the tomosynthesis device as much as possible. This will hopefully reduce noise due to scattering and results in higher contrast to noise ratio. This will be especially useful in larger breasts where more scattering is observed.

The contrast agent performance results did not provide much of an indication on contrast agents that can potentially increase lesion detection due to the small data set used. The results did, however, provide evidence on the efficacy of each one relative to the enhancement provided per unit contrast solution in the lesion tissue. Although the results did not provide insight on a potential contrast agent that far outperforms currently used iodine-based contrast agents, the results pointed out factors that can influence the enhancement provided by the contrast agents. The charts shown in **Figure 27** demonstrate a difference between the tissue distribution of Iohexol350 and tantalum nanoparticles as a function of time. This difference in distribution provides evidence that the enhancement provided by each contrast agent is optimized at different time stamps for the contrast agents studied here. By varying the timestamp in the cases studied to optimize the performance of each contrast agent studied, new trends might arise that demonstrate a correlation between a contrast agent and improved lesion detection.

The use of ANOVA testing and logistic regression to find significant results proved to be fruitful as ways to improve the data collection were highlighted. There is an urgency to collect more data with

varying lesion geometries to gather a better understanding on each contrast agent's capability to highlight lesions at various settings, such as lesion shape and stage. This thorough approach would help identify weaknesses and limitations in the contrast agents studied. The purpose of the phantom is to study contrast agents as wholistically as possible and this can only be achieved by varying every aspect of the model. Varying the physiological aspects and the structural aspects of the phantom allow users to explore every possible detail that can contribute to lesion visibility and hopefully find contrast agents that ameliorate lesion identification under a wide range of settings and geometries.

The results of this project yield a phantom capable of replicating a wide variety of breast types with various breast sizes and densities available. The phantom is created with unstructured meshes that offer flexible geometries and improved accuracy compared to voxel phantoms. The phantom has also been proven to incorporate biophysics into the model to emulate contrast agent distribution in the breast. This capability can use some improvement but otherwise provides a working model that can be used to study a wide range of contrast agents in a variety of settings. The phantom functions properly in MCNP where a realistic tomosynthesis system is incorporated to emulate a clinical setting. The breast phantom, in conjunction with the MCNP tomosynthesis setting, is capable of replicating clinical tomosynthesis. Although the detector resolution is coarse compared to the real system, the user has the option to increase the resolution if they have the resources to run simulations with billions of histories. The future work outlined in this paper provides a means to improve the currently used features in the breast model to optimize the breast phantom to its full capacity. In conclusion, the breast phantom created in this project offers several benefits and can be used to introduce a new generation of phantoms.

Bibliography

[1] Anderson, J.G. (January 1945), "William Morgan and X-rays", Transactions of the Faculty of Actuaries, 17: 219–221, doi:10.1017/s0071368600003001

[2] Glasser, Otto (1993). Wilhelm Conrad Röntgen and the early history of the roentgen rays. Norman Publishing. pp. 10–15. ISBN 978-0930405229.

[3] Markel, Howard (20 December 2012). "'I Have Seen My Death': How the World Discovered the X-Ray". PBS NewsHour. PBS. Retrieved 23 March 2019.

[4] Natale, Simone (2011-11-01). "The Invisible Made Visible". Media History. 17 (4): 345–358. doi:10.1080/13688804.2011.602856. hdl:2134/19408. S2CID 142518799.

[5] Feldman, A (1989). "A sketch of the technical history of radiology from 1896 to 1920". Radiographics. 9 (6): 1113–1128. doi:10.1148/radiographics.9.6.2685937. PMID 2685937.

[6] "Major John Hall-Edwards". Birmingham City Council. Archived from the original on September 28, 2012. Retrieved 2012-05-17.

[7] Feldman, A (1989). "A sketch of the technical history of radiology from 1896 to 1920". Radiographics. 9 (6): 1113–1128. doi:10.1148/radiographics.9.6.2685937. PMID 2685937.

[8] Glasser, Otto (1934). Wilhelm Conrad Röntgen and the Early History of the Roentgen Rays. Norman Publishing. p. 294. ISBN 978-0930405229.

[9] Hrabak M, Padovan RS, Kralik M, Ozretic D, Potocki K (July 2008). "Nikola Tesla and the Discovery of X-rays". RadioGraphics. 28 (4): 1189–92. doi:10.1148/rg.284075206. PMID 18635636

[10] Kathern, Ronald L. and Ziemer, Paul L. The First Fifty Years of Radiation Protection, physics.isu.edu

[11] Brown P. A study of the cases of accidental X-ray burns hitherto recorded. American martyrs to science through Roentgen rays. . Springfield, Illinois, Charles C. Thomas: 1936: 32

[12] Howell, Joel D. "Early clinical use of the X-ray." Transactions of the American Clinical and Climatological Association 127 (2016): 341.

[13] Strickland, Deidi, and Anthony N. Stranges. "X-rays: Laying the foundation of modern radiology, 1896-1930." Medicina nei secoli 3.2-3 (2018): 207-222.

[14] Glasser, Otto. Wilhelm Conrad Röntgen and the early history of the Roentgen rays. No. 1. Norman Publishing, 1993.

[15] Nicolaas A. Rupke, Eminent Lives in Twentieth-Century Science and Religion, page 300, Peter Lang, 2009 ISBN 3631581203

[16] Cole, Lewis Gregory. "Note on the diagnostic and therapeutic value of the Coolidge tube." Archives of the Roentgen Ray 18.10 (1914): 368-372.

[17] Breton J.L.Rayons Cathodiques et Rayons X. Librairie E, Bernard et Cie1897

[18] Behling Rolf Modern Diagnostic X-Ray Sources - Technology-Manufacturing-Reliability. (1st ed.). CRC Press - Taylor and Francis Group LLC., 2016

[19] Sharyl J. Nass; I. Craig Henderson; Institute of Medicine (U.S.). Committee on Technologies for the Early Detection of Breast Cancer (2001). Mammography and beyond: developing technologies for the early detection of breast cancer. National Academies Press. ISBN 978-0-309-07283-0.

[20] Warren, S.L. (1930). "A Roentgenologic Study of the Breast". The American Journal of Roentgenology and Radium Therapy. 24: 113–124.

[21] Diagnosis of tumors of the breast by simple roentgenography; calcifications in carcinomas. LEBORGNE R Am J Roentgenol Radium Ther. 1951 Jan; 65(1):1-11.

[22] Medich DC, Martel C. Medical Health Physics. Health Physics Society 2006 Summer School. Medical Physics Publishing. ISBN 1930524315 pp.25

[23] Shapiro, Sam; Strax, P; Venet, L (1966). "Evaluation of Periodic Breast Cancer Screening with Mammography". JAMA. 195 (9): 731–8. doi:10.1001/jama.1966.03100090065016. PMID 5951878

[24] Egan RL. Mammography. Springfield, Ill: Thomas, 1964. Google Scholar

[25] Vyborny CJ, Schmidt RA. Mammography as a radiographic examination: an overview. RadioGraphics 1989;9(4):723–764. Link, Google Scholar

[26] Wayrynen, R. E.: Fundamental aspects of mammographic receptorsfilm process. Reduced Dose Mammography, Masson Publishing pp 521-

528, Eds. W. W. Logan, E. P. Muntz, New York, NY, (1979).

[27] Ostrum BJ, Becker W, Isard HJ. Low-dose mammography. Radiology 1973;109(2):323–326

[28] Haus AG. Historical technical developments in mammography. Technol Cancer Res Treat. 2002 Apr;1(2):119-26. doi: 10.1177/153303460200100204. PMID: 12622518.

[29] Karellas, A, Harris, L. J., D'Orsi, C. J.: Small field digital Mammography with a 2048 x 2048 pixel charge coupled device. Radiology 177 pp 288 (1990)

[30] Feig SA. Mammography equipment: principles, features, selection. Radiol Clin North Am. 1987;25:897-911

[31] Pisano ED, Zuley M, Baum JK, Marques HS. Issues to consider in converting to digital mammography. Radiol Clin North Am 2007;45(5):813–830, vi. Crossref, Medline, Google Scholar

[32] Pisano ED, Hendrick RE, Yaffe MJ et al. Diagnostic accuracy of digital versus film mammography: exploratory analysis of selected population subgroups in DMIST. Radiology 2008;246(2):376–383. Link, Google Scholar

[33] Wild JJ, Reid JH. Echographic visualization of the living intact human breast. Cancer Res 1954; 14:227–282

[34] DeLand FH. A modified technique of ultrasonography for the detection and differential diagnosis of breast lesions. Am J Roentgen Radium Nuclear Med 1969; 105:446–452.

[35] Calderon C, Vilkomerson D, Mezrich R, Etzold KF, Kingsley B, Haskin M. Differences in the attenuation of ultrasound by normal, benign, and malignantbreast tissue. J Clin Ultrasound 1976; 4:249–254.

[36] Gordon PB, Goldenberg SL. Malignant breast masses detected only by ultrasound: a retrospective review. Cancer 1995;76(4):626–630

[37] Berg WA, Blume JD, Cormack JB et al. Combined screening with ultrasound and mammography vs mammography alone in women at elevated risk of breast cancer. JAMA 2008;299(18):2151–2163

[38] Skaane P, Gullien R, Eben EB, Sandhaug M, Schulz-Wendtland R, Stoeblen F. Interpretation of automated breast ultrasound (ABUS) with and without knowledge of mammography: a reader performance study. Acta Radiol

doi:10.1177/0284185114528835. Published online March 28, 2014.

[39] Stelling CB, Wang PC, Lieber A, Mattingly SS, Griffen WO, Powell DE. Prototype coil for magnetic resonance imaging of the female breast: work in progress. Radiology 1985;154(2):457–462.

[40] MR imaging of the breast: comparison with mammography and ultrasound. Heywang SH, Fenzl G, Hahn D, Krischke I, Edmaier M, Eiermann W, Bassermann R J Comput Assist Tomogr. 1986 Jul-Aug; 10(4):615-20.

[41] Jones J, Gaillard F. "MRI sequences (overview)". Radiopaedia. Retrieved 2017-10-15.

[42] Lehman CD, Isaacs C, Schnall MD et al. Cancer yield of mammography, MR, and US in high-risk women: prospective multi-institution breast cancer screening study. Radiology 2007;244(2):381–388

[43] O'Connell, Avice M et al. "Newer Technologies in Breast Cancer Imaging: Dedicated Cone-Beam Breast Computed Tomography." Seminars in ultrasound, CT, and MR vol. 39,1 (2018): 106-113. doi:10.1053/j.sult.2017.09.001

[44] Computed tomography in detection and diagnosis of breast cancer. Chang CH, Sibala JL, Fritz SL, Dwyer SJ 3rd, Templeton AW, Lin F, Jewell WR Cancer. 1980 Aug 15; 46(4 Suppl):939-46

[45] Ziedses des Plantes B. G., "Eine neue methode zur differenzierung in der roentgenographie (planigraphie)," *Acta Radiol.* 13, 182–192 (1932).10.3109/00016923209135135

[46] Tomosynthesis: a three-dimensional radiographic imaging technique. Grant DG IEEE Trans Biomed Eng. 1972 Jan; 19(1):20-8.

[47] Dobbins, James T 3rd. "Tomosynthesis imaging: at a translational crossroads." Medical physics vol. 36,6 (2009): 1956-67. doi:10.1118/1.3120285

[48] "Digital Tomosynthesis". Breastcancer.org. 2016-06-23. Retrieved 2020-04-11.

[49] Smith AP, Niklason L, Ren B, Wu T, Ruth C, Jing Z. Lesion Visibility in Low Dose Tomosynthesis. In: Digital mammography : 8th international workshop, IWDM 2006, Manchester, UK, June 18–21, 2006 : proceedings. Astley, S, Brady, M, Rose, C, Zwiggelaar, R (Eds.) (Springer, New York, 2006) pp.160.

[50] Gennaro, Gisella; Bernardi, D.; Houssami, N. (February 2018). "Radiation dose with digital breast tomosynthesis compared to digital mammography: per-view analysis". European Radiology. 28 (2): 573–581.

[51] Center for Devices and Radiological Health. "DBT Accreditation: IT'S HERE." U.S. Food and Drug Administration, FDA, https://www.fda.gov/radiation-emitting-products/mqsa-insights/dbt-accreditation-its-here.

[52] Rieder H. Radiologic examination of the stomach and intestines in the living man. Munch Med Wochenschr 1904; 51:1548-1551.

[53] Grosche, B.; Birschwilks, M.; Wesch, H.; Kaul, A.; van Kaick, G. (6 May 2016). "The German Thorotrast Cohort Study: a review and how to get access to the data". Radiation and Environmental Biophysics. 55 (3): 281–289

[54] Pasternak, Jeffrey J, and Eric E Williamson. "Clinical pharmacology, uses, and adverse reactions of iodinated contrast agents: a primer for the non-radiologist." Mayo Clinic proceedings vol. 87,4 (2012): 390-402. doi:10.1016/j.mayocp.2012.01.012

[55] Nyman U, Ekberg O, Aspelin P. Torsten Almén (1931-2016): the father of non-ionic iodine contrast media. Acta Radiol. 2016 Sep;57(9):1072-8. doi: 10.1177/0284185116648504. Epub 2016 May 25. PMID: 27225455.

[56] X-ray contrast media--an overview. Christiansen C Toxicology. 2005 Apr 15; 209(2):185-7.

[57] Fallenberg EM, Dromain C, Diekmann F et al. Contrast-enhanced spectral mammography versus MRI: initial results in the detection of breast cancer and assessment of tumour size. **Eur Radiol** 2014;24(1):256–264.

[58] Jochelson MS, Dershaw DD, Sung JS et al. Bilateral contrast-enhanced dual-energy digital mammography: feasibility and comparison with conventional digital mammography and MR imaging in women with known breast carcinoma. **Radiology** 2013;266(3):743–751.

[59] Lusic, Hrvoje, and Mark W. Grinstaff. "X-ray-computed tomography contrast agents." *Chemical reviews* 113.3 (2013): 1641-1666.

[60] (a) Mattrey, R. F.; Aguirre, D. A. Acad. Radiol. **2003**, 10, 1450

[61] Seltzer S E; Shulkin P M; Adams D F; Davis M A; Hoey G B; Hopkins R M; Bosworth M E *AJR. American journal of roentgenology (1984), 143 (3), 575-9 ISSN:0361-803X.*

[62] Eckhardt, R. (1987). "Stan Ulam, John Von Neumann, and the Monte Carlo Method" (PDF). MCNP Website - reference section.

[63] Eckert Jr., John Presper and Mauchly, John W.; Electronic Numerical Integrator and Computer, United States Patent Office, US Patent 3,120,606, filed 1947-06-26, issued 1964-02-04; invalidated 1973-10-19 after court ruling on Honeywell v. Sperry Rand.

[64] "FERMIAC", Wikipedia, 2019-08-28, retrieved 2020-01-09

[65] James, M.R. "MCNPX 2.7.x - New Features Being Developed

[66] H.L. Anderson, "Metropolis, Monte Carlo, and the MANIAC" Los Alamos Science, pp. 96-107 (Fall 1986) LA-UR-86-2600

[67] Waldby, Catherine (September 2003). The Visible Human Project: Informatic Bodies and Posthuman Medicine. Routledge. p. 4. ISBN 978-0-203-36063-7. Retrieved 2 February 2017.

[68] Tiede, Ulf; Bomans, Michael; Höhne, Karl Heinz; Pommert, Andreas; Riemer, Martin; Schiemann, Thomas; Schubert, Rainer; Lierse, Werner (1993). "A computerized three-dimensional atlas of the human skull and brain". Am. J. Neuroradiology. 14 (3): 551–559.

[69] Anderson, Casey Alan, Karen C. Kelley, and John T. Goorley. *Mesh human phantoms with MCNP*. No. LA-UR-12-01307; LA-UR-12-1307. Los Alamos National Lab.(LANL), Los Alamos, NM (United States), 2012.

[70] Anderson, Casey Alan, Karen C. Kelley, and John T. Goorley. Mesh human phantoms with MCNP. No. LA-UR-12-01307; LA-UR-12-1307. Los Alamos National Lab.(LANL), Los Alamos, NM (United States), 2012.

[71] Breast Cancer Facts and Statistics, https://www.breastcancer.org/symptoms/underst and_bc/statistics#:~:text=About%201%20in%208% 20U.S.,(in%20situ)%20breast%20cancer..

[72] Bray F, Ferlay J, Soerjomataram I, Siegel RL, Torre LA, Jemal A (November 2018). "Global cancer statistics 2018: GLOBOCAN estimates of incidence and mortality worldwide for 36 cancers in 185 countries". *Ca*. **68** (6): 394–424. doi:10.3322/caac.21492. PMID 30207593. S2 CID 5218825

[73] Bray F, Ferlay J, Soerjomataram I, Siegel RL, Torre LA, Jemal A (November 2018). "Global cancer statistics 2018: GLOBOCAN estimates of incidence and mortality worldwide for 36 cancers in 185 countries". *Ca*. **68** (6): 394–

424. doi:10.3322/caac.21492. PMID 30207593. S2 CID 5218825

[74] "Five Things Physicians and Patients Should Question". *Choosing Wisely: an initiative of the ABIM Foundation*. American College of Surgeons. September 2013. Archived from the original on 27 October 2013. Retrieved 2 January 2013

[75] "Article Tools." Journal of Oncology Practice, https://ascopubs.org/doi/10.1200/JOP.18.00796.

[76] "Financial Burden of Cancer Care." Financial Burden of Cancer Care, https://www.progressreport.cancer.gov/after/economic_burden.

[77] "Breast Cancer Early Detection." National Breast Cancer Foundation, https://www.nationalbreastcancer.org/early-detection-of-breast-cancer/..

[78]

J.G. Elmore, K. Armstrong, C.D. Lehman, S.W. Fletcher. "Screening for breast cancer." JAMA, 293 (10) (2005), pp. 1245-1256

[79]

. Soerjomataram, M. Louwman, J. Ribot, J. Roukema, J. Coebergh. "An overview of prognostic factors for long-term survivors of breast cancer." Breast Cancer Res Treat, 107 (3) (2008), pp. 309-330

[80] Close

M. Hakama, M.P. Coleman, D.M. Alexe, A. Auvinen. "Cancer screening: evidence and practice in Europe." 2008 Eur J Cancer, 44 (10) (2008), pp. 1404-1413

[81] AAPM: The American Association of Physicists in Medicine. https://www.aapm.org/meetings/amos2/pdf/42-11895-45323-762.pdf.

[82] Melnikow J, Fenton JJ, Whitlock EP, et al. Supplemental Screening for Breast Cancer in Women With Dense Breasts: A Systematic Review for the U.S. Preventive Service Task Force [Internet]. Rockville (MD): Agency for Healthcare Research and Quality (US); 2016 Jan. (Evidence Syntheses, No. 126.) Table 1, BI-RADS Breast Density Descriptions.

[83] Lynge, Elsebeth et al. "Mammographic Density and Screening Sensitivity, Breast Cancer Incidence and Associated Risk Factors in Danish Breast Cancer Screening." *Journal of clinical medicine* vol. 8,11 2021. 19 Nov. 2019, doi:10.3390/jcm8112021

[84] Sinha, Rosil. "Contrast-Enhanced Digital Mammography: Offering Patients High Sensitivity and Reliable Specificity." Collaborative Imaging, 4 Oct. 2021, https://collaborativeimaging.com/contrast-enhanced-digital-mammography-offering-patients-high-sensitivity-and-reliable-specificity/.

[85] Sudhir R, Sannapareddy K, Potlapalli A, Krishnamurthy PB, Buddha S, Koppula V. Diagnostic accuracy of contrast-enhanced digital mammography in breast cancer detection in comparison to tomosynthesis, synthetic 2D mammography and tomosynthesis combined with ultrasound in women with dense breast. Br J Radiol. 2021 Feb 1;94(1118):20201046. doi: 10.1259/bjr.20201046. Epub 2020 Dec 2. PMID: 33242249; PMCID: PMC7934319.

[86] Ghaderi, Kimeya F., et al. "Contrast-enhanced mammography: current applications and future directions." Radiographics 39.7 (2019): 1907-1920.

[87] Dromain, Clarisse, et al. "Dual-energy contrast-enhanced digital mammography: initial clinical results." *European radiology* 21.3 (2011): 565-574.

[88] BÖHLE, FLORIAN, et al. "New Iodinated Contrast Agents The Physicochemical and Biological Properties of Asymmetric Dimers." Investigative radiology 29 (1994): S264-S266.

[89] Mukundan, S., et al. "A nanoscale, liposomal contrast agent for preclincal microCT imaging of the mouse." AJR 186 (2006): 300-307.

[90] Whelehan P, Ali K, Vinnicombe S, Ball G, Cox J, Farry P, Jenkin M, Lowry K, McIntosh SA, Nutt R, Oeppen R, Reilly M, Stahnke M, Steel J, Sim YT, Warwick V, Wilkinson L, Zafeiris D, Evans AJ. Digital breast tomosynthesis: sensitivity for cancer in younger symptomatic women. Br J Radiol. 2021 Mar 1;94(1119):20201105. doi: 10.1259/bjr.20201105. Epub 2021 Jan 7. PMID: 33411577; PMCID: PMC8011263.

[91] Naeim, R.M., Marouf, R.A., Nasr, M.A. *et al.* Comparing the diagnostic efficacy of digital breast tomosynthesis with full-field digital mammography using BI-RADS scoring. *Egypt J Radiol Nucl Med* **52,** 44 (2021). https://doi.org/10.1186/s43055-021-00421-4

[92] Lei J, Yang P, Zhang L, Wang Y, Yang K. Diagnostic accuracy of digital breast tomosynthesis versus digital mammography for benign and malignant lesions in breasts: a meta-analysis. Eur

Radiol. 2014 Mar;24(3):595-602. doi: 10.1007/s00330-013-3012-x. PMID: 24121712.

[93] Sandhu, B. S., and Arvind D. Sabharwal. "Study of Effective Atomic Number of Muscle Tissue Equivalent Material Using Back-scattering of Gamma Ray Photons."

[94] Anelli, P.; Brocchetta, M.; Fretta, R.; Lattuada, L.; Mortillaro, A. Process for the preparation of triiodinated carboxylic aromatic derivatives. WO 2010105983 (A1), **2010**

[95] 10. NIST Physics Laboratory Home Page. [March 7, 2008]. http://physics.nist.gov/PhysRefData/XrayMassCoef.

[96] Gennaro G, Bernardi D, Houssami N. Radiation dose with digital breast tomosynthesis compared to digital mammography: per-view analysis. Eur Radiol. 2018 Feb;28(2):573-581. doi: 10.1007/s00330-017-5024-4. Epub 2017 Aug 17. PMID: 28819862.

[97] Ghaderi, Kimeya F., et al. "Contrast-enhanced mammography: current applications and future directions." *Radiographics* 39.7 (2019): 1907-1920.

[98] Macéa, José Rafael; Fregnani, José Humberto Tavares Guerreiro (1 December 2006). "Anatomy of the Thoracic Wall, Axilla and Breast" (PDF). International Journal of Morphology. 24 (4). doi:10.4067/S071795022006000500030.

[99] Ramsay, D T et al. "Anatomy of the lactating human breast redefined with ultrasound imaging." *Journal of anatomy* vol. 206,6 (2005): 525-34. doi:10.1111/j.1469-7580.2005.00417.x

[100] Radisky, Derek C, and Lynn C Hartmann. "Mammary involution and breast cancer risk: transgenic models and clinical studies." *Journal of mammary gland biology and neoplasia* vol. 14,2 (2009): 181-91. doi:10.1007/s10911-009-9123-y

[101] del Carmen, Marcela G., et al. "Mammographic breast density and race." *American Journal of Roentgenology* 188.4 (2007): 1147-1150.

[102] "Breast Cancer Treatment (HDQ8)" NCI. 23 May 2014. Archived from the original on 5 July 2014. Retrieved 2021. World Cancer Report 2014. World Health Oragnization 2014. pp. Chapter 5.2. ISEN 978---92-832-0429

[103] "Breast Cancer: Anatomy and Early Warning Signs." Medical News Today, MediLexicon International, https://www.medicalnewstoday.com/articles/316977#early-signs.

[104] "How Does Breast Cancer Start & Spread?: NBCF." National Breast Cancer Foundation (NBCF) | Donate Online, https://nbcf.org.au/about-breast-cancer/diagnosis/breast-cancer-anatomy/.

[105] "Stopping Tumor Cells Killing Surrounding Tissue May Provide Clue to Fighting Cancer." ScienceDaily, ScienceDaily, 4 Feb. 2016, https://www.sciencedaily.com/releases/2016/02/160204122052.htm.

[106] Boudreau, Nancy, and Connie Myers. "Breast cancer-induced angiogenesis: multiple mechanisms and the role of the microenvironment." *Breast cancer research* 5.3 (2003): 1-7.

[107] Masson N, Willam C, Maxwell PH, Pugh CW, Ratcliffe PJ: Independent function of two destruction domains in hypoxia-inducible factor-alpha chains activated by prolyl hydroxylation. EMBO J. 2001, 20: 5197-5206. 10.1093/emboj/20.18.5197

[108] Duffy AM, Bouchier-Hayes DJ, Harmey JH. Vascular Endothelial Growth Factor (VEGF) and Its Role in Non-Endothelial Cells: Autocrine Signalling by VEGF. In: Madame Curie Bioscience Database [Internet]. Austin (TX): Landes Bioscience; 2000-2013.

[109] Brown LF, Guidi AJ, Schnitt SJ, Van De Water L, Iruela-Arispe ML, Yeo TK, Tognazzi K, Dvorak HF: Vascular stroma formation in carcinoma in situ, invasive carcinoma, and metastatic carcinoma of the breast. Clin Cancer Res. 1999, 5: 1041-1056.

[110] Kurebayashi, Junichi, et al. "Expression of vascular endothelial growth factor (VEGF) family members in breast cancer." *Japanese journal of cancer research* 90.9 (1999): 977-981.

[111] Ragab, Halla Mohamed, et al. "Assessment of Ki-67 as a potential biomarker in patients with breast cancer." *Journal of Genetic Engineering and Biotechnology* 16.2 (2018): 479-484.

[112] J. Gerdes, U. Schwab, H. Lemke, H. Stein. "Production of a mouse monoclonal antibody reactive with a human nuclear antigen associated with cell proliferation" Int J Cancer, 31 (1) (1983), pp. 13-20

[113] Yerushalmi, R. Woods, P.M. Ravdin, M.M. Hayes, K.A. Gelmon. "Ki67 in breast cancer: prognostic and predictive potential" Lancet Oncol., 11 (2010), pp. 174-183, 10.1016/S1470-2045(09)70262-1

[114] R. Stuart-Harris, C. Caldas, S.E. Pinder, P. Pharoah.

"Proliferation markers and survival in early breast cancer: a systematic review and meta-analysis of 85 studies in 32,825 patients "Breast, 17 (2008), pp. 323-334

[115] Cline MJ, Battifora H, Yokota J. 1987. Proto-oncogene abnormalities in human breast cancer: correlations with anatomic features and clinical course of disease. J Clin Oncol 5:999–1006.

[116] Loibl, Sibylle, and Luca Gianni. "HER2-positive breast cancer." *The Lancet* 389.10087 (2017): 2415-2429

[117] Tsuda H, Hirohashi S, Shimosato Y, Hirota T, Tsugane S, Watanabe S, Terada M, Yamamoto H. 1990. Correlation between histologic grade of malignancy and copy number of c-erbB-2 gene in breast carcinoma. Cancer 65:1794–1800

[118] Watanabe T, Fukutomi T, Tsuda H, Adachi I, Nanasawa T,
Yamamoto H, Abe K. 1993. Determination of c-erbB-2 protein inprimary breast cancer tissue extract using an enzyme immunoas-say. Jpn J Cancer Res 84:1279–1286

[119] Dati C, Antoniotti S, Taverna D, Perroteau I, De Bortoli M. 1990. Inhibition of c-erbB-2 oncogene expression by estrogens in human breast cancer cells. Oncogene 5:1001–1006.

[120] Relative worth of estrogen or progesterone receptor and pathologic characteristics of differentiation as indicators of prognosis in node negative breast cancer patients: findings from National Surgical Adjuvant Breast and Bowel Project Protocol B-06. *Fisher B, Redmond C, Fisher ER, Caplan R J Clin Oncol. 1988 Jul; 6(7):1076-87.*

[121] P. Fausto, G. Viale, M. Cabiddu, S. Barni. "Prognostic value of different cut-off levels of Ki-67 in breast cancer: a systematic review and meta-analysis of 64,196 patients" Breast Cancer Res Treat, 153 (2015), pp. 477-491

[122] Molecular Subtypes of Breast Cancer, https://www.breastcancer.org/symptoms/types/molecular-subtypes.

[123] Anderson WF, Chatterjee N, Ershler WB, Brawley OW (2002) Estrogen receptor breast cancer phenotypes in the Surveillance, Epidemiology, and End Results database. Breast Cancer Res Treat 76:27–36

[124] Vuong, D., Simpson, P.T., Green, B. *et al.* Molecular classification of breast cancer. *Virchows Arch* **465,** 1–14 (2014). https://doi.org/10.1007/s00428-014-1593-7

[125] Horwitz KB, Koseki Y, McGuire WL (1978) Estrogen control of progesterone receptor in human breast cancer: role of estradiol and antiestrogen. Endocrinology 103:1742–1751

[126] Slamon DJ, Clark GM, Wong SG, Levin WJ, Ullrich A, McGuire WL (1987) Human breast cancer: correlation of relapse and survival with amplification of the HER-2/neu oncogene. Science 235:177–182

[127] Sorlie T, Perou CM, Tibshirani R, Aas T, Geisler S, Johnsen H, Hastie T, Eisen MB, van de Rijn M, Jeffrey SS, Thorsen T, Quist H, Matese JC, Brown PO, Botstein D, Lonning PE, Borresen-Dale AL (2001) Gene expression patterns of breast carcinomas distinguish tumor subclasses with clinical implications. Proc Natl Acad Sci U S A 98:10869–10874. doi:10.1073/pnas.191367098

[128] Parker JS, Mullins M, Cheang MC, Leung S, Voduc D, Vickery T, Davies S, Fauron C, He X, Hu Z, Quackenbush JF, Stijleman IJ, Palazzo J, Marron JS, Nobel AB, Mardis E, Nielsen TO, Ellis MJ, Perou CM, Bernard PS (2009) Supervised risk predictor of breast cancer based on intrinsic subtypes. J Clin Oncol 27:1160–1167. doi:10.1200/jco.2008.18.1370

[129] Connolly J, Kempson R, LiVolsi V, Page D, Patchefsky A, Silverberg S. Recommendations for the reporting of breast carcinoma. *Association of Directors of Anatomic and Surgical Pathology.* 2004

[130] Malhotra, Gautam K et al. "Histological, molecular and functional subtypes of breast cancers." *Cancer biology & therapy* vol. 10,10 (2010): 955-60. doi:10.4161/cbt.10.10.13879

[131] Masood, Shahla. "Breast cancer subtypes: morphologic and biologic characterization." *Women's Health* 12.1 (2016): 103-119.

[132] Martinez V, Azzopardi JG: Invasive lobular carcinoma of the breast: incidence and variants. Histopathology. 1979, 3: 467-488.

[133] Martinez V, Azzopardi JG: Invasive lobular carcinoma of the breast: incidence and variants. Histopathology. 1979, 3: 467-488.

[134] Krecke KN, Gisvold JJ: Invasive lobular carcinoma of the breast: mammographic findings and extent of disease at diagnosis in 184 patients. AJR Am J Roentgenol. 1993, 161: 957-960.

[135] Arpino, G., Bardou, V.J., Clark, G.M. *et al.* Infiltrating lobular carcinoma of the breast: tumor characteristics and clinical outcome. *Breast*

Cancer Res **6,** R149 (2004). https://doi.org/10.1186/bcr767

[136] Page DL, Kasami M, Jensen RA. Hypersecretory hyperplasia with atypia in breast biopsies, what is the proper level of clinical concern? Pathol. Case Rev. 1, 36–40 (1996).

[137] Foulkes WD, Smith IE, Reis-Filho JS. Triple negative breast cancer. N. Engl. J. Med. 363, 1938–1948 (2010).

[138] Pedersen L, Holck S, Schiodt T et al. Inter-and intraobserver variability in the histopathological diagnosis of medullary carcinoma of the breast, and its prognostic implications. Breast Cancer Res. Treat. 14, 91–99 (1989).

[139] Wargotz ES, Norris HJ. Metaplastic carcinomas of the breast. III. Carcinosarcoma. Hum. Pathol. 64, 1490–1499 (1990).

[140] Adrada B, Arribas E, Gilcrease M, Yang WT. Invasive micropapillary carcinoma of the breast: mammographic, sonographic, and MRI features. Am. J. Roentgenol. 193, W58–W63 (2009).

[141] Luna-More S, Gonzalez B, Acedo C et al. Invasive micropapillary carcinoma of the breast. A new special type of invasive mammary carcinoma. Pathol. Res. Pract. 190, 668–674 (1994).

[142] Marzullo F, Zito FA, Marzullo A et al. Infiltrating cribriform carcinoma of the breast. A clinic-pathologic and immunohistochemical study of 5 cases. Eur. J. Gynaecol. 17, 228–231 (1996).

[143] Di Saverio S, Gutierrez J, Avisar E. A retrospective review with long term follow up of 11,400 cases of pure mucinous breast carcinoma. Breast Cancer Res. Treat. 111, 541–547 (2008).

[144] Scharnhorst D, Huntrakoon M. Mucinous carcinoma of the breast: recurrence 30 years after mastectomy. South. Med. J. 1, 656–657 (1988).

[145] Cowan WK, Kelly P, Sawan A et al. The pathological and biological nature of screen-detected breast carcinomas: a morphological and immunohistochemical study. J. Pathol. 182, 29–35 (1997).

[146] Haffty BG, Perrotta PL, Ward BE et al. Conservatively treated breast cancer: outcome by histologic subtype. Breast J. 3, 7 (1997)

[147] Tavassoli FA, Devilee P. Tumours of the Breast. International Agency for Research Center, Lyon, France (2003).

[148] Abati AD, Kimmel M, Rosen PP. Apocrine mammary carcinoma. A clinicopathologic study of 72 cases. Am. J. Clin. Pathol. 94, 371–377 (1990).

[149] Holland R, van Haelst UJ. Mammary carcinoma with osteoclast-like giant cells. Additional observations on six cases. Cancer 53, 1963–1973 (1984).

[150] Tavassoli FA, Devilee P. Tumours of the Breast. International Agency for Research Center, Lyon, France (2003).

[151] Vedantham, Srinivasan, et al. "Personalized estimates of radiation dose from dedicated breast CT in a diagnostic population and comparison with diagnostic mammography." *Physics in Medicine & Biology* 58.22 (2013): 7921.

[152] Themes, UFO. "Mammography." Radiology Key, 20 Feb. 2016, https://radiologykey.com/mammography/.

[153] "What Is a Breast Mri?: Breast Cancer Screening." American Cancer Society, https://www.cancer.org/cancer/breast-cancer/screening-tests-and-early-detection/breast-mri-scans.html.

[154] HealthManagement.org. "Automated Breast Ultrasound with Computer Aided Detection." HealthManagement, 20 June 2017, https://healthmanagement.org/c/imaging/news/automated-breast-ultrasound-with-computer-aided-detection.

[155] "Giotto Class - Digital Breast Tomosynthesis Mammography Unit by IMS: Medicalexpo." The B2B Marketplace for Medical Equipment, https://www.medicalexpo.com/prod/ims/product-76442-695524.html.

[156] Gennaro, Gisella, D. Bernardi, and N. Houssami. "Radiation dose with digital breast tomosynthesis compared to digital mammography: per-view analysis." *European radiology* 28.2 (2018): 573-581.

[157] Broeders, M J M et al. "The impact of mammography screening programmes on incidence of advanced breast cancer in Europe: a literature review." *BMC cancer* vol. 18,1 860. 3 Sep. 2018, doi:10.1186/s12885-018-4666-1

[158] "Mammography-leaflet; Screening for breast cancer with mammography" (PDF). Archived (PDF) from the original on 2012-09-05.

[159] Weigel, Stefanie, et al. "Digital mammography screening: sensitivity of the programme dependent on breast density." *European radiology* 27.7 (2017): 2744-2751.

[160] Dhawan, Atam P. (2003). Medical Image Analysis. Hoboken, NJ: Wiley-Interscience. ISBN 978-0-471-45131-0

[161] Devolli-Disha, Emine et al. "Comparative accuracy of mammography and ultrasound in women with breast symptoms according to age and breast density." *Bosnian journal of basic medical sciences* vol. 9,2 (2009): 131-6. doi:10.17305/bjbms.2009.2832

[162] Macéa, José Rafael; Fregnani, José Humberto Tavares Guerreiro (1 December 2006). "Anatomy of the Thoracic Wall, Axilla and Breast" (PDF). International Journal of Morphology. 24 (4). doi:10.4067/S071795022006000500030.

[163] Berg, Wendie A., et al. "Combined screening with ultrasound and mammography vs mammography alone in women at elevated risk of breast cancer." *Jama* 299.18 (2008): 2151-2163.

[164] Lindner J.R. (2004). "Microbubbles in medical imaging: current applications and future directions". Nat Rev Drug Discov. 3 (6): 527–32. doi:10.1038/nrd1417. PMID 15173842

[165] Luo, Jun et al. "Contrast-enhanced ultrasound improved performance of breast imaging reporting and data system evaluation of critical breast lesions." *World journal of radiology* vol. 8,6 (2016): 610-7. doi:10.4329/wjr.v8.i6.610

[166] Du, Yan-Ran, et al. "Application of contrast-enhanced ultrasound in the diagnosis of small breast lesions." *Clinical hemorheology and microcirculation* 70.3 (2018): 291-300.

[167] Goscin, Christopher P.; Berman, Claudia G.; Clark, Robert A. (2001). "Magnetic Resonance Imaging of the Breast". Cancer Control. 8 (5): 399–406. doi:10.1177/107327480100800502. PMID 11579335

[168] Kuhl C, Weigel S, Schrading S, Arand B, Bieling H, Konig R, Tombach B, Leutner C, Rieber-Brambs A, Nordhoff D, Heindel W, Reiser M, Schild HH (2010) Prospective multicenter cohort study to refine management recommendations for women at elevated familial risk of breast cancer: the EVA trial. J Clin Oncol 28(9):1450–1457. doi:10.1200/JCO.2009.23.0839

[169] Krammer, Julia, et al. "Breast cancer detection and tumor characteristics in BRCA1 and BRCA2 mutation carriers." *Breast cancer research and treatment* 163.3 (2017): 565-571.

[170] Bu, Yangyang, et al. "Non-contrast MRI for breast screening: Preliminary study on detectability of benign and malignant lesions in women with dense breasts." *Breast cancer research and treatment* 177.3 (2019): 629-639.

[171] Xiao, J., Rahbar, H., Hippe, D.S. *et al.* Dynamic contrast-enhanced breast MRI features correlate with invasive breast cancer angiogenesis. *npj Breast Cancer* **7,** 42 (2021). https://doi.org/10.1038/s41523-021-00247-3

[172] Shahid, Hassan, et al. "An overview of breast MRI." *Applied Radiology* 45.10 (2016): 7.

[173] Milon, Audrey, et al. "Breast MRI: is faster better?." *American Journal of Roentgenology* 214.2 (2020): 282-295.

[174] Davis, Lauren Evoy. "Difference between a Mammogram and a Breast MRI." Verywell Health, https://www.verywellhealth.com/difference-between-a-mammogram-and-a-breast-mri-430274.

[175] Herman, G. T., Fundamentals of computerized tomography: Image reconstruction from projection, 2nd edition, Springer, 2009

[176] Žabić S, Wang Q, Morton T, Brown KM (March 2013). "A low dose simulation tool for CT systems with energy integrating detectors". Medical Physics. 40 (3): 031102. Bibcode:2013MedPh..40c1102Z. doi:10.1118/1.4789628. PMID 23464282.

[177] Wienbeck, S., Uhlig, J., Luftner-Nagel, S. *et al.* The role of cone-beam breast-CT for breast cancer detection relative to breast density. *Eur Radiol* **27,** 5185–5195 (2017). https://doi.org/10.1007/s00330-017-4911-z

[178] O'Connell, Avice, et al. "Cone-beam CT for breast imaging: Radiation dose, breast coverage, and image quality." *American Journal of Roentgenology* 195.2 (2010): 496-509.

[179] Prionas, Nicolas D., et al. "Contrast-enhanced dedicated breast CT: initial clinical experience." *Radiology* 256.3 (2010): 714-723.

[180] Hendrick, R. Edward. "Radiation doses and cancer risks from breast imaging studies." *Radiology* 257.1 (2010): 246-253.

[181] Niklason, Loren, "Breast tomosynthesis-an overview" 2018

[182] Dobbins JT, 3rd; Godfrey, DJ (7 October 2003). "Digital x-ray tomosynthesis: current state of the art and clinical potential". Physics in Medicine and Biology. 48 (19): R65–106. doi:10.1088/0031-9155/48/19/r01. PMID 14579853.

[183] Vedantham S, Karellas A, Vijayaraghavan GR, et al. Digital breast tomosynthesis: state of the art. Radiology 2015;277(3):663e84.

[184] Sechopoulos, Ioannis (2013). "A review of breast tomosynthesis. Part II. Image reconstruction, processing and analysis, and advanced applications". Medical Physics. 40 (1): 014302. doi:10.1118/1.4770281. PMC 3548896. PMID 23298127.

[185] Teertstra HJ, Loo CE, van den Bosch MA et al (2009) Breast tomosynthesis in clinical practice: initial results. Eur Radiol 20:16–24

[186] Skaane P, Gullien R, Bjorndal H et al (2012) Digital breast tomosynthesis (DBT): initial experience in a clinical setting. ActaRadiol 53:524–529

[187] Gilbert, Fiona J., et al. "Accuracy of digital breast tomosynthesis for depicting breast cancer subgroups in a UK retrospective reading study (TOMMY Trial)." *Radiology* 277.3 (2015): 697-706.

[188] Michell, M. J., and B. Batohi. "Role of tomosynthesis in breast imaging going forward." Clinical radiology 73.4 (2018): 358-371.

[189] Chae, Eun Young, et al. "Detection and characterization of breast lesions in a selective diagnostic population: diagnostic accuracy study for comparison between one-view digital breast tomosynthesis and two-view full-field digital mammography." *The British journal of radiology* 89.1062 (2016): 20150743.

[190] Alabousi, Mostafa, et al. "Digital breast tomosynthesis for breast cancer detection: a diagnostic test accuracy systematic review and meta-analysis." *European radiology* 30.4 (2020): 2058-2071.

[191] Tucker, Lorraine, et al. "Does reader performance with digital breast tomosynthesis vary according to experience with two-dimensional mammography?." *Radiology* 283.2 (2017): 371-380.

[192] Østerås, Bjørn Helge, et al. "Average glandular dose in paired digital mammography and digital breast tomosynthesis acquisitions in a population based screening program: effects of measuring breast density, air kerma and beam quality." *Physics in Medicine & Biology* 63.3 (2018): 035006.

[193] Elhendy, A; Bax, JJ; Poldermans, D (2002). "Dobutamine stress myocardial perfusion imaging in coronary artery disease". *Journal of Nuclear Medicine*. **43** (12): 1634–46. PMID 12468513

[194] Fowler, Amy M. "A molecular approach to breast imaging." *Journal of Nuclear Medicine* 55.2 (2014): 177-180.

[195] Bruening W, Uhl S, Fontanarosa J, Reston J, Treadwell J, Schoelles K. Noninvasive Diagnostic Tests for Breast Abnormalities: Update of a 2006 Review. Comparative effectiveness review no. 47. AHRQ publication 12-EHC014-EF. Rockville, MD: Agency for Healthcare Research and Quality; 2012:27–34

[196] Eo JS, Chun IK, Paeng JC, et al. Imaging sensitivity of dedicated positron emission mammography in relation to tumor size. Breast. 2012;21:66–71.

[197] Rhodes DJ, Hruska CB, Phillips SW, Whaley DH, O'Connor MK. Dedicated dualhead gamma imaging for breast cancer screening in women with mammographically dense breasts. Radiology. 2011;258:106–118.

[198] He, Peng et al. "Preliminary experimental results from a MARS Micro-CT system." *Journal of X-ray science and technology* vol. 20,2 (2012): 199-211. doi:10.3233/XST-2012-0329

[199] Cormode, David P., et al. "Atherosclerotic plaque composition: analysis with multicolor CT and targeted gold nanoparticles." *Radiology* 256.3 (2010): 774-782.

[200] Cormode, David P et al. "Atherosclerotic plaque composition: analysis with multicolor CT and targeted gold nanoparticles." *Radiology* vol. 256,3 (2010): 774-82. doi:10.1148/radiol.10092473

[201] Zhao, Li-qin, et al. "Improving image quality in portal venography with spectral CT imaging." *European journal of radiology* 81.8 (2012): 1677-1681.

[202] Fallenberg, E.M., Schmitzberger, F.F., Amer, H. *et al.* Contrast-enhanced spectral mammography vs. mammography and MRI – clinical performance in a multi-reader evaluation. *Eur Radiol* **27,** 2752–2764 (2017). https://doi.org/10.1007/s00330-016-4650-6

[203] Jong RA, Yaffe MJ, Skarpathiotakis M et al (2003) Contrast-enhanced digital mammography: initial clinical experience. Radiology 228:842–850

[204] Lewin JM, Isaacs PK, Vance V, Larke FJ (2003) Dual-energy contrast-enhanced digital subtraction mammography: feasibility. Radiology 229:261–268

[205] Koenig, Thomas, et al. "Imaging properties of small-pixel spectroscopic x-ray detectors based on cadmium telluride sensors." *Physics in Medicine & Biology* 57.21 (2012): 6743.

[206] Caschera, Luca, et al. "Contrast agents in diagnostic imaging: Present and future." *Pharmacological research* 110 (2016): 65-75.

[207] Herman, Computed tomography contrast enhancement principles and the use of high-concentration contrast media, J. Comput. Assist. Tomogr. 28 (Suppl 1) (2004) S7–11

[208] A.L. Klibanov, Ligand-carrying gas-filled microbubbles: ultrasound contrast agents for targeted molecular imaging, Bioconjugate Chem. 16 (2005) 9–17.

[209] Sosnovsky, George, and Nuti Uma Maheswara Rao. "Gadolinium, neodymium, praseodymium, thulium and ytterbium complexes as potential contrast enhancing agents for NMR imaging." *European journal of medicinal chemistry* 23.6 (1988): 517-522.

[210] McMahon, Brian K., et al. "Luminescent terbium contrast agent for bone microdamage detection." *Australian Journal of Chemistry* 64.5 (2011): 600-603.

[211] Ashokan, Anusha, et al. "A molecular receptor targeted, hydroxyapatite nanocrystal based multi-modal contrast agent." *Biomaterials* 31.9 (2010): 2606-2616.

[212] Kiessling, Fabian, and Bernd J. Pichler, eds. *Small animal imaging: basics and practical guide*. Springer Science & Business Media, 2010.

[213] D. Kim, S. Park, J.H. Lee, Y.Y. Jeong, S. Jon Antibiofouling polymer-coated gold nanoparticles as a contrast agent for in vivo x-ray computed tomography imaging J. Am. Chem. Soc., 129 (2007), pp. 7661-7665

[214] C. Peng, L. Zheng, Q. Chen, M. Shen, R. Guo, H. Wang, X. Cao, G. Zhang, X. Shi PEGylated dendrimer-entrapped gold nanoparticles for in vivo blood pool and tumor imaging by computed tomography Biomaterials, 33 (2012), pp. 1107-1119

[215] B. Zhou, L. Zheng, C. Peng, D. Li, J. Li, S. Wen, M. Shen, G. Zhang, X. Shi Synthesis and characterization of PEGylated polyethylenimine-entrapped gold nanoparticles for blood pool and tumor CTimaging ACS Appl. Mater. Interfaces, 6 (2014), pp. 17190-17199

[216] Li, Ji, et al. "A novel functional CT contrast agent for molecular imaging of cancer." *Physics in Medicine & Biology* 55.15 (2010): 4389.

[217] Popovtzer, Rachela, et al. "Targeted gold nanoparticles enable molecular CT imaging of cancer." *Nano letters* 8.12 (2008): 4593-4596.

[218] Reuveni, Tobi, et al. "Targeted gold nanoparticles enable molecular CT imaging of cancer: an in vivo study." *International journal of nanomedicine* 6 (2011): 2859.

[219] Huang, Peng, et al. "Photosensitizer-conjugated magnetic nanoparticles for in vivo simultaneous magnetofluorescent imaging and targeting therapy." *Biomaterials* 32.13 (2011): 3447-3458.

[220] Karunamuni, R., Naha, P.C., Lau, K.C. *et al.* Development of silica-encapsulated silver nanoparticles as contrast agents intended for dual-energy mammography. *Eur Radiol* **26,** 3301–3309 (2016). https://doi.org/10.1007/s00330-015-4152-y

[221] Karunamuni R, Zaki AA, Popov AV et al (2012) An examination of silver as a radiographic contrast agent in dual-energy breast x-ray imaging. LNCS - IWDM 7361:418–425

[222] Klibanov AL, Maruyama K, Beckerleg AM, Torchilin VP, Huang L (1991) Activity of amphipathic poly(ethylene glycol)-5000 to prolong the circulation time of liposomes depends on the liposome size and is unfavorable for immunoliposome binding to target. Biochim Biophys Acta 1062:142–148

[223] Bonitatibus Jr, Peter J., et al. "Synthesis, characterization, and computed tomography imaging of a tantalum oxide nanoparticle imaging agent." *Chemical communications* 46.47 (2010): 8956-8958.

[224] Oh, Myoung Hwan, et al. "Large-scale synthesis of bioinert tantalum oxide nanoparticles for X-ray computed tomography imaging and bimodal image-guided sentinel lymph node mapping." *Journal of the American Chemical Society* 133.14 (2011): 5508-5515.

[225] Chou, Shang-Wei, et al. "In vitro and in vivo studies of FePt nanoparticles for dual modal CT/MRI molecular imaging." *Journal of the American Chemical Society* 132.38 (2010): 13270-13278.

[226] Dvorak, H. F., et al. "Vascular permeability factor/vascular endothelial growth factor and the significance of microvascular hyperpermeability in angiogenesis." *Vascular Growth Factors and Angiogenesis* (1999): 97-132.

[227] Nagy, Janice A et al. "Vascular hyperpermeability, angiogenesis, and stroma generation." *Cold Spring Harbor perspectives in medicine* vol. 2,2 (2012): a006544. doi:10.1101/cshperspect.a006544

228 Maeda, Hiroshi, et al. "Tumor vascular permeability and the EPR effect in macromolecular therapeutics: a review." *Journal of controlled release* 65.1-2 (2000): 271-284.

229 Jhaveri, Aditi M., and Vladimir P. Torchilin. "Multifunctional polymeric micelles for delivery of drugs and siRNA." *Frontiers in pharmacology* 5 (2014): 77.

230 Y Noguchi, J Wu, R Duncan, J Strohalm, K Ulbrich, T Akaike, H Maeda. "Early phase tumor accumulation of macromolecules: A great difference between the tumor vs. normal tissue in their clearance rate" Jpn. J. Cancer Res., 89 (1998), pp. 307-314

231 T Konno, H Maeda, K Iwai, S Tashiro, S Maki, T Morinaga, M Mochinaga, T Hiraoka, I Yokoyama. "Effect of arterial administration of high-molecular-weight anticancer agent SMANCS with lipid lymphographic agent on hepatoma: A preliminary report" Eur. J. Cancer Clin. Oncol., 19 (1983), pp. 1053-

232 Gradishar WJ, Tjulandin S, Davidson N, Shaw H, Desai N, Bhar P, Hawkins M, O'Shaughnessy J. Phase III trial of nanoparticle albumin-bound paclitaxel compared with polyethylated castor oil-based paclitaxel in women with breast cancer. *J Clin Oncol.* 2005;23:7794–7803.

233 Aslan, Naim, et al. "Metallic nanoparticles as X-Ray computed tomography (CT) contrast agents: A review." *Journal of Molecular Structure* 1219 (2020): 128599.

234 Lee, Nohyun, Seung Hong Choi, and Taeghwan Hyeon. "Nano-sized CT contrast agents." *Advanced Materials* 25.19 (2013): 2641-2660.

235 Gao, Chunhui, et al. "cRGD-modified and disulfide bond-crosslinked polymer nanoparticles based on iopamidol as a tumor-targeted CT contrast agent." *Polymer Chemistry* 11.4 (2020): 889-899.

236 Tanaka, Masafumi, Naomi Tsujino, and Takahiro Mukai. "Preparation and Cellular Uptake of Folate-modified Lipid Nanodisks." *Chemistry Letters* 46.7 (2017): 944-946.

237 Chou, Shang-Wei, et al. "In vitro and in vivo studies of FePt nanoparticles for dual modal CT/MRI molecular imaging." *Journal of the American Chemical Society* 132.38 (2010): 13270-13278.

238 Chen, J.S., Chen, J., Bhattacharjee, S. *et al.* Functionalized nanoparticles with targeted antibody to enhance imaging of breast cancer in vivo. *J Nanobiotechnol* **18,** 135 (2020). https://doi.org/10.1186/s12951-020-00695-2

239 Iqbal, Nida, and Naveed Iqbal. "Human Epidermal Growth Factor Receptor 2 (HER2) in Cancers: Overexpression and Therapeutic Implications." *Molecular biology international* vol. 2014 (2014): 852748. doi:10.1155/2014/852748

240 Shaw, Gina. "Types of Breast Cancer: Triple Negative, ER-Positive, HER2-Positive." WebMD, WebMD, https://www.webmd.com/breast-cancer/breast-cancer-types-er-positive-her2-positive.

241 Pais, Adi, and Hadassa Degani. "Estrogen Receptor-Targeted Contrast Agents for Molecular Magnetic Resonance Imaging of Breast Cancer Hormonal Status." *Frontiers in oncology* vol. 6 100. 27 Apr. 2016, doi:10.3389/fonc.2016.00100

242 Inwald, E C et al. "Ki-67 is a prognostic parameter in breast cancer patients: results of a large population-based cohort of a cancer registry." *Breast cancer research and treatment* vol. 139,2 (2013): 539-52. doi:10.1007/s10549-013-2560-8

243 Li, Lian Tao, et al. "Ki67 is a promising molecular target in the diagnosis of cancer." *Molecular medicine reports* 11.3 (2015): 1566-1572.

244 Paulasova P and Pellestor F: The peptide nucleic acids (PNAs): a new generation of probes for genetic and cytogenetic analyses. Ann Genet. 47:349–358. 2004.

245 Vogt N and Klapper W: Variability in morphology and cell proliferation in sequential biopsies of mantle cell lymphoma at diagnosis and relapse: clinical correlation and insights into disease progression. Histopathology. 62:334–342. 2013.

246 Smolina IV and Demidov VV: Sequence-universal recognition of duplex DNA by oligonucleotides via pseudocomplementarity and helix invasion. Chem Biol. 10:591–595. 2003

247 Demidov VV and Frank-Kamenetskii MD: Two sides of the coin: affinity and specificity of nucleic acid interactions. Trends Biochem Sci. 29:62–71. 2004.

248 Yang, C., et al. "Ki67 targeted strategies for cancer therapy." *Clinical and Translational Oncology* 20.5 (2018): 570-575.

249 Inwald, E C et al. "Ki-67 is a prognostic parameter in breast cancer patients: results of a large population-based cohort of a cancer

registry." *Breast cancer research and treatment* vol. 139,2 (2013): 539-52. doi:10.1007/s10549-013-2560-8

250 Yerushalmi R, Woods R, Ravdin PM, Hayes MM, Gelmon KA. Ki67 in breast cancer: prognostic and predictive potential. *Lancet Oncol.* 2010;11:174–183. doi: 10.1016/S1470-2045(09)70262-1.

251 Urruticoechea A, Smith IE, Dowsett M. Proliferation marker Ki-67 in early breast cancer. *J Clin Oncol.* 2005;23:7212–7220. doi: 10.1200/JCO.2005.07.501.

252 Duffy, Michael J., Naoise C. Synnott, and John Crown. "Mutant p53 in breast cancer: potential as a therapeutic target and biomarker." *Breast cancer research and treatment* 170.2 (2018): 213-219.

253 Dance, David R., et al. "Breast dosimetry using high-resolution voxel phantoms." *Radiation protection dosimetry* 114.1-3 (2005): 359-363.

254 European Commission. European protocol on dosimetry in mammography. European Commission Report EUR 16263 EN (Luxembourg: EC) (1996), ISBN 92-827- 7289-6.

255 Bakic, P. R., Albert, M., Brzakovic, D. and Maidment, A. D. A. Mammogram synthesis using a 3D simulation. 1. Breast tissue model and image acquisition simulation. Med. Phys. 29, 2131–2139 (2002).

256 KW A, Alghamdi A. "Development of a realistic computational breast phantom for dosimetric simulations." *Nucl Sci Thech* 2 (2011): 147-52.

257 Fedon, Christian, Marco Caballo, and Ioannis Sechopoulos. "Internal breast dosimetry in mammography: Monte Carlo validation in homogeneous and anthropomorphic breast phantoms with a clinical mammography system." *Medical physics* 45.8 (2018): 3950-3961.

258 Dance DR, Sechopoulos I. Dosimetry in x-ray-based breast imaging. *Phys Med Biol.* 2016;**61**:R271–R304.

259 Peplow, Douglas E., and Kuruvilla Verghese. "Digital mammography image simulation using Monte Carlo." *Medical physics* 27.3 (2000): 568-579.

260 Smans, Kristien, et al. "Simulation of image detectors in radiology for determination of scatter-to-primary ratios using Monte Carlo radiation transport code MCNP/MCNPX." *Medical physics* 37.5 (2010): 2082-2091.

261 Z. Jing, W. Huda, and J. K. Walker, "Scattered radiation in scanning slot mammography," Med. Phys. 257, 1111–1117 1998.

262 I. Sechopoulos, S. Suryanarayanan, S. Vedentham, C. J. D'Orsi, and A. Karellas, "Scatter radiation in digital tomosynthesis of the breast," Med. Phys. 342, 564–576 2007.

263 Long, Daniel J et al. "Monte Carlo simulations of adult and pediatric computed tomography exams: validation studies of organ doses with physical phantoms." *Medical physics* vol. 40,1 (2013): 013901. doi:10.1118/1.4771934

264 Chao T. C., Bozkurt A., and Xu X. G., "Conversion coefficients based on the VIP-Man anatomical model and EGS4," *Health Phys.* 81, 163–183 (2001).10.1097/00004032-200108000-00010

265 Organ doses for reference adult male and female undergoing computed tomography estimated by Monte Carlo simulations. *Lee C, Kim KP, Long D, Fisher R, Tien C, Simon SL, Bouville A, Bolch WE Med Phys. 2011 Mar; 38(3):1196-206.*

266 Ay, M. R., et al. "Monte Carlo simulation of x-ray spectra in diagnostic radiology and mammography using MCNP4C." *Physics in Medicine & Biology* 49.21 (2004): 4897.

267 Khodajou-Chokami, Hamidreza, et al. "Mcnp-fbsm: Development of mcnp/mcnpx source model for simulation of multi-slice fan-beam x-ray ct scanners." *2019 IEEE International Symposium on Medical Measurements and Applications (MeMeA).* IEEE, 2019.

268 Anderson, Casey A., Karen C. Kelley, and John T. Goorley. "Unstructured Mesh Human Phantoms with MCNP." *Nuclear Science and Engineering* (2021).

269 Lee, C., D. Lodwick, and J. L. Williams. "Hybrid computational phantoms of the 15-year-old male and female adolescent: Applications to computed tomography organ dosimetry for patients of variable morphometry." *Med Phys* 35 (2008): 2366.

270 Zubal, I. George, et al. "Two dedicated software, voxel-based, anthropomorphic (torso and head) phantoms." *Proceedings of an International Workshop on Voxel Phantom Development held at the National Radiological Protection Board, Chilton, UK.* 1995.

271 Ackerman, Michael J. "The visible human project." *Proceedings of the IEEE* 86.3 (1998): 504-511.

[272] Goorley, J. T., W. S. Kiger Iii, and R. G. Zamenhof. "Reference dosimetry calculations for neutron capture therapy with comparison of analytical and voxel models." *Medical Physics* 29.2 (2002): 145-156.

[273] Talaat, Khaled, et al. "Radiation dosimetry of inhaled radioactive aerosols: CFPD and MCNP transport simulations of radionuclides in the lung." *Scientific reports* 9.1 (2019): 1-21.

[274] Kim, C. H., et al. "New mesh-type phantoms and their dosimetric applications, including emergencies." *Annals of the ICRP* 47.3-4 (2018): 45-62.

[275] Nguyen, T.T., Yeom, Y.S., Kim, H.S., et al., 2015. Incorporation of detailed eye model into polygon-mesh versions of ICRP-110 reference phantoms. Phys. Med. Biol. 60, 8695–8707

[276] "Selenia® Dimensions® Mammography System." *Hologic*, https://www.hologic.com/hologic-products/breast-health-solutions/selenia-dimensions-mammography-system.

[277] "La-UR-17-29219- Los Alamos National Laboratory." *MCNP User's Manual*. RSICC, 27 October 2017, https://laws.lanl.gov/vhosts/mcnp.lanl.gov/pdf_files/la-ur-17-29981.pdf

[278] "Standard Reference Materials." *NIST, 2022*, https://www.nist.gov/srm.

[279] Protection, Radiological. "ICRP publication 103." *Ann ICRP* 37.2.4 (2007): 2.

[280] White, D. R., R. V. Griffith, and I. J. Wilson. "ICRU Report 46: Photon, electron, proton and neutron interaction data for body tissues." *J ICRU* 24.1 (1992).

[281] Lee, Yongsook C., San Antonio, and San Antonio. "Comparison of multimodality image-based volumes in preclinical tumor models using In-Air micro-CT image volume as reference tumor volume." *Open Journal of Medical Imaging* 5.03 (2015): 117.

[282] Netter, Frank H. *Atlas of human anatomy, Professional Edition E-Book: including NetterReference. com Access with full downloadable image Bank*. Elsevier health sciences, 2014.

[283] McCunn, Don. "Underwire Charts." *Design Enterprises of San Francisco*.

[284] Hogg, Peter, Judith Kelly, and Claire Mercer. *Digital Mammography*. London, UK: Springer, 2015.

[285] Ramsay, D T et al. "Anatomy of the lactating human breast redefined with ultrasound imaging." *Journal of anatomy* vol. 206,6 (2005): 525-34. doi:10.1111/j.1469-7580.2005.00417.x

[286] Zucca-Matthes, Gustavo et al. "Anatomy of the nipple and breast ducts." *Gland surgery* vol. 5,1 (2016): 32-6. doi:10.3978/j.issn.2227-684X.2015.05.10

[287] Figueroa, Jonine D et al. "Standardized measures of lobular involution and subsequent breast cancer risk among women with benign breast disease: a nested case-control study." *Breast cancer research and treatment* vol. 159,1 (2016): 163-72. doi:10.1007/s10549-016-3908-7

[288] Mukai, Kanae, et al. "Safety of venipuncture sites at the cubital fossa as assessed by ultrasonography." *Journal of Patient Safety* 16.1 (2020): 98.

[289] Casey, Kevin, et al. "Brachial versus basilic vein dialysis fistulas: a comparison of maturation and patency rates." *Journal of vascular surgery* 47.2 (2008): 402-406.

[290] Kahraman, Halil, et al. "The diameters of the aorta and its major branches in patients with isolated coronary artery ectasia." *Texas Heart Institute Journal* 33.4 (2006): 463.

[291] Hart, M. C., M. M. Orzalesi, and C. D. Cook. "Relation between anatomic respiratory dead space and body size and lung volume." *Journal of applied physiology* 18.3 (1963): 519-522.

[292] Nori, Jacopo, and Maninderpal Kaur, eds. *Contrast-enhanced digital mammography (CEDM)*. Cham: Springer International Publishing, 2018.

[293] Pappenheimer, John R. "Passage of molecules through capillary walls." *Physiological Reviews* 33.3 (1953): 387-423.

[294] Upadhyay, Ravi Kant. "Transendothelial transport and its role in therapeutics." *International scholarly research notices* 2014 (2014).

[295] Sarin, Hemant. "Physiologic upper limits of pore size of different blood capillary types and another perspective on the dual pore theory of microvascular permeability." *Journal of angiogenesis research* 2.1 (2010): 1-19.

[296] Renkin, E. M. "Multiple pathways of capillary permeability." *Circulation research* 41.6 (1977): 735-743.

[297] "Breast Cancer - Stages." Cancer.Net, 24 May 2022, https://www.cancer.net/cancer-types/breast-cancer/stages.

[298] Teo, N. B., et al. "Vascular density and phenotype around ductal carcinoma in situ (DCIS) of the breast." *British journal of cancer* 86.6 (2002): 905-911.

[299] Mordang, J J et al. "The importance of early detection of calcifications associated with breast cancer in screening." *Breast cancer research and treatment* vol. 167,2 (2018): 451-458. doi:10.1007/s10549-017-4527-7

[300] Thomson, J., Evans, A., Pinder, S. *et al.* Growth pattern of ductal carcinoma in situ (DCIS): a retrospective analysis based on mammographic findings. *Br J Cancer* **85,** 225–227 (2001). https://doi.org/10.1054/bjoc.2001.1877

[301] Wen, Hannah Y, and Edi Brogi. "Lobular Carcinoma In Situ." *Surgical pathology clinics* vol. 11,1 (2018): 123-145. doi:10.1016/j.path.2017.09.009

[302] Britannica, The Editors of Encyclopaedia. "X-ray tube". Encyclopedia Britannica, 20 Apr. 2017, https://www.britannica.com/technology/X-ray-tube. Accessed 25 June 2022.

[303] Levick, J R (2004-06-15). "Revision of the Starling principle: new views of tissue fluid balance". *The Journal of Physiology*. **557** (Pt 3): 704. doi:10.1113/jphysiol.2004.066118. ISSN 0022-3751. PMC 1665155. PMID 15131237

[304] Roberts, W. Gregory, and George E. Palade. "Neovasculature induced by vascular endothelial growth factor is fenestrated." *Cancer research* 57.4 (1997): 765-772.

[305] Hashizume H, Baluk P, Morikawa S, McLean JW, Thurston G, Roberge S, Jain RK, McDonald DM. Openings between defective endothelial cells explain tumor vessel leakiness. Am J Pathol. 2000 Apr;156(4):1363-80. doi: 10.1016/S0002-9440(10)65006-7. PMID: 10751361; PMCID: PMC1876882.

[306] Arpino, Grazia, et al. "Infiltrating lobular carcinoma of the breast: tumor characteristics and clinical outcome." *Breast cancer research* 6.3 (2004): 1-8.

[307] Page 83 in: *Herbert Lepor (2000). Prostatic Diseases. W.B. Saunders Company. ISBN 9780721674162.*

[308] Willner, M., et al. "Quantitative breast tissue characterization using grating-based x-ray phase-contrast imaging." *Physics in Medicine & Biology* 59.7 (2014): 1557.

[309] "Hounsfield Units Archives." *Open Medscience Blog*, https://openmedscience.com/tag/hounsfield-units/.

[310] Themes, UFO. "The Physics of Tomosynthesis." *Radiology Key*, 27 Feb. 2017, https://radiologykey.com/the-physics-of-tomosynthesis/.

[311] Mittelhammer, Ron C.; Judge, George G.; Miller, Douglas J. (2000). *Econometric Foundations*. Cambridge University Press. pp. 73–74. ISBN 978-0-521-62394-0.

[312] Grimm, Lars J., et al. "Ductal carcinoma in situ: state-of-the-art review." *Radiology* 302.2 (2022): 246-255.

[313] *Do breast calcifications mean that I have breast cancer?* Cancer Center - Cancer Treatment - Portland & Vancouver. (n.d.). Retrieved July 2022, from https://www.compassoncology.com/blog/do-breast-calcifications-mean-breast-cancer

[314] OpenStax, Lumen Learning &. "Anatomy and Physiology II." Capillary Exchange | Anatomy and Physiology II, https://courses.lumenlearning.com/suny-ap2/chapter/capillary-exchange/.

[315] Deakin, Barbara Young ... [] ; drawings by Philip J.; et al. (2006). *Wheater's Functional Histology: a text and colour atlas* (5th ed.). [Edinburgh?]: Churchill Livingstone/Elsevier. p. Chapter 16. ISBN 978-0-443068508.

[316] Ebefors K, Granqvist A, Ingelsten M, Mölne J, Haraldsson B, Nyström J. Role of glomerular proteoglycans in IgA nephropathy. PLoS One. 2011 Apr 6;6(4):e18575. doi: 10.1371/journal.pone.0018575. PMID: 21494642; PMCID: PMC3071844.

[317] Dance, David R., et al. "Breast dosimetry using high-resolution voxel phantoms." *Radiation protection dosimetry* 114.1-3 (2005): 359-363.

[318] Ma, Andy KW, Spencer Gunn, and Dimitra G. Darambara. "Introducing DeBRa: A detailed breast model for radiological studies." *Physics in Medicine & Biology* 54.14 (2009): 4533.

[319] Pokrajac, David D., Andrew DA Maidment, and Predrag R. Bakic. "Optimized generation of high resolution breast anthropomorphic software phantoms." *Medical physics* 39.4 (2012): 2290-2302.

[320] Li, Christina M., et al. "Methodology for generating a 3D computerized breast phantom from

empirical data." *Medical physics* 36.7 (2009): 3122-3131.

[321] Glick, Stephen J., and Lynda C. Ikejimba. "Advances in digital and physical anthropomorphic breast phantoms for x-ray imaging." *Medical physics* 45.10 (2018): e870-e885.

[322] Chen, Feiyu, et al. "Description and characterization of a novel method for partial volume simulation in software breast phantoms." *IEEE transactions on medical imaging* 34.10 (2015): 2146-2161.